Università degli Studi della Campania *Luigi Vanvitelli*

PhD in Environment, Design and Innovation

SSD: ICAR/01 - ICAR/02

XXXI Cycle

DOCTOR EUROPAEUS

Development of an innovative breakwater for wave energy conversion

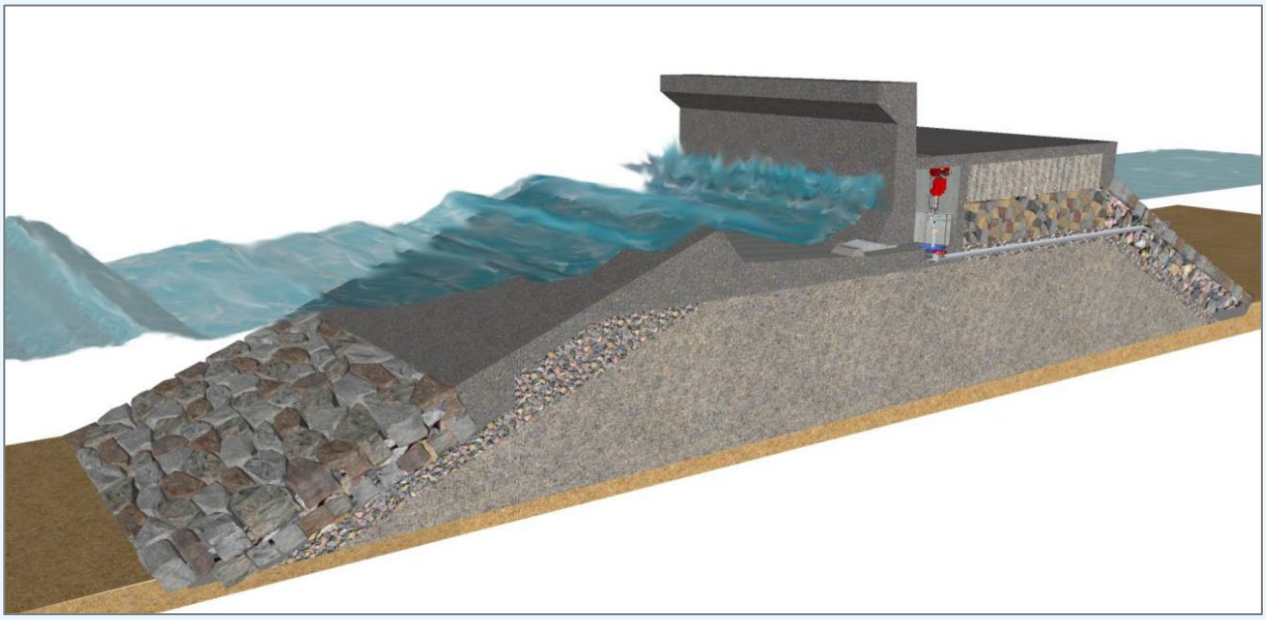

PhD Candidate: **Enrico Di Lauro**

Supervisor: Prof. Diego Vicinanza

Co-supervisors: Prof. Javier López Lara

Eng. Pasquale Contestabile, PhD

Coordinator: Prof. Mario Buono

November 2018

Scuola Politecnica e
Delle Scienze di Base
Dipartimento di Ingegneria

Dipartimento di Scienze e Tecnologie Ambientali Biologiche e Farmaceutiche

Scuola di Medicina e Chirurgia
Dipartimento di Medicina Sperimentale

Università
degli Studi
della Campania
Luigi Vanvitelli

PhD in ENVIRONMENT, DESIGN AND INNOVATION

SSD: ICAR/01 - ICAR/02

Cycle 31°

DOCTOR EUROPAEUS

Development of an innovative breakwater for wave energy conversion

Enrico Di Lauro

PhD Candidate: Enrico Di Lauro

Supervisor: Prof. Diego Vicinanza

Co-supervisor: Eng. Pasquale Contestabile, PhD

International supervisor: Prof. Javier López Lara
Environmental Hydraulics Institute "IHCantabria", University of Cantabria

Coordinator: Prof. arch. Mario Buono

November 2018

Scuola Politecnica e
delle Scienze di Base
Dipartimento di Ingegneria

Dipartimento di Scienze e Tecnologie Ambientali Biologiche e Farmaceutiche

Scuola di Medicina e Chirurgia
Dipartimento di Medicina Sperimentale

This thesis is dedicated to my beloved parents and family.

For their love, endless support and sacrifices.

Sommario

Negli ultimi decenni l'innovazione riguardante la progettazione delle opere di difesa costiera e portuale è stata principalmente orientata al miglioramento delle loro prestazioni idrauliche e strutturali. Tali miglioramenti hanno riguardato, ad esempio, la riduzione della riflessione delle onde e delle portate tracimanti l'opera, la diminuzione dei carichi impulsivi dovuti ad onde frangenti ed i loro effetti sulla stabilità globale e locale. In tali ambiti, sono stati compiuti dei progressi sostanziali nei metodi di progettazione sia di dighe marittime convenzionali che non-convenzionali, sono state altresì migliorate le caratteristiche dei materiali utilizzati e le tecniche di costruzione. L'innovazione ha riguardato anche aspetti differenti come la sostenibilità ambientale, tenendo conto, ad esempio, dell'effetto delle strutture marittime sugli ecosistemi costieri, la qualità delle acque, la morfologia e il paesaggio marino e portuale. Un'importante innovazione ha riguardato anche la visione e la fruibilità delle opere costiere che oramai non sono più delle opere strettamente di difesa, ma rappresentano anche degli spazi fruibili in maniera diversa e per diverse attività, ad esempio quella ricreativa e quella commerciale. La visione polifunzionale delle opere costiere ha permesso di ottenere una più ampia accettazione sociale dell'opera di ingegneria.

Nell'ottica di un uso polifunzionale delle opere di difesa costiera, recentemente sono nati vari progetti con lo scopo di adattare le opere di difesa costiera alla produzione di energia attraverso la trasformazione dell'energia del moto ondoso in energia elettrica. Negli ultimi anni, sono state progettate opere di difesa di nuova generazione che, attraverso l'integrazione di convertitori di energia da moto ondoso (*Wave Energy Converters, WECs*), consentono alle tradizionali opere di difesa portuale di produrre energia elettrica. Queste difese innovative aggiungono alla tradizionale funzione di protezione degli specchi d'acqua portuali, la possibilità di trasformare parte dell'energia del mare in energia elettrica. La progettazione di tali opere ha richiesto e richiede dei grandi sforzi in diversi campi della ricerca; quello che riveste un ruolo fondamentale nello sviluppo di queste opere innovative riguarda lo studio delle prestazioni idrauliche e strutturali dell'opera stessa.

Il lavoro di ricerca in epigrafe è stato condotto allo scopo di fornire un contributo effettivo allo sviluppo di un convertitore di energia dal moto ondoso denominato OBREC (*Overtopping BReakwater for Energy Conversion*). Tale dispositivo è basato sul fenomeno della tracimazione ed è stato progettato per essere integrato nelle dighe marittime tradizionali. Lo studio si è focalizzato sulla funzionalità idraulica e strutturale dell'OBREC. In particolare sono stati approfonditi gli aspetti relativi alle interazioni tra moto ondoso e struttura adoperando un approccio modellistico sia fisico che numerico . La modellazione integrata, fisica e numerica, ha permesso di ottenere di risultati di maggiore efficacia e affidabilità rispetto a quelli ottenuti con i singoli strumenti.

In particolare la modellazione parametrica in laboratorio ha consentito di ottimizzare la geometria del dispositivo, valutando l'influenza della stessa sulle sollecitazioni subite dalla struttura. Successivamente è stato utilizzato il modello numerico IH2VOF, basato su equazioni di tipo VARANS (*Volume-Averaged Reynolds Averaged Navier-Stokes*), che ha permesso di estendere ed integrare i risultati ottenuti in laboratorio. In particolare sono state ottenute informazioni estese sull'intera struttura e sul suo comportamento globale sia dal punto di vista idraulico che strutturale. Sulla scorta dei risultati ottenuti dalla modellazione in scala ridotta, sono state elaborate delle formule di progetto utilizzate operativamente durante la progettazione preliminare di un dispositivo OBREC in scala reale installato presso il porto di Napoli. Infine si è valutato, attraverso una modellazione numerica parametrica, l'applicabilità del dispositivo in esame alle dighe marittime a parete verticale.

Abstract

In recent decades, the innovations on breakwater design were mostly directed towards improving their structural and hydraulic performance. Researchers and engineers operating on coastal structure design proposed different solutions to reduce the wave reflection and wave overtopping, and to evaluate wave loads and their effects on global and local structural stability. Accordingly, substantial progress has been made on the development of new reliable methods for the design of conventional and non-conventional breakwaters. Recently, however, innovations have also covered other aspects such as the environmental integrity, taking into account, for instance, the effect of the coastal structures on marine and coastal ecosystems, water quality, morphology and seascape. An important innovation is now also directed towards the improvement of multi-purpose use, such as recreation, in order to achieve a wider acceptance of these infrastructures by the general public.

Following the concept of the multi-purpose use in coastal defence structures, researchers have proposed new ideas for these structures, transforming them into "*innovative breakwaters*". Therefore, novel breakwaters have been conceived, which consist of the integration of Wave Energy Converters (*WECs*) with traditional harbour defence structures. These innovative breakwaters still have their principal function of sheltering a location from the harmful action of the sea, but with important benefits due to the electricity production. The design of these structures requires large efforts in different research fields. Among the various aspects, the study of their hydraulic and structural response is certainly of the utmost importance to ensure the highest levels of survivability, reducing the risk of failures, which is generally very high due to the uncertainties related to their complex shape.

The present research has been conducted to close the gaps in the state of knowledge of an Overtopping WECs, named OBREC (*Overtopping BReakwater for Energy Conversion*), integrated into traditional breakwaters. The hydraulic and structural functionality of the OBREC is studied adopting a combined use of physical and numerical modelling, known in literature as *'composite modelling'*. This methodology is able to exploit the strengths and overcome the weaknesses of each approach separately.

Physical model tests allow optimizing the geometry of the OBREC embedded into rubble-mound breakwater, investigating the influence of different geometrical parameters on the wave-induced pressure and forces exerted on the model. Furthermore, a numerical model (IH2VOF), which solves the VARANS equations, is adopted to complete and extend the results obtained in laboratory. The analysis shows how the use of the numerical model can overcome some limitations of the physical model tests. In this regard, IH2VOF provides a deeper understanding of the pressure field along the different parts of the structure, in particular in locations where the laboratory measurement was not available. Moreover, the numerical model is also applied to study the influence of further geometrical parameters not tested in laboratory.

Based on the results obtained on small-scale models, a design tool for the evaluation of the wave pressure and forces exerted on the OBREC is described in the present thesis. The set of formulas has been used in the preliminary design of the first OBREC device at full-scale installed in Italy, whose performances are currently under monitoring during extreme sea conditions.

Finally, the applicability of the OBREC embedded in vertically-faced structures is examined, with a numerical study of the hydraulic and structural performance of the caisson, adopting the classical approach used for traditional coastal defence structures. Therefore, relevant phenomena such as the reflection, wave overtopping discharge at the rear side of the structure and wave pressure and forces are investigated, with a direct comparison of the numerical results with those obtained on a conventional vertical caisson.

Acknowledgements

Any doctoral dissertation could only be completed through the involvement of many mentioned and unmentioned colleagues and friends.

Firstly, I would like to express my sincere gratitude to my supervisor Prof. Diego Vicinanza, for all the support and encouragement he gave me during the last years. Without his guidance and constant feedback, this PhD would not have been achievable. I am very thankful to him for giving me the opportunity to be involved in this international project, introducing and guiding me in the field of the "*innovative breakwaters*". I would like to thank my co-supervisor Dr Pasquale Contestabile for his support of my study and research, for his motivation and enthusiasm. I am deeply grateful for the time he spent providing comments, critiques and suggestions for improvement to this research, whenever it was required. I am finally very grateful to Dr Vincenzo Ferrante for his insightful comments and for sharing with me his tremendous experience in physical and numerical modelling in coastal engineering, as well as his technical knowledge in civil engineering aspects.

During my PhD I had the unique opportunity to spent 18 months in Santander (Spain), conducting my research at the Environmental Hydraulics Institute "IHCantabria" of the University of Cantabria, under the direct supervision of Prof. Javier López Lara. He has been supportive since the first day I began working on his group and I would like to express my deepest gratitude to him for the continuous guidance of my PhD study and research, for his motivation, and wide knowledge in the coastal engineering field. His guidance helped me in all the time of my research in Spain and during the reviewing process of the present dissertation. I am very grateful to Dr Maria Maza, who assisted me with extraordinary enthusiasm during my research activity at IHCantabria, sharing her knowledge in numerical modelling and her commitment and dedication for science and research. I am finally very grateful to Prof. Iñigo J. Losada, director of the Environmental Hydraulics Institute IHCantabria, for giving me the opportunity to be part of the institute and for his valuable comments and insightful suggestions on my research.

During my experience in Santander, I have had the privilege to be assisted by many colleagues from the *"Coastal Hydrodynamics and Infrastructure Group"* of IHCantabria, which have contributed immensely to my personal and professional time there. The group has been a source of friendships as well as good advice and collaboration. I am very grateful to all of them because their help, support and stimulating discussions greatly improved the quality of my research. The assistance of many colleagues and good friends at IHCantabria was essential, making my experience in Santander exciting and fun.

This PhD thesis has required many months and hundreds of hours of hard work in the evenings, on weekends, and on holiday. It cannot be successfully completed without the understanding and support from many people. This is why I am especially deeply grateful to Carolien for her support and commitment to give me the space, undisturbed for many hundreds of hours and for her valuable assistance to improve the English language of this thesis. This dissertation would not have been possible without her love, continued patience, and endless support.

Table of contents

List of figures

List of tables

Chapter 1

Introduction

1.1 Motivation

Men have always been fascinated by waves and since ancient times they have struggled to build defence structures capable to withstand the powerful force of the ocean. Although some Roman works have endured to the modern era, very little progress in the design of breakwaters was made over their very long history. In fact, after the Roman age almost no relevant technical evolution took place until the second half of the 18^{th} century, corresponding to the Industrial Revolution. After this period, modern developments have led to a better knowledge of the wave-structure interaction, but for decades, the only principal source of guidance was the accurate study of the underlying causes of disasters of the past. Only after the end of the Second World War, relevant progress has been made in this field, with the establishment of numerous hydraulic laboratories that have become known for their research in physical modelling for coastal engineering. From then on, the progress with scale models have played an enormous role in the design of modern breakwaters, and progress in technology and facilities has evolved to the extent that physical models are now adopted as a well-established design tools for all important coastal engineering projects. In recent times a novel tool has been introduced in the design of coastal structure, based on the use of advanced numerical modelling. The combined use of the two techniques, physical and numerical modelling, is known in literature as 'composite modelling' and it is able to exploit the strengths and overcome the weaknesses of each approach separately. This integration can be considered as the most promising methodology to be adopted as a tool for the different steps in the design of the harbour defence structures. The progress in this field allows to accurately evaluate the performance of harbour defence structures with complex geometry, which are also denominated as 'non-conventional breakwaters'. These structures have the same function of the traditional rubble-mound and vertical-faced breakwaters, i.e. the wave energy reflection and dissipation, but with enhanced hydraulic performance due to their specific geometries. Some examples of non-conventional breakwaters are top sloping structures, perforated caisson breakwaters, rubble-mound breakwaters with still water basins, etc... Most of the innovations in coastal structures in recent years were directed towards improving the hydraulic performance, which consisted of the reduction of reflection and overtopping, the increasing of the structure stability and the reduction of the impact forces. Accordingly, relevant progress has been made on the development of new methods for the design of conventional and non-conventional breakwaters.

Innovations in breakwaters covered also other aspects, such as the one directed towards the improvement of multi-purpose use or hybrid structures. Following this approach, new breakwaters, here named 'innovative breakwaters', have been developed recently. They consist of the integration of Wave Energy Converters (WECs), devices able to convert energy from waves, with traditional or new coastal/harbour defence structures. This idea is one of the most promising solutions proposed by coastal engineers and scientists to reduce the costs of the WECs, which is currently still too high when compared with those of other more established renewable energy devices. Among the various lines of research in the field of the WEC-integrated breakwater, the most interesting one is the study of the wave-structure interaction, aimed to evaluate the hydraulic and structural response of these devices. Indeed, because they are still in an early stage of development, survivability is the most challenging aspect of these novel technologies. For this reason, it is necessary to design innovative breakwaters, which are reliable during ordinary operations and survivable during extreme storm events, and thus creating convincing devices able to attract stakeholders and to reduce the investment related to the risk. Only few WEC technologies are considered suitable for the integration with breakwaters. One of the latest convincing technology, is named OBREC (Overtopping BReakwater for Energy Conversion). It can be easily integrated on both rubble-mound breakwater and vertical caisson and it consists of a breakwater with an overtopping device installed on the top of it.

The main scope of this doctoral research is to contribute to the development of the OBREC, by adopting the well-established methodology used in coastal engineering to evaluate the performance of breakwaters, and by making the combined use of both physical and numerical models.

1.2 Structure of the thesis

The present thesis is structured as follows:

The present Chapter 1 describes the main scope of the research activity and the different topics covered in this thesis.

Chapter 2 is devoted to the description of the current state of the knowledge on breakwaters. First, a review of the current state of the art of the present way to conceive and design the traditional harbour defence structures is presented, comparing their pros and cons. For each of the different typologies, insights of the hydraulic and structural performances are described, indicating the worldwide accepted methods to their design. In the second part of the Chapter, the innovative breakwaters, i.e. breakwater integrated with WECs, are analysed in detail with the description of the principal technologies currently developed and the full-scale prototypes installed over the last decades. Chapter 2 introduces the latest innovation of an overtopping device integrated into a breakwater, named OBREC, whose development is the main objective of this thesis. A very brief description of the principal results of previous tests carried out on the device is presented in order to clearly understand the preliminary research activities carried out on the device before this research work.

Chapter 3 defines the principal objectives of the research work, all sharing the main motivation to fill the gaps underlined in the literature and to contribute to the development of the OBREC device. Also, the methodology followed to complete these tasks, making a combined use of the physical and numerical modelling, is presented.

In Chapter 4, the physical model tests on the OBREC device are described and the principal results of the wave pressure and forces exerted on the model are presented. The research completes the previous analysis, extending the overall knowledge of the wave-structure interaction and focusing on the influence of different geometric parameters, such as the reservoir width and the dimension and shapes of the ramp. Finally, Chapter 4 presents a new specific set of design formulas used to predict the total forces exerted on the different parts of the OBREC.

Chapter 5 presents the stability analysis of the OBREC device, carried out by combining the results of the model scale experiments and the numerical simulation based on the Volume-Averaged Reynolds-Average Navier-Stokes (VARANS) equations. The methodology named 'composite modelling' is followed to overcome some limitations of the physical model tests especially relevant for the design of a non-conventional breakwater with complex geometry such as the OBREC. The first part of the Chapter is devoted to the accurate validation of the numerical results, compared with those measured in the laboratory and described in Chapter 4. The second part describes some applications of the numerical model in order to study the influence of the submerged ramp on the uplift forces and the global stability analysis of the device.

Chapter 6 describes the first full-scale prototype of the OBREC device installed in Naples (Italy), which has been designed on the base of the results of small-scale models described in previous Chapters. The Chapter includes a description of the site where the device is installed, the geometry and the different phases of the maritime works conducted for the prototype integration into the existing rubble-mound breakwater in Naples. The second part describes the instrumental apparatus currently installed in order to evaluate its hydraulic and structural performance, as well as the performance in terms of energy production.

Chapter 7 describes an example of the application of the numerical model IH2VOF for the analysis of the wave-structure interaction on a new OTD device integrated on a vertical caisson. The Chapter starts with the description of the numerical model set and then describes the results of wave reflection, wave overtopping and wave loadings on the innovative caisson, compared with the ones computed on a traditional vertical-face structure using the same numerical model-set up.

The conclusions of this thesis are discussed in Chapter 8, with the description of the principal results obtained from this research activity and the scientific contribution yielded to science. Finally, some future lines of investigations on OBREC device and new hybrid breakwaters are delineated.

Chapter 2

State of the art

2.1 Traditional breakwaters

2.1.1 Introduction

Traditional breakwaters are coastal structures built with the objective of preventing shoreline erosion and flooding of the hinterland. Moreover, harbour breakwaters are constructed to create sufficiently calm waters for safe mooring and loading operations, handling of ships, and protection of harbour facilities. These structures are also built to improve manoeuvring conditions at harbour entrances and to help regulate sedimentation by directing currents and creating areas with different levels of wave disturbance. Protection of water intakes for power stations and protection of coastlines against tsunami waves are other applications of breakwaters.

The principal concern in the complex design process for a breakwater is to achieve required levels of wave protection in the harbour during service and extreme wave conditions. The degree of shelter required depends on harbour usage and is strongly influenced by the economics of the port operation. Wave protection is achieved by ensuring that the plan configuration and the breakwater length and height are sufficient to limit waves penetrating to sensitive areas of the harbour at selected return periods or probabilities. These considerations influence the position and length of the breakwater, principally set by levels of wave diffraction, and its freeboard, generally set so that wave transmission and overtopping over the structure is not excessive. The main hydraulic requirement is to limit any wave overtopping to acceptable levels and protect the material behind or below the breakwater from erosion by direct or indirect wave forces. A secondary consideration, but often presented as the major design case, is that any such structure should remain stable up to a given design condition, and/or that any damage should be restricted to given limits.

Despite the different typologies and specific performance, all these structures have the main function of dissipating the energy of the incoming waves. In detail, part of the wave energy is reflected and the other part is dissipated due to the wave breaking and penetration inside the porous media. The remaining part of the energy is then transmitted at the rear side of the structure due to the overtopping phenomena. Although many diverse structures are used throughout the world, conventional breakwaters can be mainly classified into rubble-mound and vertical caissons. Details of each of the two typologies are provided in the next sections, describing materials and basic design criteria used to evaluate the hydraulic performance and structural response against wave attack. A final section is devoted to the description of breakwaters with non-conventional geometries such as trapezoidal or top-sloping caissons, as well as curved slit and perforated breakwaters. Please note that the present section does not intend to provide a comprehensive description of all the characteristics and features of coastal structures, but aims to present to the reader a synthetic view of the current state of the art and the present way to conceive and design the traditional coastal structures.

2.1.2 Rubble-mound breakwaters

2.1.2.1 General description

Rubble-mound breakwaters are the most ancient maritime structures build to protect the coast and harbour against the action of the waves. Breakwater constructed in ancient times were presumably simple mounds made from stones, although already around 1800 B.C. a stone masonry was constructed in Alexandria, Egypt [239]. The oldest known coastal defence structure is the Wadi el-Jarf breakwater in the western coast of the Gulf of Suez (ca. 2600-2550 B.C.). The complex was discovered in 2008 by a joint team of the University Paris-Sorbonne and the French Institute in Cairo and it constitutes the most complete and the oldest port complex ever discovered in the world [245]. The port of Byblos (Lebanon) is from the same period, although located inside a natural cove with no known port structures [54]. Taking a brief historical look at modern rubble-mound breakwaters, thus not considering ancient ports, it seems evident that these structures have been over- or undersized with the result that very few are still well preserved today, while many others have been destroyed and are now are partly submerged [83].

The reason for many failures has primarily been the very poor understanding of the physic of rubble-mound breakwater and their interaction with waves and, as a result, a lack of application and safe engineering approaches were used in their design. Therefore, for a long time, these structures were designed based on experience gained from neighbouring breakwaters or structures, which the engineers judged to be similarly exposed [131]. The design of rubble-mound breakwater changed very little from its original concept, as opposed to other structures to which substantial innovations were applied. The development is mostly related to the deeper knowledge of wave-structure interaction as well as the progress made in the characteristics of materials and the construction technique. The overall breakwater conception, though, can be considered the same throughout its long history.

In the past as well as so nowadays, a conventional rubble-mound breakwater simply consists of *'a pile of junk'*, with rocks sorted according to their unit weight: smaller gravels for the central core and larger stones as armour layer to protect the less massive rock core from wave attack. A typical cross-section of a rubble-mound breakwater with a crown-wall is shown in Fig. 2.1.

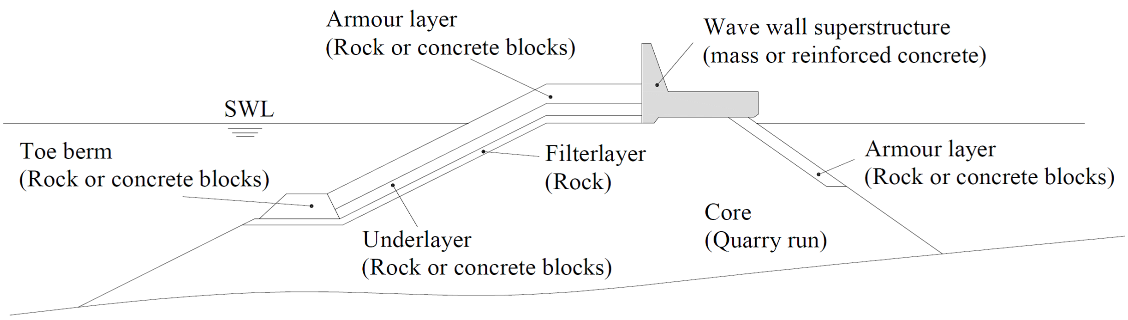

Fig. 2.1 Example of multi-layer rubble-mound breakwater with crown-wall

In detail, the structure consists of a core of sand, gravel or quarry run of the most economically available size. The core is the internal part of the structure, almost completely subtracted from the wave motion, apart during the construction phase. The ideal core of a rubble-mound has a uniform grading over a wide range of sizes so that, except in the immediate vicinity of exposed faces, fine material cannot be drawn out by wave action, ensuring low permeability in respect of wave transmission. The core is covered by one or more filter layers of grater stone dimension, adopted to prevent finer material being washed out through the armour layer due to the infiltration and exfiltration wave motion. The outer side directly exposed to the wave motion is the armour layer, consisting of natural massive rocks or artificial pre-cast concrete units of various geometries and shapes. The armour layer is probably the most important feature of a rubble-mound breakwater since damage or failure can lead to the failure of other parts (such as the collapse of the crest structure or erosion of under-layers and core material). The lower part of the armour layer is usually supported by a toe berm, except in cases of shallow-water structures. The front slope of the armour layer is in most cases straight. However, an S-shaped front or a front with a horizontal berm might be used to increase the armour stability and reduce the overtopping. A concrete crest superstructure may be constructed at the top of the mound. It can be a simple structure, whose only function is to provide an access roadway for vehicles, including cranes for inspection and maintenance, or a massive structure with a crow-wall to prevent or reduce the overtopping and incorporating land side features required for services or other commercial activities [2]. The superstructure is usually constructed in concrete and it is also called wave screen, crown-wall or parapet wall. The use of rubble-mound breakwaters especially in shallow water areas has several advantages when compared to other breakwater typologies. Firstly, the use of natural material reduces the cost, especially when a large amount of rock is available. The construction of a rubble-mound breakwater is often accomplished from land using trucks and crane, thus large-scale construction equipment (work barges) are not required. Finally, the sloping porous structure ensures high energy absorption and low reflection in front of the structure, reducing problems for navigation caused by the reflected waves.

Detailed description of the different types of breakwaters, their typical cross-sections, materials and construction methods and procedures can be found in many dedicated scientific books and monographs such as Jensen [131], Van der Meer [265], Agerschou [3], van der Meer and Sigurdarson [264] and guideline manuals such as USACE [259], the British Standards [2], USACE [260], the Rock Manual [220] and Spanish Standards (ROM 1.0-09) [68].

2.1.2.2 Hydraulic response

The design of a rubble-mound breakwater involves the accurate study of the interaction between the structure and the incident waves. This complex hydraulic interaction consists of four fundamental aspects (Fig. 2.2): the oscillation of the free surface on the armour layer (run-up and run-down), the wave penetration, the overtopping at the rear side of the structure and the wave transmission behind the structure created by the concomitance of the first phenomena. The study of these aspects, as well as the wave reflection pattern in front of the structure, is of fundamental importance for the design of rubble-mound breakwaters and these phenomena are generally included under the general definition of 'hydraulic response' of the structure.

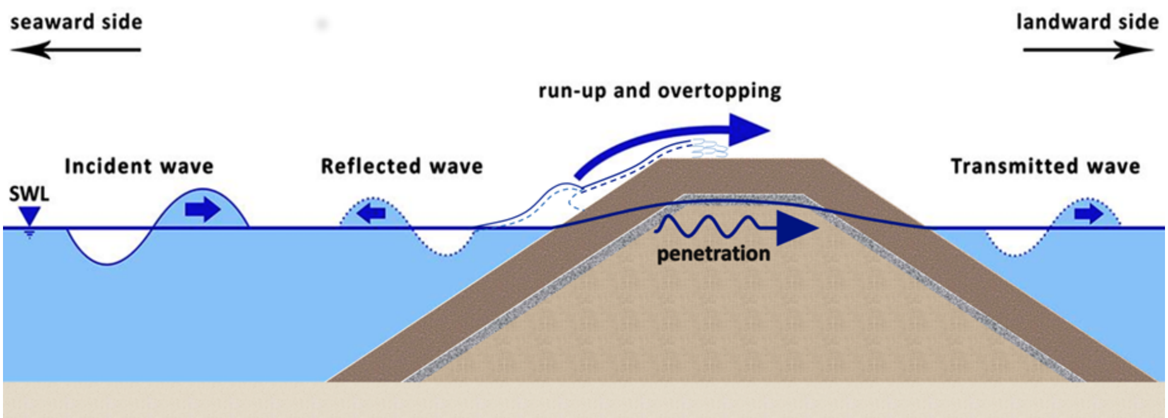

Fig. 2.2 Hydraulic performance of a rubble-mound breakwater

Design methods to predict the hydraulic response of sea defences and related coastal or shoreline structures might be developed using empirical, physical and numerical techniques. However, most of the present-day engineering design techniques were developed using laboratory test, and numerous theoretical developments and numerical results have relied on laboratory experiments for validation. Typically such models represent a structure cross-section in a 2-dimensional model tested in a wave flume. Structures with more complex plan shapes, junctions, transitions etc., may be tested in a 3-dimensional model in a wave basin. Physical models can be used to measure many different aspects of overtopping, such as individual overtopping wave volumes, overtopping velocities and depths, as well as other responses such as the run-up, run-down, wave reflection and transmission.

Even if physical modelling is well established as a valuable coastal engineering tool to predict the hydraulic performance of the rubble-mound breakwater, during the last decade, an impressive research progress has been made in the capabilities of the numerical models, making this latter tool suitable for more detailed structure design purposes. Guidance on wave run-up, overtopping and design methods for the evaluation of the hydraulic performance of rubble-mound breakwater are the results of the last 60 years of laboratory test on coastal structures, whose fundamental results are included in manuals such as the British Standards [2], USACE [260], the Rock Manual [220], and recently incorporated in the EurOtop [74]. Significant new information was collected in the DELOS Design Guidelines [146] and the CLASH project (*www.clasheu.org*) gathering data from several nations, and further advances from national research projects.

2.1.2.3 Structural response

The response of a rubble-mound breakwater under the hydraulic loadings is often indicated as the 'structural response'. The design tools allow to predict the weight and size of the armour units that compose the different porous layers of a traditional breakwater as well as the concrete crow-wall. Many methods for the prediction of the rock size of breakwater have been proposed in the last 60 years mainly based on semi-empirical relations obtained after physical model tests on rock structures.

The most important and largely adopted design formulas to obtain the weight of the armour layer units on breakwaters are those proposed almost 60 years ago by Hudson [119], based on the model tests with regular waves on non-overtopped rock structure with a permeable core. The great advantage of the Hudson formula is its simplicity and the wide range of armour units and configuration for which the relation has been derived. However, as underlined in Van der Meer [265], the Hudson formula has some limitations, such as the use of regular waves. Moreover, it does not take into account some factors which can be expected to have an influence on the rock stability such as: the wave period and the storm duration, the permeability of underlayer material, the damage level and the breaking wave conditions. To overcome these limitations, new formulas were proposed as a result of a research programme on the stability of rubble-mound revetments and breakwaters carried out at the Delft Hydraulics Laboratory and reported by Van der Meer [265]. These formulas have been widely used and tested since 1988 and more recently their field of application has been extended by Van Gent et al. [270] to take into account the shallow-water conditions. For an in-depth literature review of the other empirical methods for the design of the armour unit size required for the stability of conventional rubble-mound breakwaters, the readers are referred to the work recently presented by Herrera et al. [108]. Regarding the core and filter layers, the stability of the materials with different size has been evaluated through experimental tests, providing simple rules of thumb [259] for filter layers and core, suggesting to design their units with a weigh proportional to that of the armour layer. The overtopping at the rear side of a breakwater is often reduced through the design of a crest structure. These structures have a weight designed to resist the wave force acting on the front face and the underside of the crown-wall and their stability is verified as the traditional gravity based structure. Failure modes for crest structure can be divided into those depending on the strength of the materials (breakage) and those depending on the interaction with the material, typically the core, on which the structure is placed (sliding and overturning). Jensen [131], Bradbury et al. [36], Pedersen and Burcharth [213] and Pedersen [212] provided formulation to estimate the resultant horizontal force and overturning moment on the crest structure. Contrary, methods proposed by Iribarren and Nogales [124], Günbak and Gökce [102], and Martin et al. [173] define the force considering the pressure diagram along the crown-walls. Studies carried out by Braña and Guillén [37] and Negro Valdecantos et al. [193] indicated a heavy dispersion of the results between the different formulations, suggesting to use more than one method to design crest structure. In detail, Braña and Guillén [37] pointed out that the method presented by Pedersen [213] is the most reliable for the estimation of the maximum horizontal and vertical force on the crown-wall.

2.1.3 Vertical breakwaters

2.1.3.1 General description

Besides rubble-mound breakwaters, vertical-face structures are among the oldest and most used breakwater. Caissons in civil and military engineering have been used since the era of the Roman Empire [83] and nowadays they are built to protect harbours against the wave action. The energy of incident waves is almost completely reflected back to the sea, particularly for the high crest and non-overtopped structures traditionally designed in Europe, more precisely in Italy and Spain. For relative low-crest structures (typically designed in Japan) the energy is dissipated and partially transmitted into harbour due to the overtopping or by penetration through the foundation for composite structure (2.4). Vertical-face structures are typically used in coastal regions with low tide level and in water with sufficient depth where the wave breaking is not an issue and the use of the rock material for rubble-mound breakwater would be not economically feasible. The largest number of vertical breakwaters has been built along the Mediterranean coast and in Japan. Contrary to the European countries, in the history of the harbour construction in Japan, vertical breakwater have been built to withstand breaking waves. The large use of this typology in Japan is primarily due to the difficulties to quarry a sufficient amount of large-sized rock. Moreover, the adoption of vertical caissons in Japan has been then reinforced by many successful experiences in the design and construction of these breakwaters from the beginning of the last century [95]. A detailed historical development of vertical breakwaters, from the first primitive examples of caissons used in Roman times to the more recent structures, can be found in [81, 239, 56].

Fig. 2.3 shows the sections of a typical conventional caisson breakwaters with vertical front (on the left panel) and vertical composite caisson breakwater (on the right panel).

For traditional structures, the central part and the superstructure are composed by a single vertical element, constructed with prefabricated caissons, massive concrete blocks,

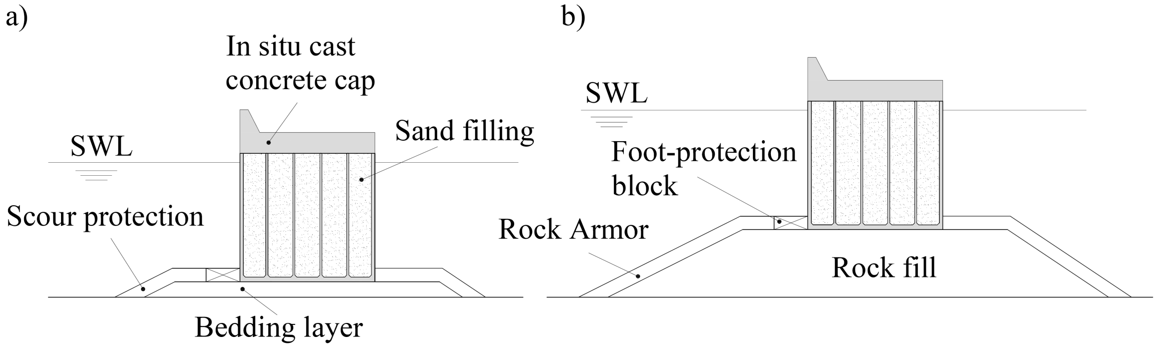

Fig. 2.3 Example of a conventional caisson breakwater with vertical front (panel a) and vertical composite caisson breakwater (panel b)

sheet piles, etc. The conventional caisson is placed on a relatively thin stone bedding layer (Fig. 2.3a), while a vertical composite breakwater is usually built on a high rubble-mound foundation made of a granular material, adequately protected so as to guarantee its stability against sea oscillations (Fig. 2.3b). The latter typology of a vertical breakwater is economical in deep waters. The foundation generally consists of a quarry run base, levelled at a depth that permits the establishment of the central portion so that its stability is not affected by the oscillations of the sea. To protect the foundation and the seabed against possible erosion, a toe berm is typically built, consisting of the extension of the quarry run central portion and the necessary number of armour layers. A guard block is also frequently placed on the berm and attached to the central portion of the breakwater aiming to reduce or produce a phase lag in the uplift pressure peak on the seaward edge of the foundation in relation to the pressure peak on the breakwater wall [68]. The superstructure is usually crowned with a parapet, also called wave screen, that can have a flat or curved seawards, which facilitates flow return. The large use of vertical breakwaters, especially in deep water, is justified by the fact that it represents a better alternative compared to the traditional rubble-mound breakwaters, mainly in terms of quantity of materials and reduction of maintenance costs, considering that the blocks of rubble-mound breakwater require relatively frequent maintenance efforts. Great advantages of this typology are also the construction rapidity, the reduction of failure during construction and the smaller environmental impact during construction. Please consider that in many cases or coastal regions, as in the Japanese case, the use of vertical structure might be the only option due to the limited availability of large-sized rocks.

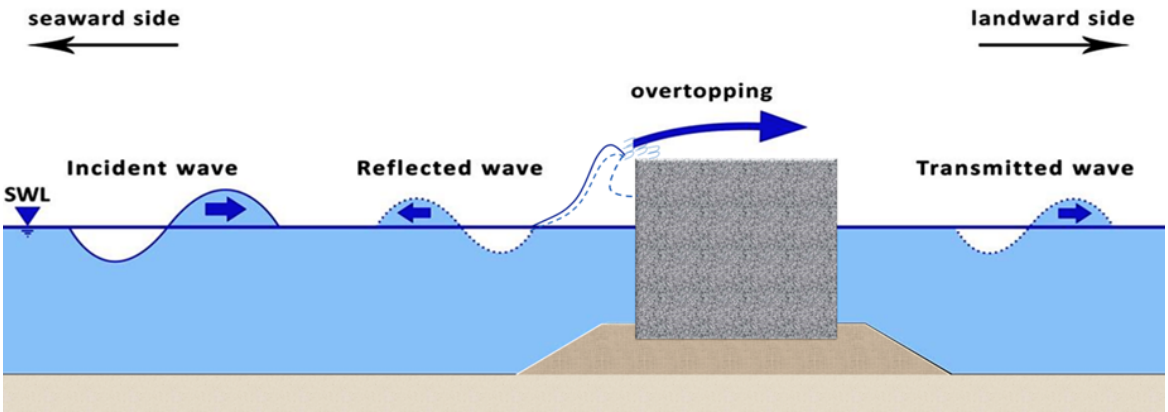

Fig. 2.4 Hydraulic performance of a vertical breakwater

2.1.3.2 Hydraulic response

Vertical-faced breakwaters are originally developed to reflect all the incident waves, which do not overtop the structure. The reflection coefficient, K_r, for non-breaking to slight breaking waves and non-overtopping condition ranges from 0.7 to 0.9 as shown by Allsop et al. [10]. Lower values must be adopted due to the effect of rubble-mound foundation and wave overtopping. In this case, K_r is considerably reduced because of the wave breaking on the breakwater, with a reflection coefficient that ranges from 0.5 to 0.7. In detail Tanimoto [247] shows that the K_r tends to decrease with the increase of the ratio between the incident significant wave height and the depth in front of the breakwater, which is a principal factor representing the degree of breaking. Moreover, K_r increases with the increase of the relative freeboard (ratio between the crest of the structure and the incident significant wave height) since the latter strongly influences the overtopping rate.

The wave transmitted behind vertical structures is principally caused by the overtopping and secondarily due to the wave penetration through the porous mound foundation. However, the governing parameter for transmission coefficient, K_r, is the relative freeboard. Empirical formulas for the determination of transmission coefficient based on regular wave test is indicated in Takahashi [239], showing the strong influence of K_r on the relative freeboard.

Wave overtopping is a relevant aspect for the design of the crest level of vertical structures. In detail, the crest level must be large enough to prevent excessive water discharge at the rear side of the structure. Wave overtopping is primarily governed by the absolute height of individual waves relative to the crest elevation of the caisson. Goda [95] provides simple design diagrams for the estimation of wave overtopping rates of vertical revetment with and without protection by concrete armour blocks, based on irregular wave tests and calculation of wave deformation on surf zone. An alternative approach was developed by Franco et al. [84] and included into the EurOtop [73]. Recently, Bruce et al. [41] proposed to divide vertical structures in structures at relatively deep water without a sloping foreshore and seawalls at the end of such a sloping foreshore. Furthermore, for an influencing foreshore, e.g. for relative intermediate and shallow water, Bruce et al. [41] divided the case in which there is or not an impulsive overtopping condition, providing for each of these conditions different semi-empirical formulas. This scheme, with slightly different formulas than those proposed by Bruce et al. [41], was recently presented in the second edition of the EurOtop [74] in 2016. The EurOtop [74] includes also some reduction coefficients which take into account the effect of oblique waves, as well as the effect of bullnose / wave-return walls used with the design motivation of reducing wave overtopping by deflecting up-rushing water back seawards.

2.1.3.3 Structural response

Regarding the wave pressure acting on a vertical structure, extensive research has been carried out starting from the first simple formula developed in 1919 by Hiroi [110]. Hiroi's formula was based on field measurements and, although the author measured a relatively high impact on localized area [95], he assumed that the pressure distribution would be uniform along the vertical direction of the structure. Hiroi's formula was apparently used for the estimation of the loading caused by breaking waves and it was used in breakwater design in Japan for more than 60 years.

In 1928, Sainflou [223] derived a wave pressure formula at wave crest and trough for standing waves, with a maximum pressure at still water level. The formula acquired immediate acceptance by coastal engineers and has been used throughout the world for many years. Prior to the development of Goda's formula, engineers in Japan recommend using Hiroi's formula for breaking waves and Sainflou's formula for non-breaking waves. However, in Japan, the use of the Sainflou's formula was not frequent because design waves are relatively large and the majority of the breakwaters at that time in Japan were built primarily to withstand breaking waves [95].

Waves breaking directly against a vertical-face structure exert high, the short-duration dynamic pressure that acts near the region where the wave crest hits the structure. Impact (impulsive) wave pressure is one of the most important problems in the design of a vertical breakwater, and its effects on breakwater structural response must, therefore, be evaluated thoroughly. Based on the first analysis on impact loading discussed by Bagnold [21], Minikin

[179] developed a formula in the early 1950's to estimate wave impact pressure due to waves breaking directly on a vertical breakwater or seawall. Please note that Minikin's method is unfortunately described incorrectly in USACE [259]. In the original publication by Minikin [179], the pressure exerting on the vertical-face structure was expressed in tonnes per square foot, which is not correct. It should be ton force per square foot. This mistake was overseen in conversion to SI units for the USACE [259] and has lead to a formula for maximum pressure which gives values that are far too large. This is why many publications warn against Minikin's method, mentioning that the equation gives values that are 10 to 15 times too large, while the original method actually gave far lower values.

In 1973, Goda [93] used his own theoretical consideration [97] and laboratory data [96] carried out using monochromatic waves, to propose a new set of wave pressure formulas for an upright section of vertical breakwaters. Goda's method represents the world's famous and most adapted for the design of vertical breakwater, which assumes the existence of a trapezoidal pressure distribution along the vertical structure, regardless of whether the waves in front of it are breaking or not breaking. In 1985 Goda [94] gives an insight of the heights of random waves to be used in the formulas in and near the surf zone. The method also one of the first that also provides an estimation of the up-lift forces under the caisson base, and thus the total overturning moment around the hill of the upright section can be evaluated for stability analysis. The resulting prediction forces are compared by the authors with very few experiments. However, much of the confidence of the Goda's formula stems from their success in predicting the sliding failure of full-scale breakwaters along the Japanese coast with a degree of success significantly greater than that found using the Minikin or Sainflou methods [95]. Please note that Goda's equations don't have an analytical base but rather an empirical foundation. Various researchers have found many uncertainties with the Goda's methods, notably with its applications. Some have identified differences with measurement of forces or pressure as largely debated in the Oumeraci et al. [207]. Bruining [42] and Van der Meer et al. [262] performed re-analysis of the data on wave forces on vertical structures noting that the forces and the moment calculated by Goda's formula are always higher than the corresponding measured forces. Goda overestimates the total uplift force by around 40%, while the total horizontal force is overestimated by 20% on average. However, a considerable scatter is present due to the different geometries evaluated. Bruining [42] discussed many of the inconsistencies in the derivation of Goda's method, in particular regarding the semi-empirical coefficients α_1, α_2 and α_3.

It is worth underlining that Goda's formula does not give the actual peak pressure, but the equivalent static load for the dynamic system of caisson, mound and foundation. The method proposed by the author was then not intended to predict impact pressure. An extension of

Goda's method is presented by Takahashi [238]. The authors investigated the stability of the caisson against impulsive pressures, carrying out sliding tests using monochromatic waves Takahashi et al. [244]. The method consists of the introduction of a new coefficient into Goda's formula for the pressure at still water level, which takes into account the occurrence and the intensity of the impact pressure. The Goda method extended by Takahashi [238] is now the most accepted method for wave loading analysis on vertical-face structures.

Under the European Research project 'PROVERBS' ('PRObabilistic design tools for VERtical BreakwaterS'), included in the European Programme 'Marine Advanced Science and Technology' (MAST III), a parameter decision map has been developed to provide easy guidance to identifying the possible loading cases of waves attacking the front face of a simple vertical or composite breakwater starting from non-dimensional parameters based on structure geometry, water depth and wave conditions in the near-field [207]. Furthermore, under the Research Project 'PROVERBS', a new and more generic method for impact pressure has been developed on the base of many experimental tests conducted on small and large-scale models. For details of the model, please refer to Oumeraci et al. [207]. Unlike the force obtained with the extended Goda method [95], the loads obtained with the PROVERBS methods are time-dependent and therefore applicable on dynamic analysis of geotechnical and structural stability. It should be noted that the reliability of this method is still not fully established and that further researches on this subject are desirable.

2.1.4 Non-conventional breakwaters

Besides conventional rubble-mound breakwaters and vertical structures, coastal and harbour defence structures employing some kind of special feature have been developed over the last decades and they are here defined as 'non-conventional breakwaters'. Although they are not commonly used, many of these typologies have a very long history and some were constructed in ancient times. In this section, a brief review of non-conventional coastal structures is presented. Please note that some kind of breakwaters have become popular in some countries and they can almost be considered as a standard breakwater there.

2.1.4.1 Horizontally-composite breakwater

Over the last 60 years, many new types of caissons have been invented and commercialized in order to overcome the limits of the traditional vertical-faced caissons. One of the greatest disadvantages of traditional fully-vertical caisson walls is the exposure to large shock wave forces. If overtopping or wave shocks will become problematic, several structural measures can be taken. The first example of a non-conventional breakwater, although very popular in some countries for decades, is the one denominated 'horizontally-composite breakwater'. It is widely used in Japan and sometimes it is also called the Japanese-type breakwater. The horizontally-composite breakwater is an improved version of the composite breakwater, where the front of the caisson is covered by wave-dissipating concrete blocks or a rubble-mound structure (multi-layered or homogeneous) adopted to reduce wave reflection and the breaking wave loading exerting on the vertical caisson (Fig. 2.5). This particular typology is typically used in shallow water. However, there have been applications in deeper water where impulsive wave pressures are likely to occur. Considering that many conventional breakwaters located in breaking zone suffered damage or failure in the past, a solution was to add large stones or concrete blocks in front of them in order to dissipate the energy of the incoming waves, thus reducing the potential impact force due to the breaking waves. The use of rubble-mound on horizontally-composite breakwaters is fundamental to prevent the failure of the upright section by scouring as well as stabilizing the foundations against the wave loading and the weight of the vertical concrete caisson.

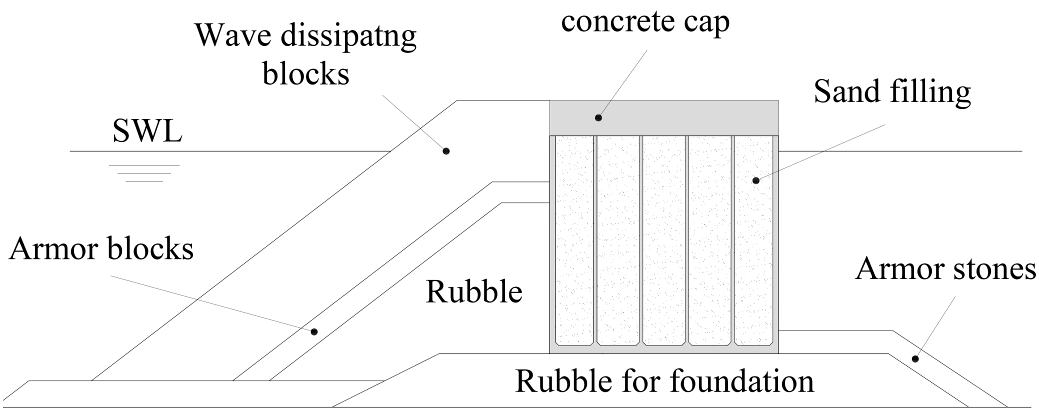

Fig. 2.5 Example of horizontally-composite caisson breakwater

Hydraulic and structural performances of the horizontally-composite breakwaters have been evaluated through several physical model test campaigns. In detail, Tanimoto [248] observed that the wave transmission coefficient for this kind of breakwater is dependent on the relative crest freeboard as well as the covering width of the frontal block layer. For relative crest freeboard $R_c/H_{mo} = 0.6$, which was a typical design value for breakwater in Japan [95], the transmission coefficient, K_t, ranges between 0.10 to 0.16, thus less than the corresponding values measured for conventional vertical-faced caisson. Reflection coefficient, K_r, of the horizontally-composite breakwater was investigated by Tanimoto [248], which observed that K_r decrease with the increase of the covering width of the blocks. A range of K_r = 0.3 to 0.6

may be adopted in the preliminary design, with the smaller values corresponding to a larger value of the covering width of the dissipation layer.

The efficiency of the dissipating block in reducing the total forces has been demonstrated in many small and large-scale model test. Currently, the stability analysis on this kind of structure is carried out applying Goda's formula after incorporating the modification factors proposed by Takahashi et al. [243] and included in the USACE [260]. A different method to estimate the reduction of wave force on caisson protected by block is the one proposed by Kortenhaus and Oumeraci [143]. As shown by the authors, the damping ratio, i.e. the ratio between the wave force on a vertical wall with and without blocks, may reach about the 80% for the horizontal forces and about the 60% for the uplift forces. The authors proposed, then, a relation for both pulsating and impact wave conditions for horizontal and vertical (uplift) loading on the caisson. Finally, the required weight of the rock to be placed in front of the caisson is usually estimated assuming the Hudson formula [119], as suggested by [239] and Agerschou [3].

2.1.4.2 Perforated Jarlan-type caisson

Another example of a non-conventional caisson breakwater is the 'perforated Jarlan-type caisson', which consists of a perforated front wall and a single wave chamber (Fig. 2.6).

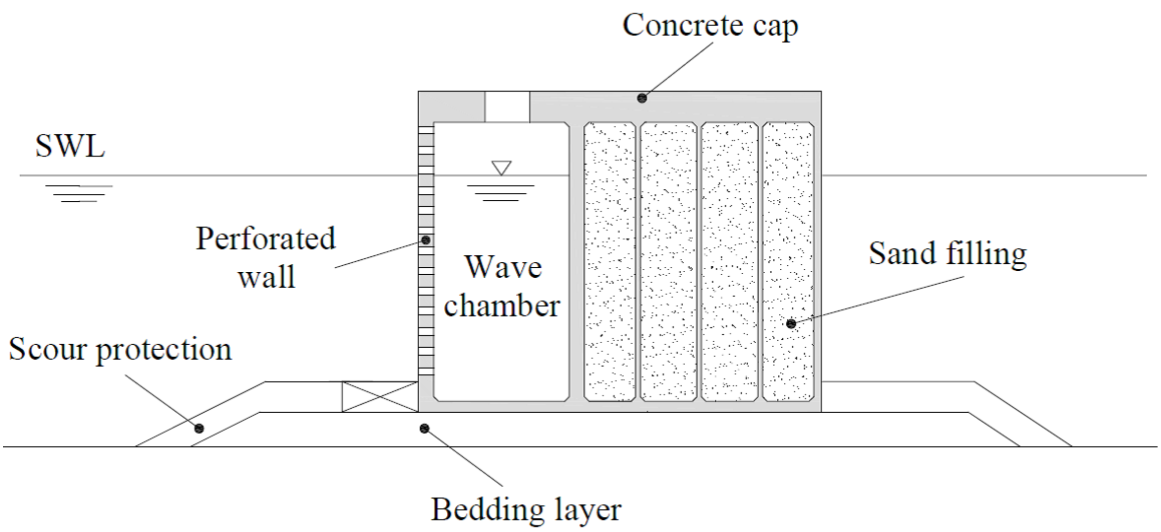

Fig. 2.6 Example of a 'perforated Jarlan-type caisson'

Despite their increased complexity and cost of construction as compared to plain caissons, Jarlan-type caissons are becoming more and more popular not only for anti-reflective quay walls inside sheltered harbours but also for harbour caisson breakwaters, in order to partly overcome the typical drawbacks of vertical structures: large reflections, forces, overtopping and toe scour. Perforated vertical breakwaters are intended to absorb part of the wave energy through various mechanisms, such as turbulence, resonance and viscous. The perforated wall for coastal engineering applications was firstly introduced by Jarlan [128] in the early 1960s with the first application at Comeau Bay in Canada, having a frontal wall perforated with circular halls. Various examples of perforated caisson breakwaters exist in Italy, France and Japan [239, 27]. In Italy, for example, such structures were used in the port area of Naples as breakwater wharves, as well as external breakwaters in Porto Torres, Sardinia, and Palermo, Sicily. Since the first constructions, many others were built around the world with various shape (vertical-slit wall, horizontal-slit wall, circular-hole walls and curved-slit caisson), different wall porosity and with more than one dissipating chamber (multi-chamber systems). If properly designed, these absorbing chambers strongly dissipate the wave energy [89], resulting in smaller horizontal wave forces, reduced wave reflection, less wave overtopping and less scouring in front of the caisson structure. The caisson type, by the way, has lower performances and is not suitable in a coastal area with very high wave periods.

For the partially perforated-wall caisson breakwater with only one single chamber, Tanimoto [246] performed a theoretical approach and laboratory experiment for the wave reflection characteristics. The results showed that the reflection coefficient, K_t, strongly fluctuates between 0.3 to 0.7, reaching a minimum value when the ratio of chamber widths ($B_{chamber}$) to the corresponding wavelengths (L_s) ranged from 0.15 to 0.20. As stated by Takahashi [239], it is generally considered that the wave chamber width must be 10 to 20 % of the wavelength to significantly dissipate the energy, thus reducing the reflection. Due to the wave absorbing behaviour, the transmission coefficient is also reduced. However, since the design waves are longer than the target waves for wave absorption, the reduction of wave transmission is not so significant for the design waves [239].

In addition to minimizing the reflection coefficients, the horizontal and vertical forces acting on perforated caisson breakwaters must also be carefully analysed when designing such structures. The total wave forces acting on these structures are generally considered as pulsating loads. However, the occurrence of impact loads cannot be completely excluded. The method firstly presented by Takahashi [237], and described by Takahashi [239], is widely accepted for preliminary design and estimation of the wave force exerting on perforated-wall caisson breakwater, and it is included in USACE [260]. The method is a modification to the well-known Goda formula with the inclusion of three modification coefficients. The authors demonstrated that, unlike wave forces acting on upright solid walls, the maximum horizontal and vertical forces acting on perforated caisson did not occur at the time when the wave crest is attacking the caisson's front barrier. Six different wave phases were then defined, three wave crest loading phases (positive peaks) and three wave thought loadings (negative peaks). For each of the three crest phases, the authors provided the values of the reduction coefficients λ_1 for pulsating pressure, λ_2 for impact pressure and λ_3 for uplift pressure. For impact wave conditions, the total horizontal force may reach up to 70% of the total force estimated using Goda's formula for traditional vertical-faced breakwaters, while for pulsating loading, the total horizontal forces may reach around 80% of the ones acting on vertical walls [239, 3]. Details of the method are described in Takahashi [239] and a review of the recent progress in the study of perforated/slotted breakwaters, with more emphasis on hydraulic performance and loading on the structure, is presented in Huang et al. [118].

2.1.4.3 Upright wave-absorbing block type breakwater

Largely adopted in Japan as an alternative solution to the caisson protected by wave-dissipating concrete blocks is the 'Upright wave-absorbing block type breakwater'. This kind of structure is similar to the perforated breakwater previously described, consisting of a vertical stacking of special blocks, called the upright wave-absorbing block, having a wave-dissipating function. With the exception of large-scale blocks to be used as a single block structure, the upright wave-absorbing block type breakwaters are generally used in inner bays or the inside of harbours where wave heights are relatively small [201]. An example of the cross-section of this kind of non-conventional breakwater is shown in Fig. 2.7.

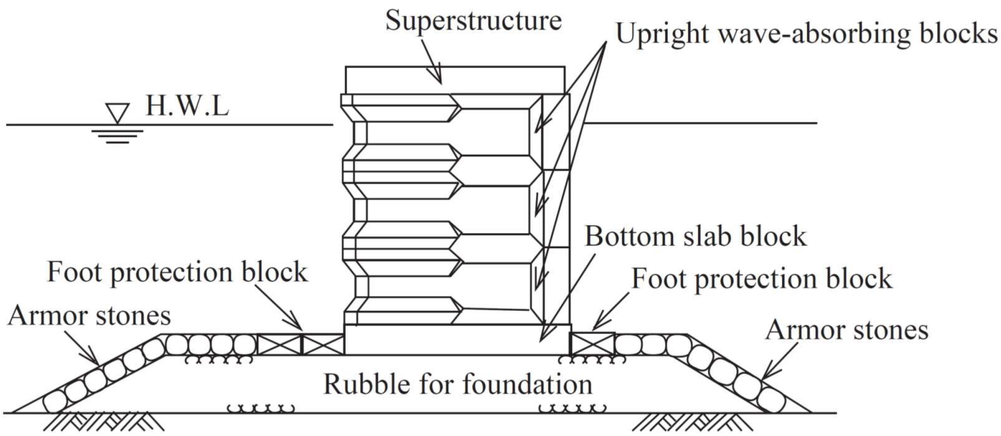

Fig. 2.7 Example of cross-section of Upright Wave-absorbing Block Type Breakwater on the right [201]

The hydraulic performance of this non-conventional caisson is similar to the one described for the Jarlan-type breakwater. The reflection coefficient ranges from 0.2 to 0.7, function of the width of the wave chamber, wavelength and the different types of perforation blocks used [239]. In terms of wave transmission, Upright Wave-absorbing Block Type Breakwater has a behaviour similar to the vertical slit caisson, namely, the reduction in the transmission coefficient through dissipating blocks is not so relevant. Contrary, a significant reduction of the overtopping occurs compared to a conventional vertical breakwater. The wave force acting on an upright wall covered with wave-dissipating concrete blocks varies depending on the composition of the wave-dissipating work. Since the block shape is very complicated, it is desirable to design this type of breakwater using the results of model tests corresponding to the design conditions. However the modified Goda formulas might be used for preliminary design, adopting as modification factor $\lambda_1 = \lambda_3$ = 0.8-1. Wave-dissipating blocks result in a considerable reduction of the breaking wave pressure, and so it is generally acceptable to set the breaking wave pressure correction factor, λ_2, in extended Goda formulas equal to zero [201].

2.1.4.4 Sloping-top caissons breakwater

Another structural measure taken by harbour engineers to reduce the tremendous loading acting on traditional caisson is the development of 'sloping-top caissons breakwater' (Fig. 2.8).

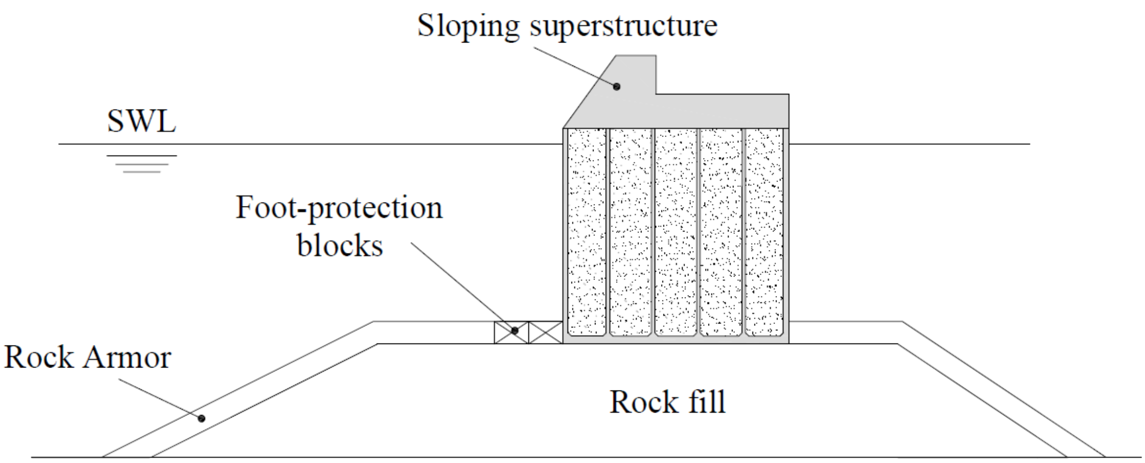

Fig. 2.8 Example of cross-section of Sloping-top Caisson breakwaters

These breakwaters incorporate caisson special shapes. This type of breakwater utilizes the wave force acting on the sloping superstructure to stabilize the breakwater body and simultaneously reduce the horizontal wave force. In fact, the downward forces on the slope strongly reduce the uplift forces, thereby increasing the overall breakwater stability. The structure is generally very stable, although the crest freeboard must be higher than the ordinary vertical-faced caisson to obtain the same overtopping and transmission at the rear side of the structure. Normally the sloping surface of the sloping-top caisson breakwater is set to begin at the still water level or higher to facilitate the construction. However, with a semi-submerged shape in which the toe end of the sloping surface is set below the still water level, further reduction of wave forces is possible.

Sloping-top caisson breakwaters have been constructed in many countries, and especially in deep water regions where the wave conditions are severe. The oldest breakwater with this geometry was built in Naples in 1906. Another relevant example is the one built in Hanstholm in Denmark in 1966, which is even more peculiar due to the cylindrical shape of the caissons. From that date, this typology became more popular and breakwaters with frontal sloping are now largely adopted in many countries, in particular in Japan [239].

Due to its shape, the reflection coefficients are smaller than those measured for conventional vertically-faced breakwaters, mostly due to the higher wave overtopping and the dissipation at the bottom edge of the frontal slope during the run-down. Takahashi [239] showed that the reflection coefficient is function of the ratio between the crest freeboard and the significant wave height, and its values range between 0.6 to 0.8.

The higher overtopping at the rear side due to the slope, induced larger transmission coefficient, K_t, compared to ordinary vertical breakwater with values that range between 0.1 to 0.4. A relation for the estimation of K_t is provided by Takahashi [239] and included in USACE [260].

The wave force on sloping-top caisson breakwaters should be calculated based on the model test results that are suited to the conditions. However, if the model test is difficult to conduct, the forces on the horizontal and sloping part, as well as the uplift force on the bottom caisson, can be estimated using the method proposed by Takahashi et al. [240]. The authors modified Goda's formula, introducing two factors to take into account the reduction of the pressure due to the slope angle, the wave steepness H/L and the height from the still-water surface to the lower end of the slope. Please note that the uplift pressure is reduced due to the rapid upward velocity induced by the slope. However, this wave force calculation should be applied in cases where the water depth is relatively deep and the period of the design wave is long [201]. Takahashi et al. [240] showed also that the necessary weight for the sloping top caisson is around the 60-80% of the one necessary for conventional vertical structures to accomplish the same stability condition, thus underlining the high performance of this kind of non-conventional breakwater against the wave action.

2.1.4.5 Breakwater with ’Stilling Wave Basin’

The last non-conventional structure here described is based on the introduction of a frontal basin in a crest breakwater. This kind of crest structures, named ’Stilling Wave Basin’ (SWB), consists of a seaward wall, a basin and a landward wall, as shown in Fig. 2.9. The seaward wall is partially permeable to allow the evacuation of the water in the basin. The SWB is based on the principle of energy dissipation: the incoming wave hits the seaward wall and is projected upward, then drops in the spilling basin before hitting the set-back crown-wall.

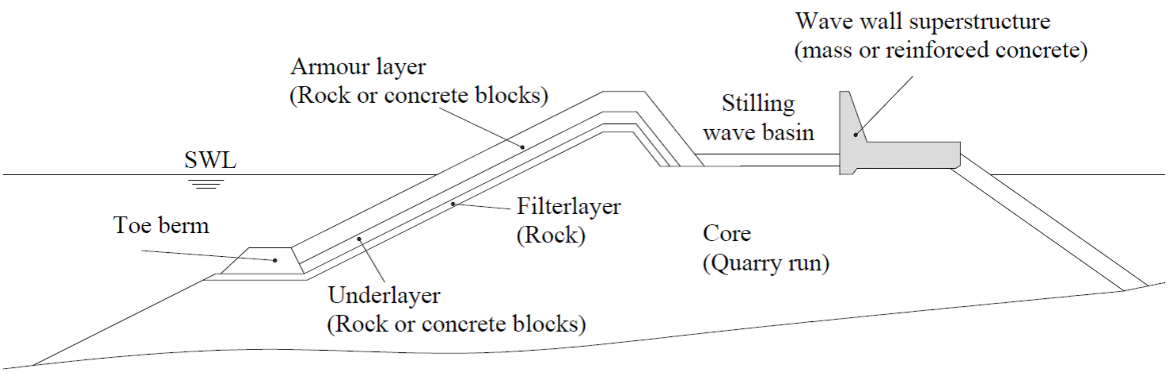

Fig. 2.9 Rubble-mound with a ’Stilling Wave Basin’

Many authors investigated this non-conventional structure. Coastal structure with a frontal reservoir was firstly introduced by Aguado and Sánchez-Naverac [4] with the aim of reducing the wave overtopping in the rubble-mound breakwater, without making the crest level higher. Burcharth and Andersen [50] conducted two-dimensional model tests in order to optimize the design of a new breakwater for the extension of Agaete Port at Las Palmas in Spain adopting a basin dissipation structure. Several cross-sections were tested, evaluating their performances in terms of overtopping discharge at the rear side of the structure and wave loading at the inner vertical crown-wall. As observed by the authors, the overtopping is dependent on the reservoir width and the necessary size of the basin is dependent on the drainage capacity between the succeeding waves. The wave loading on the crown-wall is also very sensitive to the reservoir width. Burcharth and Andersen [50] showed that the force and tilting moment on the crown-wall for a narrow reservoir can be up to three times compared to the one measured on wide reservoir for a same design wave condition. The reason is that the overtopping water hits the wall directly in case of narrow reservoir, whereas in the case of larger basin the splash-down is mainly in the reservoir armour. Finally, an approximate comparison of the cost of different geometries is carried out by the authors, indicating that the front reservoir solution is the most efficient and economical, in particular when a low-structure solution is preferable. Fig. 2.10 shows two images of the Agaete Port in Las Palmas in Spain having a rubble-mound with frontal stilling wave basin.

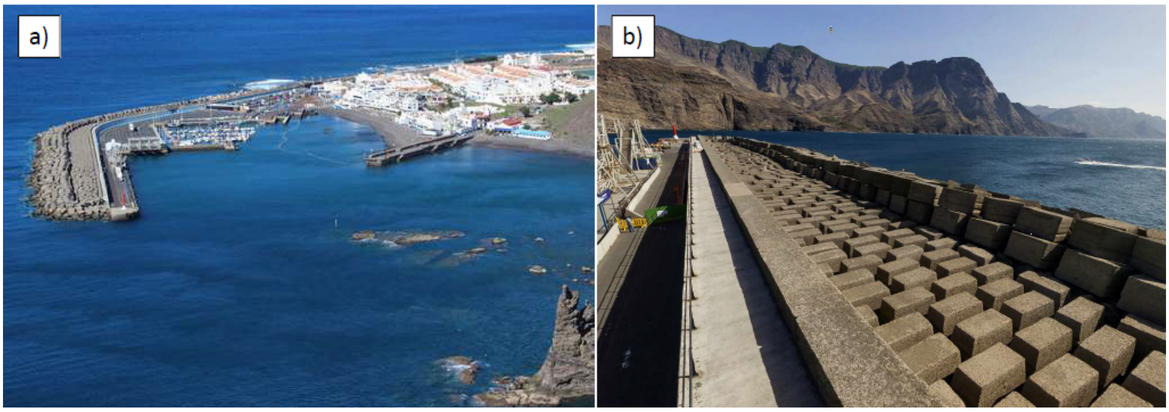

Fig. 2.10 Agaete Port in Spain on the left and details of the frontal dissipation basin on the right (Photo Source: [52])

Geeraerts et al. [92] present details of a study conducted on an innovative dyke with a special shape that reduces the amount of overtopping due to the inclusion of the SWB. The comparison of the overtopping discharge between a simple dyke with and without the SWB indicates that the inclusion of the latter geometry is able to strongly reduce the wave overtopping for both non-breaking and breaking wave conditions. Two values of reduction factor were then provided by the authors in order to take into account the effect of the SWB on the overtopping reduction for breaking and non-breaking waves.

Cappietti and Aminti [53] compared results for physical model tests on a classical-shaped breakwater and a model equipped with an overspill basin, concluding that the latter design decreases the mean overtopping rate by up to a factor of 2.

Finally, Van Doorslaer et al. [268] present the results of 1000 physical tests carried out on models with different types of crest modifications, including the stilling wave basin. Since a multitude of variation in the geometry of the SWB is possible, one uniform reduction formula was not determined by the authors. Some suggestions for the design of SWB are recently reported in the EurOtop [74], based on the results of Geeraerts et al. [92].

It is worth noting that this particular design is suitable not only for rubble-mound breakwaters but also for vertical caisson applications. One of the first examples of non-conventional caissons with this geometry is the one built between 1968/1970 at Fontvieille in the Principality of Monaco. The vertical caisson has a wave dissipation basin on top with a frontal perforated parapet and a backward crown-wall with a recurved shape. A cross section of the breakwater is shown in Fig. 2.11a and a detail of the dissipation basin is shown in

Fig. 2.11b. The idea of a frontal dissipating basin was adopted after physical model tests aiming to reduce the wave overtopping at the rear side of the structure due to the interaction of the incident waves with the wave overflow in the basin, as reported in Benassai [27].

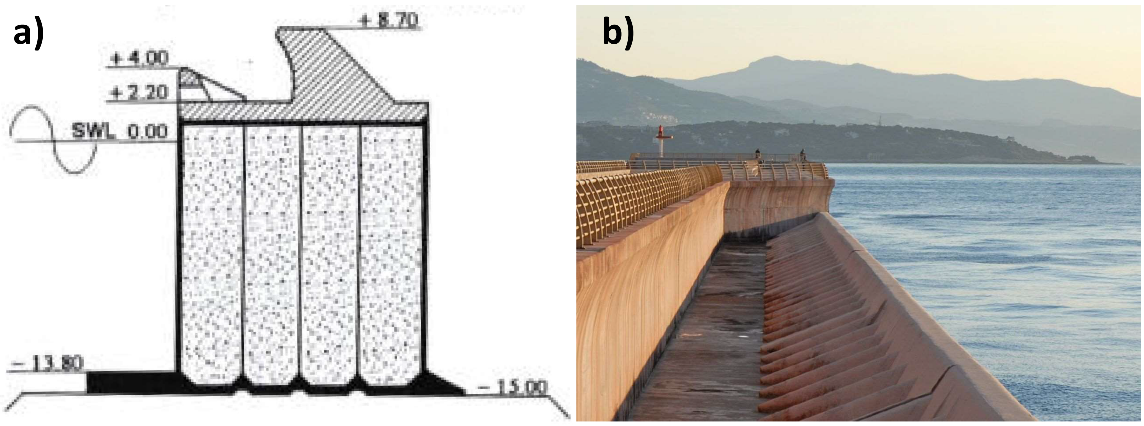

Fig. 2.11 Cross-section of the Fontvieille breakwater on the left [27] and detail of the frontal dissipation basin on the right (Photo Source: [67])

2.1.5 Recent innovations

Most of the innovations on breakwaters and coastal structures in recent decades were particularly directed towards improving the hydraulic performance. This has been accomplished by the reduction of wave reflection, overtopping, breaking wave loads and their effects on the structural stability and its foundation. Accordingly, substantial progress has been made in the design methods of conventional and non-conventional breakwaters. Integrated design methods on the basis of lessons learned from recent failures of harbour defence structures have been proposed. In this line, an interesting field of research is the study of the influence of climate change effects such as sea-level rise, wave-height increase, and storm surge increase, into the performance-based design of both rubble-mound and caisson breakwaters using advanced probabilistic methods in which the uncertainties of the involved parameters are considered [49]. The effect of climate change will increase the risk of flooding of low lying areas, accelerate erosion of exposed soft beaches, causing damage to existing coastal protection structures. This makes it necessary to upgrade the structures so they comply with the original design performance criteria. Examples of the studies of the effect of climate change on the performance-based design of the vertical-faced structure and rubble-mound breakwaters can be found in [234, 51, 164].

In recent years, however, innovations have also covered other aspects such as the environmental integrity, taking into account, for instance, the effect of the coastal structures on coastal ecosystems, water quality, morphology and seascape. An important innovation is now directed also towards the improvement of multi-purpose use such as recreation in order to achieve a wider acceptance of these infrastructures. As an example, large floating caissons, incorporating shopping centres, parking lots as well as office buildings, have been considered as an alternative for the marina in Monaco [191]. Outstanding progress was also made on construction technique, aiming to reduce the cost and time with relevant improvements on standardisation achieved through the use of prefabrication of most of the structure. Due to the flexibility offered by the prefabrication, crest structures of marine breakwaters and seawalls can be used also for walkways and promenades and other recreational activities or can be shaped to incorporate pipelines or facilities for port operation. The progress in prefabrications allows designing structures with a non-conventional shape able to combine the hydraulic/structural requirement with the aesthetic and architectonic reasons, increasing the social acceptance and transforming a simple defence work into a piece of art and a symbol for the coastal community. Examples of this combination, such as the crown-wall with a hyper-elliptical or elliptic shape in Tazacorte and Malaga (Spain), are described in Negro Valdecantos [192] and displayed in Fig. 2.12. The large parapet which, conventionally forms an insurmountable barrier between the city and the sea, becomes part of the urban landscape, such as the case of the port of La Restinga in Canary Islands (Spain). Another recent and extraordinary contribution of harbour engineers to the design of new breakwater can be found in the Ciutadella outer breakwater in Minorca in 2008 and the Castellón Port breakwater in 2010, both described by Negro Valdecantos et al. [194].

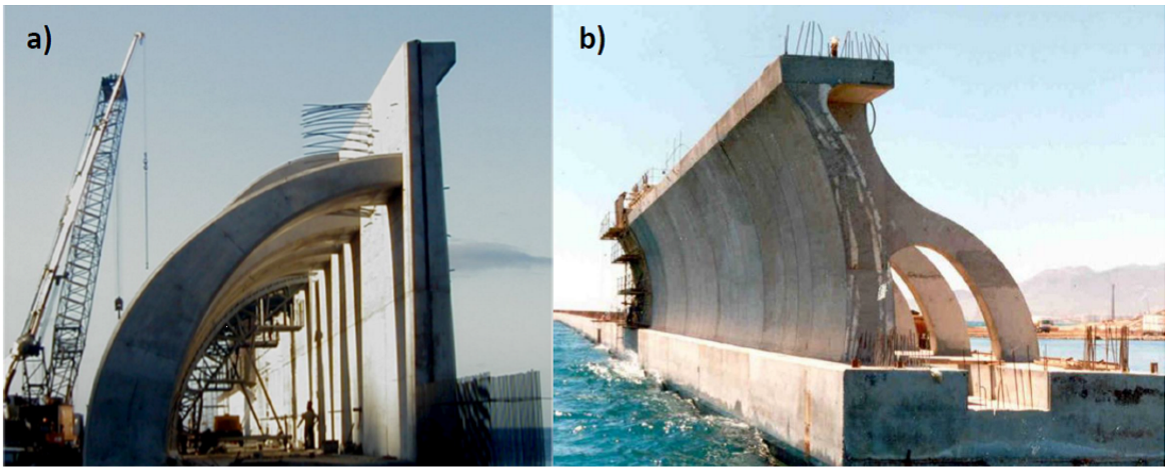

Fig. 2.12 Slender reinforced concrete parapets in Tazacorte (left panel) and 'Gothic parapet' in Málaga (right panel)

2.2 Innovative breakwaters

2.2.1 Introduction

In the last decades, following the ongoing global economic crisis, the international community recognised the importance of investing in diverse, reliable and affordable energy sources, which present an alternative to the traditional ones like oil and gas. Among the renewable energy resources, the oceans represent a safe, inexhaustible and largely untapped source that may significantly contribute to the electrical energy supply of vast coastal regions [23]. The idea to harvest energy from waves has always fascinated scientists and engineers. After the oil crisis in 1973, a large number of university researchers re-examined the potential of generating energy from ocean waves. In the 1980s, as the oil price went down, wave-energy funding was drastically reduced. Nevertheless, a few first-generation prototypes were tested at sea. More recently, following the issue of climate change, there is again a growing interest worldwide for renewable energy, including wave energy, and currently, more than 1000 Wave Energy Converters (*WECs*) have been designed and developed worldwide [76]. These systems are designed to exploit part of the available ocean energy and convert it into electricity. Despite the effort of engineers and researchers to improve the WECs, one of the greatest issues for developing these technologies is the economical aspect. Compared to other renewable energy technologies, the capital and operational expenditures (CAPEX/OPEX) of the WECs are still very high, which makes the devices not economically feasible and not competitive on the global market [155, 165].

Wave energy technologies are still at the initial stage of research and it is difficult to correctly estimate the costs and performance of the devices as well as the rest of the installation. The largest part of current economic studies is often oversimplified, which consequently creates uncertainty and diffidence for investors. Due to these reasons, an extended part of the entire wave energy sector heavily relies on incentives and public financial support. In detail, within the wave energy sector, the financial support is often given by means of a higher sales price for each kWh produced, i.e. feed-in tariffs, green certificates, ROCs, or by financial installation support, being a percentage of the construction costs of the facility. The feed-in tariff based kWh prices have some incentive to improve their competitiveness and encourage development but might enable economically infeasible solutions even while R&D support is in status quo [156, 12].

Due to the early stage of development, the WECs growth heavily depends on their demonstrated full reliability and operability in open waters, given that they are exposed to extreme environmental conditions. However, WECs development has not been helped by the fact that some full-scale prototypes were wrecked in storms [76]. Two of the most powerful wave energy devices, the OSPREY in the UK [252] and the greenWAVE in Australia, both of 1 MW of installed power rate, were damaged respectively in 1995 and 2014 [78]. Before the Mutriku power station (in Spain) was completely built, severe storms hit it in December 2007, March 2008, and January 2009 resulting in significant structural damage to a number of OWC cells, both to the front face and to the chamber roof [178, 254, 253]. Very few devices in the world are developed in a prototype scale to demonstrate the technical capabilities and structural reliability, reaching high Technology Readiness Levels (TRL). All these aspects do not help increasing potential investors interest neither their entry into the wave energy market.

2.2.2 Breakwater-integrated WECs

Nowadays, the main task and challenge for the scientific community operating in this sector are to reduce the construction, installation and maintenance costs for these novel hybrid systems, and to ensure high levels of operational efficiency and structural survivability during normal conditions and storm events. Engineers and researchers operating mostly on maritime and coastal structure design proposed a solution to significantly decrease the WECs costs. The idea consists of the development of hybrid devices that can be totally integrated into existing or expanding coastal infrastructures. These innovative structures still have their principal function of sheltering a location from the action of waves, i.e. the coastal and harbour protection, but with important benefits of the energy production thanks to the inclusion of a WEC. This concept was primarily introduced to reduce the WEC costs, ensuring at the same time an increase of their reliability. The last goal is achieved by designing the innovative structures adopting the well-established methodology and design criteria used in coastal engineering for traditional breakwaters, as described in previous sections.

The integration of a WEC into a new breakwater has several advantages [78, 188] such as the low construction costs, considering that the breakwater would be built regardless of the inclusion of the WEC device (cost-sharing). Furthermore, the access for the construction, installation and maintenance are much easier compared to other standalone WEC devices located offshore. On the other hand, the energy extracted with these new technologies is minor compared to those located in deep sea. Moreover, not all breakwaters are appropriate and feasible for the integration, depending on their type, geographical location and orientation with respect to the incident waves. The most relevant challenge for coastal engineers involved in this sector is to design these non-conventional structures ensuring hydraulic performance and global stability similar to the one provided by traditional breakwaters. The aim is to develop innovative structures, which are economically competitive, with the same or improved hydraulic performance, and with the benefit of the energy production.

Although several different types of WECs are under development, only two typologies are currently considered appropriate to be entirely embedded into traditional coastal defence structures: the Oscillating Water Column (hereafter *OWC*) and the OverTopping Device (hereafter *OTD*). The general description of the two typologies, their principle of working and the hydraulic and structural performance against the wave action will be defined in more detail in the next sections. Please note that these devices are considered primarily as coastal/harbour defence structures, thus more emphasis is placed in this work on the wave structure interaction in terms of pressure/force acting on the devices, overtopping at the rear side and the wave reflection, comparing their performance with those of conventional breakwaters.

2.2.3 Breakwater-integrated OWC

2.2.3.1 General description

Almost all the innovative breakwaters tested in real ocean conditions are integrated with the OWC system, which is the most famous and probably the most successful WEC device. Although the concept was already known in the 1940s due to the work of a former Japanese navy officer, Yoshio Masuda, several OWCs in prototype scale were constructed and operated with varying degrees of success over the last 40 years [78, 77]. The basic concept of this technology consists of a chamber, submerged in the seawater and opened below the water surface so that waves can enter into the box (Fig. 2.13). An air-duct with an air turbine connects the chamber to the atmosphere. Under the wave motion, the air in the chamber is alternately compressed and decompressed, creating a bi-directional flow in the duct. This flow drives a self-rectifying turbine connected with a generator for the electricity production.

This class of WEC is the most extensively studied with the largest number of existing developed devices. This represents one of the main reasons for its adoption of the integration into breakwaters. An advantage consists of its relative simplicity, being a rigid structure with the only moving part represented by the rotor of turbines. Moreover, it is not actually the seawater itself that moves the turbines, thus the latter is never exposed to water, which considerably extends the service life of the equipment. Finally, the integration is probably the easiest solution from the economical, constructional and operational point of view.

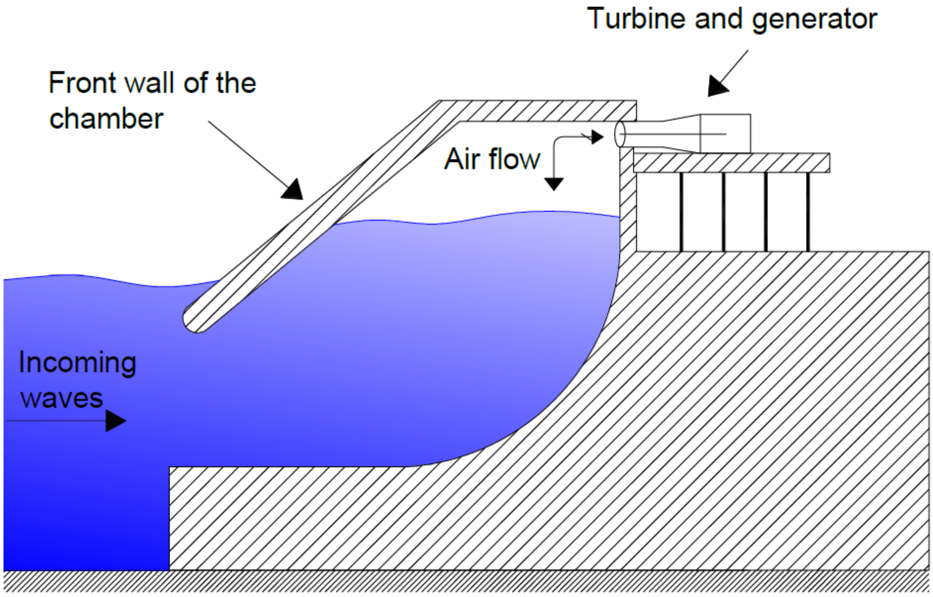

Fig. 2.13 Cross section of a generic shoreline OWC device

2.2.3.2 Structural response

The analysis on the OWC-integrated within a breakwater is essential for the design of the structural components of the caisson. The estimation of vertical and horizontal forces, as well as the pressure distribution, are important for the design against the two most relevant failure modes, i.e. sliding and overturning. Although many studies on the hydraulic performance of the OWC-integrated breakwaters are available in literature, there is no accepted and well-defined empirical method to design structures with this innovative configuration.

Evans [75] conducted one of the earliest studies on the wave pressure distribution on OWC-integrated breakwaters, providing a first simple relation between pressure distribution and the energy absorption, based on classical linear water-wave theory. Some years later, Takahashi [236] investigated the stability of vertical and sloping OWC wave power extracting caisson-breakwaters with physical model scales. The dynamic pressure exerted on the device was compared with the theory of Goda [94], indicating that the Goda formulas can be applied even for the wave power extracting caissons with vertical walls, setting the coefficient $\lambda_2 = 0$, due to the wave energy absorption. In the same study, Takahashi [236] provided also formulas to estimate the horizontal and vertical components of the forces on the OWC with a frontal sloping wall. Sliding tests proved that the stability of the OWC with the sloped front wall is higher than other tested geometries, including the ordinary caisson with a sloped front face and traditional caisson covered with wave-dissipating blocks. Müller and Whittaker [185] confirmed these results, founding that a sloped front wall reduces the impact pressure compared with those measured on vertical structures. The authors also found that the pressure peaks move above the SWL with the increase of the backwards wall slope. Jayakumar [129] conducted an experimental study on multi-resonant OWC caisson model, finding that the wave forces on an OWC caisson model were lower than the conventional one, in particular when the air damping maintained inside the OWC model was decreased. Muller and Whittaker [186] indicated that the wave pressure on the inner wall of the chamber is one order of magnitude greater than the wave pressure on the front wall, mainly due to flow field turbulence and large vortices around the lip wall. Neumann et al. [196] indicated that the impact loading has the most relevant influence on the stability and hence on the overall costs of the caisson. Hull and Müller [122] indicated that the maximum impact pressure occurs around the sea water level. Moreover, the authors found that if the pressure distribution corresponding to the highest maximum pressures were used for the design, it would underestimate the design of wave force. Boccotti [31] conducted analysis on different types of caisson breakwaters embodying an OWC, with an innovative shape that includes an additional vertical duct. In this way, the waves do not propagate directly in the inner chamber, but the oscillation of the inner water surface is induced by the wave pressure fluctuation at the opening vertical duct (Fig. 2.14).

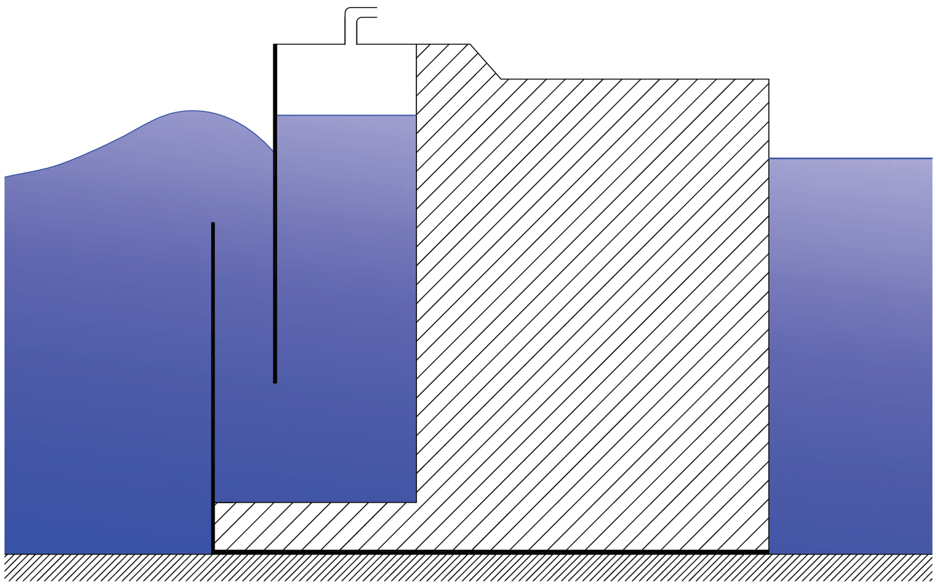

Fig. 2.14 Scheme of the U-shaped OWC integrated into a caisson breakwater

The U-OWC caisson has the great advantage of obtaining with his shape a natural resonance without any device for phase control, increasing in amplitude the wave pressure into the air pocket and amplifying the overall performance [32, 34]. Compared to a traditional

OWC, the device has greater eigenperiod and better performances with swells and large wind waves [33]. Moreover, Boccotti [33] found that under the same weight, a breakwater embodying the U-OWC has slightly greater safety factors compared to the conventional OWC. Further analyses on the U-OWC were conducted by Strati et al. [232], Malara et al. [166] and Malara et al. [167], concerning novel theoretical models describing water column oscillations. Thiruvenkatasamy et al. [251] studied the influence of the OWC configuration on the force distribution in terms of structure sizing, the density of the caisson, and the size of the vent. Preen and Robertshaw [216] proposed a design method for a generic OWC based on Goda's approach, with localised impact estimated adopting the PROVERBS method [207]. Patterson et al. [210] showed that the sloped wall provides a slight decrease of the sliding forces and overturning moment compared to vertical wall caissons. The author suggested a new design method for the OWC front wall with a quarter-circle cross-section, which would reduce the overturning moment even more from the wave loading on the front face. Huang et al. [117] applied a linear potential flow theory to calculate the horizontal wave force for an oscillating water column system with caisson breakwater, developing a proper design method. Liu et al. [159] conducted a two-dimensional physical model test, providing a focus on the stability analysis of the OWC-integrated vertical breakwater. The results from laboratory confirm that the wave forces on OWC caissons are smaller than those acting on vertical caissons. Similar results were obtained by Kuo et al. [149]. The authors conducted physical model tests on an OWC under regular waves, and the results indicated that Goda's formulas give an overestimation of the maximum resultant forces, compared with the measured data on OWC caissons. Conversely, Goda's formulation underestimates the momentum, which could affect the overall OWC stability against the overturning. Viviano et al. [286] presented the results of a unique large-scale experiment carried out on the OWC device integrated into vertical breakwater. Allsop et al. [9] provide details of the large-scale test set-up. Viviano et al. [286] evaluated the wave loading on the device for different wave conditions, water depth and geometries. The results suggest that the maximum forces are inversely related to the orifice opening. Moreover, the formula for vertical structures [238] overestimates the force for small wave height ($H_{m0}/h < 0.2$). Conversely, when H_{m0}/h increases, the measured forces are greater than the ones predicted by Takahashi [238]. Naty et al. [190] observed that wave loadings on the OWC front wall for an optimized configuration were quite accurately predicted by Sainflou [223] as used for vertical walls, if they were multiplied for a safety coefficient equal to 1.1. Ashlin et al. [19] conducted an experimental campaign to study the nature and magnitude of the dynamic pressures and forces exerted on a circular bottom profile OWC-integrated caisson breakwater exposed to the action of regular waves. The authors indicated that the horizontal wave force acting on the OWC structure is more than

2.5 times the vertical wave force acting on the structure. Moreover, the total horizontal and vertical forces increase with the increase in wave steepness because of the high wave energy conversion at low wave steepness. The author compared the measured horizontal wave forces with the values obtained from Goda's formulas, showing that the semi-empirical formula overpredicts the shoreward peak forces, particularly for low frequencies, whereas it underpredicts the seaward peaks by approximately 5-50%. Recently, Viviano et al. [285] compared the results of the wave loading on the frontal wall between small and large-scale models. Results show that extreme loadings on the frontal wall can be underestimated by the small scale but safe conditions are always achieved for the high-chamber model. The reason is caused by to the effect of the viscous stress, which changes the hydrodynamics inside the OWC by reducing flow velocity near the wall. In detail, for the highest incident wave conditions, the forces obtained for the small scale model with a high chamber have a better agreement with the large scale model. Therefore, a little increase in the height of the pneumatic chamber is sufficient to provide a fairly safe prediction of the maximum loadings.

In conclusion, the experimental studies conducted on the OWC-integrated caisson in small and large scale over the last decades confirm that the device has an undebatable advantage on the reduction of total wave forces because of wave phase dispersion. As a consequence, the maximum forces on the different parts of the OWC occur at different instants, thus improving the device's overall stability. Apart from some distinctions, all the experimental results reveal that the nature and magnitude of peak forces exerting on the frontal wall device differ from the forces on the traditional vertical caisson [40]. The total horizontal forces can be greater or lower than those acting on the vertical breakwater, mainly depending on the specific geometry of the internal chamber and the turbines dimension. A sloped front wall has been used in many design method as it offers better performances compared to traditional vertical wall configurations. Although no direct comparison has been presented, a curved front wall may also provide an auspicious alternative to the vertical structure, due to the increase of the energy extraction rate for small height waves [258]. However, it is worth noting that the structural design of the device may not necessarily agree with the optimum design in terms of efficiency or constructibility, as recently pointed out by Bruce and O'Callaghan [40].

2.2.3.3 Wave reflection

In the design of port and harbour facilities, the investigation of the reflection is of primary importance, because high-reflected waves can exercise a disturbance in the navigation of vessels at harbour entrances, making in some case the navigation unsafe. Therefore, the study of the reflection coefficients from the OWC-integrated breakwater is essential to compare them with traditional structures.

Takahashi [236] investigated the reflection of the sloping caisson integrated OWC device with laboratory experiments, comparing the results with traditional sloping breakwater with and without frontal dissipating blocks. The reflection coefficients of the OWC-integrated sloping caisson range between 0.45-0.55 depending on the wave height. In general, the results show that the reflection coefficients are smaller than those measured on the sloped front-wall caisson, but larger than those measured on the caisson with wave-dissipating blocks.

Zanuttigh et al. [289] analysed wave reflections from an OWC device, adopting the method proposed by Mansard and Funke [169]. The results of the 2D experimental test highlight that the reflection coefficients decrease with the increase of the wavelength, being the chamber width constant. The values of the reflection coefficient provided by the OWC device never exceed the 0.55, which are very low if compared to the typical values on vertical caissons [10].

The results of the aforementioned large-scale experiments carried out by Viviano et al. [286] also provide details on the wave reflection on the OWC for different wave conditions and geometries. The reflection coefficients of the non-conventional breakwater are highly dependent on the orifice dimension located on the chamber ceiling. When the orifice is closed, (i.e. the air cannot flow through the turbine) the reflection coefficients are around 0.9, which are very similar to the typical values of reflection coefficients on vertical walls [10]. However, by optimizing the orifice dimension, Viviano et al. [286] demonstrated that the reflection coefficients on the OWC can reach values lower than 0.6.

Naty et al. [190] found that the reflection coefficient, K_r, is highly dependent on the ratio between the width of the internal chamber, B, and the peak wavelength, L_p. In particular, K_r is in the range 0.55–0.9 for the greatest values of B/L_p. Furthermore, K_r tends to converge toward the value of 0.7 when B/L_p decreases, independently from the geometry of OWC. The obtained reflection coefficients are compared with the results of large-scale tests [286], giving reflection coefficients about 10% bigger than the large-scale experiments, which represent a fairly acceptable difference considering the different scale model.

Viviano et al. [285] also compared the results of the reflection coefficient for small-scale generalized OWC devices to those measured on a similar large-scale model under random waves. The most evident result, contrary to previous studies conducted by Naty et al. [190], is that the small-scale experiments provide values of K_r lower than those measured on large-scale tests. The authors found that the scale effects are more prominent on wave reflection for incident waves having the peak period close to the natural oscillation period of the OWC. Therefore, the small-scale models give the greatest errors when the device is near to the resonance, with a maximum reduction of the reflection coefficient of about 20% in comparison with the large-scale configuration.

In conclusion, the experimental campaigns carried out in model scale indicate an important reduction of the reflection coefficient, due to the energy absorption into the internal chamber of the OWC device. The studies suggest that OWC integration can improve the hydraulic performance of the breakwater, strongly reducing the disturbance in the navigation compared to traditional vertical caissons.

2.2.3.4 Wave transmission and overtopping

Minimizing the wave transmission and overtopping is fundamental in harbour breakwater design since their principal function is to reduce the wave propagation, creating a calm water area behind them. The quantification of wave transmission is important for example in the case of long wave periods transmitted through the breakwater, which could cause movement of ships or other floating bodies. Wave overtopping is relevant because it affects the functionality, safety of transit and mooring on the rear side of the breakwater, as well as the wave transmission in the sheltered area. Despite the importance of hydraulic performance in terms of overtopping and transmission of the non-conventional breakwater integrated into OWC, limited information exists in the literature.

Takahashi [236] investigated the wave transmission of the OWC-integrated sloping caisson in the laboratory. Comparing a sloping and vertical caisson integrated with an OWC found that the transmission coefficient of the sloping device was a little larger than that of the vertical one. Moreover, the transmission coefficients of the OWC-caisson were lower than those measured on conventional structures, such as the sloping caissons and caissons with dissipating blocks. Considering the impermeable nature of the caisson, the wave transmission at the rear side of the structure is mainly due to the wave overtopping. Although no results were shown, Takahashi [236] stated that the wave transmission characteristics were observed also considering the overtopping rate, which seems to confirm that the difference found on the transmission coefficients between the different caissons were found also on the analyses of the overtopping discharge.

2.2.4 Breakwater-integrated OTD

2.2.4.1 General description

Contrary to the OWC, breakwater-integrated OverTopping Devices (OTD) utilize a frontal sloping plate that leads the incident waves to overtop into one or more storage basins, placed at a level higher than the sea water level. Due to the hydraulic head between the reservoir level and the sea water level, the potential energy of the stored water is converted into mechanical and electrical energy, passing through very low-head hydraulic turbines coupled with generators, located behind the structure. Moving from the design concept of breakwaters with Stilling Water Basin (SWB), coastal engineers and designers involved into the wave energy field considered to exploit the energy from the frontal reservoir to convert into electricity, combining a front reservoir breakwater or seawall with a WEC device, thus introducing the concept of the OTD-integrated into maritime and coastal structures. The slit wall of the SWB structures is replaced by a smooth sloped ramp, which enhances the wave overtopping into the reservoir.

From the point of view of construction and operation activities, overtopping devices might be more attractive than the OWC device, due to their simplicity and independence of wave period. In detail, the fluctuations of the energy produced by these devices are relatively small, considering that the conversion takes place in the basin where the water is temporarily stored. Moreover, contrary to the OWC device, it is possible to combine an OTD with both conventional rubble-mound breakwaters and vertical caisson. Finally, the technology allows the recirculation of the water inside the harbour as the water flowing through the turbines goes to the rear part of the structure.

2.2.4.2 The SSG device

In the next sections, the structural and hydraulic performance of a particular OTD, named SSG (*Seawave Slot-Cone Generator*), will be examined. The device consists of an OTD with three reservoirs and represents the first example of an overtopping device embedded into a traditional rubble-mound breakwater. Two pilot plants were planned to be installed during 2008 at small islands near Stavanger in Norway. Unfortunately, environmental issues required locating the SSG pilots to another location, but, after more than ten years, these projects have not been realized. Although several studies, such as the one presented by [137], suggest that the use of multiple reservoirs improve the efficiency compared to structures with only one reservoir, on the other hand, this complex geometry leads the device to be still not economically competitive with respect to other WEC devices embedded into breakwaters. However, the studies conducted on this device are fundamental in order to understand all the aspects related to the interaction of the waves with a non-conventional breakwater having this peculiar geometry, which inspired the design of the OBREC device studied in this thesis.

Structural response

Survivability is probably the most challenging aspect of these novel structures, due to the early stage of development. For this reason, it is imperative that OTD-integrated breakwaters are both highly reliable during operations, and survivable through extreme conditions. However, to create a convincing technology able to attract stakeholders, it requires reliable confidence levels. In detail, many authors carried out physical model tests in order to study the wave loading on the different parts of the structure, comparing with design formulas of conventional breakwater or providing semi-empirical formulas for these novel structures.

First results of wave loading acting on the SSG device are described in Kofoed et al. [140], Margheritini et al. [170] and Vicinanza and Frigaard [278]. The SSG consists of an OTD-device with three frontal reservoirs located one on the top of each other (Fig. 2.15). Kofoed et al. [140] identified two different behaviours of wave loading acting on the SSG: surging waves on the front sloping plate, and impact waves on the vertical recessed wall with a typically *"church-roof"* of the force time-series shape as defined in Oumeraci et al. [207].

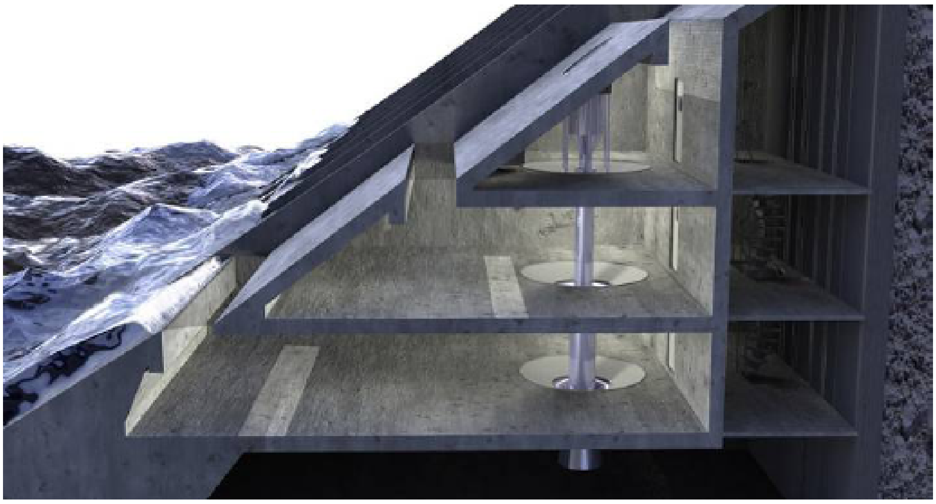

Fig. 2.15 Artistic view of the SSG device [278]

Margheritini et al. [170] showed that the measured wave pressure on the three ramp does not vary substantially from one plate to the other, confirming a quasi-static loading time history of the pressure signals.

Vicinanza and Frigaard [278] showed that maximum pressures on front plates are quasi-static or pulsating loads generated by non-breaking waves ($p \sim \rho_w g H_s$), where ρ_w is the water density, g is the acceleration due to the gravity and H_s is the significant wave height. Loading on the rear vertical wall exhibits a small impact pressure ($p \sim 2-3\rho_w g H_s$), which is damped by the preceding foamy mass. The authors compared pressure on the three ramps with the prediction design formulas used for caisson breakwaters with the sloping top [238], showing that the formula underestimates the forces between 20% to 50%. A reason for the underestimation can be addressed considering that the SSG model was a fixed structure, while Takahashi [238] proposed its design method using data from sliding experimental tests.Vicinanza and Frigaard [278] indicated that wave directionality has a different effect on each plate. On average, the obliquity loading reduction is around 12%-17%, while the spreading loading reduction is about 10% for front attacks and 13% for side attacks.

A further two-dimensional laboratory test in a wave flume was carried out by Vicinanza et al. [274] to derive more information on loading acting on the structure. The tests were thought to serve as a guidance for the design of a pilot project to be built in Svåheia in Norway. The analysis of the forces of the frontal ramp indicated that two classical approaches of the Japanese design practice, Hiroi [110] and Goda [93], could be used to have safe estimates of measured forces on the sloping ramp.

Buccino et al. [45] confirmed these results, showing that maximum vertical and horizontal forces on the SSG are not simultaneous. When the vertical force attains its maximum, which presumably corresponds to the peak of the uplift component, the horizontal force is relatively small, around half of its maximum.

Buccino et al. [43] re-analysed data of the 3D experimental test carried out by Kofoed et al. [140] to obtain design methods for the estimation of wave forces on the three frontal ramps of the SSG. The authors presented a new method based on the wave momentum flux method, originally proposed by Hughes [121] for the prediction of the run-up at the smooth slope, reaching a very good agreement with the laboratory data. However, the investigation encompassed a very narrow set of data, with a limited variation of the hydraulic parameters.

To fill the gap, based on the analysis of new physical model tests using regular waves, Buccino et al. [43] and Buccino et al. [46], provided indications on the spatial distribution of the dynamic loadings. The authors derived new design equations for estimating the magnitude of the wave pressures acting onto the outer face of the device along with the respective rise times. The reliability of the design formulas was verified against experiments of Vicinanza and Frigaard [278] carried out with a random wave, suggesting the formulas can also be employed for engineering applications of the SSG.

Wave reflection

Wave reflection is a leading process for the SSG device. The need of large overtopping into the basin requires a steep and smooth ramp. Moreover, steep slopes are necessary for the occurrence of the surging type break, which produces low energy dissipation.

Zanuttigh et al. [289] showed that reflection coefficients in the SSG device with a 35° ramp subjected to random waves range between 45-90%, which are similar to the ones obtained for vertical composite breakwaters [247]. Zanuttigh et al. [289] modified the formula presented one year before by Zanuttigh and van der Meer [290] for traditional rubble-mound breakwaters, to provide an adequate prediction of the reflection coefficient also for the SSG-integrated breakwater. In detail, the authors introduced an equivalent slope for the calculation of the surf similarity parameter, ξ_0, calculated as the weighted average of the mean slope in the run-up/run-down area and the slope of the approach ramp. Moreover, the formula by Zanuttigh and van der Meer [290] is modified introducing a reduction factor to account for the water volume *"lost"* inside the first reservoir, which is always placed in the run-up area. Please, note that the formula for the estimation of the reflection coefficient on the SSG does not take into account the effect of the water that overtops at the rear side of the structure, which would reduce the reflection coefficient, as it occurs for traditional structures with low-crest freeboard [290].

In order to overcome this gap, physical model tests were conducted on the SSG model in scale 1:66 at the University of Naples [224]. Results suggested that a modification might be introduced in the reduction factor proposed by Zanuttigh et al. [289] in order to improve the reliability of predictions, which is function of the ratio between the crest freeboard of the highest reservoir and the incoming wave height, as indicated by Vicinanza et al. [279].

Wave transmission and overtopping

In the design of many breakwaters, the crest level is chosen to take into account the mean overtopping discharge, which should be kept under certain allowable volumes in relation to inconvenience or danger to people and vehicles [220, 74]. Regarding the OTD-integrated breakwater, the challenge is to keep the overtopping discharge similar to the one that occurs for traditional breakwaters, without increasing the crest height of the structure. Theoretical and experimental works conducted by Birks [29] indicates that the composite structure with a front reservoir may reduce the amount of water that overtops the seawall by up to 61%. Regarding the SSG device, no measure of overtopping at the rear side of the structure is provided in literature, and all the studies conducted in model scale investigate only the overtopping rate into the frontal reservoirs, which strongly affect the efficiency of this kind of WEC in terms of energy production [139, 282, 279, 171, 203, 202].

2.2.4.3 The OBREC device

Inspired by the extensive investigation carried out on the SSG, a slightly different device, denominated *Overtopping BReakwater for Energy Conversion* (hereafter OBREC), is conceived by the Research Team of the University of Campania in Italy.

The OBREC is an innovative harbour defence structure with a special shape designed to accommodate an OTD-device. It consists of a concrete structure with a frontal ramp and, contrary to the SSG, only one reservoir, whose base is located above the Sea Water Level (Fig. 2.16). This technology is able to capture and collect part of the energy from incident waves that overtop the frontal sloping ramp. The potential energy of the water stored in the reservoir is then converted into kinetic energy, exploiting the hydraulic head between the reservoir and the sea water level. The water flows through low-head hydraulic turbines, located in a machine room behind a vertical crown-wall, for the energy conversion.

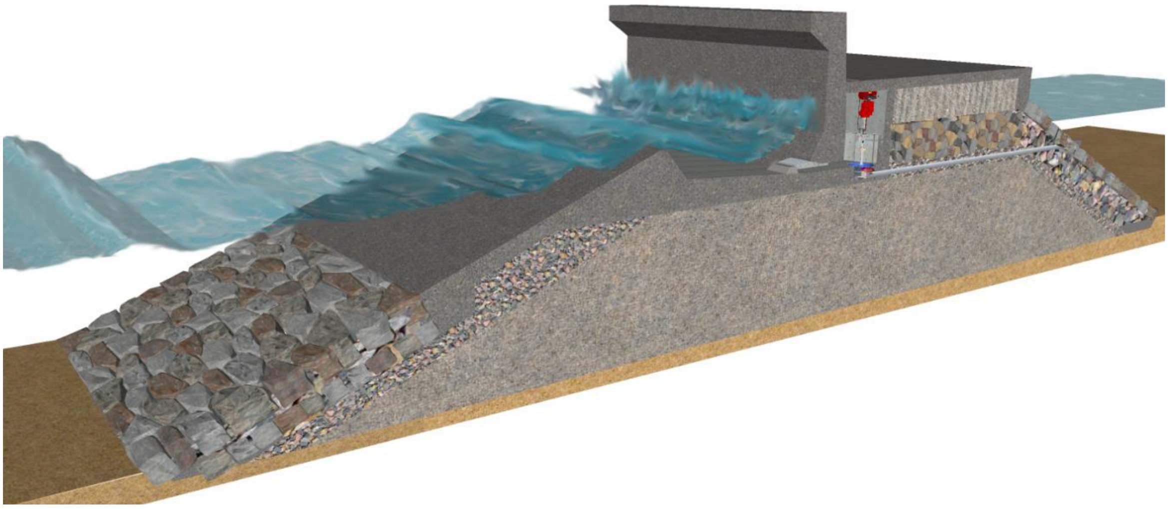

Fig. 2.16 Conceptual design of the OBREC device

Similar to the SSG, this OTD-device is particularly appropriate for breakwater application and integration, presenting several advantages: accessibility of grid connection and infrastructure, recirculation of water inside the harbour, easy installation and maintenance, no need for costly deep-water mooring or long lengths of underwater electrical cable. Furthermore, the presence of only one simple frontal ramp and reservoir significantly reduces its costs compared to the SSG, leading the device to be more economically competitive with respect to other more-established WECs integrated into breakwaters.

The study of the wave-structure interaction started in 2012, with a fist model test campaign conducted at in Denmark at Aalborg University (hereafter *AAU12*) [281, 280, 276]. The research was carried out on small scale (Froude scaling 1:30) with the principal intention to match the performance and estimate the main differences between the OBREC device and a traditional rubble-mound breakwater, which had the same configuration as presented by Nørgaard et al. [199].

The main goal was to evaluate the OBREC functionality as a harbour defence structure, thus essential parameters have been evaluated such as the reflection coefficients, the mean overtopping rate at the rear side of the structure as well as the volume of water into the frontal reservoir. The measure of the mean overtopping discharge into the reservoir for different sea state conditions has been used to estimate the potential wave energy that can be extracted from this hybrid WEC.

Analysis of the pressure and forces exerting on the device was also carried out and details on the hydraulic and structural performance are provided in the next sections.

Hydraulic performance

Regarding the reflection coefficients in front of the OBREC device, Vicinanza et al. [276] showed that they are similar or lower than those measured for the conventional rubble-mound breakwater, depending on the ratio between the frontal crest ramp and the significant wave height. In the best case, the inclusion of the OBREC reduces the wave reflection by approximately 22%, mostly due to the presence of the reservoir in which waves are captured, losing a large amount of energy.

Regarding the overtopping at the rear side of the crown-wall, preliminary results were presented by Vicinanza et al. [281]. The authors compared the overtopping at the rear side of the traditional rubble-mound breakwater and the OBREC with same crest freeboard, showing similar values. The results confirmed that the effect of the reservoir can be considered comparable to the presence of a rubble-mound in terms of wave dissipation.

Further analysis presented by Vicinanza et al. [276] showed some difference with respect to preliminary results, indicating that the OBREC slightly increases the wave overtopping at the rear side compared to a traditional breakwater, due to the presence of the ramp. The results are not surprising, considering the very smooth slope ramp that replaces part of the armour layer.

A triangular parapet was installed on the top of the vertical wall to decrease the wave overtopping rate. Results indicated a significant reduction (up to 89%) of the overtopping behind the innovative structure due to the parapet, with mean values even lower than those measured on traditional structures (see Fig. 9 in Vicinanza et al. [276]). Results suggested that the innovative breakwater can be designed with a crest height lower than a conventional rubble-mound breakwater, with a same allowable mean overtopping. This increases the social acceptance of this innovative breakwater in term of environmental and visual impacts.

Although the importance of the transmission phenomena behind the harbour defence structure, there is a lack of information regarding the wave agitation behind the OBREC-integrated rubble-mound breakwater. However, considering that the device is placed on a mound breakwater, the difference between traditional structures and this OTD-integrated breakwater might reasonable follow the same behaviour described for the overtopping phenomena.

Structural response

The results of the structural response of the OBREC model in terms of wave pressure and forces after the AAU12 tests are presented in Vicinanza et al. [281, 280, 276]. Preliminary results of the wave pressure distribution on a traditional crown-wall superstructure and those acting on OBREC were presented by Vicinanza et al. [281]. As expected, results show that the presence of a frontal smooth ramp increases the total force on the vertical crown-wall of the OBREC device.

Vicinanza et al. [280] described the load time history along the different parts of the overtopping device, identifying the typical behaviour of the wave-structures interaction. Similar to the SSG [46], over the front sloping plate and under the reservoir base, a quasi-static loading time history was recognizable, with hydrostatic pressure magnitude. Correlated video-camera analysis revealed that the incoming surging waves were not involved in breaking processes due to the large slope angle of the ramp ($\alpha = 34$). Conversely, the water jet from the overtopping waves directly hit the vertical crown-wall. In this area, pressures exhibited relatively impulsive behaviour ($p \sim 10\rho_w g H_{m0}$), slightly attenuated due to the energy dissipation in the reservoir.

Vicinanza et al. [276] presented the first tentative formulas for the prediction of the wave force on the different parts of the OBREC. Regarding the loading on the ramp, the formula from Tanimoto and Kimura [249] was adopted using the Goda's formula [93] with and without the modification introduced by Takahashi [238] to include impulsive forces from head-on breaking waves. The authors demonstrated that the best estimation was obtained by averaging the non-impulsive and impulsive force calculated using the method proposed by Tanimoto and Kimura [249]. Based on the vertical loads from Tanimoto and Kimura [249], Vicinanza et al. [276] assumed a triangular pressure distribution under the base reservoir. The comparison showed that Tanimoto and Kimura [249] underestimate the uplift forces under the basin with a relative error lower than 20%. A new design method for horizontal force on the OBREC upper crown-wall was presented, based on modification of the Nørgaard et al. [200] formula. For the lower part of the crown-wall, a correction parameter is introduced to amplify the force deriving from Takahashi et al. [242].

2.3 Prototype devices

2.3.1 Introduction

Because of the complex geometry of the OWC-integrated breakwater, research on full-scale prototype exposed to the real environmental condition are necessary to conduct, in order to have a better knowledge of the hydrodynamic wave-structure interaction as well as a reliable study of the energy production. It is clear that the commercialization step of these non-conventional breakwaters can be reached only when the reliability of the structure can be proved via field monitoring under extreme wave conditions.

Next sections present a brief description of the most important worldwide OWC-prototypes embedded into breakwaters, emphasising the results on the hydrodynamic performance and wave loading of the devices compared with traditional structures. The sections contain also the description of two standalone fixed plants placed along or near the coastline. Although they were designed with the single aim of energy production, they are included in this review due to their geometry, because they can potentially be integrated into breakwaters.

2.3.2 OWC-caisson, Japan

The first example of a full-scale OWC device embedded into a breakwater was installed at the Sakata Port in Japan [98, 189, 241, 90, 235, 235], aimed to demonstrate the technical feasibility of the technology (Fig. 2.17a). The 20 m long caisson, open to the sea below the water surface, was able to trap air above the inner free surface. Wave action alternatively compresses and expand the air, which activates two Wells turbines coupled to a generator with a rated power of 60 KW. A machine and monitoring room was installed behind the caisson for the mechanical and electrical equipment. The front wall of the OWC caisson was inclined to 45° (Fig. 2.17b), designed in order to reduce the horizontal loading acting on it, which causes vertical downward forces that contribute to stabilizing the caisson [236].

Field monitoring tests were mainly focalized on wave energy production [189, 241]. Tests conducted from October 1990 to March 1991 show that with an average incident wave power of 20.3 kW/m, the average electric power of the system was 13.25 kW [241], which corresponds to 0.663 kW/m. The wave-to-wire efficiency, computed as the ratio between the available wave power and the output power for the instrumental apparatus, was only 3.26%. It should be noted that the diameter of the installed turbine was set to be smaller than the ideal turbine for that wave climate, due to the limitation of research funds [241]. A number

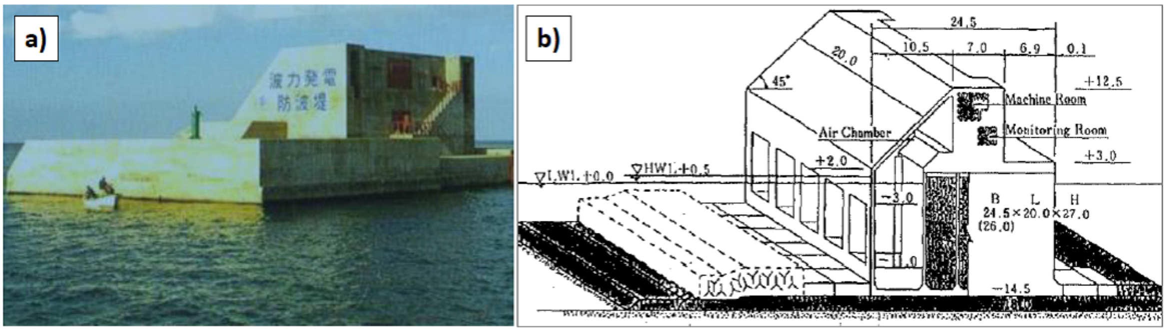

Fig. 2.17 The OWC-caisson at Sakata Port in Japan (left panel) [78] and scheme and dimensions of the device (right panel) [241]

of sensors were used to measure the incident wave conditions in front of the device, wave and air pressure and the stability of the wall members.

Goda et al. [98] presented the results of pressure acting on the prototype from tests carried out from 1987 to 1991. The data measured on the frontal wall confirmed a relatively good agreement with the pressure distribution calculated with the Goda formula [93], assuming the modification factor $\lambda_1 = 1.0$ and $\lambda_3 = 1.0$. Maximum pressure on the wall, inside the chamber and on the internal slope were also compared to the design method proposed by Takahashi [236] after the physical model test, showing a slight overestimation of the method, probably caused by the scale effects.

2.3.3 OWC-caisson, India

The second example of an OWC integrated caisson was installed in 1991 in front of the breakwater of the Vizhinjam Fisheries Harbour in India [217, 219]. Although included in this study, the device cannot be considered integrated into the breakwater because the caisson was installed at a short distance from a pre-existing breakwater structure (Fig. 2.18). The system consists of a concrete caisson with a length of 23.2 m, the width of 17.0 m and height of 15.3 m. Although the device was not designed for harbour defence and was not integrated into the breakwater, the wave forces for stability analysis were estimated by treating the caisson as a traditional vertical wall. However, no information on wave loading measured on the device, as well as the hydraulic performance of the structure, is available. The pilot was used to perform turbines coupled with a generator with a total power rate of 150 kW. After several improvements made to the instrumental apparatus incorporated in a new module, a field monitoring was carried out from April to July 1996.

Fig. 2.18 The OWC plant installed in 1991 at Trivandrum in India [78]

Despite the improvements, the results revealed an important drop in the device efficiency with the increase of the incident wave energy and an overall average efficiency of 6.3%. Moreover, after this test campaign, the operational performance of the device revealed that the seasonal amount of generated power varied considerably. For most of the time, the amount of generated power was too low to be transferred to the grid. The pilot in Vizhinjam slowly went out of use over the years, and it was completely decommissioned in 2011 for its very low amount of generated power [272].

2.3.4 Mutriku plant, Spain

In Europe, a first OWC device embedded into a breakwater was installed in 2008 at the Port of Mutriku (Fig. 2.19a) in Northern Spain [254]. The site was chosen due to the opportunity presented by the new Mutriku breakwater, which was to be built imminently at that time. The integration of a WEC in the breakwater had the condition to not transform the preliminary breakwater design or modify its principal functions. Then, the OWC was chosen to be the most suitable technology that could be incorporated in a breakwater with minimum alterations, respecting both the alignment of the planned breakwater and its function of harbour protection. Despite the indication, a significant difference introduced to accommodate the OWC system was the cross-section. The original project was a rubble-mound with a concrete wall running along the entire length, while the pilot plant installed is a vertical caisson-type.

It is worth underlying that the difference between the two configurations regarding the hydraulic performance is not provided, neither any measure of the interaction between waves

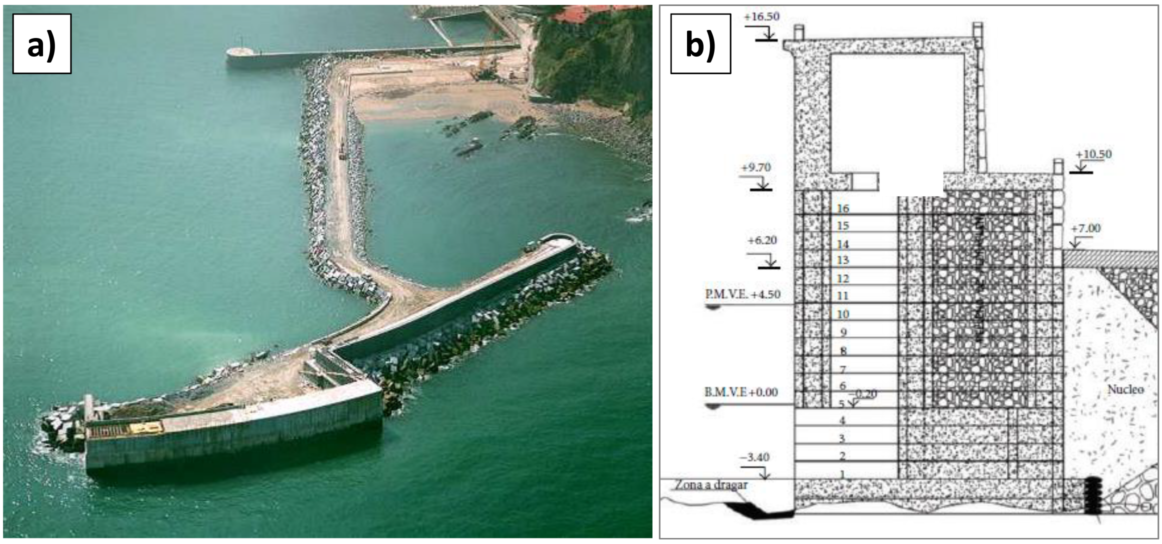

Fig. 2.19 OWC-breakwater in Mutriku, Spain (left panel) [254]; cross section of the device (right panel) [91]

and the vertical structure is available in the literature. The OWC section consists of 16 chambers designed with prefabricate parts with a total length of 100 m. In each chamber (Fig. 2.19b), a Wells turbine is connected to a turbo-generator with a capacity of 18.5 kW, giving a total nominal power of the device of 296 kW.

Despite the expectation, the average yearly output for the period that runs from 1 January 2014 to 7 October 2016 was only 41% of initial estimate [123], with a total yearly output of 246.47 MWh/y instead of the initially expected 600 MWh/y [254]. The initial expectations have not been met due to the poor design of two air chambers and regular maintenance activities. Ibarra-Berastegi et al. [123] utilized the data from the Bilbao-Bizkaia buoy to compute the available power of the energy resource in the years 2014–2016, which was 22.8 kW/m. Considering the output annual average power for the instrumental apparatus of 0.28 kW/m and using the data from the Bilbao-Bizkaia buoy, the wave-to-wire efficiency of the Mutriku pilot plat is only 2.56%. Despite the relatively low efficiency, the Mutriku plant is the only commercial OWC-integrated breakwater that regularly supplies electricity to the grid, reaching a milestone in 2015 with its first GWh of electricity supplied to the national grid [20].

Regarding the stability of the caisson, storms hit it in December 2007, March 2008 and January 2009 resulting in structural damage both to the frontal wall and roof of four chambers [253]. Preliminary analysis conducted by Horvath [114] showed that wave loads become impulsive at high tide and wave pressure might have been larger than those for which the OWC structure was designed. Furthermore, numerical analysis was carried out by Medina-Lopez et al. [178] to find possible reasons for the damage caused to the pilot in Mutriku. Calculated pressures on the front wall suggested that even the operational condition may have exceeded the OWC structure resistance, as estimated by Horvath [114]. CFD calculations also suggested that negative pressures at the bottom of the OWC front wall could have dropped below the cavitation limit, explaining the damages to the front wall.

2.3.5 ReWEC3, Italy

The construction of a full-scale device of the U-OWC [31], denominated ReWEC3, started in 2012 in Italy. The device was integrated into the vertical breakwater of the Civitavecchia harbour as shown in Fig. 2.20a.

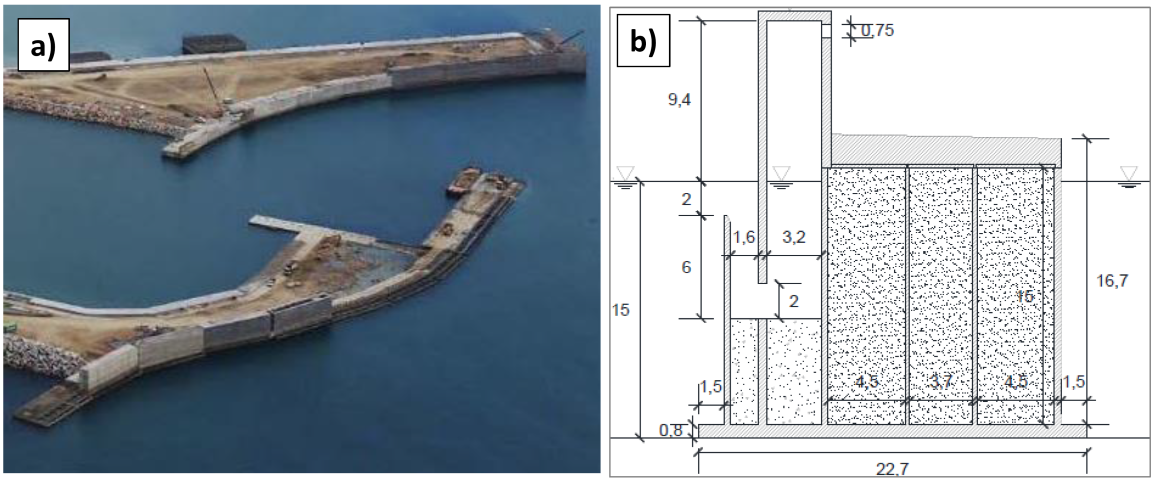

Fig. 2.20 Construction of the ReWEC3 caisson at Civitavecchia port (left panel) and cross-section of the device (right panel) [18]

The prototype represented at that time the first WEC-integrated breakwater in the Mediterranean Sea and one of the biggest in the world [16, 15]. The project of the ReWEC3 is an integration of a pre-existing project for the extension of the port of Civitavecchia in order to improve the service and quality of the infrastructure. The embodiment of the device has a twofold objective: it has been employed to reduce the reflection coefficient in front of the caisson due to the wave energy absorption and at the same time to exploit wave energy and convert it into electricity. This is a relevant aspect of the ReWEC3 because the technology was proposed as a valid alternative of a traditional caisson based on its hydraulic performance, regardless of the energy production. Furthermore, adding a ReWEC3 to a breakwater during the design stage would increase the cost for the structural change of only 5% of the total cost, as stated by Arena [14].

The entire plant in Italy includes 136 chambers for a total length of 578 m, and two specific ReWEC3 caissons are equipped with 15 pressure transducers placed inside the pneumatic chamber and vertical duct [17]. A cross-section of a ReWEC3 chamber is shown in Fig. 2.20b. The instrumentation allows investigating the ReWEC3 dynamics pressure, fundamental for calculating the average absorbed wave power, and obtaining all the essential information for the energy performance. Results show that the device absorbs about 50-70% of the average incident wave power, with some specific records where the absorption coefficient ranges from 70% to the 90% [18]. Only one traditional Wells turbine, without any optimization for the specific location, was installed on one chamber, but no data of energy production is available. Assuming that the device is fully equipped with Wells turbines of around 20 kW for each chamber, a preliminary study [14] indicates that the expected annual average electrical power delivered by the ReWEC3 in Civitavecchia Port is 2,800 MWh/y, with an average power per unit length of 0.55 kW/m. Considering that the annual average power for unit length in front of the Civitavecchia breakwater is 2.1 kW/m [15], the overall estimated efficiency of the device is then 26.33%. Direct comparison between performance indicators of the Mutriku OWC installed in the North of Spain and the ReWEC3 plant in Civitavecchia shows that the ReWEC3 device might be able to convert a significantly larger percentage of the incident wave power into electrical power.

2.3.6 LIMPET 500, Uk

The LIMPET 500 (Land Installed Marine Powered Energy Transformer -500 kW) is a full-scale device of a sloping face-OWC installed between 1998 and 2000 on the island of Islay, in Scotland [107]. The pilot consists of a collector that contains three chambers inclined at an angle of 40° to the horizontal (Fig. 2.21).

Contrary to the OWC with vertical walls, the inclined chamber offers an easier path for water ingress and egress, resulting in less turbulence and hence a lower energy loss [107, 30]. Tests carried out by McStay [177] confirmed the better hydrodynamic performance when using the sloping wall compared to traditional vertical OWC devices. On the other hand, it is well known that a sloping wall highly increases the wave overtopping discharge at the rear side of the structure for the same caisson crest [220]. For this reason, a concrete wave breaker was installed on the sloping structure with the aim to reduce the wave overtopping. Front wall inclination was also chosen to reduce the wave impact loads, resulting in a pressure

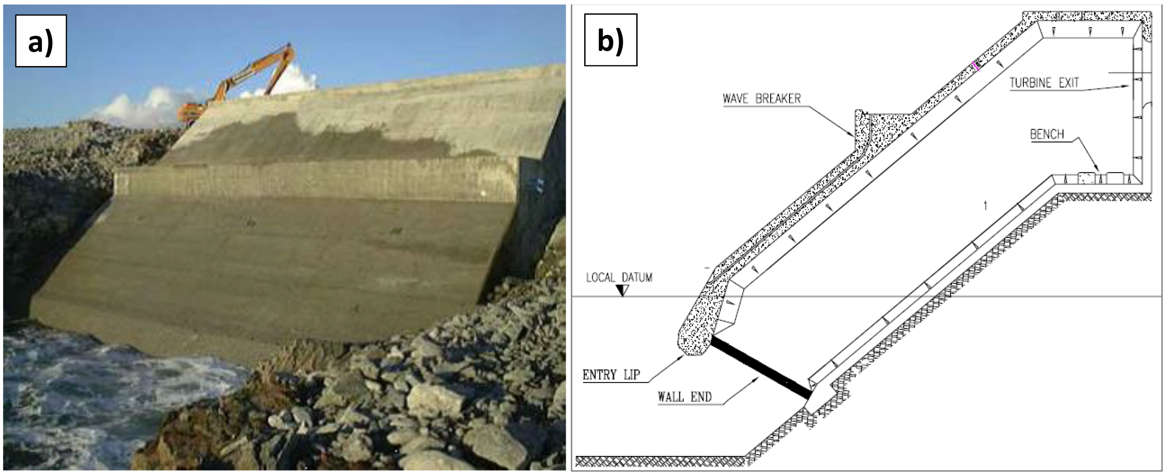

Fig. 2.21 Shoreline OWC Limpet device (left panel); cross-section of the collector (right panel) [30]

decrease of 5-7% when compared with Standard BS 6349-1:1984 [1] values for vertical walls [185]. The 50-year return pressures were extrapolated from the field pressure measurements and compared with the results of available formulas, such as those from the USACE [259], 6349-7:1984 [1] and Goda [94], showing that none of the suggested formulas resulted in an adequate agreement with the extrapolated values.

The concrete sloping caisson was equipped with a pair of the back, horizontal axis, self-rectifying Wells turbines driving each of that to 250 kW generator, giving a total installed capacity of 500 kW. The electrical equipment was installed behind the rear wall of the structure. An acoustic chamber installed behind the turbine was used in order to reduce the noise produced by the airflow through the turbine rotors. Since the construction, the device has proven to be robust surviving extremes wave condition with minimum maintenance operations and costs.

One of the main problems of the project was the relevant overestimation of the overall efficiently of the pilot, due to the overestimation of the wave resource at the site installation [288]. Measured efficiency of the device was only 8.0% compared with that predicted of about 48.0% [72]. Despite the low efficiency, the LIMPET facility was the world's first grid-connected wave energy plant. In May 2010, after ten years of operation, the plant met a significant milestone by accumulating more than 50,000 grid connected generating hours, which is at least an order of magnitude greater than most of the other technologies in this sector [230].

2.3.7 PICO, Portugal

The last European OWC pilot mentioned in this Chapter is the one installed on the Pico island in the Central Group of the Portuguese Azores. The site was chosen due to the high energy levels on Pico's North coast, which, in addition, offers some shoreline gully rocky formations, providing a natural hot spot due to the energy concentration [39]. The installation had the aim to prove the technical viability of the OWC device for remote locations, such as the isolated small islands. The device, as the aforementioned LIMPET, is a bottom-mounted shoreline structure (Fig. 2.22). However, due to its peculiar geometrical configuration, it might be potentially combined with a breakwater, for coastal or harbour defence purposes. The pilot consists of a fixed concrete chamber, with a frontal sloping wall having a width of 12 m and a height of 15 m above sea water level.

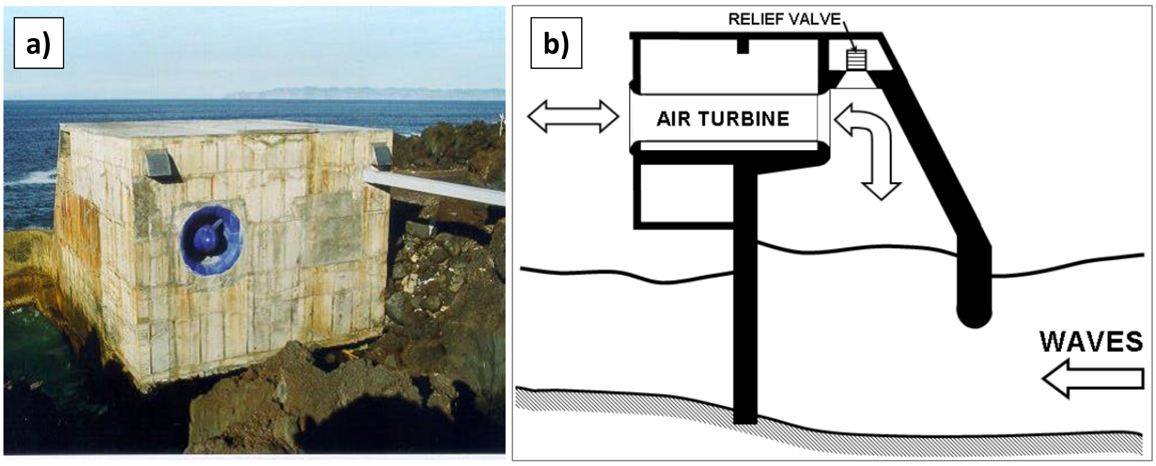

Fig. 2.22 Back view of the Shoreline OWC Pico device (left panel) [77]; cross-section of the chamber (right panel) [76]

The instrumental apparatus for energy conversion is located immediately behind the upper part of the collector wall, consisting of a horizontal-axis Wells turbine coupled with a generator with a rated power of 400 kW. At the time of its installation, the pilot was estimated to deliver around 0.5 GWh per year, having an overall (estimated) efficiency of 35% [72]. Although commissioned in 1999, the Pico plant was reactivated and connected to the local power grid only in 2005 [39], due to several technical problems and damages of the electrical equipment. Unfortunately, plant operation remained problematic and infrequent mainly due to the persistence of serious technical limitations of the turbo-generation apparatus, limiting it to power production in the range of 20-70 kW.

Despite the problems, the pilot has been operational for more than 16 years demonstrating the survivability of the OWC technology under very extreme natural condition [195, 78].

After successful tests from September to December 2010, a total annual production of 45 MWh was achieved in 1450 hours of operation [174]. Considering that the plant fulfilled its objectives as a pilot, in February 2016 the plant was closed and it was disconnected from the network in 2018 after the partial collapse of the plant [38].

2.4 Conclusions

The state of art of the traditional way to conceive and design coastal and harbour defence structures illustrates that most of the innovations introduced over the last 60 years on this field are directed towards the improving of hydraulic performance in terms of reduction of wave reflection, overtopping or new design criteria for wave loading and stability analysis for a better description of the wave-structure interaction. Despite this efforts and the innovations proposed, the main function of the breakwater, both conventional and non-conventional, still are the protection of the coasts and harbours with the reflection and dissipation of the wave energy.

A new idea is proposed in coastal engineering over the last 30 years, consisting of the conversion of traditional breakwaters into novel structures able to capture part of the wave energy in order to convert it into useful energy, i.e. electricity. Following this approach, the breakwaters are combined with wave energy devices and the new structures are here defined as "innovative breakwaters". The two WEC typologies (OWC and OTD) currently adopted for this purpose are described in this chapter, with a particular attention to the hydraulic and structural response of each of the existing technologies, analysing the pro and contra in comparison with traditional breakwaters. Finally, the chapter gives a brief description of the very few prototypes of WEC-integrated breakwater installed in the world, their principle of working and performance in terms of energy production.

Although the technologies are being developed for about 3 decades, the devices are still in an early stage of development. Among the various issues, the survivability is probably the most challenging aspect of these devices. For this reason, it is imperative that the innovative breakwaters are reliable during mild and extreme storm conditions, in order to create a convincing technology able to attract stakeholders.

Starting from the studies on OTD-integrated breakwater, a new technology, named OBREC, is currently under development. First laboratory tests allowed to compare the hydraulic and structural response of the traditional breakwater and the OBREC. However, the influence of some relevant geometrical parameters was not evaluated during the first test campaign carried out in 2012. Indeed, the tests did not allow to understand how the wave-structure interaction is affected by the reservoir width, frontal ramp length and shape, and shaft dimension.

In order to evaluate the influence of such parameters and to have a better comprehension of the wave-structure interaction, new laboratory tests were carried out in 2014 and detail will be described in Chapter 4.

Chapter 3

Objectives and methodology

3.1 Objectives

The objectives of this research have been set to close the gaps in the state of knowledge of a specific overtopping device, named OBREC, integrated into traditional breakwaters. All the proposed objectives share the same fundamental goal, which is to **study and evaluate the hydraulic and structural response of this non-conventional superstructure embedded into rubble-mound and vertical breakwaters**.

The main aim is to gain a better knowledge of the complex phenomena involved in the wave-structure interaction and to optimize the device geometry in order to reduce the uncertainties and thus limiting the risk of structural failures, ensuring the highest levels of survivability.

The objectives of the present research can be summarized as follows:

3.2 Objective 1

Evaluate the structural response of the OBREC integrated into rubble-mound breakwaters.

The OBREC device has a complex shape with a ramp and a single front reservoir designed to capture part of the wave energy in order to convert it into electricity. Due to its particular geometry, it is necessary to study every geometrical parameter that influences its structural response, as well as its global and local stability. This objective contains three sub-objectives that are formulated as follows:

Objective 1.1

Influence of the ramp shape

The design of the frontal ramp is a fundamental aspect for the OBREC device. Its geometry and shape need to be designed to maximize the hydraulic efficiency for the wave energy absorption. On the other hand, the study of the wave-interaction and stability analysis due to different ramp shapes needs to be investigated. Therefore, the wave pressure and force exerted on the device need to be analysed in detail. The principal goal of this objective is to study the resultant forces exerted on the frontal ramp, base reservoir and vertical wall under extreme wave conditions on two different shapes of the frontal ramp, flat and curved, evaluating the different performances of the two alternatives.

The influence of the frontal ramp shape on the structural response of the OBREC integrated into a rubble-mound breakwater will be studied adopting physical model tests described in Chapter 4.

Objective 1.2

Influence of the reservoir width

The design of the OBREC reservoir is the second important aspect to be considered for the device optimization. The width and the height of the reservoir highly influence the amount of water that can be stored and it needs to be designed aiming at maximizing the storage efficiency of the device. This is commonly accomplished by minimizing the rate of water overflow for the normal sea state for which the device is designed.

On the other hand, the reservoir geometry influences the structural performance of the device in terms of pressure distribution and forces exerted on it. The goal of this objective is to study this influence by investigating different reservoir widths under extreme wave conditions, focusing on the pressure and the force on different parts of the OBREC.

The influence of the reservoir width on the structural response of the OBREC embedded into a traditional rubble-mound breakwater will be investigated with physical model tests presented in Chapter 4.

Objective 1.3

Influence of the submerged ramp

The ramp in the OBREC device is designed with a submerged part, named shaft. The shaft in the OBREC has two purposes: to increase the amount of overtopping into the frontal reservoir, by reducing the roughness of the sloping structure, and to reduce the uplift forces at the horizontal base of the device. The goal of this objective is to investigate the influence of the shaft length on the reduction of the uplift loading and its effect on the global and local stability of the device integrated into a rubble-mound breakwater.

The influence of the shaft on the stability analysis of the OBREC integrated into a rubble-mound breakwater will be studied using numerical model tests described in Chapter 5.

3.3 Objective 2

Provide design formulas for the estimation of the forces exerted on the device for stability analysis.

One of the main goals of this thesis is to offer specific tools to the scientific community and harbour engineers involved in the wave energy field to be adopted for the design of the OBREC at full-scale in real environmental conditions. The goal of this objective is to present a new specific set of design formulas to predict the total forces exerted on the frontal ramp, under the horizontal base and on the vertical wall of the OBREC. By achieving this objective, engineers will benefit from these formulas to design OBREC prototypes at real scale, as described in Chapter 6.

The analysis of the total forces exerted on different parts of the OBREC device integrated into a rubble-mound breakwater will be investigated in Chapter 4 and Chapter 5 adopting both physical and numerical modelling.

3.4 Objective 3

Extend the applicability of the OBREC into vertical caissons

The OBREC device can be incorporated not only in rubble-mound breakwaters but also in vertical caissons. The goal of this objective is to evaluate the hydraulic and structural response of an innovative caisson integrated with an OBREC. The analysis will be studied with numerical model tests described in Chapter 7 .

This objective contains two sub-objectives that are formulated as follows:

Objective 3.1

Study of the hydraulic performance of the OBREC integrated into vertical caissons

The hydraulic performances of innovative caisson in terms of wave reflection and wave overtopping needs to be investigated and the results need to be compared with those obtained on traditional vertically-faced structures. Finally, the influence of the ramp crest and the position of the set-back wall on the hydraulic performances of the innovative caisson need to be studied.

Objective 3.2

Study of the structural performance of the OBREC integrated into vertical caissons

This innovative caisson has a particular shape with a conventional caisson on the central part and an OBREC device on the top. Due to the innovative configuration, the wave-structure interaction in terms of structural performance need to be investigated. The total forces exerted on the novel caisson need to be compared with those exerted on the traditional vertical breakwater, thus comparing their global stability.

As for the study of the hydraulic performance, also for the wave forces and stability analysis, the influence of the crest freeboard of the ramp and the position of the set-back wall need to be examined.

3.5 Methodology

Harbour defence structures are designed relying on three complementary techniques to deal with the complex fluid flow regime that occurs in wave-structure interaction. These techniques are the physical, numerical modelling and the field measurements.

The first one is conducted on models tested in the laboratory. Physical models can be also classified into design and process models, based on their purpose, as suggested by Kamphuis [135]. The design models are adopted to obtain information on specific models, which are small-scale replicas of a prototype with a defined geometry and boundary conditions. Conversely, the process models do not model a specified prototype but are typically adopted to investigate a more general physical process. However, physical modelling is a well-established methodology adopted worldwide with a very long tradition. Nowadays, the use of a physical model represents an accepted standard for the design of coastal structures, remaining an irreplaceable tool, which is essential for coastal engineers today as it was more than 30 years ago Baird et al. [22].

The second technique adopted to study the wave-structure interaction is based on the use of numerical models. During the last three decades, numerical models have been largely developed to be used nowadays as a complementary tool to improve our understanding of the complicated phenomena that govern the hydraulic and structural response of coastal structures. This model relies on the mathematical representation of complex turbulent process and system, in which the governing equations are discretized and solved using a computer, and it is largely adopted to assist engineers during the different phases of the design process of coastal structures.

The third technique is the field experiments, which provide much better results compared to the ones obtained in the laboratory, due to the absence of the scale and laboratory effects. On the other hand, the measures carried out on prototype have important drawbacks. They are very expensive and the tests are typically conducted over a short period of time. Field measurements of wave-structure interaction have been carried out on very few cases in the world in the past and the techniques and equipment to collect field data are still not well-established. Finally, the experimentation in hight energetic environments is very difficult, and extreme conditions with high return periods are rarely tested on prototypes.

Clearly, a single tool cannot adequately reproduce the complex processes involved in many hydraulic problems and thus replace all the others. Although the physical model still represents the traditional method to study the hydraulic interaction of the waves with coastal structures, the remarkable progress in advanced numerical models suggests the scientific community to combine more methods, adopting the approach known in the literature as *'Composite Modelling'* [134, 205, 135]. The method, recently defined by Frostick et al. [88] as *'... the integrated and balance use of physical and numerical models.'*, appears as the most advanced approach in coastal design and modelling to exploit the strengths and overcome the weaknesses of each individual approach and reducing their uncertainties. Following this novel approach in coastal engineering, it appears natural to also apply the composite modelling to the design process of the non-conventional breakwater with complex geometries such as the OBREC device.

In this research activity, the interaction of waves with the OBREC device and its structural response are firstly investigated by conducting two-dimensional physical model tests in a laboratory. The model tested in the laboratory is scaled according to the Froude model low, which is the most adopted hydraulic criterion when dealing with wave interaction with coastal structure models. The criterion is used for the modelling of a free surface in which the inertial forces are balanced by the gravitational forces. This is the typical case for water waves, also known as gravity waves because gravity is the primary restoring force. Despite the absence of an OBREC reference prototype, the reduction scale chosen for the physical models can be considered equal to 1:30. Tests are carried out generating irregular waves in the wave flume covering a relatively high range of spectral characteristics (significant wave heights and periods) for different water depths. Free surface elevation and pressure signals are gathered to evaluate the pressure distribution and resultant wave forces exerted on the OBREC model for each incident wave condition, analysing the structural response of the model for different geometrical configurations.

Besides the results obtained from the laboratory tests, numerical modelling of the interaction between irregular waves and the OBREC device is also investigated in this research using an advanced two-dimensional numerical model, named IH2VOF [163, 154], based on the VARANS (Volume Averaged Reynolds-Averaged Navier-Stokes) equations. Results of the numerical model are firstly calibrated and then validated against the laboratory data. The computational domain is designed to faithfully replicate the flume geometry, the experimental set-up, the geometry and the porous material properties of the model tested in the laboratory. Furthermore, IH2VOF is adopted to overcome some limitations of the physical model tests, which not fully represent the wave-structure interaction process. Additional numerical simulations are then carried out on different OBREC geometries not tested in the laboratory to better investigate the influence of specific geometrical parameters and their effect on the global and local stability of the device. The numerical model is also adopted to study the hydraulic and structural performance of the OBREC integrated into a vertical caisson, and the principal difference with a conventional vertical-face structure are investigated.

The combined use of the physical and numerical modelling allowed to obtain a design tool for the evaluation of the wave pressure and forces exerted on the OBREC, which has been used in the preliminary design of the first full-scale device installed in Italy and under monitoring at the time of writing this thesis.

Chapter 4

Physical model test

4.1 Introduction

The reliability of WEC-integrated breakwaters is one of the most important pre-requisites for their success and future commercialization. Therefore, in order to reduce the cost and risk of the wave energy technologies, a detailed study on their structural response against extreme waves is required.

This Chapter aims at providing the results of the physical model tests carried out in 2014 on the OBREC, with more emphasis on the analysis of wave pressure and forces under extreme wave conditions. As described in Section 2.2.4.3, Vicinanza et al. [276] presented the results of model tests carried out in 2012, describing the hydraulic and structural response of the device, compared to a similar rubble-mound breakwater designed according to traditional criteria. Results showed that the integration of OBREC in the traditional rubble-mound breakwater improves the global hydraulic performance. Moreover, the authors found that due to the particular shape of the structure, the wave forces on the main structure could not be estimated directly using the well-established prediction formulas adopted for traditional breakwaters.

In order to have a more accurate comprehension of the complex phenomena of the wave-structure interaction, finding the optimal geometrical configuration, new physical model tests were carried out at the Hydraulic and Coastal Engineering Laboratory of Aalborg University [64]. This research completes the previous analysis, and it is intended to be of direct use to engineers in the preliminary design of this innovative breakwater.

The goal is to understand the influence of some geometrical parameters, such as the horizontal reservoir width and frontal ramp shape and length, on the hydraulic performance and wave pressure/forces exerted on the different parts of the OBREC. Differently to the previous test campaign, an extension of the ramp below the still water level is introduced to reduce the uplift loading at the base device and to increase the overtopping in the front reservoir, thus increasing the performance in terms of wave energy absorption.

The Chapter is organized as follows: Section 4.2 provides the description of the wave flume and the OBREC model tested in it, the characteristics of the generated waves and the instrumentation adopted for the wave pressure analysis; Section 4.3 describes the results obtained from the physical model analysis, comparing the different geometric configurations tested and presenting semi-empirical design formulas to estimate the total wave forces acting on the device with a specific ramp shape.

It is worth underlying that results of the hydraulic performance were presented by Iuppa et al. [126] and the wave loading described in this chapter were used for preliminary analysis of the design of the first full-scale OBREC demonstration plant constructed at Naples harbour in Italy and under monitoring at the time of writing this thesis.

4.2 Experimental set-up and procedure

4.2.1 Wave flume

The 2D experimental tests campaign are performed in a 25 m long, 1.50 m wide and 1.2 m deep wave flume, running a total of 200 tests considering a scale of 1:30 (Froude scaling) compared to the typical prototype dimension.

The wave flume bottom is horizontal for the first 6.5 metres starting from the piston wave paddle, followed by a step of 3.5 cm, a 1:98 slope section with a length of 9 metres and a final horizontal section where the model is placed (Fig. 4.1).

At the end of the flume, a dissipative gravel beach with a slope between 1:4 and 1:5 is positioned in order to absorb the energy of the waves transmitted at the rear side of the models and minimize the reflection in the channel. The flume is separated in two sub-sections by a guiding wooden wall with a total length of 5.00 m located in the central part of the wave flume. The aim is to test two different OBREC configuration models, simultaneously placed in the wave flume and adjacent to each other. Each sub-section has a width of 0.73 m, and the two models are displayed in Fig. 4.2.

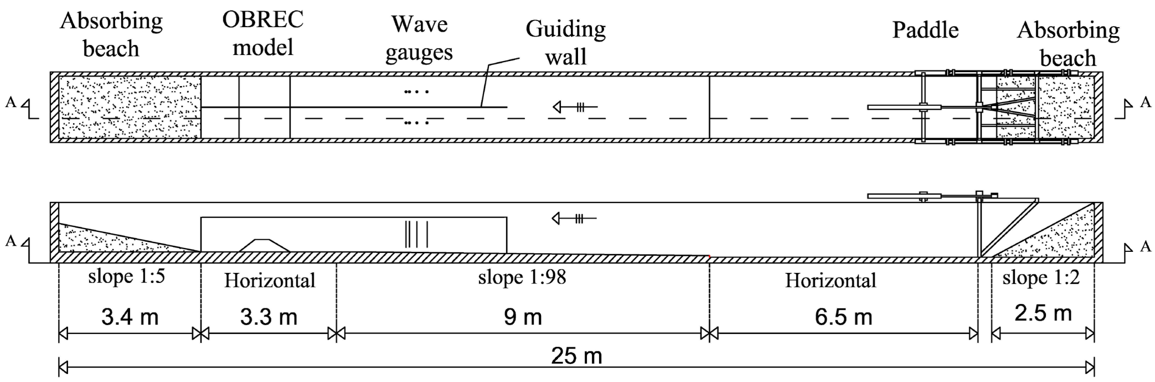

Fig. 4.1 Layout of the 2D wave flume at the Aalborg University.

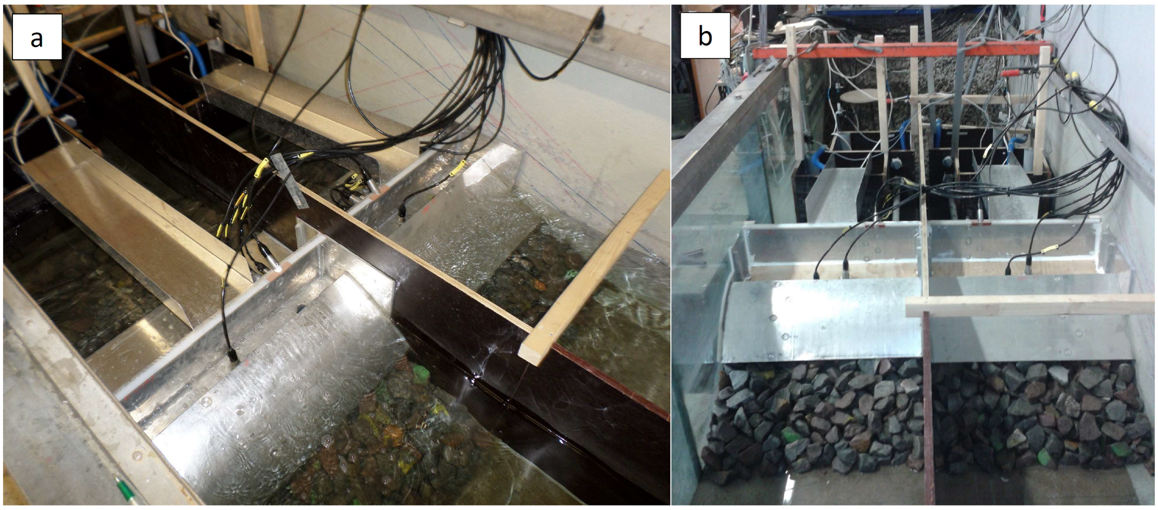

Fig. 4.2 Lateral (a) and frontal view (b) of the two configuration tested in the wave flume.

4.2.2 Tested configurations

The physical model tests in the wave flume are carried out on two different composite models, which both consist of rubble-mound foundations and steel structures on the top, modelling the ramp, reservoir and vertical wall of the OBREC device. The thickness of the steel structures is around 5 mm. The superstructures are well-fixed to the channel borders and central wooden wall, thus no displacement was allowed during the tests.

The models are installed in the flume in different steps as shown in Fig. 4.3. Firstly, the two steel models are fixed to the channel with the bases placed at 0.30 m from the wave flume bottom. Subsequently, the rubble-mound foundations, with the different layers of rock material, are installed under the fixed structures.

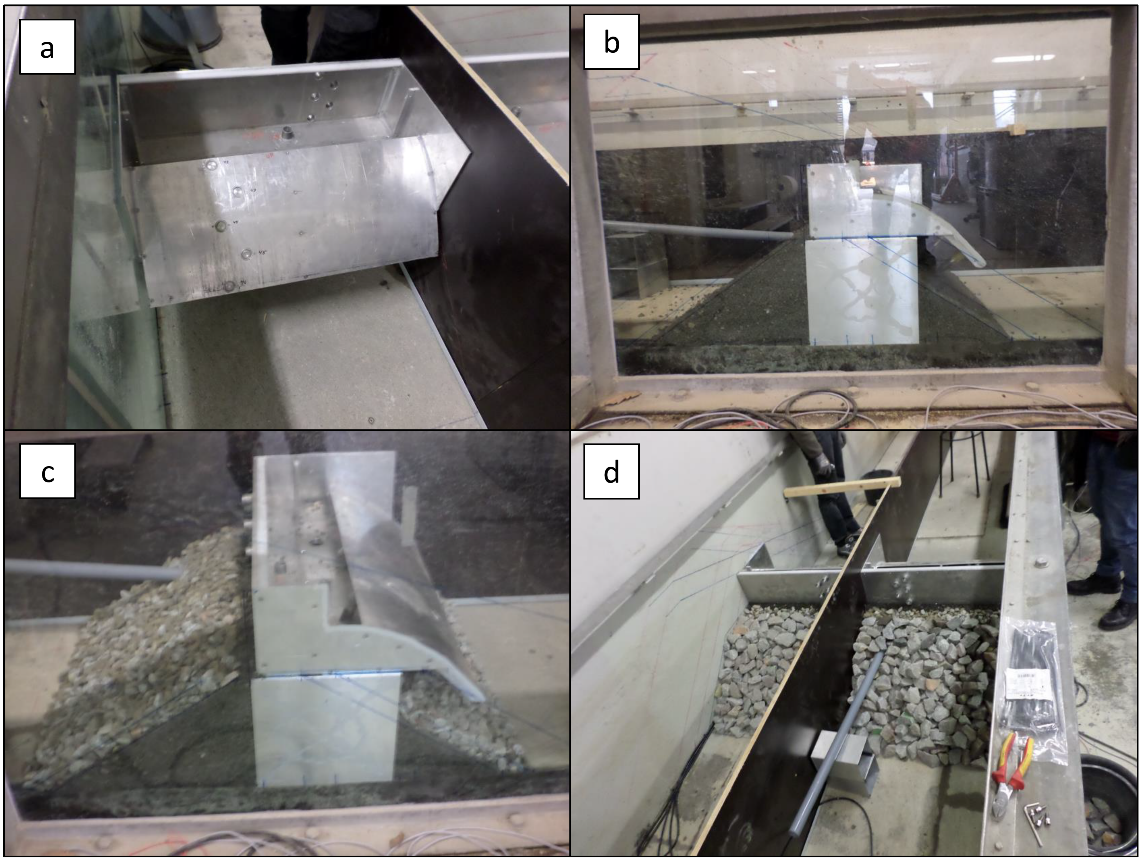

Fig. 4.3 OBREC models construction phases: installation of the steel structures (a), positioning of the core material (b), filter layer (c) and armour layers (d)

The two adjacent configurations are similar, except for the shape of the frontal ramps, which are flat for one configuration (hereafter *'flat configuration'*) and curved for the other one (hereafter *'curved configuration'*). The ramp in the flat configuration has a planar slope of 34° with respect to the horizontal (Fig. 4.4). It is worth noting that Kofoed [138] conducted physical model on an OTD-device, analysing the role of the ramp angle on the overtopping rate and overall hydraulic efficiency. The results indicated that a ramp of 19° has a slightly better performance (maximum gain about 4%) compared to a ramp with an inclination of 30° and 35°. However, the author argued that a ramp with a low angle slope could lead the steepest waves to collapse as plunging waves. This would lead to an increase of the energy losses and possible higher pressure on the frontal ramp due to the breaking process. Kofoed [138] expressed a formula for the overtopping behaviour of offshore OTD devices with a single level reservoir, indicating an empirical coefficient that takes into account the reduction of hydraulic efficiency for slope angles α deviating from $\cot\alpha = 1.7$ (α=30°), which was assumed by the author as the optimal slope inclination for the offshore OTD-devices.

Following this suggestion, the frontal ramp of the flat configuration of the OBREC device is then designed steep enough (34° in this case) to minimize the occurrence of the breaking waves and maximize the wave overtopping into the reservoir. Please note that a similar slope was adopted also by Vicinanza et al. [276] for first physical test campaign on the OBREC device.

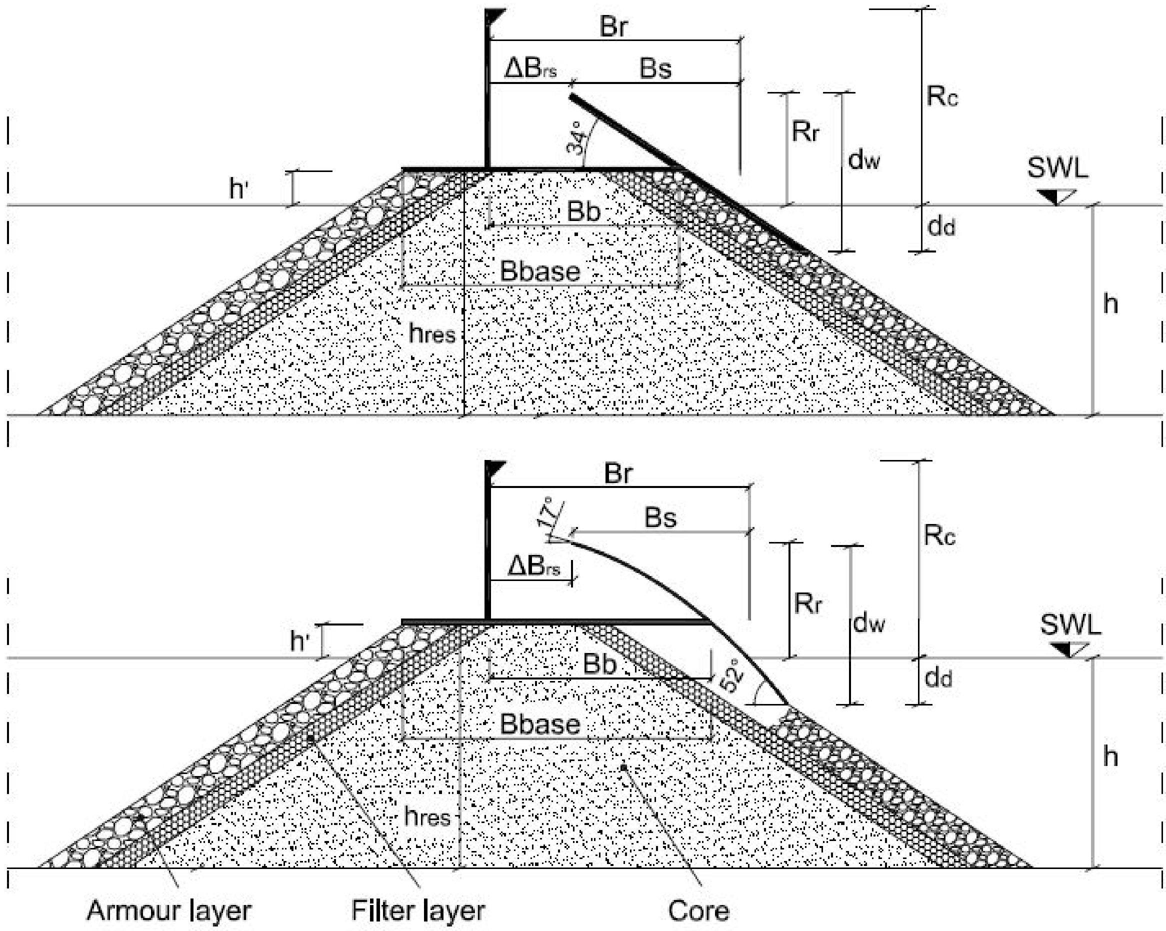

Fig. 4.4 Laboratory model cross section and definition of the principal geometrical parameters

The curved configuration has a curvilinear ramp with an initial slope of 52° at the lower part, which gradually decreases until reaching the crest of the ramp with a slope of 17° (Fig. 4.4). This configuration is proposed to verify if results obtained by Kofoed [137] for offshore OTD devices with a curved ramp can be extended also for devices integrated on breakwaters and located in intermediate or shallow water depth, such as the case of the OBREC.

In Fig. 4.4, B_r stands for the emerged structure width, B_s is emerged sloping plate width, B_b is the lower side reservoir width, B_{base} is base width, ΔB_{rs} is the horizontal distance between the crown-wall and the ramp crest, d_w is the ramp height, d_d is the submerged shaft, h stands for the water depth at the toe of the structure, h_{res} is the vertical distance between the base reservoir and the bottom, R_r is the crest freeboard of ramp and R_c crest freeboard of the crown-wall. Table. 4.1 summarizes the range of the model geometrical characteristics.

Table 4.1 Geometrical characteristics of the two models.

	R_c (m)	d_w (m)	R_r (m)	B_b (m)	ΔB_{rs} (m)	h_{res} (m)
Min	0.147	0.19	0.04	0.219	0.10	0.30
Max	0.227	0.19	0.12	0.419	0.30	0.30

A parapet, also defined as *bullnose*, is placed on the top of the upper crown-wall in order to reduce the overtopping discharge passing the overall structure. It has the shape of an isosceles triangle with horizontal and vertical sides of 2 cm. Vicinanza et al. [276] already demonstrated that the presence of this "nose" on the OBREC device causes a reduction of the overtopping rate at the rear side of the model up to 89% compared to the same configuration without the nose.

Each of the two adjacent configurations is tested for three different dimensions of the reservoir, obtained by a horizontal translation of the crown-wall:

- Small reservoir ($\Delta B_{rs} = 0.10$ m);
- Large reservoir ($\Delta B_{rs} = 0.20$ m);
- Extra-Large reservoir ($\Delta B_{rs} = 0.30$ m);

The rubble-mound materials were chosen to ensure the stone stability under the wave action and to reproduce the main hydraulic behaviour of the structure. The porous media below the OBREC base is composed of three layers with different equivalent cube side lengths exceeding by 50% the stones ($D_{n,50}$). In detail the rubble-mound foundation consists of a core with nominal diameter $D_{n,50}$ = 5 mm, filter layers with $D_{n,50}$ = 20 mm and a seaward and leeward external armour layer with $D_{n,50}$ = 50 mm.

4.2.3 Instrumentation

Laboratory tests allowed to measure the following data: wave surface elevation in the flume, wave pressure on the device and wave overtopping discharge both in the front reservoir and behind the whole structure. Please note that in this Chapter it will only describe the instrumentation used for the analysis of the structural response of the device, which is the main objective of the research work, thus the wave surface measurement in the channel and pressure transducers along the two adjacent models are here considered. For details of the instrumentations used for the wave overtopping measurements into the reservoir and at the rear side of the structure, please refer to the work of Di Lauro [70], Iuppa [125], Iuppa et al. [126].

4.2.3.1 Resistance Wave Gauges

Eight resistance wave gauges (WG), displaced in two parallel arrays, are located along the wave flume in front of the structure, based on suggestions by Klopman and Meer [136].

The first wave gauge (WG-1) is placed at 14 m from the initial position of the wavemaker and other three free surface gauges at 0.30 m, 0.55 m and 0.70 m from the position of WG-1, according to the wave direction (Fig. 4.5).

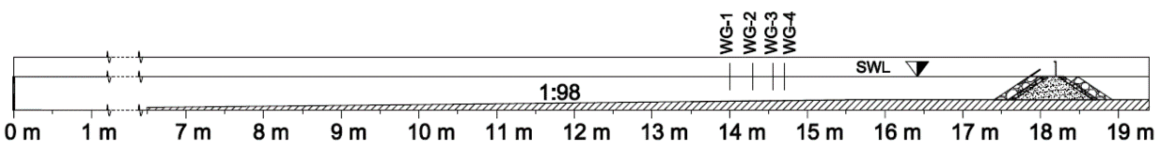

Fig. 4.5 Sketch of the experimental setup and position of the wave gauges in the wave flume

The gauges are installed to measure the wave free surface time series and separate the incident and reflected waves in front of the model. The incident and reflected spectra are separated and estimated using the method of Zelt and Skjelbreia [291], which is based on linear wave theory and it is used for an arbitrary number of wave gauges. Additionally, the wave field in front of the OBREC device is also separated into the incident and reflected waves using the time-domain method proposed by Frigaard and Brorsen [87], which is based on the use of digital filters, showing similar results of the ones computed with the method of Zelt and Skjelbreia [291]. For this reason, the data of the incident and reflect spectra here considered refer to the result obtained from the method of Zelt and Skjelbreia [291].

The resistance wave gauges used in the campaign test operate on the principle of measuring the current flowing in an immersed probe consisting of a pair of parallel stainless

Fig. 4.6 Two parallel arrays of wave gauges placed in the wave flume

steel wires. The absence of other support reduces the interaction between the measuring device and the incoming/reflected waves. The current passing between the stainless wires is proportional to the immersion depth. When the steel wires are immersed, the circuit is closed, and the established potential difference, ΔV, is expressed as:

$$\Delta V = R \cdot i \tag{4.1}$$

where i is the intensity of electric current and R is the resistance. The resistance value is directly proportional to the wire conductor length, l, and inversely proportional to its section, s, (second law of Ohm) and it can be written:

$$R = \rho \cdot \frac{l}{s} \tag{4.2}$$

where ρ is the electrical resistivity. The electrical potential difference, measured by a voltmeter placed in the top box of the probe, is directly proportional to the submerged portion of the probe, and consequently to the water surface elevation in the channel. The current is converted into a signal in Volts proportional to the depth of immersion. The length of the steel wires adopted in the laboratory allows the reading of waves with a height up to 0.40 m, which is higher than the maximum wave height expected during the tests.

The calibration process of resistance probes in the channel was daily carried out in the laboratory using WaveLab3 developed by the Department of Civil Engineering of the Aalborg University [86]. The methodology is the following: the level of quiet expressed in Volts is first measured; the probes are vertically raised with respect to the level of quiet of a known value (0.10 m) and the measurement is repeated; the probe is lowered again with respect to the level of quiet and the measurement is again carried out. This activity allows evaluating three points that link the measurement of the tension to the free surface. The signal in Volts is converted to metric units by a linear relation:

$$\eta = V_0 + k \cdot V \tag{4.3}$$

where η is the measure of the oscillation of the free surface in meters, V is the measure of the oscillation of the free surface in Volts, V_0 is the intercept of the linear conversion relation (in Volts) and k the slope of the same relation. The parameters of the linear regression V_0 and k are calculated with a line passing through the three points representing the measurements made during the calibration phase at three known water levels in the channel.

During the test campaign, it was necessary to calibrate the depth gauges every day, before the tests, and always after the variation of the water level in the channel and when tests were interrupted for more than two hours. Repeating the calibration in the same day was often necessary to avoid possible errors due to the conductivity variation in the water when the temperature and the salinity concentration might change.

The data of the gauges in the channel were acquired with a sampling frequency of 1000 Hz and are analysed using the Wavelab3 [86].

4.2.3.2 Pressure transducers

The wave-induced pressures on each of the two adjacent OBREC models were measured using 14 pressure transducers of model series *Druck PMP UNIK 5000* produced by the General Electric Company (Fig. 4.7). The pressure transducers have a diameter of 25 mm and a correct frequency response up to 5 kHz. The pressure data was also acquired with a sampling frequency of 1000 Hz.

The data of the pressure signal is processed through the low-pass digital filter. It aims at filtering out the high-frequency components from the raw signals in order to reduce the

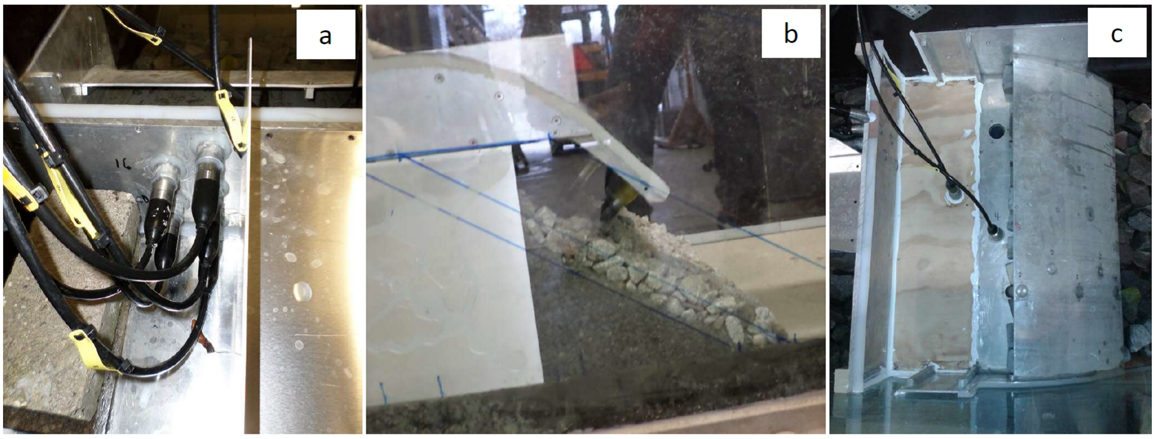

Fig. 4.7 Pressure transducers on the wall (panel *a*), frontal ramp (panel *b*) and base reservoir (panel *c*) for the curved configuration)

noise and to avoid sporadic spikes in pressure signals. Filtering the signal of the pressure data is a very delicate task. An appropriate low-pass filter should be designed to only remove unrealistic disturbs from the pressure signal and not significantly influence the outcome of the experiments, thus keeping the original shape and dimension of the eventual wave impact signal as best as possible. A cut-off frequency is selected based on the wave celerity and the spacing of the pressure sensors using the approach proposed by Lamberti et al. [150]. Hence, the integral of the pressure on the sloping plate and of the uplift pressure was digitally filtered to 100 Hz while the pressure on the crown-wall was filtered to 250 Hz. Although a slight reduction of the peak forces was noted for some sporadic peaks, the selected cut-off frequencies are considered as the best choice for the data analysis of the physical model tests.

For each configuration of the two OBREC models located in the wave channel, 5 pressure transducers are positioned on the front sloping ramp, 3 along the reservoir bottom in order to measure the uplift pressure, 5 on the vertical crown-wall behind the reservoir and 1 on the triangular parapet located on the top of the wall, as displayed in Fig. 4.8.

4.2.4 Wave characteristics

The wave motion was triggered by a hydraulic driven piston-type wavemaker, whose movement is electrically controlled. The software AwaSys3 [85], developed at the Department of Civil Engineering of the Aalborg University, was used during the test campaign in order to produce the signal to send to the wave paddle to generate different sea states. The system allows generating both regular (linear, second-order or approximated by the theory of stream function) and random waves, with energy spectrum chosen among JONSWAP,

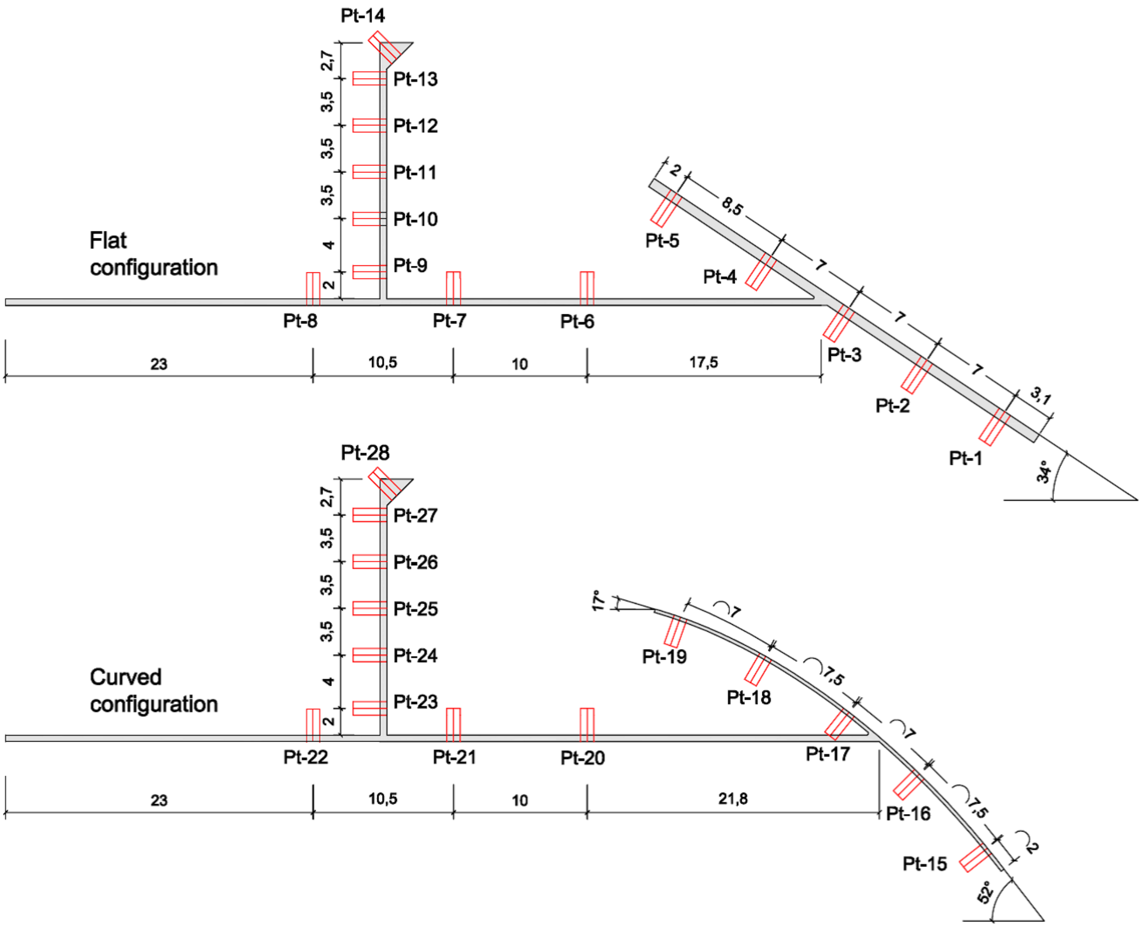

Fig. 4.8 Positions of the pressure transducers on the two OBREC models

Pierson-Moskowitz, Bretschneider-Mitsuyasi, Texel Marsen Arsloe. Regarding the irregular wave generation, a standard JONSWAP-type spectrum [105] with a peak enhancement factor of 3.3, is considered for all the tests.

The software AwaSys3 [85] features with an active absorption system, as recently described in Andersen et al. [13], controlling the signal measured by two resistive wave elevation gauges mounted directly on the front of the wave board, thus moving with the wave paddle. The active absorption system is based on 2-D linear wave theory including nearfield disturbances (evanescent modes). The theory is almost identical to that of Schäffer and Jakobsen [226] except that the wave gauges mounted on the moving paddle might have a gap to the paddle face. The signal acquired by the two probes, appropriately processed by the AwaSys3 software, allows modifying in real time the wavemaker motion in order to absorb reflecting waves, minimizing the presence of re-reflection waves that would cause an agitation in the channel, thus contaminating the desired incident waves. An advantage of wave gauges moving with the wavemaker is that they measure a more or less Lagrangian frame of reference. The wave kinematics and dynamics in a Lagrangian frame of reference extends the range of validity of linear wave theory as used in the derivation of active absorption systems [227]. Fig. 4.9 shows a detail of the wavemaker and of two resistive gauges positioned on it.

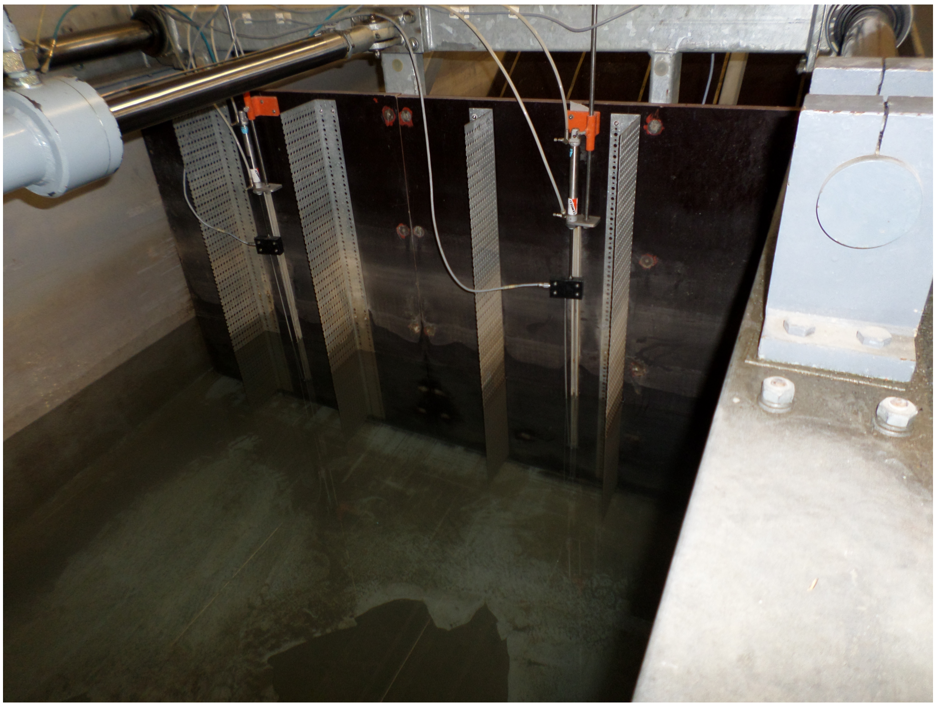

Fig. 4.9 Wave gauges near the pyston wavemaker

The total duration of each test was chosen in order to obtain a long time series with around 500-1000 waves, depending on the test. The data series was chosen to be long enough to fully define reliable wave spectra. Moreover, the length of each test can be considered sufficient to obtain consistent statistical values of the peak pressures/forces, as largely debated in the PROVERBS [207], as well as to perform the necessary statistical reliability for the wave overtopping analysis, as suggested by Romano et al. [222].

The incident and reflected spectra are separated and estimated using the method described in Zelt and Skjelbreia [291], in order to compute the wave characteristics in front of the model. From the incident variance density spectra, $S_\eta(f)$ (m^2/Hz), the 'nth-order moment' m_n is computed as:

$$m_n = \int_{f_{in}}^{f_{fin}} f^n \cdot S_\eta(f) df \qquad \text{for n = ..., -2, -1, 0, 1, 2, ...} \tag{4.4}$$

Please note that in the present analysis, m_n is determinate based on the integral of the estimated incident spectra truncated at $f_{in} = 0.33 \cdot f_p$ and $f_{fin} = 3.0 \cdot f_p$, where f_p is the peak frequency of the spectra. From the incident wave spectra, the following main parameters are considered in the analysis:

$$H_{m0} = 4.004 \cdot \sqrt{m_0} \tag{4.5}$$

$$T_p = \frac{1}{f_p} \tag{4.6}$$

$$T_{m-1,0} = \frac{m_{-1}}{m_0} \tag{4.7}$$

$$T_{m0,1} = \frac{m_0}{m_1} \tag{4.8}$$

$$T_{m0,2} = \sqrt{\frac{m_0}{m_2}} \tag{4.9}$$

where H_{m0} represents the significant wave height, T_p is the peak period, i.e. the inverse of the peak frequency, $T_{m0,1}$ is the spectral period based on the first order moment, $T_{m0,2}$ is the spectral period based on the second order moment and $T_{m-1,0}$ is the energy wave period.

Only 79 tests are considered for wave loading analysis, with different significant wave heights, H_{m0}, energy wave periods, $T_{m-1,0}$, and water depths, h. The tests are characterized by extreme wave conditions and Table. 4.2 summarizes the range of the wave characteristics of incident waves measured at the toe of the models for the tests here analysed.

Table 4.2 Ranges of incident wave characteristics for extreme waves.

	H_{m0} (m)	T_p (m)	$T_{m-1,0}$ (m)	h (s)
Min	0.079	1.42	1.36	0.270
Max	0.139	2.56	2.20	0.350

4.3 Results

This section presents the results of the physical model tests in terms of the wave pressure and forces exerted on the different parts of the OBREC. The principal objective is to investigate the overall structural functionality of the OBREC integrated into a traditional rubble-mound breakwater.

As the loadings and structural performance of this innovative breakwater strongly depend on the run-up and overtopping processes, a short preliminary section, named "Hydraulic performance" (Section 4.3.1), is also included in this Chapter and describes the principal results obtained by Iuppa et al. [126].

4.3.1 Hydraulic performance

4.3.1.1 Overtopping at the rear side

Iuppa et al. [126] compared the measured overtopping at the rear side of the OBREC, with the prediction formulas for overtopping over a dyke slope with promenade, storm wall and parapet provided by Van Doorslaer et al. [268]. Results showed that the formula proposed by Van Doorslaer et al. [268] tends to underestimate the measured values, and Iuppa et al. [126] addressed the reason due to the absence of the reservoir. The author proposed a new formula that takes into account not only the incident significant wave height and peak period, but also the combined effect of the shaft dimension, the reservoir width, as well as the crest of the wall on the mean overtopping value. The mean wave discharge at the rear side of the OBREC, q_{rear}, can be estimated as follows:

$$\frac{q_{rear} \cdot T_{m-1,0}}{L^2_{m-1,0}} = 0.0139 \cdot \exp(-7.17 \cdot X_{rear}) \tag{4.10}$$

where $T_{m-1,0}$ is the energy wave period at the toe of the structure and $L_{m-1,0}$ is the deep water wave length using $T_{m-1,0}$. The parameter X_{rear} in Eq. 4.10 is defined by the following relation:

$$X_{rear} = \left(\frac{R_c}{H_{m0}}\right) \cdot \left(\frac{\Delta R_c}{d_w}\right)^{0.25} \cdot \left(\frac{\Delta B_r}{B_r}\right)^{0.5} \tag{4.11}$$

where $\Delta R_c = R_c - R_r$ represents the vertical distance between the crest ramp and the crest wall.

4.3.1.2 Overtopping into the reservoirs

Regarding the overtopping discharge in the front reservoir, q_{res}, Iuppa et al. [126] observed that the shorter the length of the submerged sloping plate (d_d) with respect to the wavelength $L_{m-1,0}$, the larger the effect of the amour roughness. For this reason, in order to estimate q_{res}, the authors suggested using the formula from EurOtop [73] adopting the probabilistic approach:

$$\frac{q_{res}}{\sqrt{g \cdot H_{m0}^3}} = 0.2 \cdot \exp\left(-2.6 \frac{R_c}{H_{m0} \cdot \gamma_f \cdot \gamma_\beta \cdot \gamma_b}\right) \tag{4.12}$$

where γ_f is the reduction factor due to the roughness and permeability of the slope, γ_β is the reduction factor in the case of oblique wave attack and γ_b is the influence factor for the presence of a berm. The relations for γ_β and γ_b can be found following the instructions presented in the EurOtop [73]. Regarding the parameters γ_f, due to the configuration of the device with a smooth impermeable ramp on the higher part of the armour layer, a new formula is proposed by Iuppa et al. [126]:

$$\gamma_f = \begin{cases} \tanh\left[7.47\left(\frac{d_d}{L_{m-1,0}}\right)^{0.42}\right] & \text{if } \frac{d_d}{L_{m-1,0}} \geq 0.006 \\ 0.7 & \text{if } \frac{d_d}{L_{m-1,0}} < 0.006 \end{cases} \tag{4.13}$$

The authors observed also a reduction of approximately 20% in overtopping discharge in the front reservoir and at the rear side of the structure for the curved configuration when compared to those calculated on the flat configuration. These results affect the potential energy production of the system. On the other hand, the curved ramp ensure higher safety levels at the rear side of the crown-wall. However, since the safety level could be increased by using a wider front reservoir, Iuppa et al. [126] suggested that the configuration with a flat ramp is the most desirable for the OBREC device integrated into rubble-mound breakwater.

4.3.1.3 Reflection

Iuppa et al. [126] showed that the reflection values of the OBREC ranges between 0.5 to 0.9. The author argued that reflection coefficients mostly depend on the ratio between the ramp freeboard, R_r, and the significant wave height, H_{m0}. In detail, the reflection is significantly reduced by the wave energy dissipation into the reservoir for lower values of the ratio R_r/H_{m0}, and the reflection coefficient ranges between 0.5-0.7. With the increase of R_r/H_{m0}, almost no waves overtop the frontal ramp, thus leading to higher reflection coefficients ($K_r \approx 0.7-0.9$).

The authors investigate the influence of the submerged ramp length on the wave reflection, showing that K_r increases with the increase of the latter. In order to take into account also the effect of the submerged ramp length on K_r, a corrective coefficient was presented by Iuppa et al. [126], adapting the formula from Zanuttigh and van der Meer [290] also for the OBREC device. The reflection coefficient of the OBREC, K_r, can be evaluated with the following formula from Zanuttigh and van der Meer [290]:

$$K_r = \tanh(a \cdot \xi_{m-1,0}^{b}) \tag{4.14}$$

where $\xi_{m-1,0}$ is the breaking parameter referenced to $T_{m-1,0}$, and the parameters a and b are defined as:

$$a = 0.167[1-\exp(3.2 \cdot \gamma_{f,K_r})] \tag{4.15}$$

$$b = 1.49(\gamma_{f,K_r} - 0.38)^2 + 0.86 \tag{4.16}$$

Iuppa et al. [126] proposes a relation for the coefficient γ_{f,K_r}, which is slightly different than that originally proposed by Zanuttigh and van der Meer [290]:

$$\gamma_{f,K_r} = c_{\gamma_f} \cdot \gamma_f \tag{4.17}$$

in which γ_f is the parameter already presented in Eq. 4.13 and the corrective coefficient c_{γ_f} is evaluated with the following relation:

$$c_{\gamma_f} = \tanh\left[2.64 \cdot \left(\frac{R_r}{H_{m0}} \cdot \frac{d_d}{L_{m-1,0}}\right)^{0.28}\right] \tag{4.18}$$

4.3.2 Wave loading analysis

A correct prediction and evaluation of wave pressure and forces are crucial for the design of traditional coastal structures, as well as for innovative breakwater with non-conventional geometry. This section presents the results of the analysis on wave loading exerted on the OBREC models, with a discussion of two different aspects: i) the effect of the ramp shape on the wave loads and ii) the prediction formula for the forces estimation. The analysis is carried out by considering the wave-induced loadings at various parts of the OBREC: the frontal ramp, the base device and the vertical wall. In the analysis it has been decided to consider the vertical wall in two different sections named lower and upper crown-wall, indicating respectively the part of the wall immersed when the reservoir is filled and the superior exposed part (Fig. 4.10). Please note that the 79 tests considered in this analysis refer only to extreme wave conditions, i.e. when the two reservoirs are saturated for almost the entire test duration, as indicated by Iuppa et al. [126].

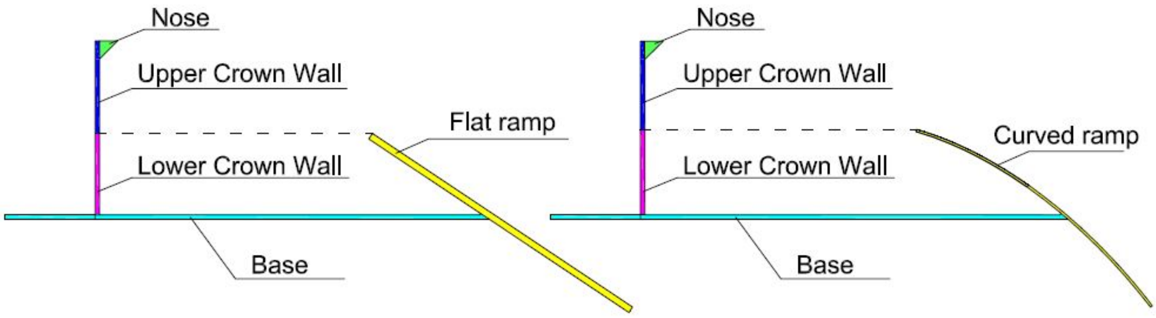

Fig. 4.10 OBREC structural elements scheme for flat and curved configurations

The measured pressure and the computed resultant forces take into account only the dynamic component of the pressure exerted on the model. The latter is obtained considering that the recorded pressure is null at the beginning of the test, regardless of whether the transducers is immersed or not in the water for the specific water depth analysed. It is clear that for the stability analysis the forces calculated in this section need to be increased considering the hydrostatic force acting on the submerged part of the OBREC.

The resultant wave forces are calculated assuming a linear pressure distribution between the (dynamic) pressure measured by the transducers placed along the models. This assumption can be considered valid, in particular for the force acting on the frontal ramp and the vertical wall, considering the short distance between the individual pressure transducers. Regarding the vertical force on the horizontal base, this methodology might be less accurate due to the presence of only three pressure transducers covering the entire length of the base.

A linear extrapolation of the neighbouring measured pressures is used in order to define the pressure on the structure wedges where no direct measure is available. Moreover, the pressures acting underneath the ramp are not measured, thus the total forces acting on the device do not take into account the force underneath the shaft.

It is known that wave forces acting on coastal structures are highly variable, even more than the waves that generate them, so these forces may be best described by their statistic rather than deterministic values. However, it is traditionally adopted in literature [94, 238, 207] to describe the force on structure based on the average of the highest $1/250^{th}$ peaks of loadings in a given random sequence (also denoted as $F_{1/250}$). Please note that this value is dependent on sample size and it is not possible to identify the exceedance level equivalent to $F_{1/250}$ with certainty. Considering that most of the work here is finalised on the comparison of the measured force with methods and formulas proposed in the literature and based on the $F_{1/250}$ [95, 7, 207], all results discussed in the following sections refer to this average value to maintain consistency with existing formulas. This choice is also made to reduce dependence on highly variable extreme loads.

4.3.2.1 Influence of the ramp shape

The first goal of the present physical model test carried out on the OBREC device is to analyse the influence of the ramp shape on the resultant force acting on the different parts of the OBREC.

The resultant forces $F_{1/250}$ measured on the curved and flat ramp are compared in Fig. 4.11. The values of $F_{1/250}$ measured on the flat ramp are larger than those on the curved ramp for all the tests here analysed, with a mean value of the ratio between the $F_{1/250}$ on the flat and curved configuration of 1.37. This significant difference is due to the peculiar shape of the curved ramp, which has a milder slope on the upper part compared to one of the flat ramp (34°). Pressures acting on the upper part of the curved plate are lower than those on the flat ramp, leading to a lower resultant normal force. Please note that the normal force acting on the curved ramp is calculated assuming the curvilinear distance between the pressure transducers installed on it (Fig. 4.8).

Considering that the base widths of the two configurations have a slight different dimensions, the non-dimensionless uplift force on the OBREC base ($F_{1/250}/\rho g H_{m0} B_{base}$) is used for the comparison (Fig. 4.12). Despite the high scatter due to the complex interaction of the waves with porous media having different layers, the results demonstrate that dimensionless uplift forces exerting on the curved configuration are slightly larger than those on the flat

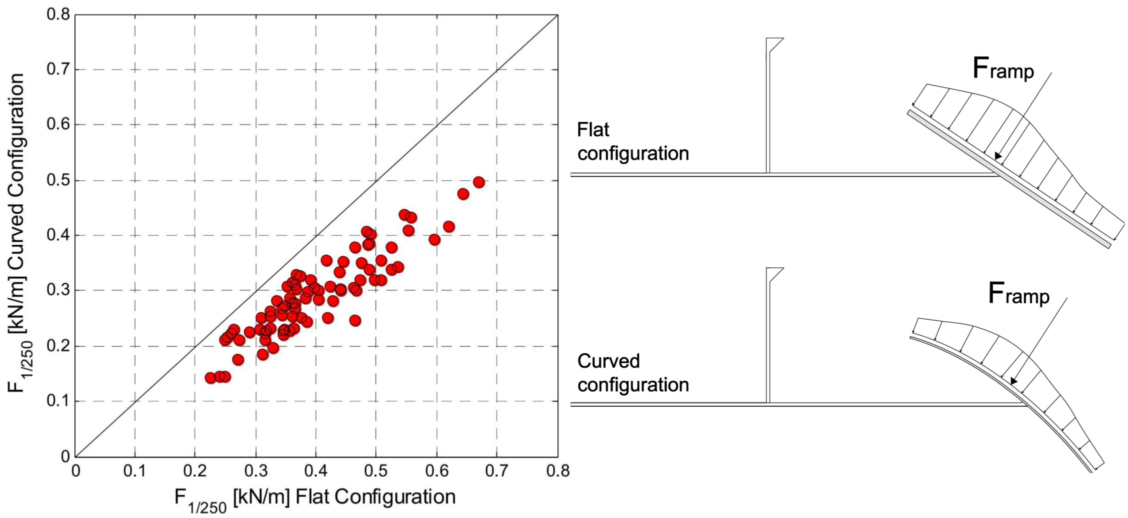

Fig. 4.11 Normal forces measured on the frontal ramps: flat versus curved configuration (left panel); sketch of the pressure distribution and force (right panel).

configuration. The reason could be addressed considering that the lower part of the curved ramp has a slope larger than those in the flat one as shown in Fig. 4.4. Indeed, experiments on trapezoidal caissons conducted by [249] demonstrated that uplift wave pressures on the caisson bottom are reduced due to the upward water particle velocity enhanced by the slope. Therefore, a more inclined lower part of the ramp implies the greatest uplift loading under the base of the device.

Concerning the loading acting on the vertical crown-wall (see Fig. 4.13), the forces measured for the two analysed configurations are comparable, with the mean ratio of the $F_{1/250}$ on the wall between the flat and curved configuration of 1.05. Results suggest that the shape of the frontal ramp has not a relevant influence on the total horizontal force on the crown-wall. As expected, the forces on the vertical crown-wall increase with decreasing of the ramp crest freeboard, R_r, for both flat and curved configurations. Fig. 4.14 shows how the dimensionless valued of the peak forces $F_{1/250}/\rho g H_{m0}^2$ varies function of the relative ramp crest freeboard, R_r/H_{m0}. In detail, for small values of R_r/H_{m0}, the highest waves exceed the top of the ramps, hitting directly on the crown-wall. Conversely, loads on the wall for higher R_r/H_{m0} are mainly reduced due to the wave energy attenuation along the frontal sloping ramps and in the reservoirs.

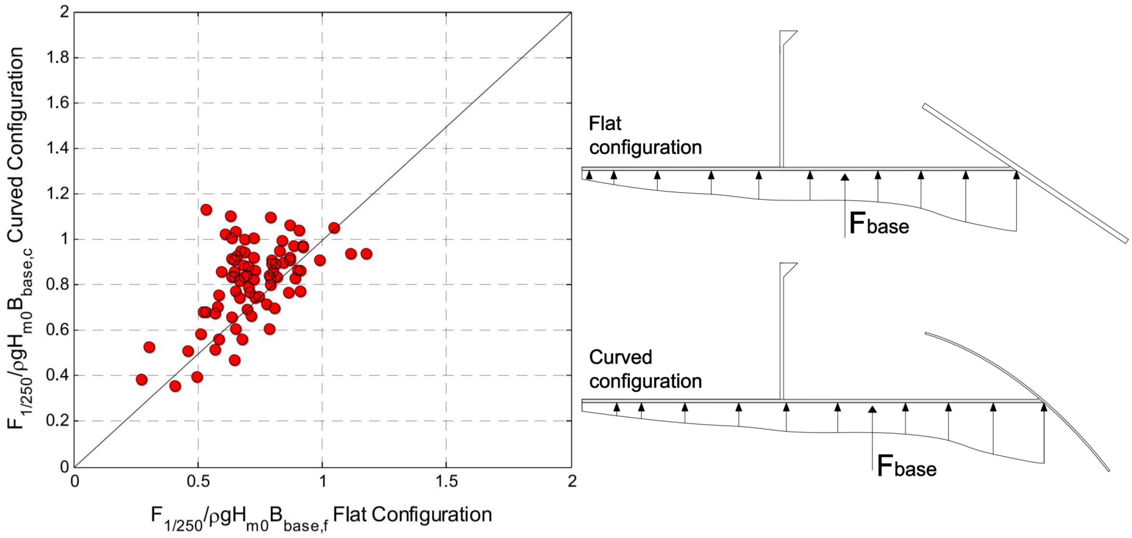

Fig. 4.12 Dimensionless uplift forces $F_{1/250}/\rho g H_{m0} B_{base}$ on the horizontal base: flat versus curved configuration (left panel); sketch of the pressure distribution and force (right panel).

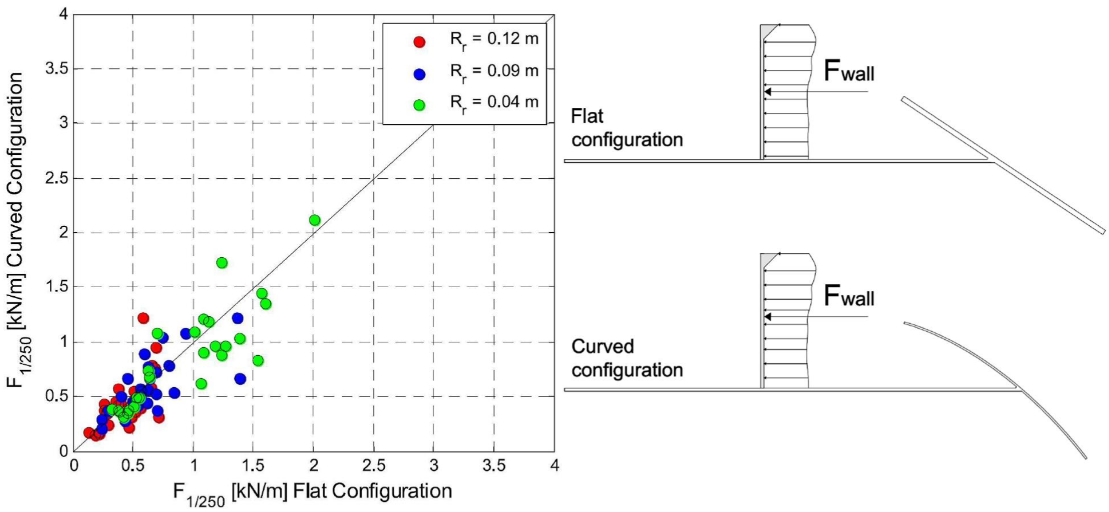

Fig. 4.13 Measured forces $F_{1/250}$ on the vertical wall: flat versus curved configuration (left panel); sketch of the pressure distribution and force (right panel).

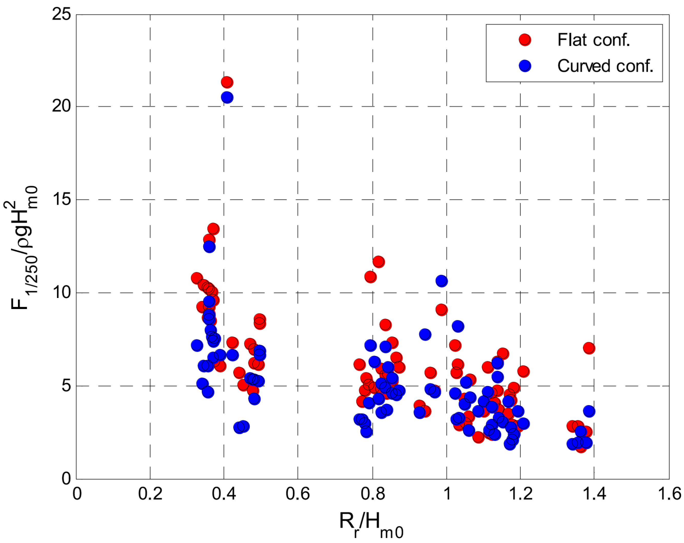

Fig. 4.14 Influence of the dimensionless crest ramp (R_r/H_{m0}) on the dimensionless loading acting on the vertical wall ($F_{1/250}/\rho g H_{m0}^2$) for flat and curved configuration.

Fig. 4.15 shows a comparison of the time history forces on the ramp F_{ramp}, base F_{base} and vertical wall F_{wall} for flat and curved configuration for a test characterized by a significant wave heigh $H_{m0} = 0.112$ m, a peak period $T_p = 2.096$ s and a wave depth $h = 0.35$ m. The three figures represent the typical behaviour of the time series signals of the forces exerting on the different parts of the two OBREC models, with a typical signals of pulsating loads on the frontal ramp and horizontal base, and a slight impulsive loading on the vertical crown-wall, characterized by one or two peaks for both curved and flat configuration. Such wave structure interaction is similar to the one described by Vicinanza et al. [276] after the first test campaign on the OBREC model and it will further analysed in the next section.

As mentioned before, the interaction of the waves with the OBREC vertical wall under extreme conditions can be analysis dividing the structure into two sections: the lower part, which is submerged when the reservoir is saturated, and the upper part. The latter is the most important part for the wave loading analysis because it is highly exposed to the impact of the incoming overtopped waves which might break directly in front of this section.

An insight on the force on the upper part of the crown-wall is then provided, analysing the values of b_H, i.e. the distance from the bottom reservoir of the resultant horizontal forces $F_{1/250}$ acting on the upper wall. Fig. 4.16 compares the values of b_H for each test between the curved and flat configuration. It is worth mentioning that the position of the resultant horizontal force, F_{upper}, on the flat configuration is generally higher compared with those on curved configuration, due to the different shape of the frontal ramps. The phenomenon

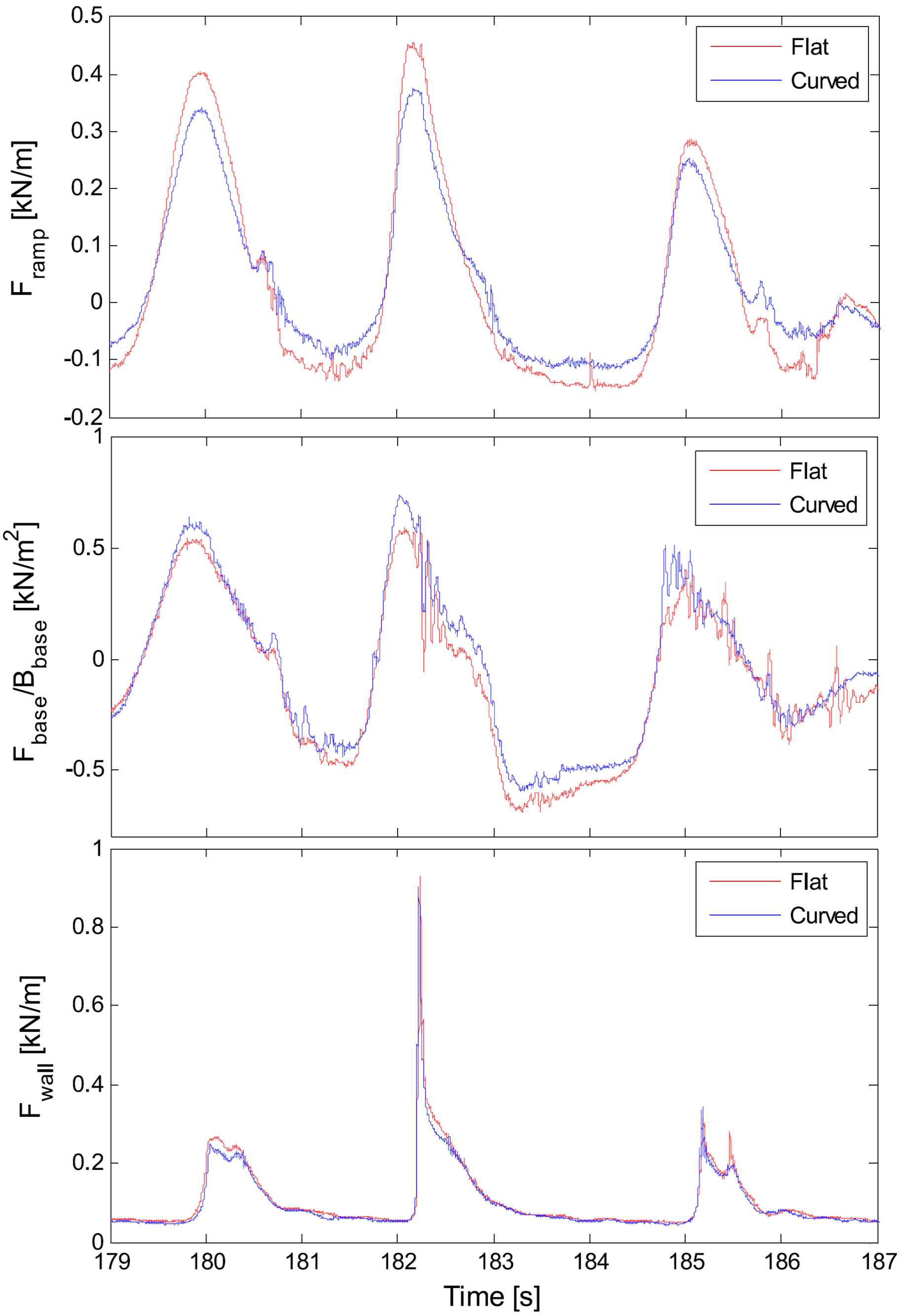

Fig. 4.15 Time history between flat and curved configuration for an extreme wave test ($H_{m0} = 0.112m$; $T_p = 2.096s$; $h = 0.35m$) of the normal force on the ramp (F_{ramp} (a), mean uplift pressure at the base (F_{base}/B_{base}) (b) and force on the vertical wall (F_{wall}) (c).

is clarified taking into account the path of the up-rushing water. Assuming that the water jets follow the tangent of the ramp crest, which works as a deflector, the greater the slope of the ramp (i.e. the upper part of the ramp), the greater the value of b_H. Hence, water jets are driven directly on the upper part of the crown-wall for flat configuration, resulting in larger values of b_H.

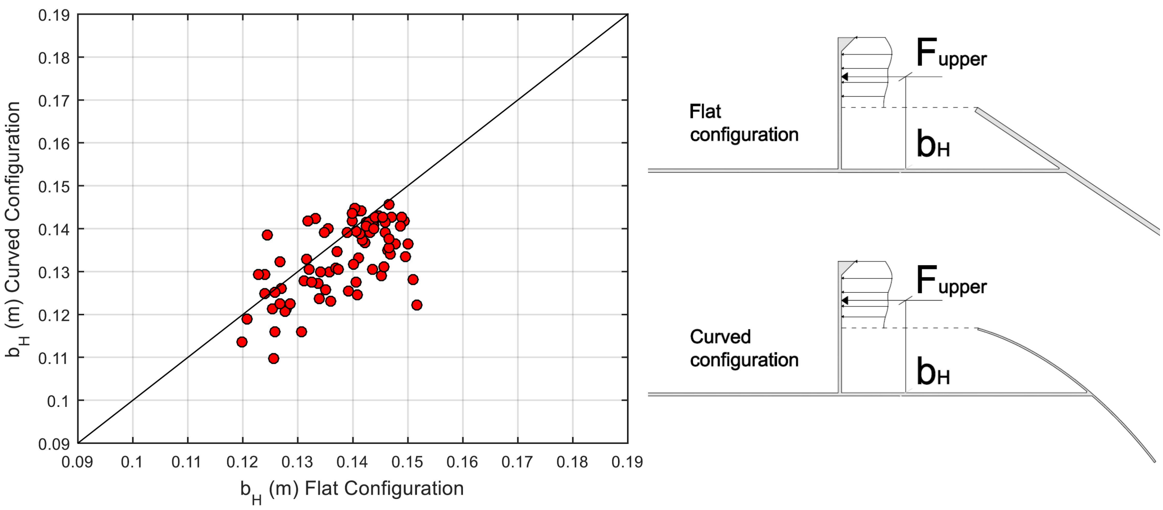

Fig. 4.16 Distance b_H (m) from the bottom reservoir of the resultant force acting on the upper crown-wall: flat versus curved configuration; sketch of the pressure distribution and force (right panel).

The position of the resultant force on the exposed upper wall of the OBREC is correlated with the momentum at the base of the wall, relevant for local stability analysis of the wall. Fig. 4.17 presents the measured overturning moments, $M_{1/250}$, around the base of the vertical wall due to the loading on the upper crown-wall. Considerations made above for the position of the resultant forces, b_H, can be mutually repeated: $M_{1/250}$ measured on the flat configuration are generally higher than those on the curved ramp, mainly for $R_r = 0.04$ m, with a mean ratio between the flat and curved configuration of 1.13.

As mentioned previously, loading measurements on the triangular parapet on the top of the crown-wall are carried out by measuring the pressure in the middle of the inclined side of the parapet for both configurations (see Fig. 4.18). Fig. 4.18 shows clearly that $F_{1/250}$ on the nose for flat configuration are larger than those on the curved one for almost all the extreme wave condition tests, with a mean ratio of the force between the flat and curved configuration of 1.42, confirming the same behaviour explained for the loading acting on the upper crown-wall.

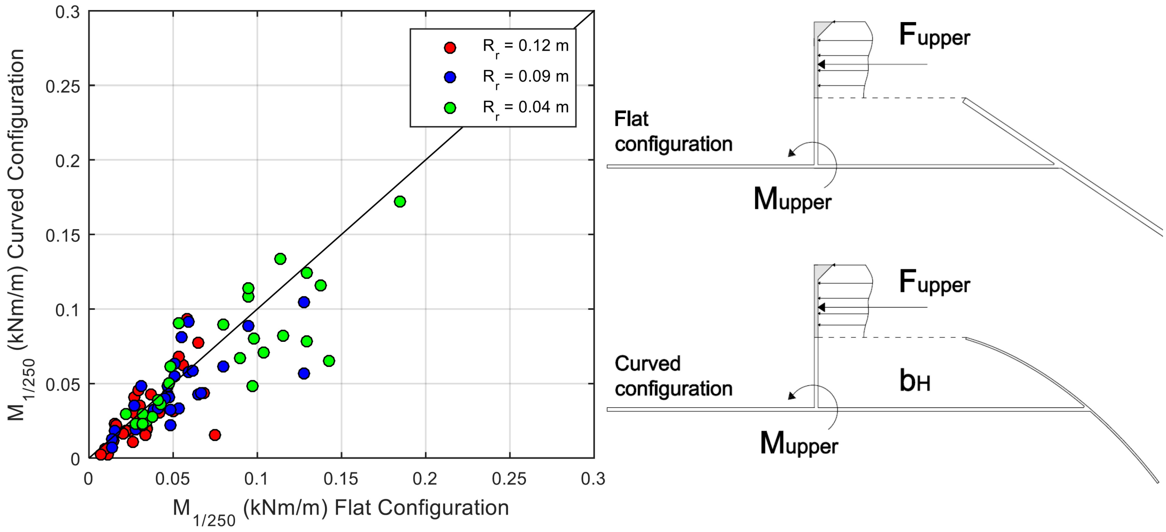

Fig. 4.17 Measured overturning moments around the base of the vertical wall due to the pressure on the upper crown-wall: flat versus curved configuration; sketch of the pressure distribution, force and moment (right panel).

Fig. 4.19 shows the influence of the reservoir width, B_b, on the pressure on the nose, p_{nose}, for test with $H_{m0} = 0.11$ m and $T_p = 2.0$ s. The figure shows that maximum pressure peaks occur for lower values B_b, i.e. Small and Large reservoir. For the Extra-Large reservoir, waves do not impinge directly on the nose, resulting in lower pressure impulses. Furthermore, maximum pressures on the nose occur for lower values of R_r, because the water jet impacts directly on the triangular parapet with an extreme impulsive load while, for higher values of R_r, a large amount of wave energy is attenuated due to the dissipation along the frontal ramp. Fig. 4.20 shows a heuristic interpretation of these physics previously explained, with the water jet profile due to the different shape of the frontal ramp.

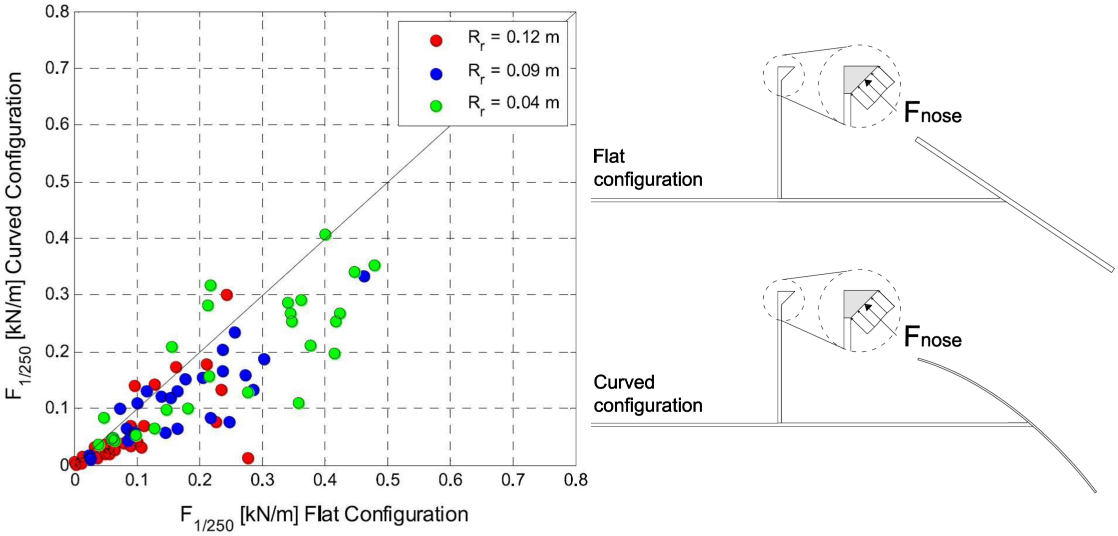

Fig. 4.18 Measured forces $F_{1/250}$ on the nose: flat versus curved configuration; sketch of the pressure distribution and force (right panel).

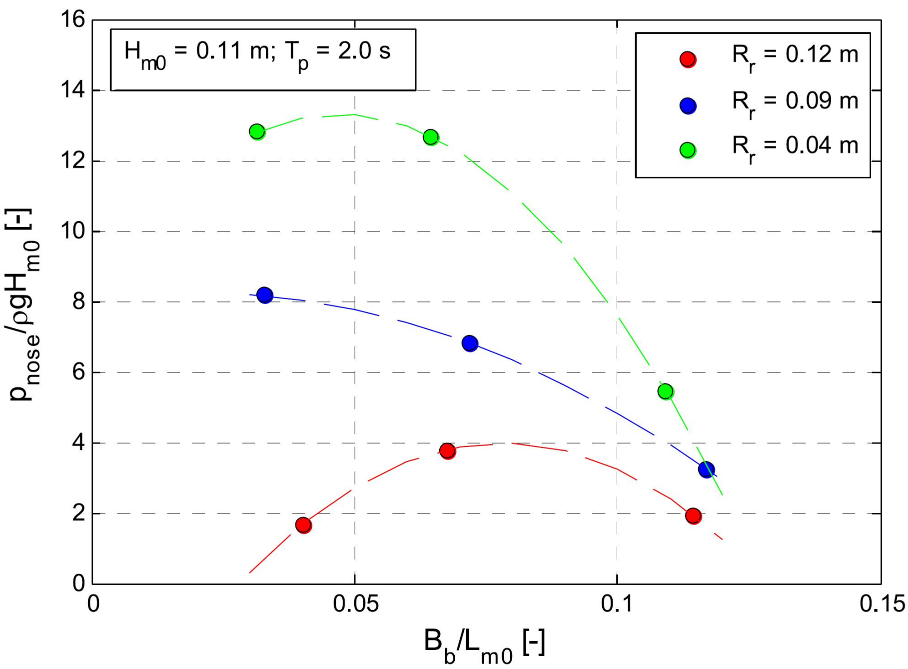

Fig. 4.19 Dimensionless pressure on the triangular parapet for different dimensionless reservoir widths and crest freeboard R_r (flat configuration) [$H_{m0} = 0.11m$ and $T_p = 2.0s$].

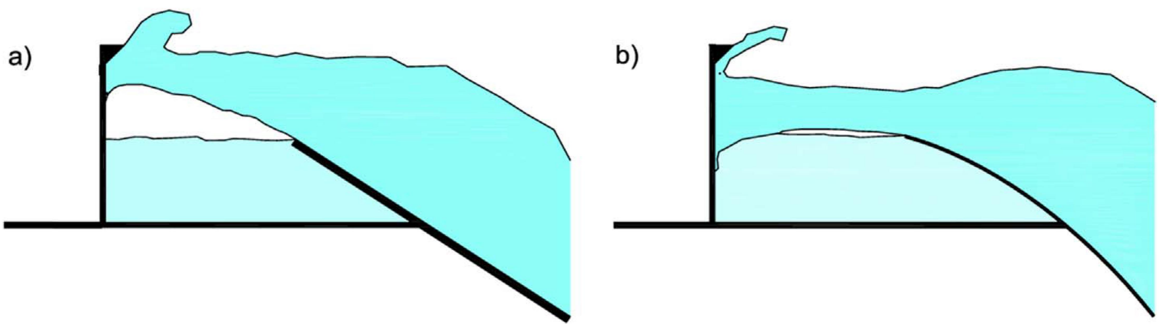

Fig. 4.20 Schematic representation of the water jet profile due to the shape of the front ramp: a) flat configuration; b) curved configuration.

4.3.3 Load time history on the flat configuration

Load time history and spatial pressure distribution are reported in this section to identify the wave loading regime on the different structural parts of the OBREC device. The following analysis refers only to the flat configuration, which is chosen based on the hydraulic performance analysed and reported in Iuppa et al. [126].

Fig. 4.21, 4.22 and 4.23 show the pressure time histories recorded by pressure transducers located on the Extra-Large configuration under extreme wave condition. The three figures show the load time history for an extreme wave test ($H_{m0} = 0.112$ m; $T_p = 2.096$ s; $h = 0.35$ m) and the spatial pressure distribution at the time of the maximum normal force on the ramp (Fig. 4.21), the maximum vertical force on the base (Fig. 4.22), and the maximum horizontal force on the wall (Fig. 4.23). To better visualize pressure time histories, only the horizontal component of the loading on the nose is graphically represented. Over the ramp, the wave loading slowly varies in time with a relatively mild gradient. Thus, a quasi-static loading time history is recognizable, and the pulsating pressure is almost hydrostatic ($p \approx \rho g H_{m0}$). Under the base, the uplift hydrodynamic force time history is, in general, characterized by three different phases. At the instant of the contact between the wave and the base, the wave slam may be considerable in magnitude but short in duration. Those impulsive forces can reach for some extreme tests almost 1.5 times the value of corresponding quasi-static loads. In this wave slam phase, it is possible to note the importance of entrained air, involving several rebound peaks in the time history, of which the first is often simultaneous to the horizontal force peak. These peaks are followed by a pulsating phase, with slowly-varying positive forces of less magnitude but considerable duration. During the backwash, a negative force has been recorded. For both positive and negative quasi-static components, the air pocket oscillations are noticeable. Fig. 4.24 visually describes the three phases of typical uplift forces on the reservoir.

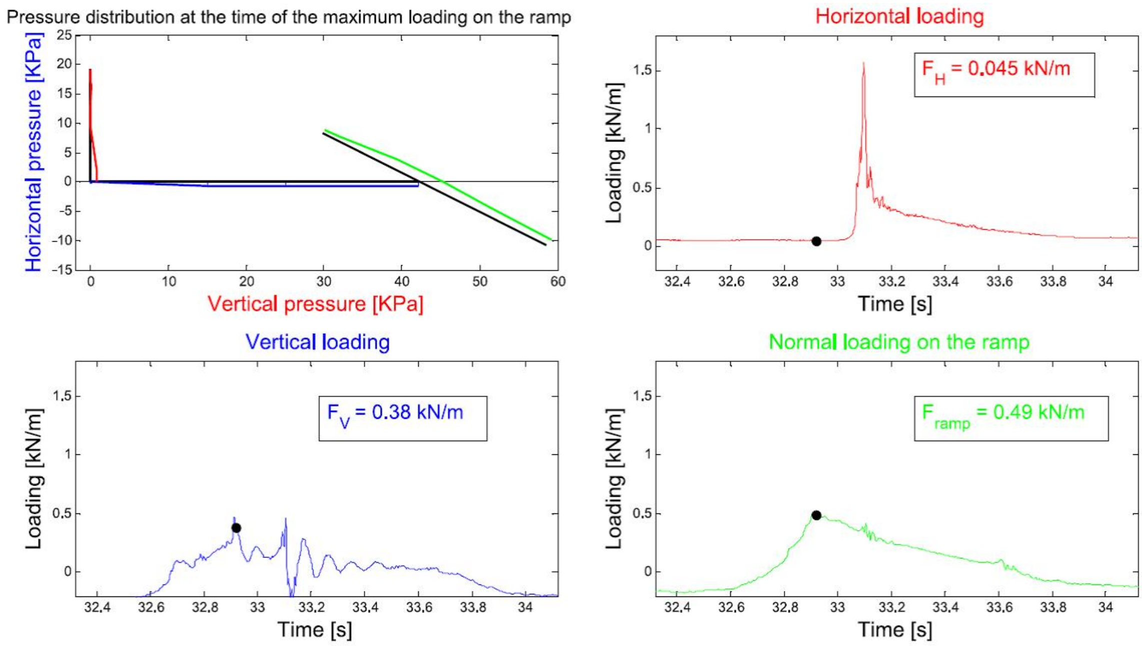

Fig. 4.21 Load time history for an extreme wave test ($H_{m0} = 0.112$ m; $T_p = 2.096$ s; $h = 0.35$ m) and the spatial pressure distribution at the time of the maximum force on the ramp.

A different behaviour is recognized from the time history analysis of vertical wall loadings. The signal shows evident rapid variations in time, with high force peaks typically described as impact wave loads. It is worth mentioning that the impact pressure signals on the upper crown-wall and on the nose have relatively small peak pressure ($p \approx 10\rho g H_{m0}$) if compared to the general pressure peaks for violent impact loading on vertical walls, which can be up to $50\rho g H_{m0}$ as shown by many authors [228, 106, 8, 207, 48]. The energy dissipation of the wave run-up over the ramp and on the reservoir evidently attenuate the pressure peaks, as Vicinanza et al. [276] already recognized in the previous test campaign conducted in 2012.

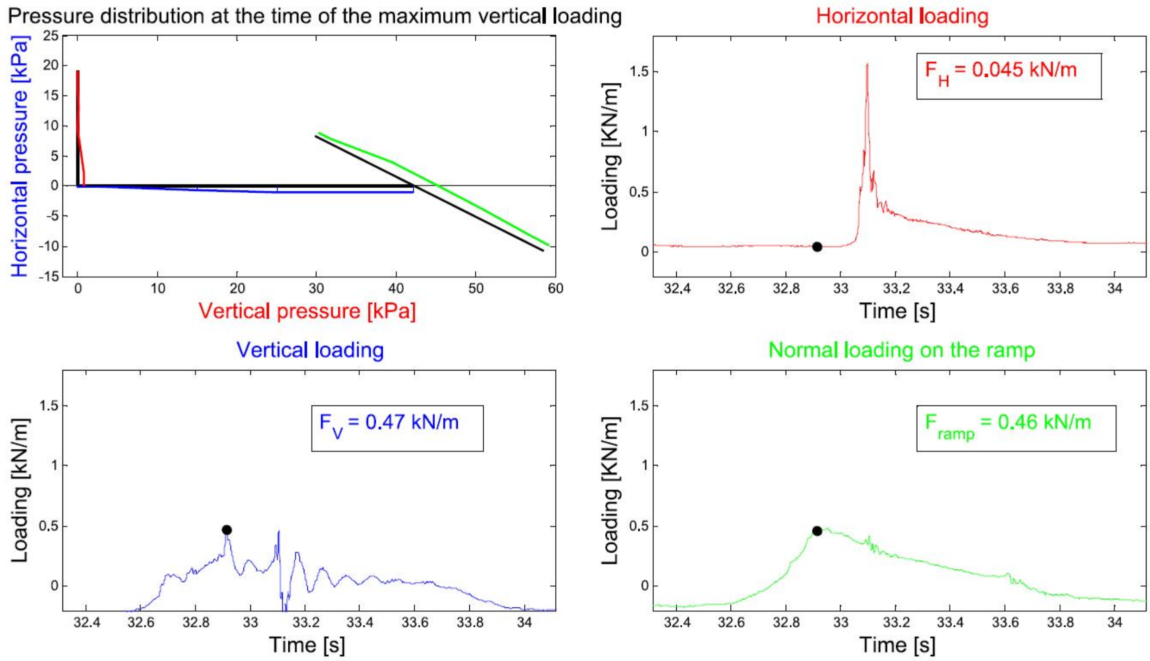

Fig. 4.22 Load time history for an extreme wave ($H_{m0} = 0.112$ m; $T_p = 2.096$ s; $h = 0.35$ m) and the spatial pressure distribution at the time of the maximum vertical force on the base.

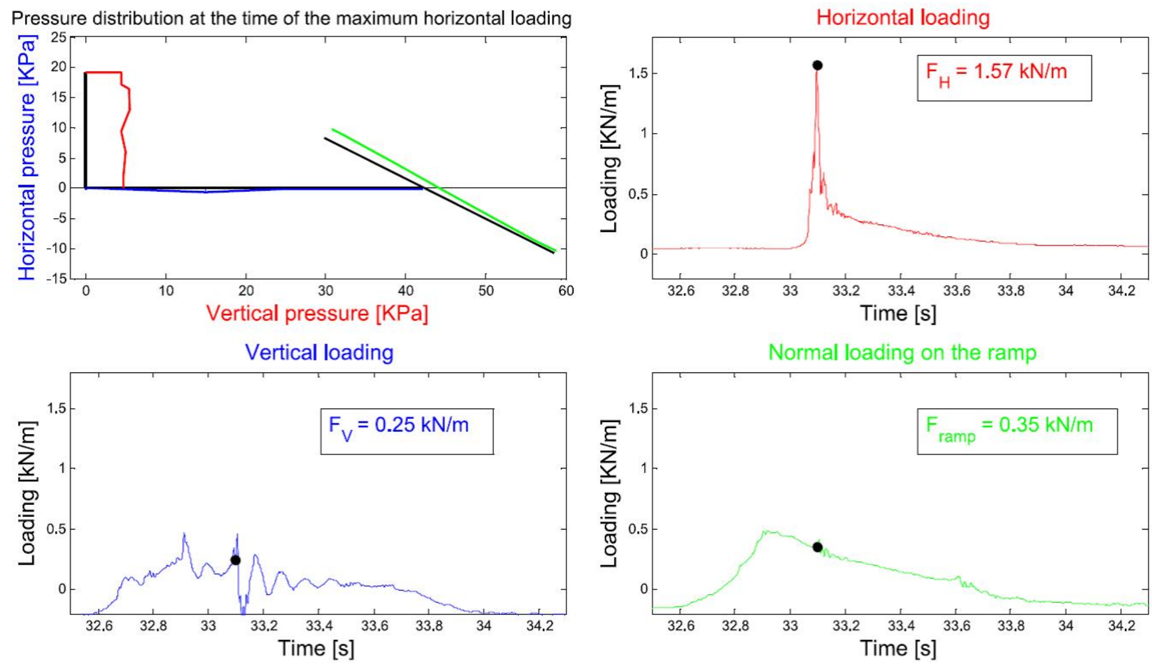

Fig. 4.23 Load time history for an extreme wave ($H_{m0} = 0.112$ m; $T_p = 2.096$ s; $h = 0.35$ m) and the spatial pressure distribution at the time of the maximum horizontal force on the wall.

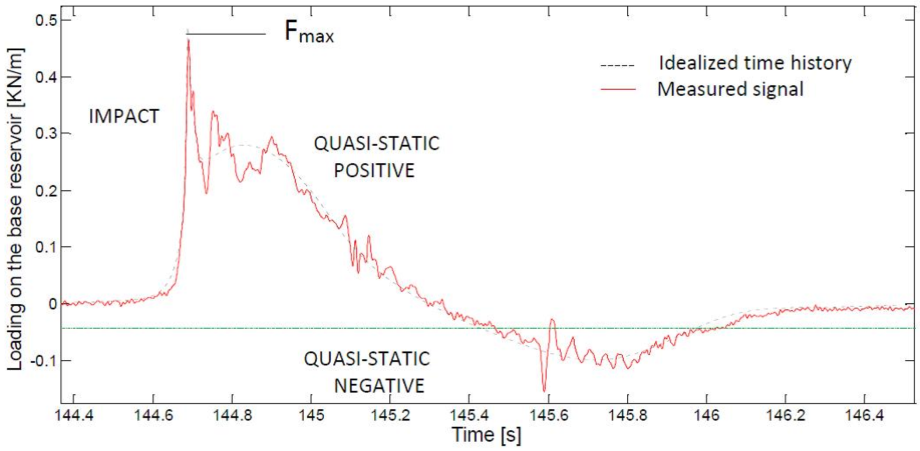

Fig. 4.24 Idealized force time history and typical force signal recorded on the base.

4.3.4 New methods for wave loading prediction

In order to provide useful tools to engineers for designing future prototypes of this innovative breakwater, prediction methods to evaluate the wave loadings on the ramp, base, and crown-wall are here proposed.

4.3.4.1 Loading on the ramp

A possible point of strength of the OBREC may be its similitude with structures usually employed in the field of maritime engineering. Regarding the loading acting on the flat ramp, the reference is the monolithic sloping top caissons, already described in Section 2.1.4.4.

The first design method for the sloping top caisson was initially proposed by Morihira and Kunita [183] who modified Goda's formulas [93] for vertical breakwaters. The authors followed the traditional Japanese approach to estimate the pressure on the caisson conducted at the beginning of the last century by Hiroi [110], measuring in situ the wave pressure by using a spring-type instrument. Defining M_f as the moment flux of the incoming jet, Morihira and Kunita [183] calculated it as the integral of the pressure (p_{Goda}) from the well-known Goda [94] formulas along the vertical (F_1) from the lower tip of the sloping part (d_c) to the crest of it (h_c), as indicated in Fig. 4.25:

$$M_f = F_1 = \int_{d_c}^{h_c} p_{Goda} dz \tag{4.19}$$

Takahashi et al. [240] modified the Morihira and Kunita [183] formula (Eq. 4.19) to take into account the influence of the wave height on the force distribution at the inclined wall. Indeed, the author found out that the Morihira and Kunita [183] formula underestimates the forces for small waves and overpredicts them for high waves. For this reason, Takahashi et al. [240] proposed to calculate the moment flux introducing a modification factor λ_{SL} to be applied at the Goda [94] model for the sloping part of the caisson:

$$M_f = \lambda_{SL} \cdot F_1 \tag{4.20}$$

Based on the dependence of λ_{SL} on H_D/L_D and the slope angle α, the formulation for the modification factor from Takahashi et al. [240] is expressed as:

$$\lambda_{SL} = \min\left[\max\left(1.0; -23\frac{H_D}{L_D \tan\alpha^2} + 0.46\frac{1}{\tan\alpha^2} + \frac{1}{\sin\alpha^2}\right); \frac{1}{\sin\alpha^2}\right] \tag{4.21}$$

Please note that H_D and L_D are the wave height and wavelength used to calculate the design wave force. Following the method used by Goda [94], Takahashi et al. [240] adopted the wavelength L_D calculated by linear wave theory at the water depth at distance $5 \cdot Hs$ seaward of the structure, using the significant wave period $T_{1/3}$. Regarding the design wave heigh H_D, Goda [95] defined it as the highest wave in the design sea state at the location just in front of the breakwater. If seaward of surf zone, for practical design Goda [95] recommends to use a value of $H_D = 1.8 \cdot H_{m0}$, that correspond to the 0.15% exceeedance value for Rayleigh distributed wave heights, which corresponds to $H_{1/250}$ (mean of the highest 1/250 of the waves hight). If within the surf zone, the design wave height is taken as the highest of the random breaking waves at the distance $5 \cdot Hs$ seaward of the structure [260, 95].

Under the hypothesis that after the collision with the slope, the velocity of the fluid is tangential to the sloped wall, the normal load F_p (Fig. 4.25) on the wall is calculated as:

$$F_p = M_f \cdot \sin(\alpha) = F_1 \cdot \lambda_{SL} \cdot \sin(\alpha) \tag{4.22}$$

where α is the slope angle of the front face to the horizontal.

Buccino et al. [43] analysing the SSG-device, considered that the effect of the wave steepness on λ_{SL} is best represented by the significant wave steepness H_{m0}/L_D rather than

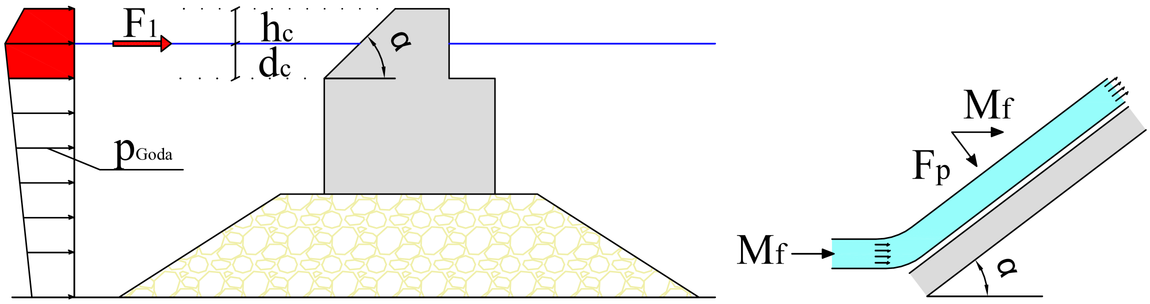

Fig. 4.25 Pressure distribution on sloping top caisson after Morihira and Kunita [183] (left panel); a fluid jet hitting an inclined wall (right panel)

$H_{1/250}/L_D$ computed by Takahashi et al. [240]. This assumption is then adopted in the present study for the calculation of λ_{SL}.

The force acting on the OBREC ramp computed from the measured pressure data are compared to those calculated with the method proposed by Morihira and Kunita [183], modified by Takahashi et al. [240] and Buccino et al. [43] for the sloping top caisson. The comparison is reported at prototype scale in Fig. 4.26. In order to compare the data, the mean relative error, μ_{error}, and the standard deviation, σ_{error}, of the relative error between measured and calculated values are computed. Please note that the relative error, expressed in percentage, is here calculated as the difference between the measured and calculated values, divided by the measured values. Negative values of the error represent an overestimation of the method and vice versa. The method gives very good agreement with the measured data forces with a mean of relative error $\mu_{error} = -2.1\%$ and the standard deviation of relative error $\sigma_{error} = \pm 22.4\%$.

4.3.4.2 Loading on the base

Aiming at estimating the uplift force exerted on the horizontal OBREC base, a linear pressure distribution between the pressure transducers and a linear extrapolation of the neighbouring measured pressures is assumed to define the pressure on the base wedges where no measures were available. Please, note that pressure acting underneath the ramp are not considered in this analysis and the linear interpolation is carried out only the horizontal base.

This methodology is adopted considering that in the design of coastal structures such as crown-wall or vertical caisson, it is a common practice to assume that the uplift pressure linearly varies towards the leeward edge of the structure ([131, 36, 212, 173, 182]. The distribution law is triangular or trapezoidal depending upon the porosity of the layers immedi-

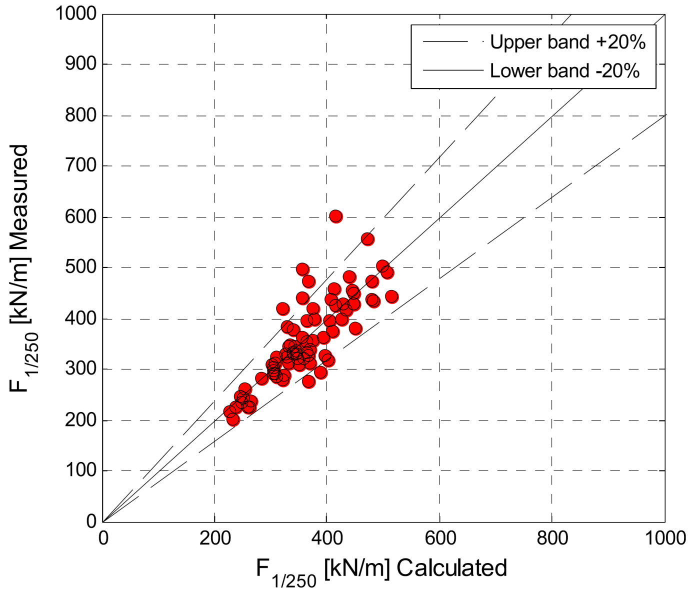

Fig. 4.26 Measured $F_{1/250}$ on the front ramp versus calculated forces using Morihira and Kunita [183] (Prototype scale)

ately beneath the superstructure. However, many authors, based on numerical models [161], physical models [144, 176, 11] and field investigation [81] pointed out that the assumption of the linear distribution under the caisson or crown-wall could be not entirely correct.

The problem of the wave uplift pressure on coastal structures is still under debate and there is a heavy dispersion of the results between the different adopted formulations, as indicated in Braña and Guillén [37] and recently pointed out in Negro Valdecantos et al. [193]. Moreover, the semi-empirical relations for uplift pressure distribution included in USACE [260] and the Rock Manual [220] do not take into account the influence of the nominal diameter of the material, neither the presence of multiple different layers in which the superstructure is founded, which is the case of the OBREC device tested in laboratory.

The closest design formula, found by Vicinanza et al. [276] to predict the uplift forces under the OBREC base, is the one proposed by Goda [93] and corrected by Tanimoto and Kimura [249] for trapezoidal caissons. Tanimoto and Kimura [249] conducted a series of model experiments to investigate the wave forces exerted on this peculiar typology of vertical caisson. The experiments conducted by the authors demonstrated that the uplift pressure on the base plate is reduced compared to the vertical face case due to the upward water particle velocity enhanced by the inclined wall. The modification factor λ_3 for the uplift pressure in Goda [94] formula is expressed as:

$$\lambda_3 = \exp\left[\left(-2.26(7.2l_d/L_D)^3\right)\right] \tag{4.23}$$

where $l_d = h' \cdot \cot\alpha$. Considering the original Goda's annotation, h' is the distance from the design water level to the bottom of the upright section. In the present analysis h' is calculated as follows:

$$h' = h_{res} - h \tag{4.24}$$

where h_{res} is the vertical distance between the bottom and the base reservoir while h is the water depth in front of the model. It is important to note that in some tests conducted on the OBREC, the base reservoir is located above the still water level leading to negative values of h' in Eq. 4.24. It is important to underline that slope of the OBREC flat ramp ($\alpha = 34$) is out of the validity ranges of the Eq. 4.24, which is applicable only to a trapezoidal caisson with an inclination α grater than 70°.

Fig. 4.27 shows the comparison between measured forces $F_{1/250}$ under the OBREC base with those calculated using the formula provided by Tanimoto and Kimura [249]. When the base reservoir is below still water level (i.e. $h_{res}/h \leq 1$), the uplift forces on the base are correctly predicted with the formula. Conversely, the application of the formula leads to an overestimation of the uplift forces when the OBREC base is above still water level (i.e. $h_{res}/h > 1$). Hence, in order to predict the uplift forces on the OBREC, it is necessary to distinguish the case in which the base is located above the sea water level and when it is located below. In the latter case, the pressure impulse is directly transmitted under the base of the structure and the filtering capacity of the armour and filter layers are considerably reduced.

The extensive literature on tests conducted on horizontal platform decks [231, 256], horizontal slabs [233], and exposed jetties [66] close to the sea water level (SWL) showed that pressure peaks of the uplifts increase with the decreasing values of the vertical distance between the horizontal element and the SWL. The same behaviour was recognized for the OBREC, as shown in Fig. 4.28.

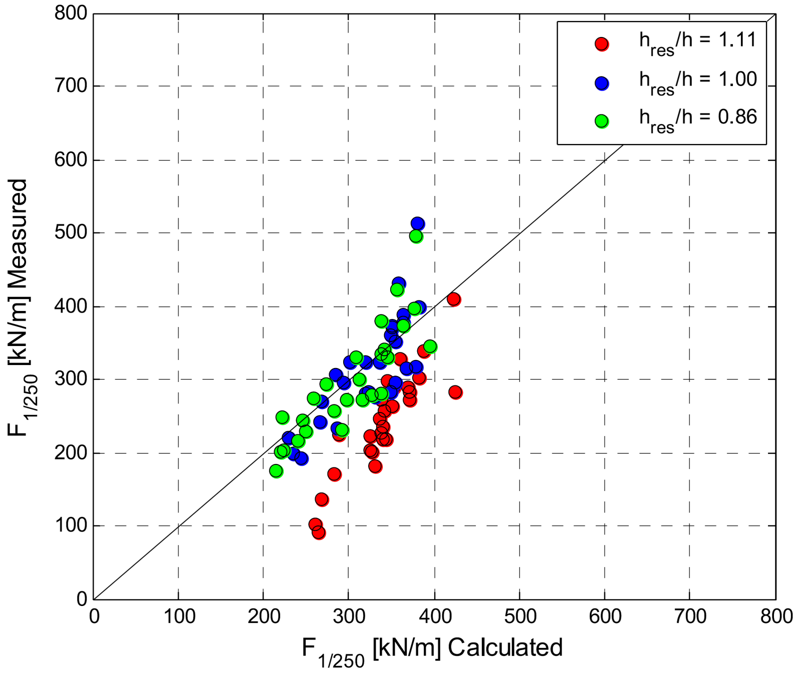

Fig. 4.27 Measured $F_{1/250}$ under the OBREC base versus calculated forces using the formula provided by Tanimoto and Kimura [249] (Prototype scale)

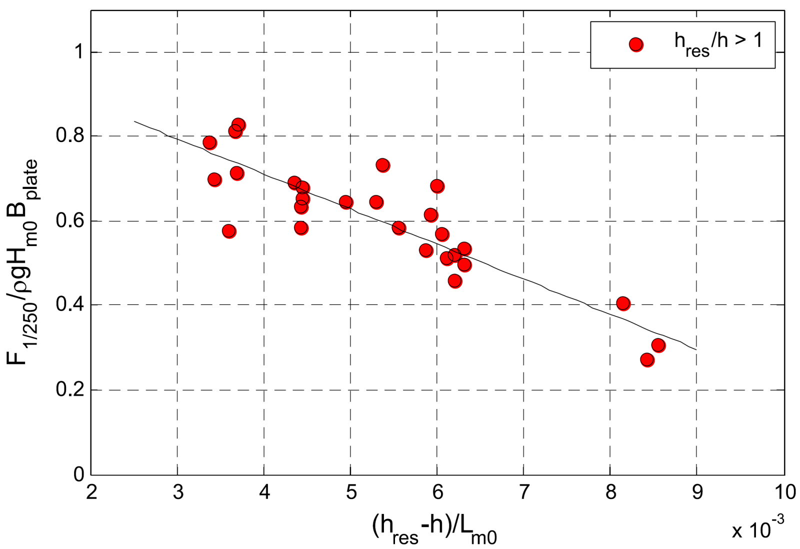

Fig. 4.28 Influence of the dimensionless distance between the base reservoir and the sea water level on the dimensionless uplift loading acting on the OBREC base

In order to give a more reliable prediction of the forces $F_{1/250}$ under the base, a new relation is derived from a linear regression analysis, when the base reservoir is located above sea water level (i.e. $h_{res} > h$).

$$F_{base} = \rho g H_{m0} B_{base} \left[a_{base} \frac{h_{res} - h}{L_{m0}} + b_{base} \right] \tag{4.25}$$

where L_{m0} is the deep water wavelength referenced to the energy period $T_{m-1,0}$, $a_{base} = -83$ and $b_{base} = 1.04$. It is recommended to apply the Eq. 4.25 only under the following validity range: $0.0034 < \frac{h_{res}-h}{L_{m0}} < 0.0085$.

The uplift resultant forces $F_{1/250}$ measure on the base versus the force calculated with Tanimoto and Kimura [249] when $h_{res}/h \leq 1$ and with Eq. 4.25 when $h_{res}/h > 1$, are shown in prototype scale in Fig. 4.29, reaching satisfactory agreement, with a mean relative error $\mu_{error} = -4.6\%$ and the standard deviation of relative error $\sigma_{error} = \pm 19.2\%$.

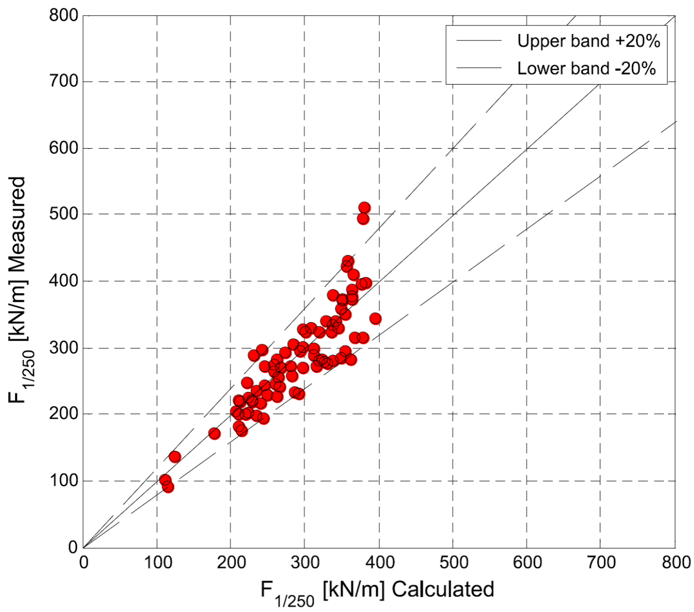

Fig. 4.29 Measured $F_{1/250}$ versus calculated uplift forces at the OBREC base (Prototype scale)

4.3.4.3 Loading on the upper wall

The analysis of the loading at the vertical wall is divided into upper and lower crown-wall, as schematized in Fig. 4.10. The hydrodynamic behaviour recognized for the upper OBREC wall can be considered similar to the classical configuration of a crown-wall on a rubble-mound breakwater.

Jensen [131], Bradbury et al. [36], Pedersen and Burcharth [213] and Pedersen [212] provided formulation to estimate the maximum horizontal force and overturning moment at the wave wall. Conversely, methods proposed by Iribarren and Nogales [124], Günbak and Gökce [102], and Martin et al. [173] define the force considering the pressure diagram along the wall. There is no well-established method to estimate the wave loads on crown-wall for all the configurations. Moreover, there is a very wide divergence between the different data set available and the calculation methods that have been used. Studies carried out by Braña and Guillén [37] and Negro Valdecantos et al. [193] indicated a heavy dispersion of the results between the different methods, suggesting to use more than one method to determine results coming closer to the reality. In detail, Braña and Guillén [37] point out that the Pedersen method is the most reliable for the estimation of the maximum horizontal and vertical force on the crown-wall.

One of the governing parameters used by Pedersen [212] for his method is the fictive run-up height exceeded the 0.1% of the incoming waves, $R_{u,0.1\%}$. Pedersen [212] used the run-up formula by Van der Meer and Stam [267] valid for deep water wave condition with head-on wave attack and non-overtopped rough-armoured straight slopes with impermeable core:

$$R_{u,0.1\%} = \begin{cases} 1.12 \cdot H_s \cdot \xi_m & \text{for } \xi_m \leq 1.5 \\ 1.34 \cdot H_s \cdot \xi_m^{0.55} & \text{for } \xi_m > 1.5 \end{cases} \tag{4.26}$$

where H_s is the time domain incident significant wave height at the toe of the structures and ξ_m is the surf similarity parameter based on the mean wave period T_m.

Nørgaard et al. [200] modified the Pedersen [212] formulation to include the effects of shallow water wave conditions on the pressure distribution on the crown-wall ($H_{m0}/h > 0.2$), and to correct the overprediction of impact pressures on the unprotected parts. The authors introduced $H_{0.1\%}$ instead of H_s in the run-up formula by Van der Meer and Stam [267] used by Pedersen [212]. According to the Rayleigh distribution, $H_s/H_{0.1\%} = 0.538$, then the Eq. 4.26 is replaced as follows:

$$R_{u,0.1\%} = \begin{cases} 0.603 \cdot H_{0.1\%} \cdot \xi_m & \text{for } \xi_m \leq 1.5 \\ 0.722 \cdot H_{0.1\%} \cdot \xi_m^{0.55} & \text{for } \xi_m > 1.5 \end{cases} \tag{4.27}$$

Since the statistic of wave height in shallow water significantly differs from the Rayleigh-type distribution function, $H_{0.1\%}$ is calculated following the distribution proposed by Battjes and Groenendijk [25]. Battjes and Groenendijk [25] proposed the use of a combination of two Weibull distribution to describe the cumulative distribution of wave height in shallow water and breaking zone.

Given that the test campaign on the OBREC is carried out in shallow water condition ($H_{m0}/h > 0.2$), the measured data is first compared with the results of the forces evaluated by Nørgaard et al. [200] for the unprotected part of the crown-wall. Results indicate that Pedersen formula [212] corrected by Nørgaard et al. [200] strongly underestimates the forces measured on the upper crown-wall for almost all the tests, which can be up to twice the calculated one.

The first reason of this underestimation is that the upper part of the OBREC consists of a very smooth ramp (steel plate) instead of the armour layer with rock as used for the rubble-mound breakwater model by Nørgaard et al. [200]. It is worth considering that the highest waves directly impinge on the OBREC upper crown-wall, particularly for low crest freeboard R_r, with low energy dissipation when the waves overtop from the ramp and pass over the saturated reservoir. Furthermore, the roughness of the front slope of the rubble-mound breakwater has a high influence on the loading. For instance, tests with different armour layers conducted by Pedersen [212] revealed that cubes placed in a regular pattern forming a smooth surface on the front slope result in wave force 2.5 times greater than the condition with randomly placed Dolos units. Secondly, the parapet on the top of the OBREC wall used to reduce the overtopping rate at the rear side, leads to an inversion of the momentum of the water flows hitting the walls, causing an additional increase of the resultant horizontal forces. Several test campaigns with physical and numerical models conducted on a vertical wall with different parapet configurations [141, 145, 211, 55] showed that the horizontal forces on the wall with inclined parapet can be up to twice higher than an ordinary vertical wall.

It is also important to highlight that the wave characteristics and the structural geometry of the OBREC tested in this test campaign are outside the range of validity of the formulas used by Nørgaard et al. [200]. The authors strictly advice to apply the modified formulas only in the validated ranges. Moreover, Van der Meer and Stam [267] formula for run-up used by Pedersen [212] and modified by Nørgaard et al. [200] is valid only for rock on permeable underlayer. A different formula for run-up should be used taking in account the lower roughness observed for the OBREC, particularly when a submerged ramp is considered. Nørgaard et al. [200] suggested that other run-up formulas may be applied for the estimation of $R_{u,0.1\%}$. However, this might change the empirical scale factors derived by Nørgaard et al. [200] for the total horizontal and vertical wave force, as well as the turning moment around the bottom of the wall.

Considering the extension of the OBREC smooth ramp, Nørgaard et al. [200] method is modified considering the run-up formula for smooth impermeable slopes [5] instead of the Eq. 4.27 proposed by Nørgaard et al. [200] for shallow water conditions. Assuming that the run-up height follows the wave height distribution (hypothesis of equivalence introduced by Saville [225] and Battjes [24]), then $R_{0.1\%}/R_{2\%} = H_{0.1\%}/H_{2\%} = 1.286$. Furthermore, $H_{0.1\%}$ is used in the run-up formula instead of H_s, following the same approach used by Nørgaard et al. [200] for shallow water condition, $H_s/H_{0.1\%} = 0.538$. Formula from Ahrens [5] for large values of the breaker parameter (i.e. $\xi_p > 2.5$) is adjusted as follows:

$$R_{0.1\%} = 0.538 \cdot (1.286\, H_{0.1\%}) \cdot (A\ \xi_p + C) \cdot \gamma_f \tag{4.28}$$

where ξ_p is the breaker parameter evaluated considering the peak period, T_p, $A = 0.2$ and $C = 4.5$ are semi-empirical coefficients adopted according to Ahrens [5]. $H_{0.1\%}$ is estimated from the distribution by Battjes and Groenendijk [25] and the reduction factor γ_f is estimated by Eq. 4.13 as suggest by Iuppa et al. [126]. Furthermore, in order to take into account the presence of the triangular parapet located on the top of the crown-wall, an amplification factor of resultant wave loading is introduced, $K_f = 1.6$. The value assumed by this coefficient and evaluated by a fitting procedure to the measured loading is in accordance with the previous studies on the vertical wall with parapet [141, 145, 211, 55].

Please note that Nørgaard et al. [200] further modified the Pedersen [212] equation to predict more accurately the wave slamming pressure on the unprotected crown-wall with different values of the empirical factor b=1, instead of $b = 1.6$ indicated by Pedersen [212]. This modified factor takes into account the different type of pressure transducers used in the test carried out by Pedersen [212], which was found in further experiences to be influenced by dynamic amplification. Nørgaard et al. [200] in their test campaign used Druck PMP UNIK series pressure transducers, which are unaffected by dynamic amplification. The same pressure transducers series are used also for the present test campaign, thus a coefficient

$b = 1$ in the Nørgaard et al. [200] equation for $F_{0.1\%}$ on the unprotected wall is used in the present study for the calculation of the force on the OBREC upper wall.

Fig. 4.30 shows the measured force $F_{0.1\%}$ on the upper crown-wall of OBREC (in prototype scale) versus the force calculated by the Nørgaard et al. [200] using the run-up formula in Eq. 4.28. The results are good in terms of mean error ($\mu_{error} = 13.2\%$), albeit relatively high scatter on the results are obtained ($\sigma_{error} = \pm 42.7\%$). The large scatter on the results might be due to the higher uncertainties involved in the peak pressure in a time series, due to sporadic violent impact loadings, which occur on the upper crown-wall and on the triangular parapet.

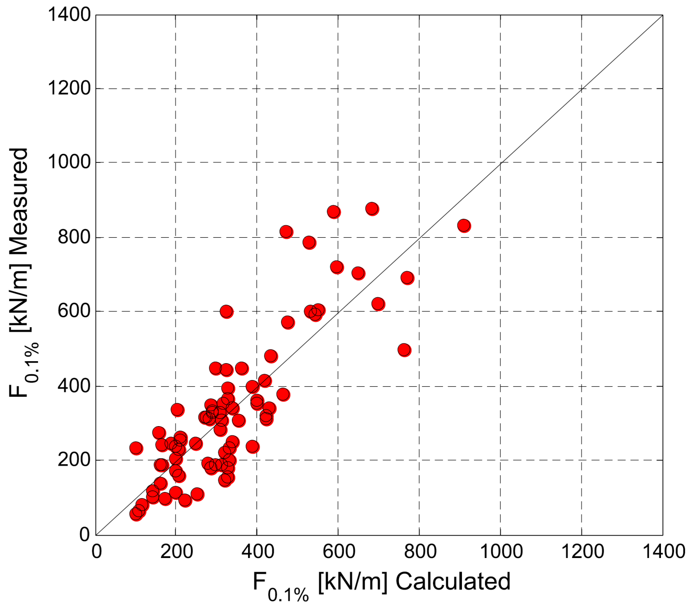

Fig. 4.30 Measured versus calculated forces $F_{0.1\%}$ at the OBREC upper wall using Nørgaard et al. [200] assuming the run-up formula by Eq. 4.28 (Prototype scale)

Accordingly, the method proposed by Nørgaard et al. [200] for the estimation of the overturning moment does not correctly interpret the results for OBREC, showing a strong underestimation of the overturning moment for the same reasons previously explained for the horizontal forces on the upper crown-wall. The empirical factor e_2 proposed by Nørgaard et al. [200] for the overturning moment is here modified as $e_2 = 1.2$, to obtain a more reliable fit between such method and the observed data. This approach appears again satisfying, as can be noted in Fig. 4.31 ($\mu_{error} = 9.4\%$ and $\sigma_{error} = 41.9\%$), albeit high scatter can be noted for the same reasons considered before for the wave forces.

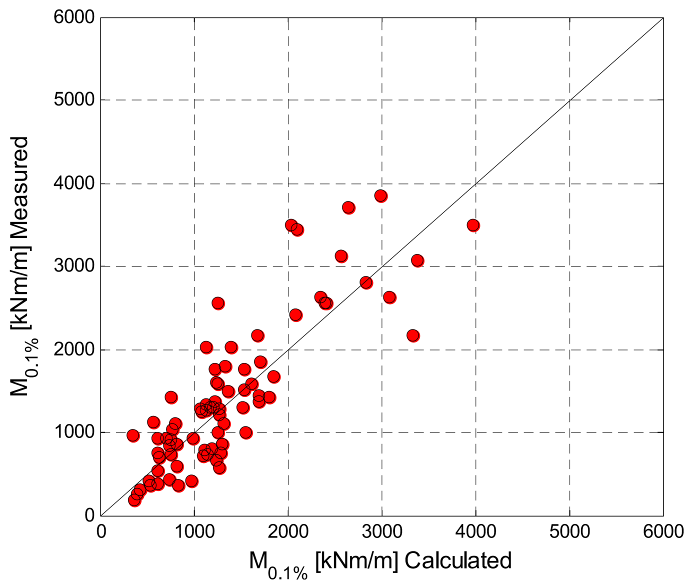

Fig. 4.31 Measured versus calculated overturning moment $M_{0.1\%}$ caused by $F_{0.1\%}$ at the upper wall using Nørgaard et al. [200] assuming the run-up formula by Eq. 4.28 (Prototype scale)

.

4.3.4.4 Loading on the lower wall

A tentative design method is proposed to evaluate the forces on the lower part of the crown-wall. It takes into account a parabolic path of the water jet. Therefore, four parameters are considered as shown in Fig. 4.32: the potential travel distance of the water jet, X_j, the impact point location along the lower crown-wall from the bottom reservoir, Y_j, the flow thickness on the crest ramp exceeded by 2% of the up-rushing waves, $t_{2\%}$, and the ramp freeboard, R_r.

It is assumed that the starting point of the parabolic path starts at still water level at a seaward horizontal distance equal to $t_{2\%}$. The impact point location of the water jet, Y_j, is calculated as the y-coordinate of the parabolic path at the horizontal distance between the crown-wall and the jet starting point. Therefore:

$$Y_j = (B_r + t_{2\%})\tan\alpha - \left[\frac{g(B_r + t_{2\%})^2}{2u_{2\%}^2 \cos^2\alpha}\right] \tag{4.29}$$

where $u_{2\%}$ is the run-up velocity exceeded by 2% of the up-rushing waves. According to the analysis of the overtopping flow [229, 263] and reported in the EurOtop [73], the equations for (maximum) run-up velocity and (maximum) flow thickness on the crest ramp are given respectively in Eq. 4.30 and Eq. 4.31:

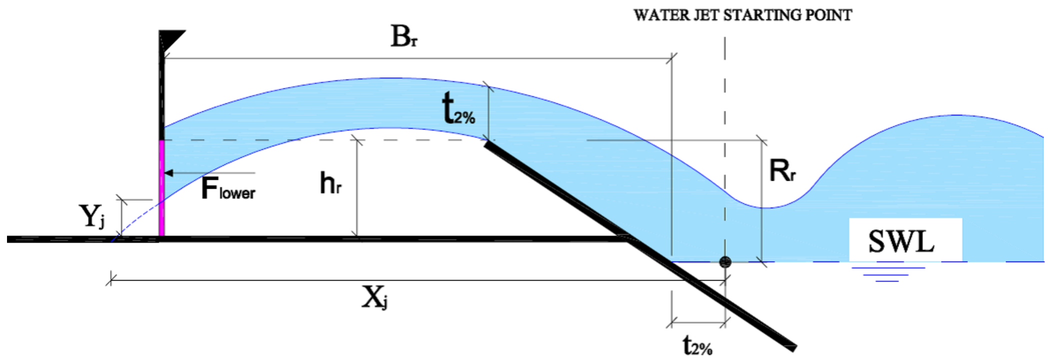

Fig. 4.32 Sketch with the main geometrical parameters for the analysis of the wave forces on lower part of the OBREC wall

.

$$u_{2\%} = c_{u,2\%}[g(R_{u,2\%} - R_r)]^2 \tag{4.30}$$

$$t_{2\%} = c_{t,2\%}(R_{u,2\%} - R_r) \tag{4.31}$$

where $R_{u,2\%}$ is the 2% level of wave run-up related to the still water level. The coefficients $c_{u,2\%} = 0.997$ and $c_{t,2\%} = 0.1507$ are used in the formulas, averaging the values proposed by EurOtop [73] and the recent work carried out by Bosman et al. [35]. In order to take into account the variation of water depth during the tests, an effective height of water jet is introduced as follows:

$$Y_j' = Y_j + (h_{res} - h) \tag{4.32}$$

The expression for the prediction of the force on the lower part of the crown F_{lower} is obtained as follows:

$$F_{lower} = \rho g (R_r - Y_j')^2 \exp\left(220 \frac{(X_j - B_r)t_{2\%}}{h_r^2}\right) \tag{4.33}$$

where h_r is the water depth into reservoir and X_j is estimated as:

$$X_j = \frac{u_{2\%}^2 \sin(2\alpha)}{g} + t_{2\%} \tag{4.34}$$

Measured resultant force on the upper wall versus the ones calculated by Eq. 4.33 are compared in Fig. 4.33, reaching good agreement, with a mean relative error $\mu_{error} = -3.47\%$ and the standard deviation of relative error $\sigma_{error} = \pm 19.9\%$. It is advised to only apply the Eq. 4.33, valid for $Y_j' < R_r$, within the validated ranges reported in Tab. 4.1 and Tab. 4.2.

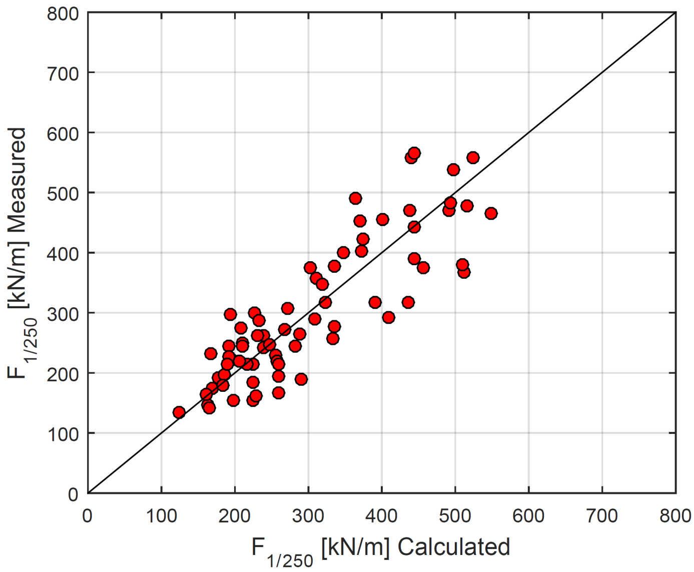

Fig. 4.33 Measured forces $F_{1/250}$ on the lower crown-wall in prototype scale versus calculated forces using the Eq. 4.33.

4.3.5 OBREC design

The previous sections showed that the maximum loadings on the different parts of OBREC are not simultaneous. The stability analysis of the device is strictly linked to this condition. For instance, at the time of the maximum loading on the ramp (Fig. 4.21), the crown-wall is unloaded. Fig. 4.34 presents an example of the force time-history on the wall, base, and ramp for different dimensions of the base reservoir (Test wave conditions: $H_{m0} = 0.11$ m; $T_p = 2$ s, $R_r = 0.09$ m).

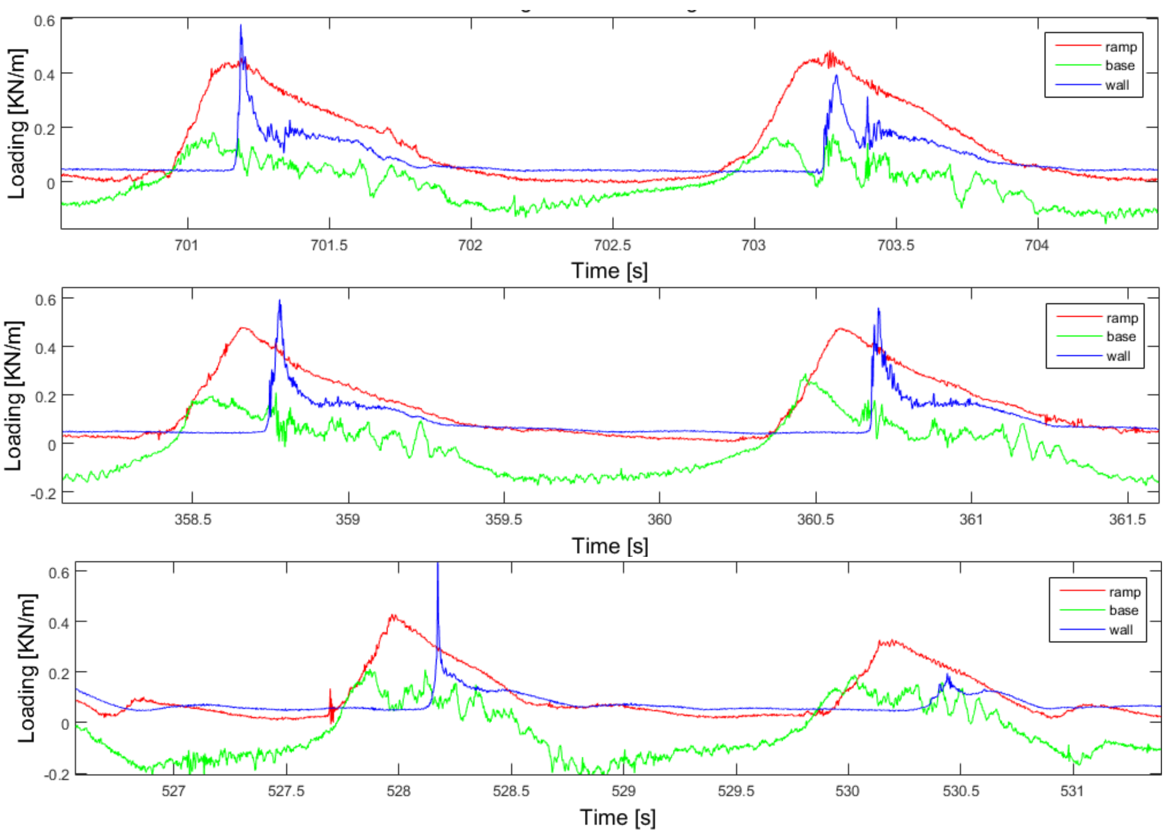

Fig. 4.34 Force time history on the wall, base, and ramp for Small reservoir (upper panel), Large reservoir (central panel), and Extra-Large reservoir (bottom panel) [$H_{mo} = 0.11$ m; $T_p = 2$ s, $R_r = 0.09$ m]

As expected, the reservoir width has a significant influence on the time lag between the maximum force peaks acting on the ramp and on the wall. Fig. 4.35 shows the correlation between the maximum ramp load, $F_{ramp,max}$, and the ramp force at the instant of the maximum gross horizontal load, $F_{ramp,FH}$.

The tendency indicates that $F_{ramp,max}$ is significantly larger compared to $F_{ramp,FH}$, meaning that the assumption of the maximum loadings, as calculated with the predicted formulas

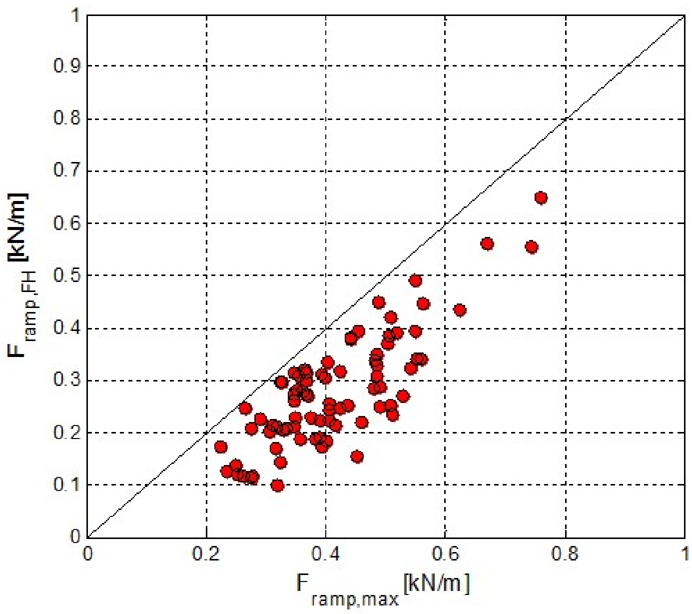

Fig. 4.35 Correlation between maximum ramp load $F_{ramp,max}$ and ramp loading at the instant of the maximum gross horizontal load, $F_{ramp,FH}$.

in the previous sections, applied simultaneously on OBREC are very conservative. The large difference between $F_{ramp,max}$ and $F_{ramp,FH}$ is not only due to the reservoir width, but also due to the stochastic nature of wave loading exerting on the OBREC. Indeed, for almost every test, the maximum loadings on the wall and on the ramp do not occur for the same wave.

In order to design the OBREC device in prototype scale, the critical loading conditions on OBREC can be considered for two instants: the time of maximum loading on the ramp, t_{ramp}, and the time of the maximum loading acting on the wall, t_{wall}. At the instant of the maximum loading on the ramp, the loading on the OBREC is as follows:

$$F_{OBREC\ (t,ramp)} = F_{ramp,max} + F_{base,max} \tag{4.35}$$

while at the time of the maximum loading on the wall, the loading acting on the device can be calculated as follows:

$$F_{OBREC\ (t,wall)} = \beta_{design} \cdot F_{ramp,max} + F_{base,max} + F_{wall,max} \tag{4.36}$$

Table 4.3 shows the terms in Eq. 4.35 and Eq. 4.36 while the parameter β_{design}, represented in Fig. 4.36, denotes the ratio $F_{ramp,FH}/F_{ramp,max}$. β_{design} is function of the wave length and the reservoir width and it can be expressed with the Eq. 4.37 obtained with non linear regression of the measured points:

$$\beta_{design} = 1.048 - 1.177 \cdot \left(\frac{L_D h}{\Delta B_{rs}^2}\right)^{-0.3443} \tag{4.37}$$

It is advised to apply Eq. 4.37 only for $8 < \frac{L_D}{\Delta B_{rs}} < 55$ and $0.9 < \frac{h}{\Delta B_{rs}} < 3.5$ since small values of ΔB_{rs} could be misleading.

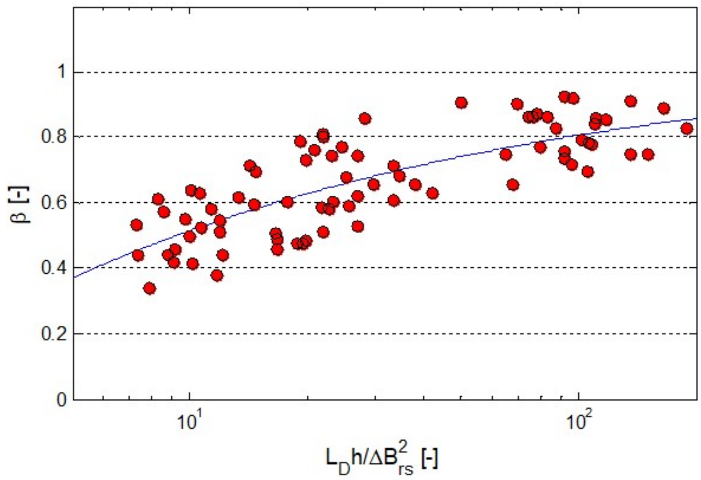

Fig. 4.36 Correlation between β with dimensionless reservoir width $\frac{L_D h}{\Delta B_{rs}^2}$.

Table 4.3 Formulas for the estimation of wave forces on the OBREC device.

$F_{ramp,max}$	Morihira and Kunita [183], assuming the wave steepness H_s/L_D
$F_{base,max}$	Eq. 4.25 for $h_{res}/h > 1$
	Tanimoto and Kimura [249] for $h_{res}/h > 1$
$F_{wall,max}$	$F_{wall,upper} + F_{wall,lower}$
$F_{wall,upper}$	Nørgaard et al. [200] modified with Eq. 4.28
$F_{wall,lower}$	Eq. 4.33

4.4 Conclusions

This chapter describes the physical model tests carried out on the OBREC device integrated into a rubble-mound breakwater. The purpose is to focus on the hydraulic and structural functionality of the OBREC device, completing the previous analysis carried out by Vicinanza et al. [276] and extending the overall knowledge on the wave pressure and resultant forces exerted on this innovative breakwater.

The first part of the Chapter describes the influence of the ramp shape on the force exerted on the different elements of the model. Results showed that the forces on the flat ramp are around 30–40% greater than those measured on the curved one. Despite the relative high scatter due to the complex interaction of the waves with different porous layers, results demonstrated that uplift loadings at the base of the curved configuration are slightly larger than those measured for the flat one. No significant differences between the two configurations were found on the magnitude of the resultant forces acting on the crown-wall. Pressures on the nose were also measured in laboratory and results indicated that the loading on the flat configuration are greater than those on the curved one for almost all the laboratory tests. The difference between the two configurations became more relevant considering the position of the resultant forces exerted on the upper part of the OBREC wall. Although with similar magnitude, the force on the flat configuration wall is located at a higher position compared to the one on the curved configuration, hence influencing the overturning moment around the base. The conclusion that can be drawn from this comparison is that the wave forces exerted on the OBREC with a curved ramp are generally lower compared to the flat one, so the first configuration can offer slightly better performance in terms of the overall stability.

Contrary to the ramp shape, laboratory models indicated that the reservoir width has less influence on the wave loading acting on the device. The only remarkable influence is the pressure measured at the upper wall and at the nose. For the Extra-Large reservoir, waves do not impinge directly at the nose, resulting in lower pressure impulses, compared to the configuration with a smaller reservoir. Contrary, maximum pressures on the nose occur for lower values of the reservoir width, because the water jet impacts directly on the triangular parapet with an extremely impulsive load while, for higher values of reservoir width, a large amount of wave energy is attenuated due to the dissipation in it.

The second part of the Chapter presents the comparison between the forces measured in the laboratory on the flat configuration and those computed with the semi-empirical design formulas used for traditional breakwaters. A new specific set of design formulas is then presented to predict the total forces exerted on the frontal ramp, under the horizontal base, and on the upper and lower wall.

Regarding the normal forces at the sloping ramp, results suggested that the best method to evaluate them is the one proposed by Morihira and Kunita [183] and modified by Takahashi et al. [240] for the sloping top caisson. However, for the calculation of coefficient λ_{SL} [240], results suggested using the significant wave steepness H_{m0}/L_D rather than $H_{1/250}/L_D$, originally indicated by Takahashi et al. [240].

Concerning the forces acting on the horizontal base, the analysis suggested distinguishing the case in which the base is located above or below the Still Water Level (SWL). Indeed, for the second case, the pressure impulse is directly transmitted under the base and the filtering capacity of the porous layer is reduced. In this configuration, the uplift forces were correctly predicted by the method presented by Tanimoto and Kimura [249]. Contrary, when the base is located above the SWL, results indicated that pressure peaks of the uplifts forces increased with the decreasing values of the vertical distance between the horizontal base and the SWL, and a new relation has been derived for the estimation of the uplift forces.

Two new design methods were proposed to estimate the horizontal forces at the upper and lower part of the OBREC wall. The first one consisted of a modification of the Nørgaard et al. [200] formula. The formula is modified adopting a different relationship for the run-up elevation, which takes into account the smooth frontal ramp. Furthermore, an empirical coefficient is included in the modified version of the Nørgaard et al. [200] formula to take into account the increase of the horizontal forces due to the presence of a triangular parapet located on the tip of the wall. Finally, forces at the lower wall were evaluated with a method that considers the path of the water jet, the (maximum) run-up velocity and (maximum) flow thickness on the crest ramp.

An insight of the time series analysis of the total forces indicated that the maximum forces on different parts of the OBREC were not simultaneous, and a method to estimate the total force to be applied on the structure for design purposes is proposed.

The analysis of the hydraulic and structural functionality described in this Chapter, as well as the design formulas here proposed, have been adopted for the preliminary design of the first full-scale device installed in Italy, which is currently under monitoring. Results of the physical model tests have also been used to validate an advance numerical model, which has then been adopted to extend the knowledge of the wave-structure interaction for further wave conditions and geometries not tested in laboratory. Details of the use of both numerical modelling and monitoring prototype in a real environment will be described in the next chapters of this thesis.

Chapter 5

Numerical model test

5.1 Introduction

After the laboratory tests, whose results are described in Chapter 4, some issues on the development of the OBREC device still remained unresolved. Uncertainties of the global stability are caused by the lack of information of the pressure field on some specific parts of the device. Indeed, the pressures acting underneath the ramp were not measured in laboratory. The analysis of the total forces exerted on the device did not take into account the forces underneath the shaft, which makes it difficult to accurately study the overall stability analysis of the structure. Furthermore, the OBREC ramp tested in the laboratory was a fixed structure, thus the direct influence of its submerged part on the total forces and global stability was not evaluated after the laboratory test. Despite the wide study of the wave-structure interaction, the limitations of the physical modelling have required further investigations.

To resolve these issues and uncertainties, numerical modelling has been used to extend the results obtained with the laboratory tests. Therefore, the objective of this chapter is to present the results of numerical model tests, which have been conducted to increase the knowledge of the interaction of waves with the OBREC device integrated into a rubble-mound breakwater and its hydraulic and structural functionality. One of the greatest advantages of the use of numerical models, once validated against experimental data, is the more accurate and detailed analysis of the wave forces exerted on a structure, due to the numerical pressure field data obtained on the entire domain. Furthermore, the numerical modelling can be used to test different geometries and wave conditions not evaluated on laboratory experiments.

Traditionally, harbour defence structures are designed relying on empirical formulations or using physical model tests when dealing with complex geometries. Nevertheless, during the last two decades, numerical models have been largely developed to be used as a complementary tool to design coastal structures.

Although there is an extensive literature on numerical modelling of traditional breakwaters, there is a lack of information about innovative structures, in particular, regarding the OTD-integrated in rubble-mound breakwaters.

Palma et al. [209] and Formentin et al. [80] used IH2VOF [163, 154], a 2D Volume-Averaged Reynolds Averaged Navier–Stokes (VARANS) model, combined with a Volume of Fluid (VOF) method, to study the performance of a OBREC integrated into a rubble-mound breakwater. The numerical results have been compared with data from the physical model test campaign carried out in 2012 [276]. Numerical and physical model data generally agreed, although some relevant differences were noticeable regarding the overtopping at the rear side of the structure and the obtained reflection coefficients, showing differences up to 35% between the numerical results and the experimental data. The simulations carried out by Palma et al. [209] and Formentin et al. [80] were performed using the wave generation procedure based on the target wave spectrum characteristics. Consequently, numerical temporal wave series were not the same as the ones used in the laboratory. This difference might explain the differences found between laboratory and numerical data since individual waves sequence and groups can be determinant when analysing effects such as overtopping and reflection.

The latest works on numerical modelling on the OBREC device were carried out by Maliki et al. [168] and Musa et al. [187]. In these two works, the authors used the commercial suite package Flow 3D ($FlowScienceInc.$ 2009) which solves the RANS Equations combined with the VOF method and coupled with a Re-Normalization Group (RNG) k-epsilon turbulence closure model. Maliki et al. [168] and Musa et al. [187] evaluated the overtopping behaviour on the OBREC device, comparing the result with measured data from test campaign carried out in 2012 [276]. Nevertheless, the results of the analyses focus only on wave overtopping discharge performance in the front reservoir, neglecting the studies on wave reflection and wave loading acting on the structures.

The interaction between the waves and the SSG [172, 46], has been also investigated numerically by Vicinanza et al. [277] and by Buccino et al. [44] using Flow 3D model. Vicinanza et al. [277] studied the nature and magnitude of the wave loading action on the frontal sloping face of the SSG device by running five bi-dimensional CFD numerical tests. The comparison with experimental test showed relatively good agreement in terms of wave reflection in front of the device. However, some differences were observed between predicted and simulated peaks occurred at percentiles as high as 99%, as result of impact waves. Tests carried out considering regular waves were numerically performed by Buccino et al. [44] in full scale, scaling up the identical geometry, at scale 1:66, employed in the laboratory [46]. The magnitude and the statistical properties of the simulated wave loadings were found to be in agreement with the physical model measurements, although slight differences were noticeable regarding the presence of sporadic pressure peaks on numerical tests, not observed in laboratory data. The authors attributed these differences to the absence of air in the model that reduces the pressure peaks in the physical model test [44].

The lack of a robust and direct validation of a numerical model used to study the wave interaction and the pressure acting on the OBREC device under extreme wave conditions is the main motivation of the present research. The purpose of this work is to validate and evaluate the capability of a two-dimensional numerical model based on the VARANS equations to study the wave interaction with the non-conventional rubble-mound breakwater integrated with the OBREC device under extreme wave conditions and its structural performance. Furthermore, IH2VOF is here used as a complementary source of information to complete the experimental data and enable a deeper understanding of the pressure behaviour acting on the device.

The chapter is organised as follows: the numerical model description is presented in Section 5.2; Section 5.3 is devoted to the description of the numerical simulations; the complete numerical model validation of the wave surface in front of the device and the wave pressure of the structure is presented in Section 5.4; in Section 5.5 an insight of the pressure distributions and resultant force acting on the device for stability analysis is presented and finally, the main conclusions are drawn in the last section.

5.2 Brief description of the model

In this work, IH2VOF model [163, 154] is used with the aim of evaluating its performance in reproducing the complex wave-porous structure interaction observed on the OBREC device in the laboratory as described in Chapter 4. IH2VOF, a 2-D numerical model that solves the VARANS equations, is a modified and improved version of COBRAS-UC Torres-Freyermuth et al. [255], Losada et al. [163]. The numerical model is based on the decomposition of the instantaneous pressure field, p, and velocity, u, into mean (ensemble time-average) and turbulent components. The free surface movement is tracked by the VOF method for only one phase, water and void. The VOF method, pioneered by Hirt and Nichols [111], is the powerful tool that allows the representation of free surfaces and interfaces that are arbitrarily oriented with respect to the computational grid. The numerical grid featured in IH2VOF is an orthogonal structured grid mesh and it uses a cutting-cells method [60] in order to consider obstacles into the domain. The mesh generation time is quite fast, and the method is highly efficient in terms of accuracy, CPU time and memory requirement, in particular for geometrically simple solution domain as the case of breakwaters cross-section. A drawback of the method can be the concentration of points in one specific region for reason of accuracy that would produce unnecessary small spacing in other parts of the computational domain and a waste of the time consuming [79]. The VARANS equations, derived by the integration of the RANS equations over a control volume, are coupled with the volume-averaged $k-\varepsilon$ turbulence closure model [115], obtained taking the volume averaging of the standard k and ε equations, which represents the evolution of the volume-averaged turbulent kinetic energy, k, and turbulent dissipation rate, ε. IH2VOF uses a finite difference scheme to discretize the VARANS equations and solves them using the two-step projection method [59]. For further details of the two-step projection method implemented into the model, please refers to Lara et al. [154]. The influence of the turbulence fluctuations on the mean flow field is represented by the Reynolds stresses $\rho\langle\overline{u_i'u_j'}\rangle$, while a non-linear algebraic Reynolds stress model is employed to relate the Reynolds stress tensor and the strain rate of mean flow [221]. The complete VARANS equations, Eq. 5.1 and Eq. 5.2, as derived in Losada et al. [162], can be written as follows:

$$\frac{\partial\langle\overline{u_i}\rangle}{\partial x_i}=0 \tag{5.1}$$

$$\begin{aligned}(1+c_m)\frac{\partial}{\partial t}\left[\frac{\rho\langle\overline{u_i}\rangle}{n}\right]+\frac{1}{n}\frac{\partial}{\partial x_j}\left[\frac{\rho\langle\overline{u_i}\rangle\langle\overline{u_j}\rangle}{n}\right]+\frac{1}{n}\frac{\partial}{\partial x_j}\left[\rho\langle\overline{u_i'u_j'}\rangle\right]= \\ -\frac{\partial\langle\overline{p}\rangle^f}{\partial x_i}+\rho g_i+\frac{1}{n}\frac{\partial}{\partial x_j}\left[\mu\frac{\partial\langle\overline{u_i}\rangle}{\partial x_j}\right] \\ -\frac{1}{n}\left[\alpha\frac{(1-n)^2}{n^2}\frac{\mu}{D_{n,50}^2}\langle\overline{u_i}\rangle+\beta\left(1+\frac{7.5}{KC}\right)\frac{1-n}{n^2}\frac{\rho}{D_{n,50}}\sqrt{\langle\overline{u_j}\rangle\langle\overline{u_j}\rangle}\langle\overline{u_i}\rangle\right]\end{aligned} \tag{5.2}$$

where $\langle\rangle$ represents the superficial volume averaging operator, $\langle\rangle^f$ represents the intrinsic volume averaging operator, ρ is the density of the fluid, g is the acceleration due to the gravity, μ is the dynamical viscosity, n is the porosity, t is the time, u stands for the velocity and p for the pressure and $D_{n,50}$ represents the mean nominal diameter of the porous media. The terms i and j represent the horizontal and vertical direction, the over-bar indicates the ensemble time-averaged values, while the single prime represents the Reynolds averaged (temporal) fluctuation with respect to the ensemble mean.

The last term of the right-hand sides of the Eq. 5.2 is the well-known extended Darcy-Forshheimer relation, which includes the linear and non-linear drag forces, whose friction coefficients are here expressed according to van Gent [269]. In the non-linear drag term of the Darcy-Forshheimer relation, KC is the Keulegan-Carpenter number defined as follows:

$$KC = \frac{T_0 \cdot u_M}{D_{n,50} \cdot n} \tag{5.3}$$

where u_M stands for the maximum oscillatory discharge velocity and T_0 is the characteristic period of oscillation, chosen as the mean wave period, T_m, as suggested by Losada et al. [163]. The KC number takes into account the effects of the oscillating flows produced by the waves inside the porous media. Please note that, under the wave action, the value of u_M varies over the time, yielding the resistant coefficient due to non-linear (quadratic) flow resistance in Darcy-Forshheimer relation varying in time. Contrary to recent works [130, 127] where constant values of KC number were used based on the incident wave field and shallow water wave theory, IH2VOF model takes into account the variation in time of the non-linear flow resistance coefficient in the Darcy-Forshheimer relation. As matter of fact, the values of KC number in IH2VOF is dynamically updating at any time step, considering the computed maximum oscillatory discharge velocity within the porous media. This approach allows to correctly evaluating the graduate increase in the nonlinear resistance coefficient when the waves are dampened inside the porous media, i.e. when the wave orbital velocities decrease.

It is worth observing that the two empirical parameters α and β, present in the linear and non-linear terms of the Darcy-Forshheimer relation respectively, are not only dependent on the porous media physical properties but also on the flow regime. Therefore, they are evaluated in a calibration process comparing experimental data and numerical results. In the first term of the Eq. 5.2, the parameter c_m denotes the effect of the added mass involved with the flow acceleration in the porous media, defined van Gent [269] as:

$$c_m = c\frac{1-n}{n} \tag{5.4}$$

where c represents a non-dimensional empirical parameter that takes the phenomenon added mass into account.

Obviously the Eq. 5.1 and Eq. 5.2 return to the original RANS equation in the free fluid region, i.e. the porosity coefficient is equal to the unit. For further details of the mathematical procedure to derivate the VARANS equations, please refers to del Jesus et al. [69], Jensen et al. [130], Higuera [109] and Losada et al. [162].

IH2VOF has been successfully adopted over the last decade in coastal engineering to evaluate the interaction between both regular and irregular waves with various porous coastal defence structures. Lara et al. [151] used the model to simulate the generation and propagation of irregular wave trains over a flat bottom as well as irregular wave interaction with submerged porous breakwaters. Losada et al. [163] and Lara et al. [152] used IH2VOF to investigate the hydraulic response, run-up and overtopping of high mound and low mound breakwaters, according to the definition contained in the PROVERBS Parameter Map suggested by Allsop et al. [11] and extended by Kortenhaus and Oumeraci [142]. Neves et al. [197] used the model to calculate the mean wave overtopping discharge for an emerged breakwater, which is a combination of an impermeable concrete vertical wall with a two-layer permeable rock slope in front of it. Guanche et al. [101] simulated the wave pressure distribution and wave loads for stability analysis on different geometries of rubble-mound breakwaters under regular and irregular wave conditions. Lara et al. [153] studied the evolution of a solitary wave over a porous step analysing the influence of porous coefficients (α and β). Raosa et al. [218] adopted IH2VOF to study the wave overtopping and the related fluxes velocity over sea dikes, comparing the results with the laboratory tests provided by Hughes and Nadal [120] on impermeable submerged or zero freeboard dike. Guanche et al. [100] showed the capability of the numerical model to reproduce with good accuracy the pore pressure damping inside a rubble-mound breakwater, comparing the results with the semi-empirical formulation proposed by Oumeraci and Partenscky [208], Troch et al. [257] and Vanneste and Troch [271]. Recently, Vílchez et al. [283] have presented an original engineering method to calculate the hydraulic performance of different types of breakwater using IH2VOF calibrated against experimental data provided by Vílchez et al. [284].

5.3 Numerical model set-up

In order to evaluate the capability of the numerical model to reproduce the performance of the device, the results are here validated against the experimental data. The computational domain is designed to faithfully replicate the Aalborg University wave flume geometry, the experimental set-up and the geometry an porous material properties of the breakwater as described in Chapter 4.

It is important to underline that only the geometry with a flat frontal ramp is considered in the present work to validate IH2VOF model. Please note that the choice of the flat ramp is due to the better overall performance of this geometry compared with the curved configuration as resulted by [126]. A sketch of the chosen specific geometry including the material properties is presented in Fig. 5.1. As previously described, the porous media below the OBREC base is composed of a core with nominal diameter $D_{n,50}$ = 5 mm, a seaward and leeward filter layers with $D_{n,50}$ = 20 mm and a seaward and leeward external armour layer with $D_{n,50}$ = 50 mm. The position of the pressure transducers on the examined geometry is presented in Fig. 5.2.

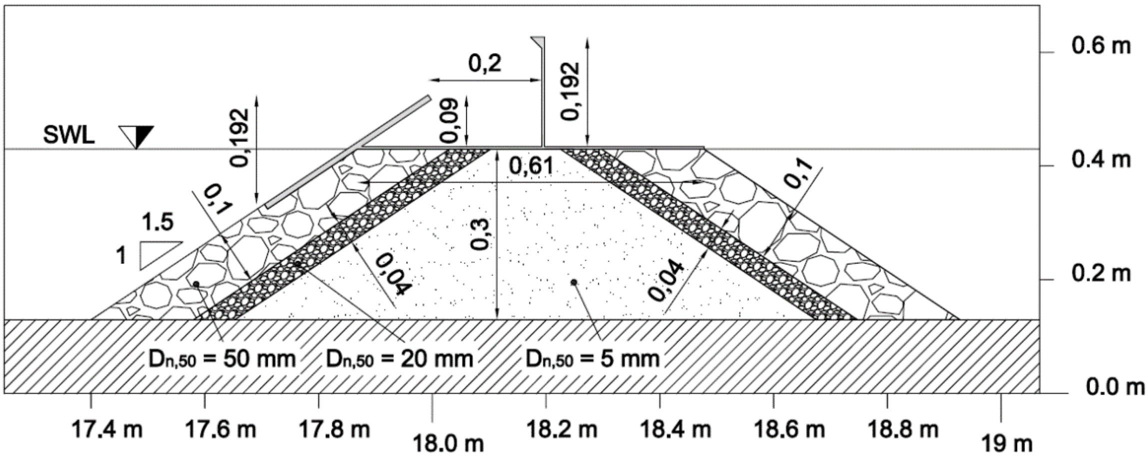

Fig. 5.1 Cross section of the OBREC flat configuration considered (*Large configuration*).

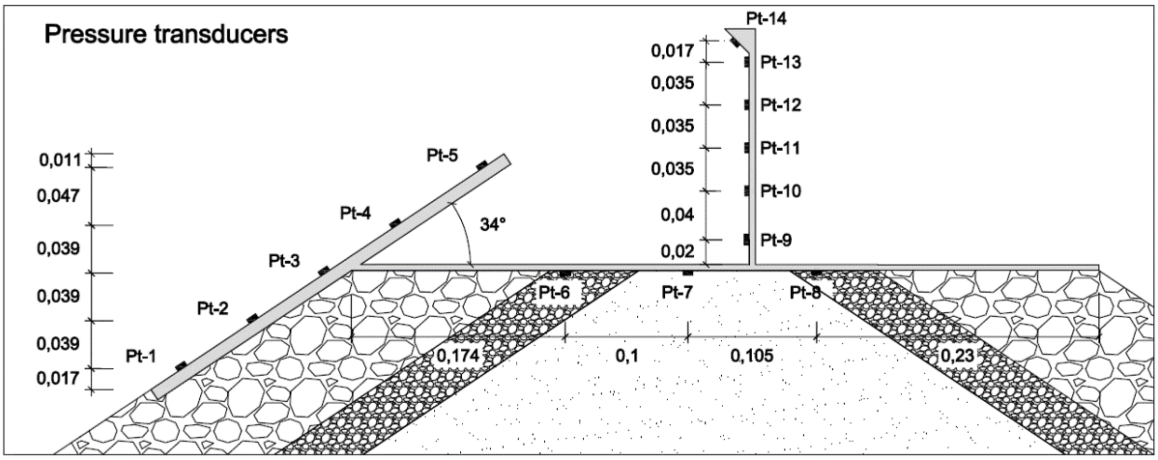

Fig. 5.2 Position of the pressure transducers along the model.

Please note that in the laboratory experiment, the water stored inside the frontal reservoir was able to flow in a box at the rear side of the structure, throughout a pipe. Conversely, the base reservoir is modelled in IH2VOF as a closed structure (see Fig. 5.1), i.e. the water stored into it is not able to flow and the reservoir is always saturated. It is worth underlining that, with the wave conditions tested in this work and shown in Table 5.1, the reservoir of the OBREC model tested in the laboratory is full for almost all the test duration, as shown in Iuppa et al. [126]. For this reason, the assumption of a closed reservoir as modelled with IH2VOF in this work can be considered valid.

Table 5.1 Incident wave characteristics measured at the toe of the model for the tests considered for the validation analysis

	H_{m0} (m)	T_p (s)	$T_{m,01}$ (s)	$T_{m,02}$ (s)	h (m)
$Test\_01$	0.100	2.16	1.72	1.63	0.27
$Test\_02$	0.103	1.78	1.46	1.38	0.27
$Test\_03$	0.092	1.49	1.24	1.17	0.27
$Test\_04$	0.098	1.95	1.69	1.59	0.30
$Test\_05$	0.099	1.78	1.48	1.40	0.30
$Test\_06$	0.090	1.58	1.31	1.26	0.30
$Test\_07$	0.097	1.91	1.69	1.61	0.35
$Test\_08$	0.103	1.78	1.48	1.42	0.35
$Test\_09$	0.090	1.46	1.32	1.27	0.35

According to the laboratory test campaign, the device is located in the numerical domain at a distance of 17.4 m from the wavemaker (*inlet boundary condition*); the first wave gauge ($WG-1$) is placed at 14 m from the initial position of the wavemaker and the other three free surface gauges at 0.30 m, 0.55 m and 0.70 m from the position of $WG-1$. Following the analysis performed in the laboratory, the numerical incident and reflected spectra are separated and estimated using Zelt and Skjelbreia [291] method. Additionally, both, the wave field in front of the OBREC device, is also separated into incident and reflected waves using the time-domain method proposed by Frigaard and Brorsen [87], based on the use of digital filters.

Irregular wave time series were generated in IH2VOF using the wave paddle motion measured in the laboratory, with a sampling frequency of 25 Hz. This movement was transferred to the model using the measured wave paddle position over the time, $X(t)$, and the associated velocity, $V(t)$, following the numerical techniques called $'virtual force method'$ [181]. More details on the method used to simulate moving bodies within the computational domain and the wavemaker implementation in IH2VOF are described in Lara et al. [154]. This procedure allows replicating wave-by-wave the wave conditions tested in the laboratory. Then, numerical pressures exerted on the structure can be obtained reproducing the same wave time series as the one generated in the laboratory.

Wave absorption at the outlet boundary condition is set, following the methodology proposed by Schäffer and Klopman [227]. This approach allows reducing the computational domain since a dissipative zone, as the one used in the laboratory experiments by means of a gravel beach, is not necessary. Instead, the computational domain at the rear side of the structure was reduced in comparison to the one in the laboratory, saving computational efforts. IH2VOF contains also the possibility of combining wave generation with wave absorption, that is active wave absorption. However, this feature was not included in the present work because the real movement of the wavemaker at the laboratory, that already includes the motion associated to active wave absorption, is used to generate the wave trains in the numerical model.

Nine tests are simulated in the numerical flume in order to validate the model. Table 4.2 summarises the incident wave parameter and water depths measured in the laboratory at the toe of the structure for the tests here analysed. The numerical domain is set up with a total length of 19.7 m and a height of 0.90 m. The grid system is uniform along the vertical direction with a constant cell size equal to $\Delta y = 0.005$m. Contrary, the horizontal direction is discretized with a non-uniform grid size mesh having a width that starts with 0.03 m close to the wave maker and it decreases until 0.005 m in the vicinity of the OBREC device. The errors due to the grid non-uniformity are minimized using smoothly varying grids in the horizontal direction. The function is defined in such a way that the second derivate of the coordinate of each cell is lower than 0.05, achieving a first-order accuracy of the numerical solution, as on a uniform grid. The resultant numerical domain has 1294 cells in the x-direction and 180 cells in the y-direction leading to a total of $232,920$ computational cells. The use of the highly refined computational grid mesh (0.005 m x 0.005 m) around the area of interest of the OBREC model was necessary due to the non-conventional geometry of the device with the presence of a thin sloping ramp and base, and a triangular parapet on the top of the vertical crown-wall. The parapet in laboratory model has the shape of an isosceles triangle with horizontal and vertical sides of only 2 cm. Moreover, a fine grid resolution is chosen to resolve the large velocity variation near the solid wall during the wave impact. All the nine simulations were executed on a desktop computer with Intel(R) Core(TM) 2.20 GHz processors with 12 GB RAM, simulating, on average, 100 s in 24 h of CPU time. The time step in the model is dynamically adjusted following Courant number, ranging between $1 \cdot 10^{-4}$ s to $1 \cdot 10^{-3}$ s. The numerical output data is then unified by using a linear interpolation to get a constant sampling frequency of 1000 Hz. The latter is chosen to be identical to the sampling frequency in the laboratory test.

The material properties of the porous media below the OBREC structure is set in the numerical models according to the experimental test, as shown in Table 5.2. Linear (α) and nonlinear (β) drag parameters in Eq. 5.2 are the calibration coefficients. They are selected matching the numerical and experimental results of both the free surface time series in the wave flume and the uplift pressure exerted at the base of the OBREC. The value of α is constant and set to 200 for all porous media following Lara et al. [154], while β is set to 0.8 for the core, 1.0 for the two filter layers and 1.1 for the seaward and leeward armour layers. Please note that the values are in accordance with previous studies with similar conditions [101]. The added mass coefficient, c in Eq. 5.4, which affects the inertia term in the momentum equation, is set to a constant value for all porous media, following Losada et al. [163]. A value equal to 0.34 is chosen based on the recommendations firstly suggested by van Gent [269] and largely adopted in literature for the numerical analysis of the wave interaction with porous media structures [158, 116, 163, 152, 101, 69, 130, 283].

Table 5.2 Porous media characteristics

	n	$D_{n,50}$	α	β	c
	$[-]$	(m)	$[-]$	$[-]$	$[-]$
Core	0.40	0.005	200	0.80	0.34
Filter layers	0.45	0.020	200	1.00	0.34
Armour layers	0.45	0.050	200	1.10	0.34

5.4 Validation analysis

This section is devoted to compare the obtained numerical results with the experimental data to demonstrate the ability of IH2VOF to replicate the main physical processes involved in the wave-OBREC interaction. The analysis discussed along this section focuses on the processes derived from the action of irregular waves on the innovative device. These processes are analysed by comparing statistical and spectral parameters of wave elevation signals close to the structure, wave reflection coefficients and wave pressure and force acting on the device. It is worth emphasising that, since the simulations are performed using the real movement of the wavemaker, the numerical results are validated in detail also through a direct time series comparison with the signals measured in the laboratory test. This approach is one of the most relevant differences with respect to previous numerical studies carried out on the OBREC device [209, 80], in which the comparison were carried out only considering the target wave spectrum as a wave generation procedure.

5.4.1 Free surface elevation

Fig. 5.3 shows the comparison between the free surface time series obtained from the model simulation and measured at the laboratory, for the $Test\_08$ (see 4.2 for the details of the incident wave characteristic of each test). For a better visualization of the comparison, Fig. 5.3 shows 60 s of the entire time series with approximately 40 waves. Results for the four wave gauges in the wave flume show a good agreement between the numerical and the experimental data. Comparable results is obtained for all the tests simulated in this work, getting a good agreement for both, wave phases and wave heights. The highest discrepancies are found for very small and short waves, as can be seen in Fig. 5.3. These differences can be due to the dimensions of the cell size, which are possibly still not refined enough to reproduce very high-frequency waves. However, the overall comparison results of the wave surface time series show that the model can replicate, with a high level of accuracy, the $2D$ local wave propagation and wave transformation processes, such as wave shoaling and non-linear interaction between waves in depth-limited wave conditions, along the sloping wave flume bottom. In addition, the simplification made by considering a closed reservoir (i.e. the water inside cannot flow behind the structure as it happened in the laboratory) is supported by the signals comparison in Fig. 5.3, since they also contain the energy of reflected waves from the structure, so similar reflection patterns are produced both, in the laboratory and the numerical domain.

The data of the free surface elevation from the four wave gauges are analysed using both the spectral analysis and the zero-down crossing method in order to evaluate and compare the wave parameters of the signals between numerical and laboratory data. Fig. 5.4 shows a comparison between numerical and measured data of the significant wave height, $H_{1/3}$, the average of the highest $1/250^{th}$ of waves in the wave record, $H_{1/250}$, the mean zero-crossing wave period, T_m and the significant wave period, T_s. All the figures contain the values of the mean relative error, μ_{error}, and the standard deviation, σ_{error}, of the relative error between measured and calculated values. Please note that the relative error, expressed in percentage, is here calculated as the difference between the measured and numerical values, divided by the measured values. Negative values of the error represent an overestimation of the numerical model.

Results confirm that the model predicts very well both the significant wave height $H_{1/3}$ and $H_{1/250}$ with mean errors around the 1%. A slight overestimation of the wave period in the wave signals is evident on the two panels at the bottom of Fig. 5.4. The reason of this very small overestimation, as mentioned before, can mainly be due to the numerical model

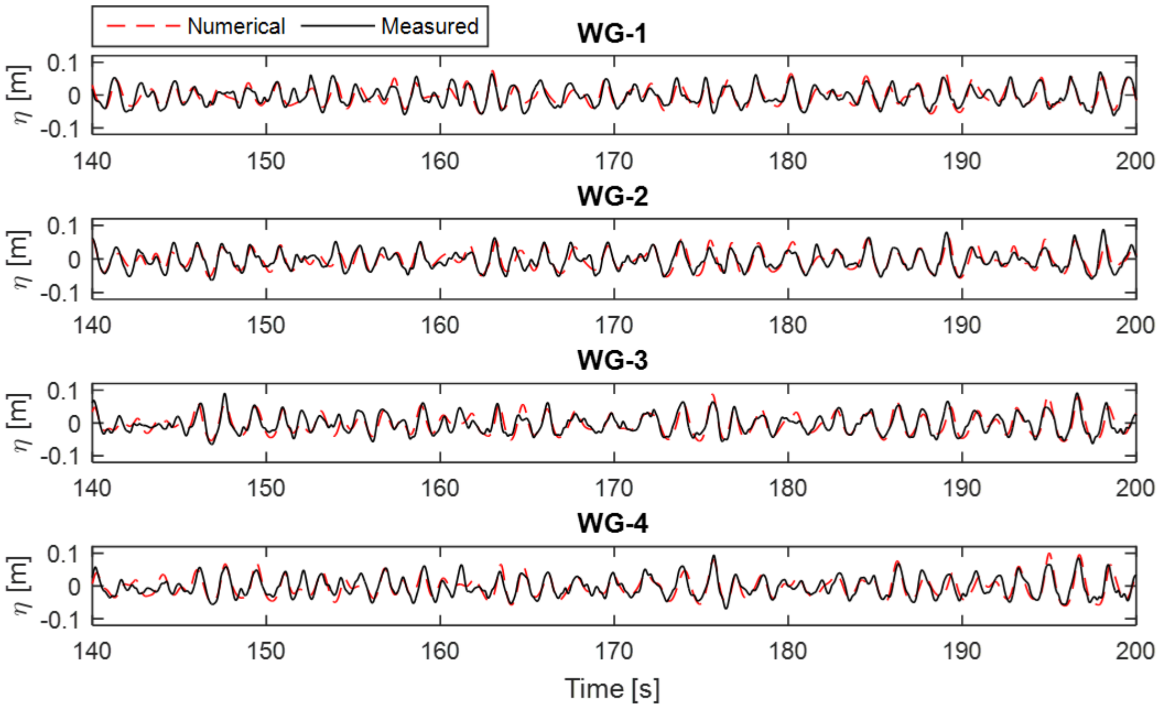

Fig. 5.3 Time series of the free surface elevation in the vicinity of the OBREC model for the $Test\_08$ (black line: laboratory measurement, red dashed line: numerical computations).

cell size, which is too large to replicate the high-frequency waves in the wave channel that are considered in the statistical analysis of laboratory signals.

5.4.2 Spectra analysis

A spectral analysis of the wave surface elevation in front of the OBREC is carried out, and the bulk spectra of the measured and numerical results is compared in order to provide an insight of the model performance in reproducing the wave energy evolution in the flume as well as the interaction with the OBREC model. As an example, Fig. 5.5 shows the variance density spectra of the wave surface elevation at the four wave gauges position for both measured and numerical signals, for the $Test\_01$. The accurate result confirms that the model simulates very well not only the energy evolution along the wave flume, but also the interaction of the waves with the porous spectra, since the spectra contain both the incident and the reflected components. Moreover, the reflection process due to the structure is well captured by the numerical model and partially standing wave pattern is notable in the flume with the presence of minimum wave amplitude at the quasi-nodes ($WG1$ in Fig. 5.5). The comparison shown in Fig. 5.5 indicates also that the numerical model is able to replicate the wave non-linearity in

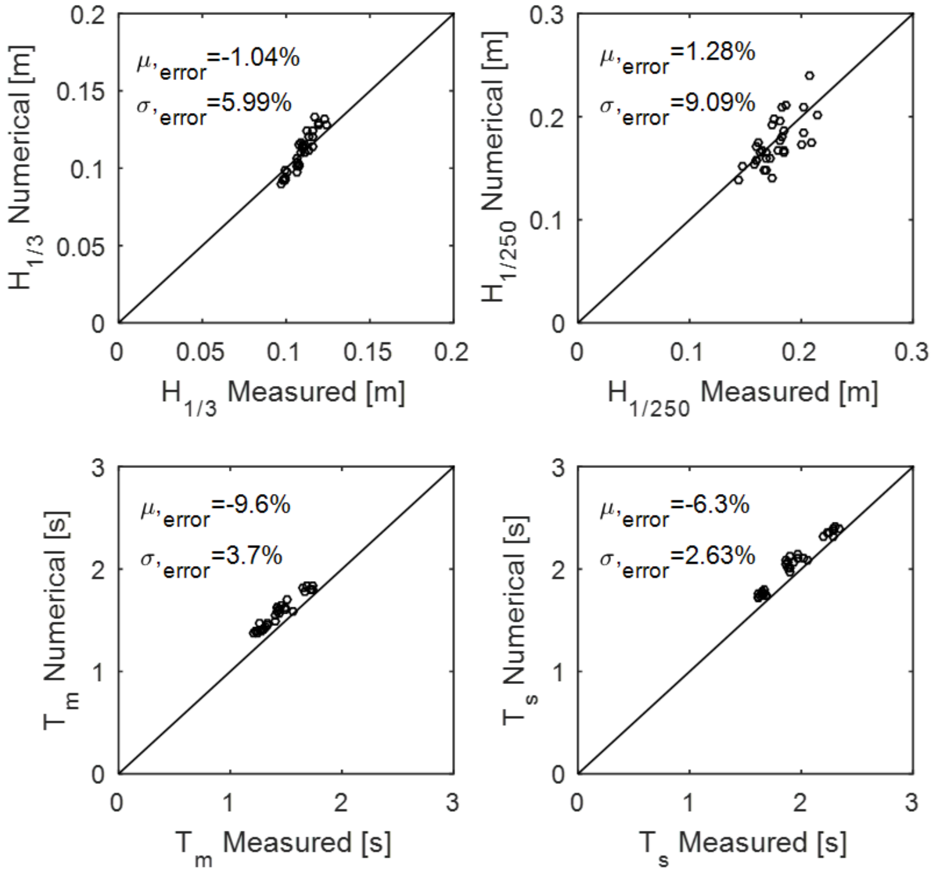

Fig. 5.4 Comparison between numerical and measured data of the significant wave height, $H1/3$, the average of the highest $1/250^{th}$ wave height, $H_{1/250}$, the mean wave period, T_m and the significant wave period, T_s, computed from the data of the free surface elevation of the four wave gauges using the zero-down crossing method.

the flume, whose effects are enhanced in shallow water. The non-linearity can be appreciated by the presence of both the sub- and super-harmonics around the peak frequency, well captured by the numerical model.

From the variance spectra of the free surface elevation, four spectral parameters are computed for each signal, and compared between numerical and laboratory results, as shown Fig. 5.6. The spectral parameters analysed here are the significant wave height H_{m0}, the peak period T_p, and the two mean periods, $T_{m,01}$ and $T_{m,02}$, respectively based on the first, m_1, and second order, m_2, moments of the variance spectra. The nth-order moment of the variance spectra is computed in a frequency range $0.33 \cdot f_p < f < 3.0 \cdot f_p$, where f_p is the peak frequency. The results obtained with the spectral analysis are very similar to those shown in Fig. 5.4, where the statistical wave parameters were obtained via the zero-down crossing analysis of the surface elevation. The model is found again to provide very good agreement

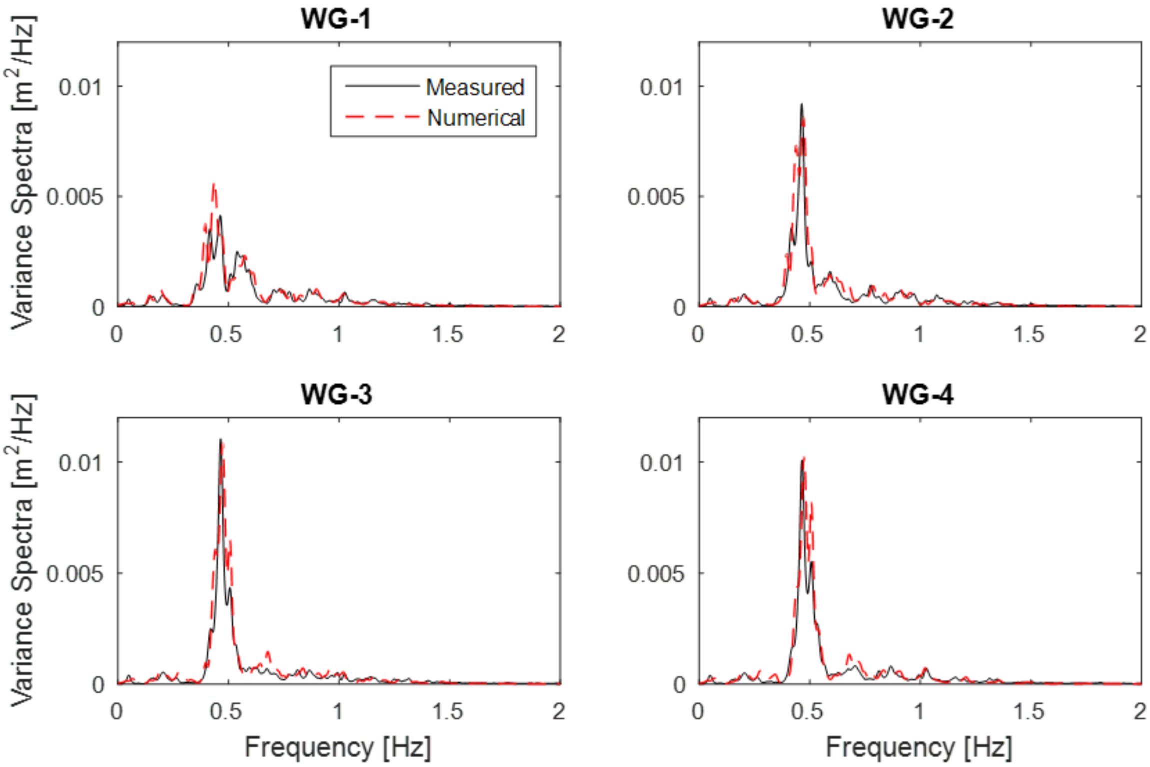

Fig. 5.5 Example of the variance density spectra of the free surface elevation near the model for the *Test*_01 (black line: laboratory measurement, red dotted line: numerical computations).

between the numerical and the laboratory data regarding the significant wave height, H_{m0} and peak periods, T_p with a mean error, μ_{error}, around the 1%. A minor overestimation of the mean periods $T_{m,01}$ and $T_{m,02}$ could be again addressed by the limitation of the model to simulate high-frequency wave components.

5.4.3 Wave reflection

Wave reflection is an important process in the OBREC device. The need of a large discharge rate into the frontal basin requires a steep and smooth ramp. Moreover, steep slopes are necessary for the occurrence of surging type break, which produce low energy dissipation. Iuppa et al. [126] showed that reflection coefficients dependent on the ratio between the ramp freeboard, R_r, and H_{m0}. When R_r/H_{m0} is high, almost no waves overtop the frontal ramp, thus leading to relative high reflection coefficients. Contrary, for lower values of the ratio the reflection coefficients are reduced due to the wave energy dissipation into the reservoir. This process ends for extreme wave conditions, i.e. low values of R_r/H_{m0}, in which the reservoir

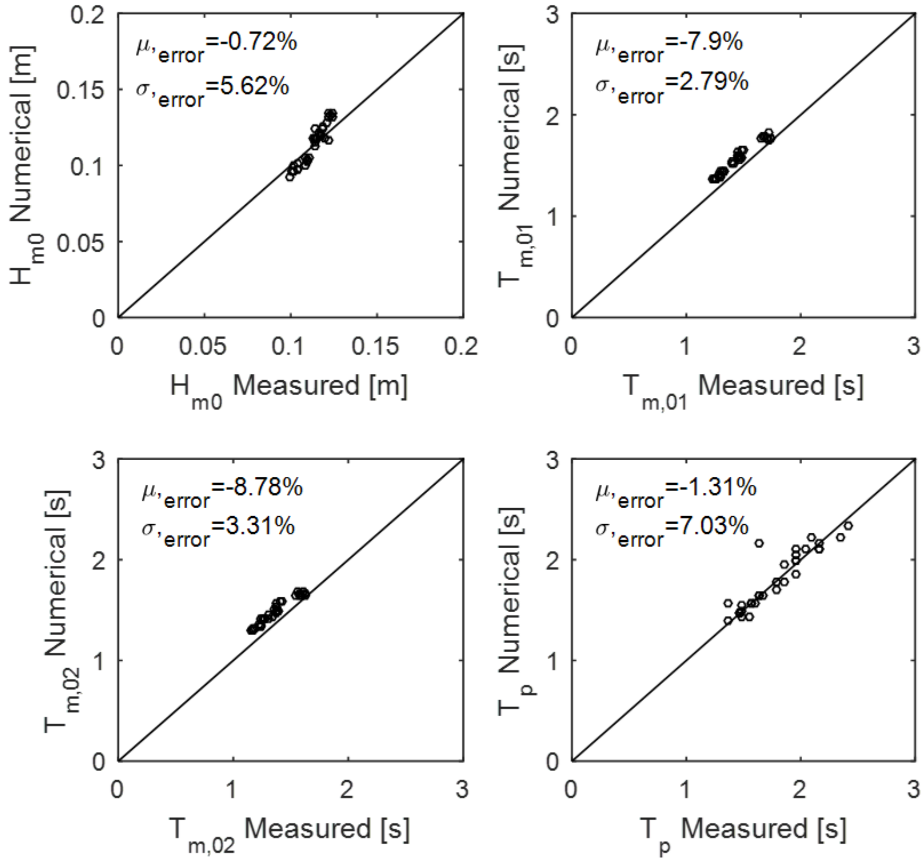

Fig. 5.6 Comparison between numerical and measured data of the significant wave height, H_{m0}, mean period based on the first moment spectra, $T_{m,01}$, mean period based on the second moment spectra, $T_{m,02}$ and peak period, T_p, computed from the data of free surface elevation of the four wave gauges using a spectral analysis.

is always saturated, thus leading again to higher reflection coefficients ($K_r \approx 0.5-0.7$). Due to the constraint of a closed wave reservoir in the present numerical analysis, only the latest extreme conditions have been simulated with IH2VOF.

In order to compute the reflection coefficients K_r, the incident and reflected spectra are separated and estimated using the method described in [291]. The zero-moment orders of the incident and reflected wave spectra, m_{0i} and m_{0r}, are determined based on the integral of the estimated spectra truncated at $0.33 \cdot f_p$ and $3.0 \cdot f_p$. The (bulk) reflection coefficient K_r is calculated as $\sqrt{m_{0r}/m_{0i}}$ and a comparison of K_r for the numerical and laboratory data is shown in Fig. 5.7. The results ($\mu_{error} = -5.35\%$ and $\sigma_{error} = \pm 10.30\%$) confirm the very good accuracy of the numerical model to simulate the wave interaction with the device. Please note that the slight overestimation of the reflection coefficients can be due to the difference between the model tested in the laboratory and the numerical model. Indeed, in laboratory, although the reservoir was always saturated, the water stored into it was able to flow throughout a pipe. Conversely, in IH2VOF the reservoir was modelled as a closed structure, thus slight higher wave reflection coefficients compared to the measured data were expected.

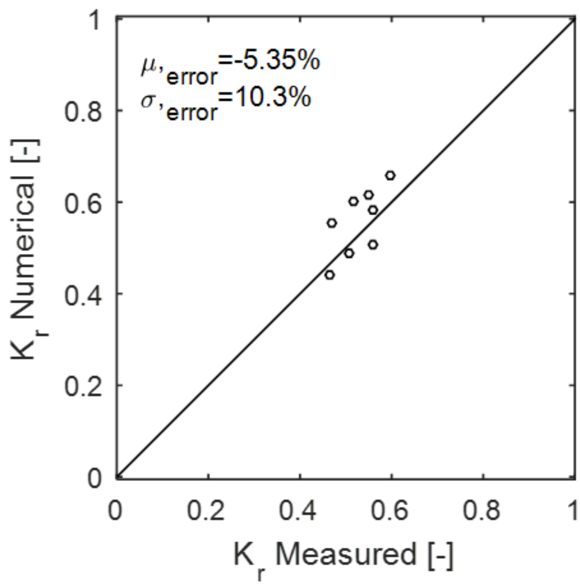

Fig. 5.7 Comparison between numerical and measured data of the (bulk) reflection coefficient K_r.

Fig. 5.8 shows the comparison between numerical and measured incident wave parameters at the toe of the structure. These incident wave parameters show a very good agreement with the measured data for all the nine tests analysed. The overall comparison of the wave surface elevation in front of the structure, as described in Sections 5.4.1, 5.4.2 and 5.4.3, is very satisfactory with a mean relative error always below 10% for all the computed statistical and spectral parameters, which can be considered tolerable, bearing in mind the complex processes involved, as well as the non-conventional geometry of the OBREC cross-section.

5.4.4 Wave pressure

A correct prediction and evaluation of the wave pressure are crucial for the design of traditional coastal structures as well as for non-conventional breakwaters with complex geometry. In order to offer a comprehensive validation process of the numerical model used in this work, the wave pressure exerted on the OBREC device are analysed and compared with the experimental data. The laboratory and numerical data of the pressure signal were processed through the low-pass digital filter. The aim was to filter out the high-frequency

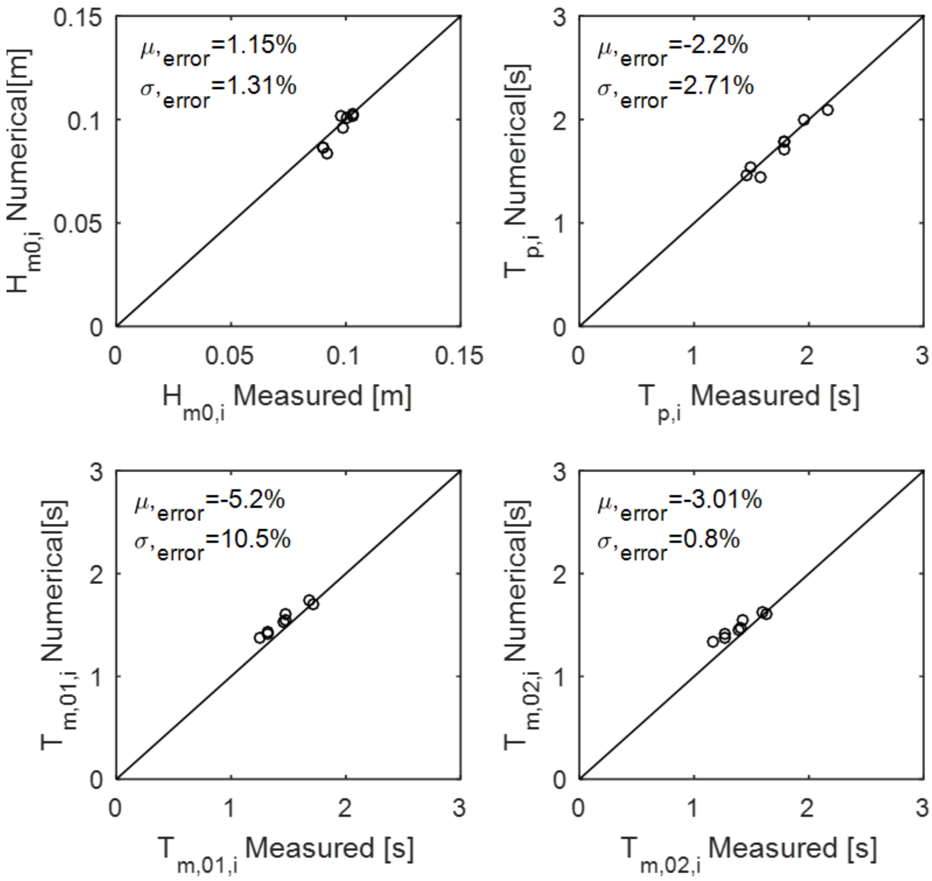

Fig. 5.8 Comparison between numerical and measured data of the main spectral parameters of incident waves computed using the method described in Zelt and Skjelbreia [291]: significant wave height, $H_{m0,i}$, mean period based on the first moment spectra, $T_{m,01,i}$, mean period based on the second moment spectra, $T_{m,02,i}$ and peak period, $T_{p,i}$

components from the raw signals in order to reduce the noise and to avoid sporadic unrealistic spikes in pressure signals. In this work, dealing with wave data from different nature, the process of obtaining the correct filter has been accomplished using a process of trial and error, and a cut-off frequency of 50 Hz was chosen for numerical and measured signals.

Fig. 5.9 shows an example of the computed time series force acting on the OBREC vertical wall for the *Test*_04. The red line indicates the raw signals and the blue line is the filtered signal using a cut-off frequency of 50 Hz. Although a slight reduction of the peak forces is noted for some waves, the selected cut-off frequency is considered as the best choice for the present validation analysis.

Figs. 5.10, 5.11 and 5.12 show a comparison of the measured and calculated dynamic pressure time series for the *Test*_08.

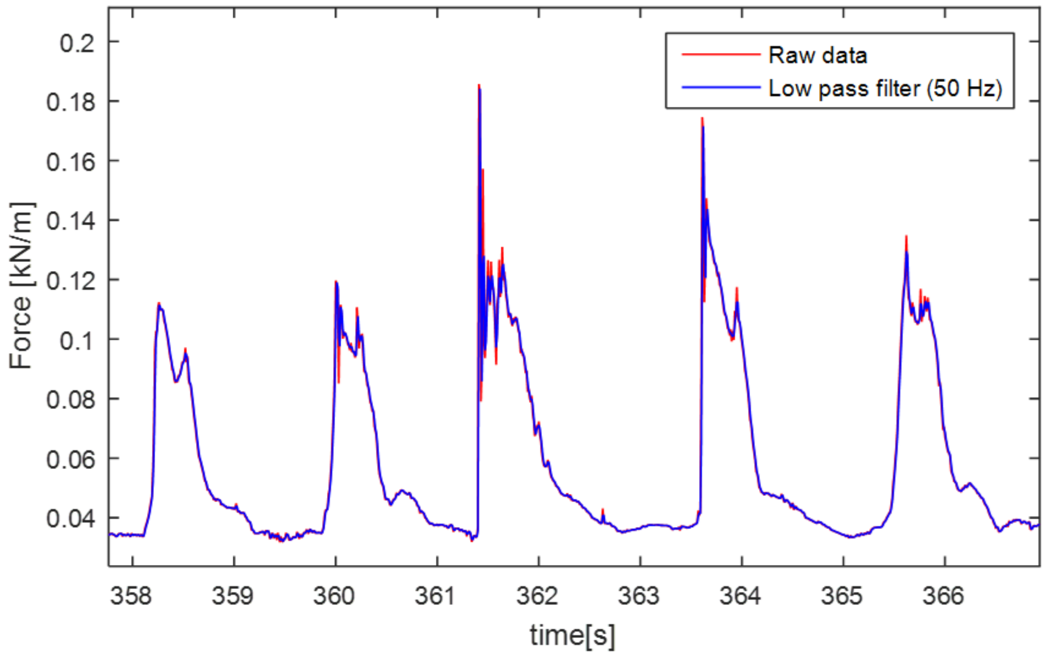

Fig. 5.9 A comparison of types of the computed time series impact force on the vertical wall (*Test*_04). Red line indicates the raw data and blue line is the filtered signal using a cut-off frequency of 50 Hz

For a better visualization of the overall pressure validation, the results plotted here refer to the same test and time window (140 s - 200 s) previously shown in Figs. 5.3, with the pressure signal impacts due to nearly 40 incident waves. In detail, the comparison includes five pressure gauges along the sloping ramp (Pt-1 to Pt-5) (Fig. 5.10), three pressure gauges underneath the horizontal plate (Pt-6 to Pt-8) (Fig. 5.11) and six pressure gauges on the vertical wall (Pt-9 to Pt-14) (Figs. 5.12). The red dashed line indicates the numerical results obtained with IH2VOF and the black solid line is the signal measured in the laboratory. As can be observed in Figs. 5.10 and 5.11, the model accurately predicts the pressure at the frontal ramp and underneath the structure. It is noted that the calculated pressure signal is correctly in phase and magnitude with the measured signal, and only minor discrepancies are present for some waves. Fig. 5.11 shows the good performance of the model when dealing with porous media flow. It can be appreciated that the numerical model is able to simulate the pore pressure damping induced by the different porous media on the waves, leading to a relevant reduction of the pressure in the direction of the wave propagation, i.e. from Pt-6 to Pt-8. It is worth to mention that the linear (α) and nonlinear (β) drag parameters in Eq. 5.2 were calibrated based on the good agreement between the numerical results and the experimental data in free surface time series and uplift pressures. Thus, the correct definition

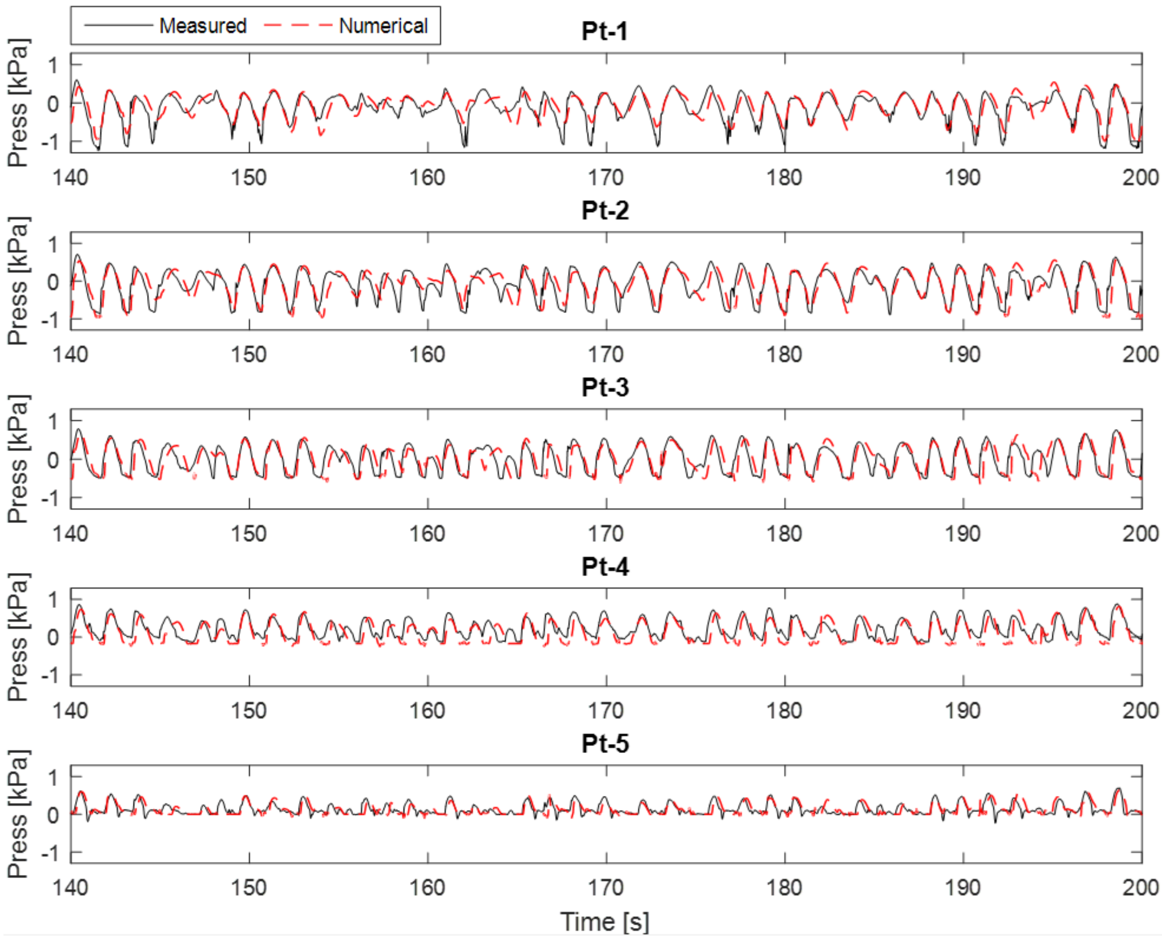

Fig. 5.10 A comparison of pressure time series on the frontal ramp (*Test*_08). Red dashed line indicates the numerical results and the black solid line is the measured signal

of these coefficients leads to a good representation of the porous media flow behaviour across different porous media.

The pressure on the vertical wall is a very important factor in determining the stability of the device. Fig. 5.12 presents the time history of the measured and numerical solution of the total pressure, i.e. also considering hydrostatic component when the reservoir is full after the first incident waves, along the front face of the vertical crown-wall. The good agreement observed at Pt-9 again supports the simplification of the closed reservoir. Total pressure due to the water stored in the saturated reservoir during the entire test is compared at this position and there is a good agreement. Fig. 5.12 also shows that the best results are achieved for the pressure gauges located on the lower part of the reservoir (Pt-9 to Pt-12) with small discrepancies. Major differences are noted on the pressure gauges located on the upper part of the crown-wall (Pt-13 and Pt-14). On this part, discontinuous record signals can be noted,

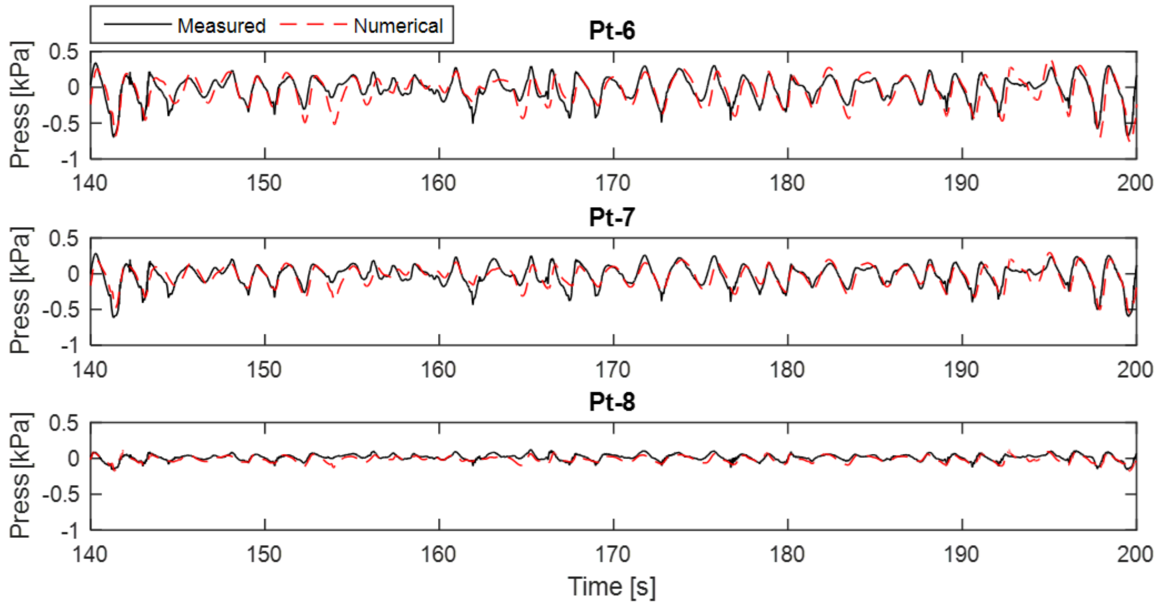

Fig. 5.11 A comparison of uplift pressure time series underneath the base model (*Test*_08). Red dashed line indicates the numerical results and the black solid line is the measured signal

since the gauges only register pressure for the largest wave overtopping events when waves reach them. Numerical records at Pt-13 and Pt-14 in Fig. 5.12 show a good agreement in phase with the experimental data but there are differences in magnitude for some waves, especially when pressures are small (i.e. below 0.2 kPa). It is important to note that the prediction of the time series along the upper wall is very challenging since it requires an excellent simulation of the very thin flux layer that overtops the ramp and impact on the pressure gauges.

Apart from the time series comparison, several statistic parameters of the wave pressure peaks are additionally considered for the model validation. In particular, four percentiles of the peak pressures ($p_{85\%}$, $p_{90\%}$, $p_{95\%}$ and $p_{99\%}$) in time series are examined for the comparison. Please note that the number of wave impacts acting on the vertical wall is lower than the number of waves, because some small waves were not able to overtop the frontal ramp and impact on the wall. For this reason, the percentiles are here computed using the total number of incident waves measured in the flume, which is around 500-1000 for analysed tests. Fig. 5.13 shows the comparison of the four percentiles of pressure peaks obtained numerically and in the laboratory for all the 14 pressure gauges positioned along the OBREC model. Please note that the axis limits are kept constant for all the sub-plots, to better represent the magnitude of the peak pressures on the structure.

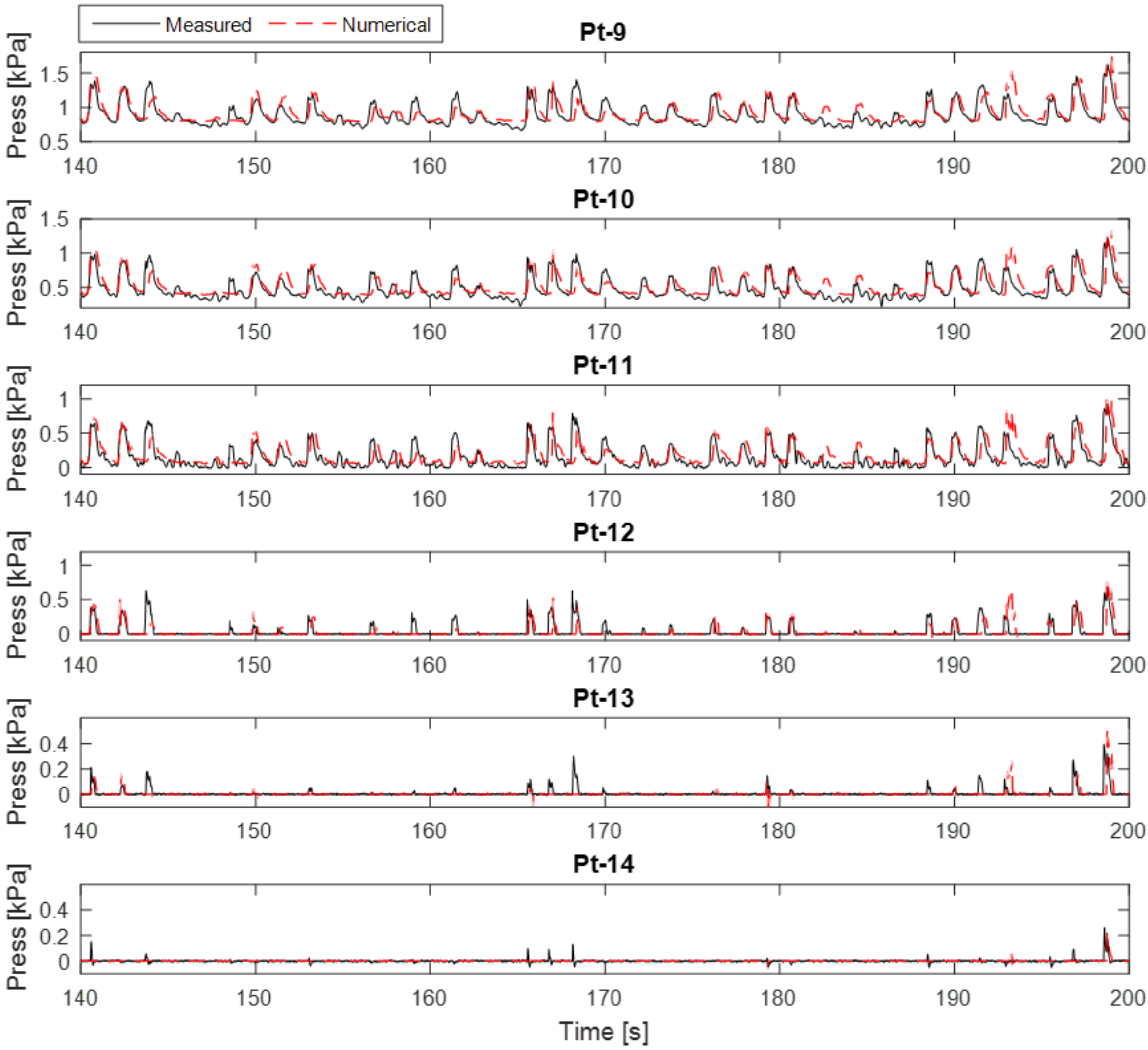

Fig. 5.12 A comparison of pressure time series on the vertical wall (*Test*_08). Red dashed line indicates the numerical results and the black solid line is the measured signal

The root-mean-square (*rms*) error is used to measure the difference between the pressure peaks predicted by the model and the values measured in the laboratory. This parameter is chosen since the aforementioned relative error is undefined when measured peak pressures are zero. The comparison of the dynamic pressure peaks on the frontal ramp (Pt-1 to Pt-5) is very satisfactory, with an overall mean value of the root-mean-square error, μ_{rms}, equal to 0.08 kPa. Similar values are computed considered the uplift pressure peaks measured and calculated by the three pressure gauges on the device base (Pt-6 to Pt-9), with μ_{rms} = 0.09 kPa. However, the numerical model underestimates the peak pressures along the OBREC vertical wall, mainly on the upper part of it (Pt-13 and Pt-14), with μ_{rms} = 0.141 kPa.

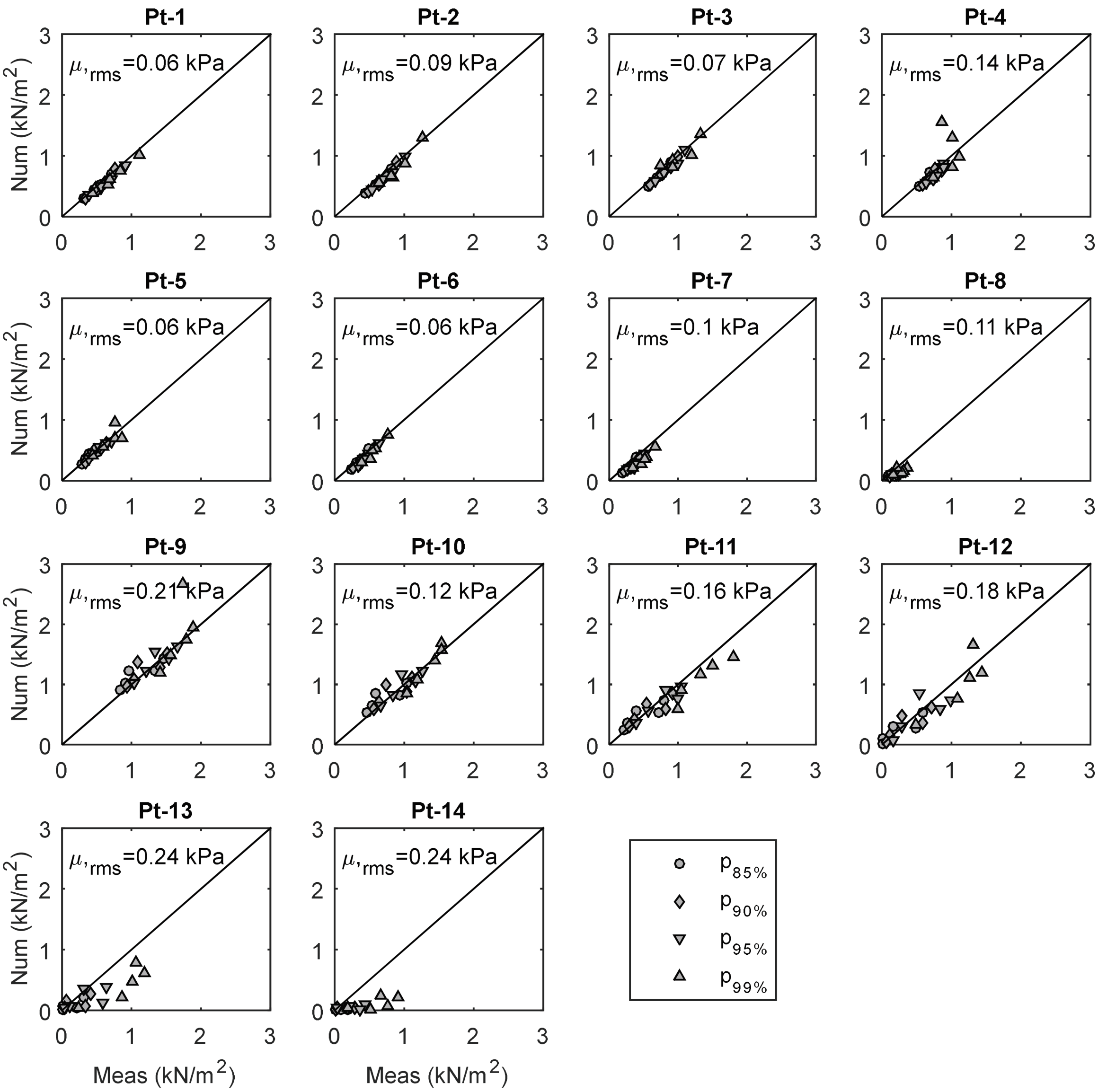

Fig. 5.13 Comparison of the four percentiles of pressure peaks ($p_{85\%}$, $p_{90\%}$, $p_{95\%}$ and $p_{99\%}$) obtained numerically and in the laboratory.

5.4.5 Pressure distribution and force

The resultant wave forces acting on the structure are calculated in this work by integrating pressure distribution between the adjacent cells in the numerical domain and the pressure transducers in the laboratory experiments. Fig. 5.14 shows a scheme of the vertical and horizontal components of the forces acting on the OBREC device.

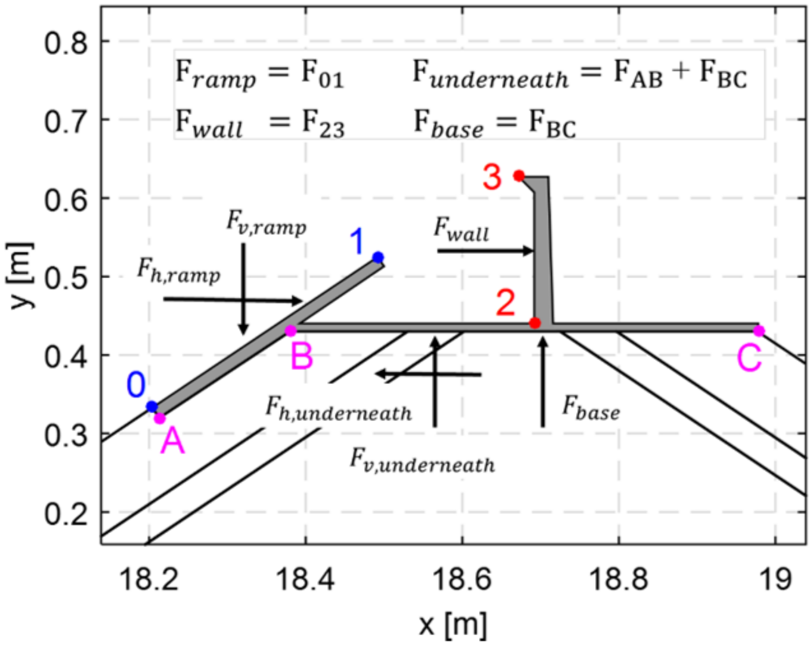

Fig. 5.14 Sketch of the horizontal and vertical forces acting on the different parts of the OBREC device.

As described in Chapter 4, a linear extrapolation of the neighbouring measured pressures in the laboratory was used to estimate the pressure on the structure wedges where no transducers were placed. The resultant horizontal and vertical force time series on the frontal ramp, named as $F_{h,ramp}$ and $F_{v,ramp}$ respectively, the vertical forces on the horizontal base, F_{base}, and the horizontal forces on the wall, F_{wall}, are displayed in Fig. 5.15 for the *Test*_08. Forces acting on the ramp and base reservoir are well captured showing a good agreement with laboratory data (top three panels in Fig. 5.15).

The highest differences are found at the forces exerted on the vertical wall where the numerical model overestimates the forces for some events. Four percentiles associated to peak forces ($F_{85\%}$, $F_{90\%}$, $F_{95\%}$ and $F_{99\%}$) are also compared. Fig. 5.16 shows the horizontal and vertical components of the forces exerted on the ramp, the base and the vertical wall. Forces exerted on the ramp, horizontal and vertical components, agree very well with those measured in the laboratory (top two panels in Fig. 5.15), with a μ_{error} of the four percentiles lower than

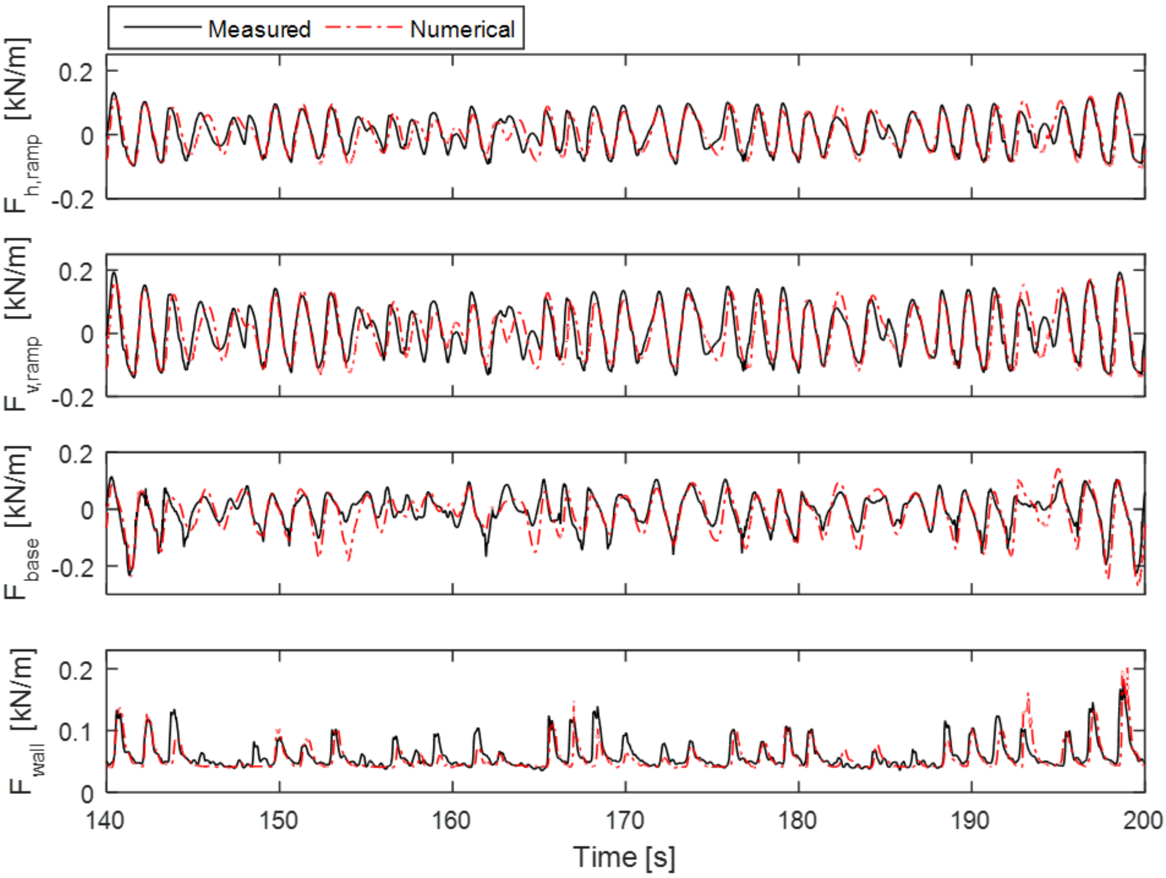

Fig. 5.15 A comparison of the time series of the forces acting of the ramp, base and vertical wall (*Test*_08). Red dashed line indicates the numerical results and the black solid line is the measured signal.

8.0%. A small underestimation of the total vertical force acting at the horizontal base can be noted in the lower left panel in Fig. 5.15, with μ_{error} = 17.87% and $\sigma_{error} = \pm 9.55\%$.

More details on the uplift resultant forces will be discussed in Section 5.4.6. Regarding the horizontal loading on the vertical wall, the comparison gives the largest underestimation of the wave forces with μ_{error} equal 24.66% and a $\sigma_{error} = \pm 8.86\%$.

The overall comparison of the wave pressure acting on the device can be considered very satisfactory bearing in mind the complexity of the fluid-structure interaction, as well as the non-conventional geometry of the breakwater cross-section. The main differences observed on the upper part of the vertical wall can be due to the complex processes involved, such as the run-up and overtopping produced over this composite structure and the wave energy dissipation on the reservoir. Moreover, the model used for this analysis takes into

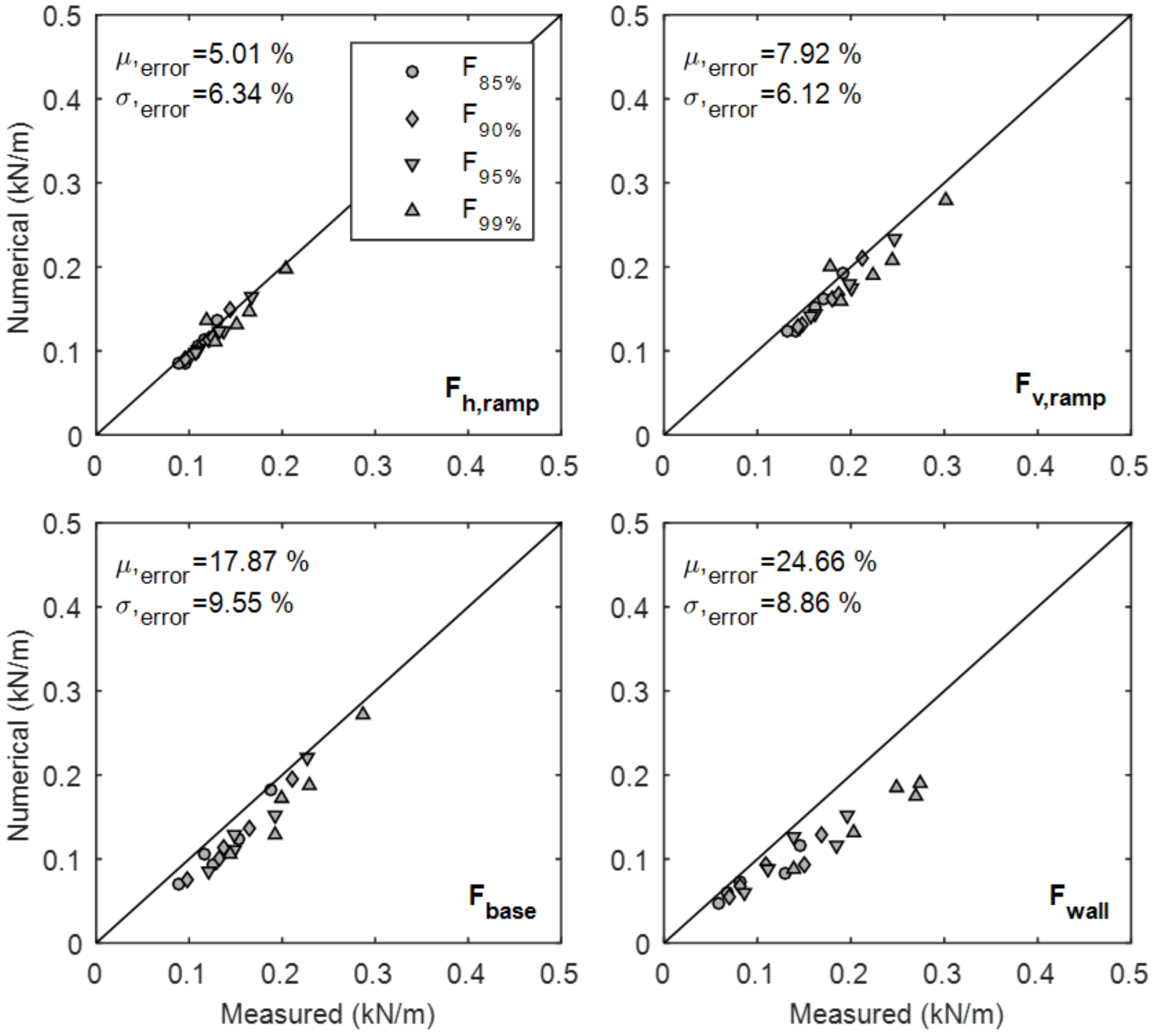

Fig. 5.16 Comparison between numerical and measured data of four percentiles of resultant peak forces ($F_{85\%}$, $F_{90\%}$, $F_{95\%}$ and $F_{99\%}$).

account only one phase (i.e. water and void), which may have some influence on the correct representation of some sporadic impact waves that can occur on the OBREC wall.

Fig. 5.17 shows the time series of the numerical horizontal, F_h, (top panel) and vertical forces, F_v, (middle panel) acting on the different parts of the OBREC model for two incident waves for *Test*_08 (from 372.5 s to 376.0 s).

The forces are positive when they act towards the structure, and only the dynamic component of the force is displayed. Bottom panel in Fig. 5.17 shows the time series of the total horizontal, $F_{h,total}$, and vertical forces, $F_{v,total}$, acting on the entire structure. $F_{h,total}$ is positive when its direction follows the wave direction, while $F_{v,total}$ is positive when it is directed upward. The four time instants displayed in Fig. 5.17 by vertical dashed lines, and presented in Fig. 5.18, show the characteristic behaviour of the waves-OBREC interaction.

At the instant t = 372.95 s, the vertical uplift force underneath the device reaches a local peak value, while the incident surging breakers is still rising along the frontal sloping ramp. The latter results in a quasi-static force path until reaching the ramp crest (t = 373.10 s). Until that instant, the upper part of the vertical wall is unloaded, and only the hydrostatic pressure component, due to the water stored in the wave reservoir, can be seen on the lower part of the crown-wall (see the two top panels in Fig. 5.18). Afterwards, the wave overtops the frontal ramp, firstly impinging on the upper part of the vertical wall, at t = 373.25 s, and then reaching the parapet located on the top of it at t = 373.30 s. It is worth pointing out that at the instant of the peak force exerted on the vertical wall (t = 373.30 s), the resultant vertical force underneath the structure and on the ramp are lower than their local peak values. From the bottom panel of Fig. 5.17, it is also clear that the maximum vertical and horizontal forces for each single incident wave do not act at the same instant, which denotes an important positive aspect regarding the global stability of the device. In this regard, the vertical force acting on the frontal sloping ramp, $F_{v,ramp}$, and the horizontal force underneath the structure, $F_{h,underneath}$, improves the global stability of the OBREC, reducing the overall total vertical and horizontal force acting on the device. In particular, at the instant of the local maximum total horizontal force, $F_{h,total}$, the total vertical force is null or, even more, negative (i.e. overall vertical force directed downward). Contrary, at the instant of the local maximum total vertical force, the horizontal force acting on the device is around its minimum value. Fig. 5.18 shows the instantaneous free surface (VOF function) and pressure distribution along the ramp, vertical wall and underneath the structure for the four time instants of $Test\_08$ displayed in Fig. 5.17. Red solid lines show the pressure distribution obtained with IH2VOF, while the black solid lines are referred to the pressure signal measured in the laboratory. The example further confirms the model capability of resolving pressure distribution on the OBREC at any time step.

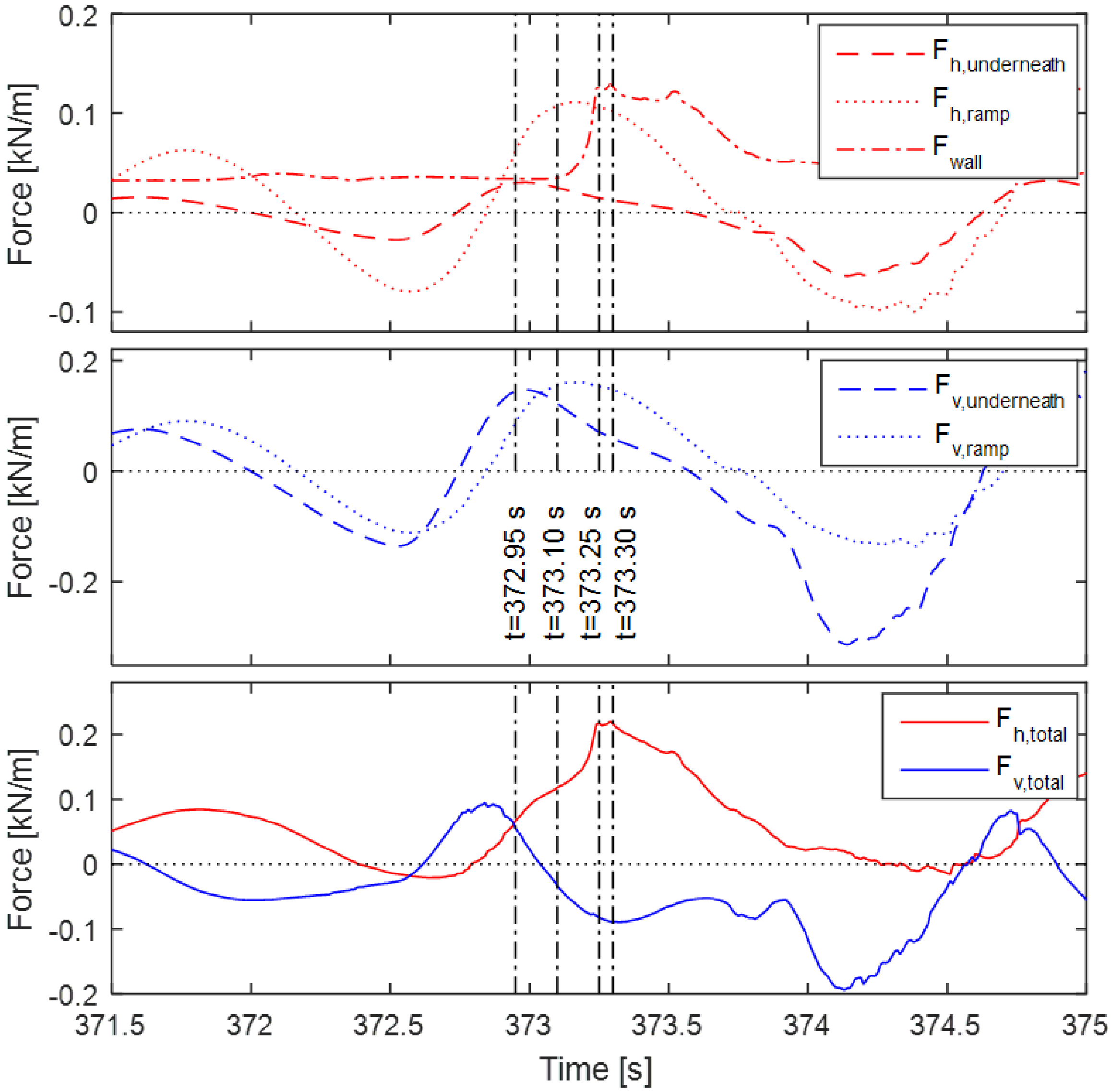

Fig. 5.17 Time series of the numerical results of the horizontal force (top panel) and vertical force (middle panel) acting on the different parts of the OBREC model (*Test*_08). The time series of the total horizontal and vertical forces are displayed in the bottom panel.

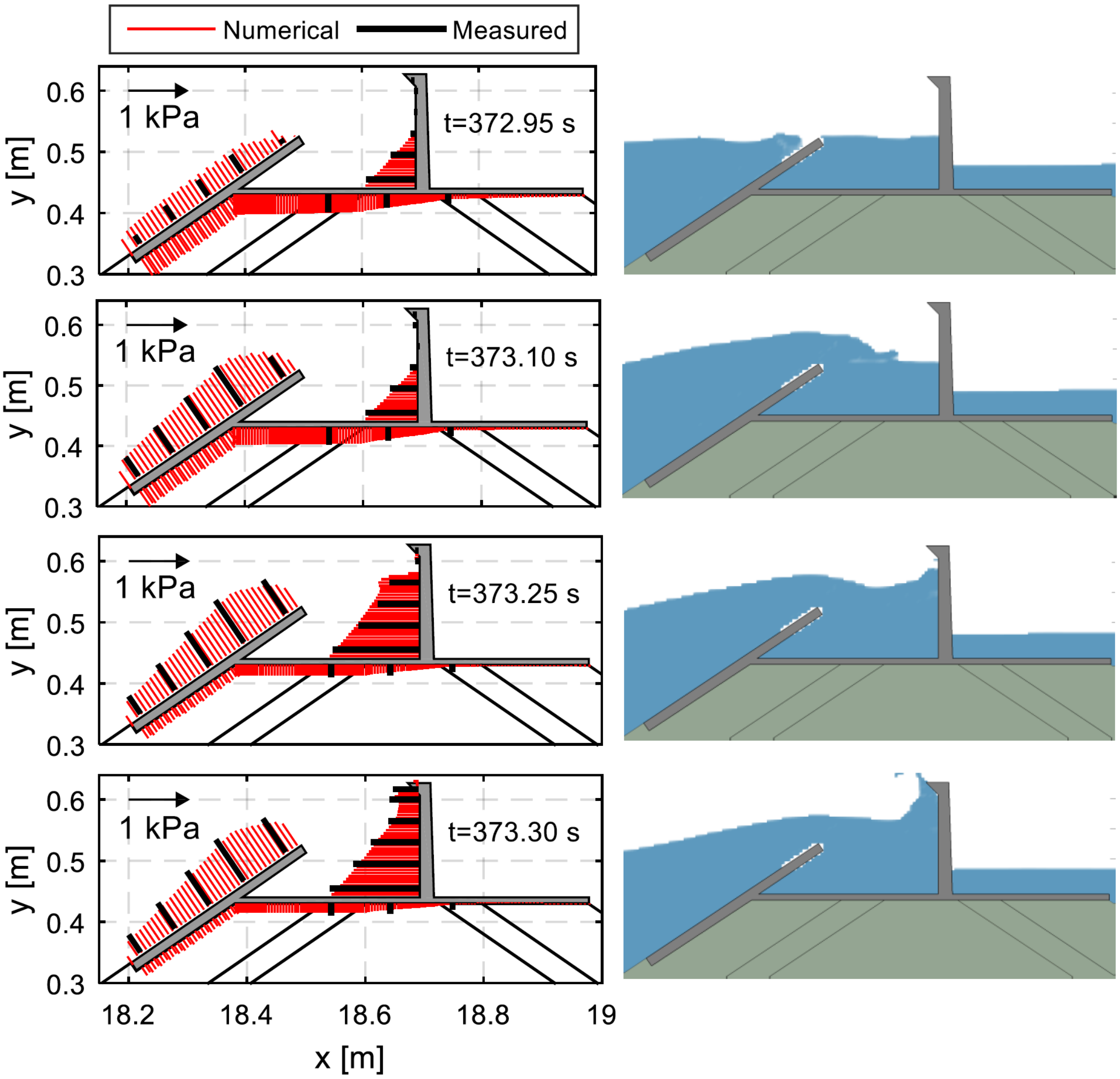

Fig. 5.18 Four snapshots of the dynamic pressure distribution and free surface (VOF function) along the structure for the *Test*_08. Red line on the left-panels indicates the numerical dynamic pressure and the black solid line is the measured pressure signal.

5.4.6 Discussion on the uplift pressure and forces

Since the model validation has shown satisfactory results, this section aims to extend laboratory results and provide a deeper understanding of the pressure and force behaviour along the different parts of the structure. In particular, the numerical model provides additional information regarding the pressure distributions underneath the OBREC, where only three transducers were installed during the laboratory tests, as described in Chapter 4 and indicated in Fig. 5.2. These transducers three (pt-6, pt-7 and pt-8) were located respectively on the seaward filter layer, the core and the leeward filter, thus no direct measure of the pressure at any point of the armour layer underneath the structure was carried out.

Chapter 4, aiming to estimate the uplift force exerted on the base, it is assumed a linear pressure distribution between the pressure transducers and a linear extrapolation of the neighbouring measured pressures to define the pressure on the horizontal base wedges where no measures were available. Pressure component acting underneath the ramp was not measured, then the total underneath force under the whole OBREC structure was not computed after the physical model test.

This approach used for the measured uplift pressure is the traditional approach used for traditional crown-walls, which are usually founded on the core. However, due the lack of direct measure on different layers under the OBREC, this approach might lead incertitudes for the estimation of the uplift force, which is extended up to the all seaward slope. Then, the influence of the different layer hydraulic behaviour is of interest to be studied.

To further explore pressure distributions underneath the OBREC, four reference points are considered, as shown in Fig. 5.14. In detail, Point-0 represents the lower edge of the frontal part of the ramp, Point-A indicates the lower edge of the internal part of the ramp, while Point-B and Point-C represent respectively the initial and final edge of the internal horizontal base of the OBREC. Two reference systems are introduced in the sketch for the analysis: the first having the origin at Point-A pointing towards Point-B , while the second has the origin at Point-B and it points towards Point-C . The length of the internal ramp (i.e. the linear distance between the points A and B) is indicated as L_{AB}, while L_{BC} stands for the horizontal base length (i.e. the distance between the points B and C). Computed forces are referred to the force estimated as the average of the highest $1/250^{th}$ peaks of loading in a given random sequence, $F_{1/250}$.

Fig. 5.19 shows the comparison of the numerically computed peak pressure, normalized by the corresponding hydrostatic force, at the Point-0, $p_{0,1/250}/(\rho g H_{1/250})$ with measured data. Please note that the measured pressure values at Point-0 are evaluated by a linear extrapolation between the pt-1 and pt-2 located on the ramp. Results show good agreement, similar to the ones shown in Fig. 5.13 for pt-1, but with larger scatter due to the higher uncertainties involved in the determination of maximum pressure values. Considering the small thickness of the slope plate, the pressure at Point-A is considered to be equal to the one computed at Point-0.

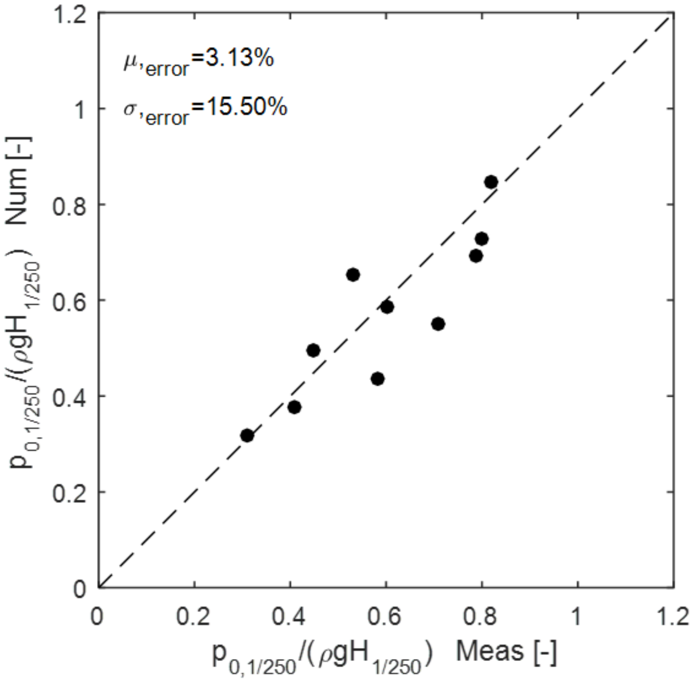

Fig. 5.19 Comparison between numerical and measured data of the dimensionless peak pressure $p_{1/250}$ at the reference point Point-0.

Taking this pressure as a reference, the distribution of the uplift pressure under the ramp and base reservoir is analysed. Fig. 5.20 shows the ratio between $p_{1/250}/p_{A,1/250}$ along the dimensionless values of the internal ramp point (top panel) and the horizontal base (bottom panel) for six tests (*Test*_4 to *Test*_9) in which the still water level coincides or is higher than the OBREC base, i.e. porous media is saturated.

Numerical results of the tests indicated with dash-dotted grey lines, are compared with the dimensionless peak pressure data measured in the laboratory, indicated with blue triangles. Again, the good agreement between numerical and measured data confirms that the model correctly reproduces the damping induced by the porous material. From Fig. 5.20 it is evident that the different layers forming the rubble-mound foundation influence the pressure distribution underneath the OBREC and a large amount of pressure dissipation occurs on the core immediately beneath the obstacle, whose nominal diameter, $D_{n,50}$, is ten times smaller than the one in the armour layer (Table 5.2). The variation of the pressure still can

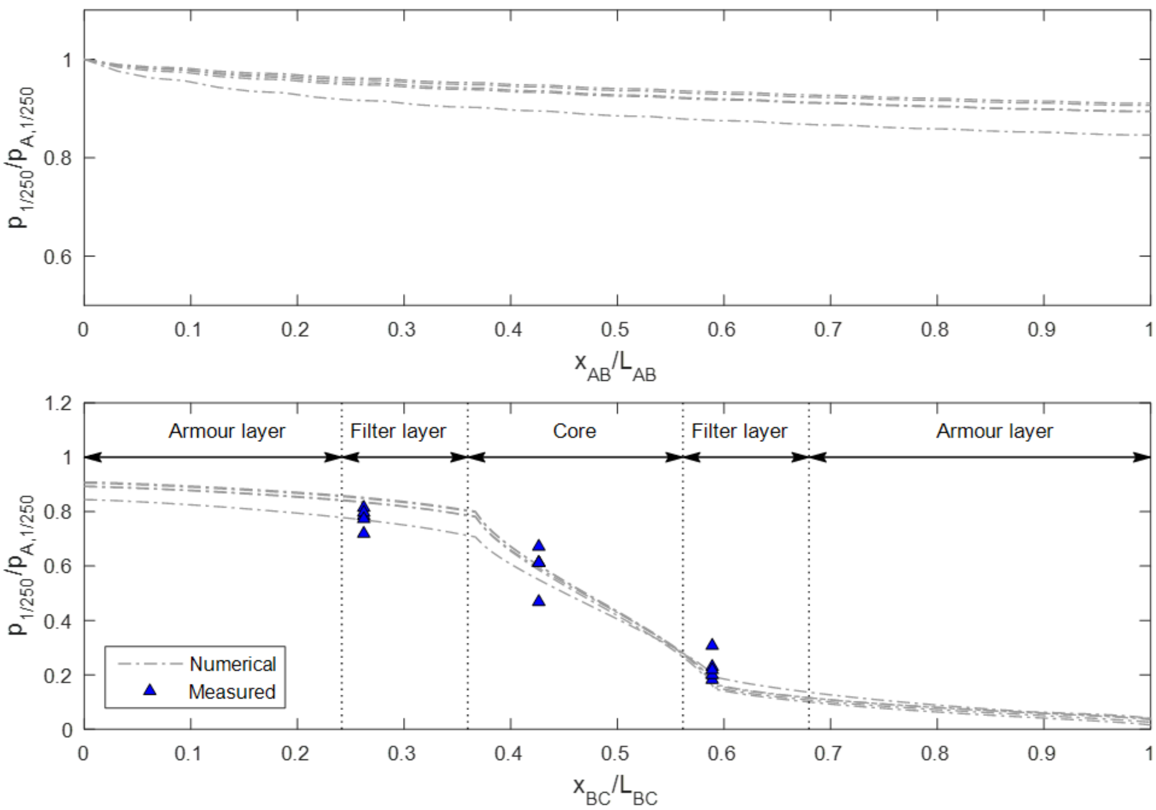

Fig. 5.20 Dimensionless uplift peak pressures along the dimensionless values of the internal ramp point (top panel) and the horizontal base (bottom panel) for test in which the still water level coincides or is higher than the OBREC base (*Test*_4 to *Test*_9). Dotted grey lines indicate the numerical results and the blue triangles are the measured data.

be approximated as linear from the seaward edge of the base reservoir, but with a different pressure damping depending on the permeability (i.e. the porosity and nominal diameter) of the different layers. Please, note also that the pressure peaks on Point-C are almost zero for all the tests analysed.

The measured and numerical dimensionless forces acting on the horizontal base, $F_{1/250,base}$ / $(\rho g H_{1/250} L_{BC})$, are represented in Fig. 5.21 as a function of the relative water depth $h/L_{m,01}$, in which $L_{m,01}$ stands for the deep water wavelength based on the spectral mean period $T_{m,01}$.

Although the comparison of the uplift pressures shown good agreement, the resultant forces computed from the measured signal of three pressure transducers are higher than those calculated with the numerical model by integrating the pressure distributions, with a mean error of 17.62% and a standard deviation error of 9.86%. This overestimation is due to the method used to evaluate the forces from the lab data, which is based on linear extrapolation and then it does not take into account the different pore pressure damping

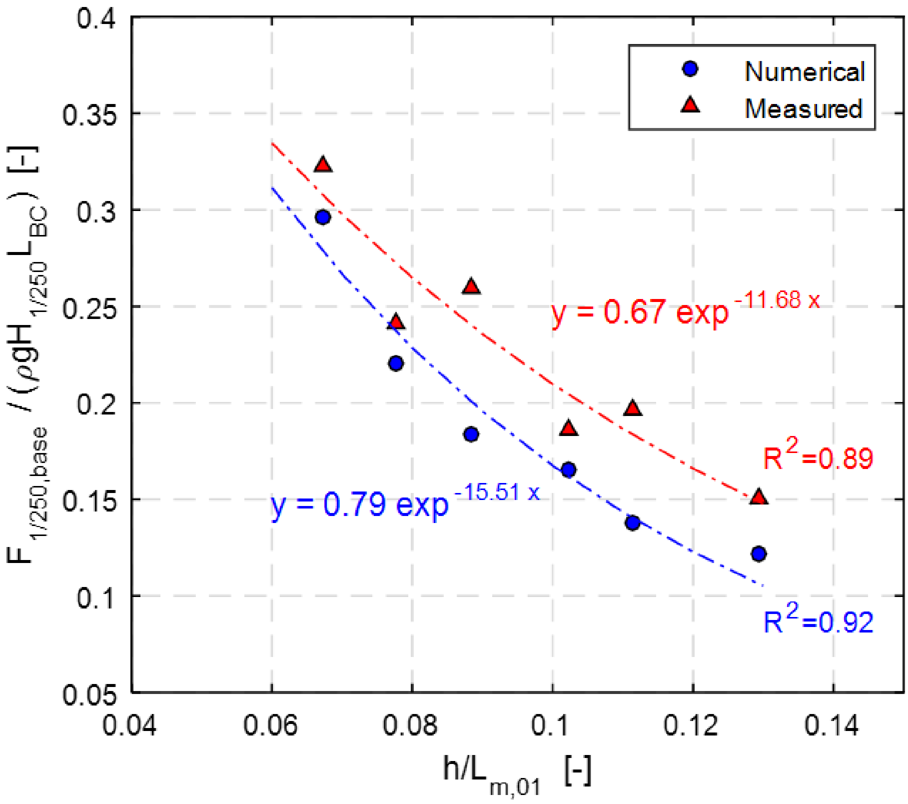

Fig. 5.21 Comparative results of the dimensionless measured and calculated forces acting on the horizontal base as a function of the relative water depth.

produced inside the different layers that conform the rubble-mound foundation. Then, the uplift forces acting on the OBREC calculated numerically, which considers the different porous media characteristics and the continuous pressure distribution, can lead to more accurate results than those computed using the pressure signals measured in the laboratory and using linear extrapolation. The points in Fig. 5.21 fit reasonably well to two exponential laws, whose coefficients are evaluated fitting the data with the non-linear least square method. The values of the correlation coefficient R^2 are also indicated in Fig. 5.21 for numerical (in blue) and measured data set (in red). Despite the limited number of evaluated data, the analysis suggests that the overestimation of the forces computed using the measured pressure increases with the increase of the relative water depth $h/L_{m,01}$.

5.5 Additional numerical simulations

Results of the physical model test campaigns allowed understanding the behaviour of the OBREC structure, as well as providing prediction methods for preliminary design of full-scale prototype. However, some issues still arise, in particular regarding the uplift pressure acting underneath the horizontal base, which is of relevant importance for the stability analysis of the non-conventional OBREC superstructure.

It is known in literature that horizontal elements close to the sea water level can be exposed to large upward vertical forces. Moreover, uplift pressure peaks increase with the decreasing values of the clearance, i.e. the vertical distance between the horizontal element and the SWL. Although it is located on a porous media foundation, a similar hydraulic behaviour on the OBREC base was observed in the first physical model test campaign in 2012 [276]. A ramp with a submerged part, indicated as shaft, was adopted in physical model test in order to evaluate its effect on the overtopping into the frontal reservoir [125]. Although design method is presented in Chapter 4 to provide an estimation of the uplift wave force under the horizontal base, the OBREC ramp tested in laboratory was a fixed structure, thus the direct influence of its submerged part on the total forces and global stability is not evaluated after the laboratory test.

In order to study the effect of the vertical shaft length, d_d, on the force and moment on the OBREC device, additional numerical simulations are carried out and described in this section. The numerical simulations are performed using the numerical set-up previously described in Section 5.2 for the validation analysis. Table 5.3 summarizes the target spectral incident wave characteristics of the generated waves.

In detail, nine wave conditions are generated, with three peak periods for each of the three different significant wave heights. A standard JONSWAP-type spectrum with a peak enhancement factor of 3.3 is considered for all the irregular wave tests. Each test is carried out three times for three different dimensions of the shaft d_d. A case without the submerged ramp ($d_d = 0.0$ m) and two cases with $d_d = 0.10$ m and $d_d = 0.20$ m are considered. The rest of the geometry is kept as in Fig. 5.1. Please, note that for all these additional numerical simulations, the still water level is located at the same level of the reservoir base (i.e., $h = 0.30$ m). This water level represents the most critical condition for the uplift force on the horizontal base, as indicated in Cuomo et al. [66] for horizontal structures and discussed in Chapter 4 for the loading measured on the horizontal OBREC base after the physical model test. For each one of the numerical tests indicated in Table 5.3, the same signal is used for wave generation input, in order to investigate the influence of the shaft length. Bearing this in mind, the

Table 5.3 Incident wave characteristics for the numerical analysis of the draft influence on OBREC stability

	H_{m0} (m)	H_{max} (m)	T_p (s)	h (m)
$Shaft\ test$_01	0.100	0.179	1.64	0.30
$Shaft\ test$_02	0.102	0.186	1.82	0.30
$Shaft\ test$_03	0.100	0.179	2.17	0.30
$Shaft\ test$_04	0.124	0.212	1.60	0.30
$Shaft\ test$_05	0.122	0.219	1.84	0.30
$Shaft\ test$_06	0.122	0.226	2.09	0.30
$Shaft\ test$_07	0.144	0.249	1.72	0.30
$Shaft\ test$_08	0.144	0.256	1.84	0.30
$Shaft\ test$_09	0.144	0.251	2.26	0.30

following results take into account the force exerted on the OBREC due to the maximum wave height in the time series.

5.5.1 Global and local stability analysis

The numerical tests run considering different dimensions of the shaft allows analysing its influence on the global and local stability of the OBREC. The stability criteria analysis presented here is similar to the one traditionally adopted for concrete crown-walls on rubble-mound breakwaters. Then, failures modes can be grouped into those depending on the strength of the superstructure (such as 'breakage') and those depending on the interaction with the underlying foundation (such as sliding and overturning). Fig. 5.22 shows the principal hydraulic failure modes of the OBREC superstructure. On the left side, the two main modes of the global hydraulic failure are drawn: sliding failure between the superstructure and the rubble-mound foundation (a) and overturning failure around the base heel C (b). The local failure modes are displayed on the right, which are the breakage of the reservoir base on $point-2$ (c) and the breakage of the shaft on point-B (d).

Please note that the present study focuses only on hydraulic failure modes, thus geotechnical failures such as the slip failure or erosion of the rubble-mound foundation are not taken into account.

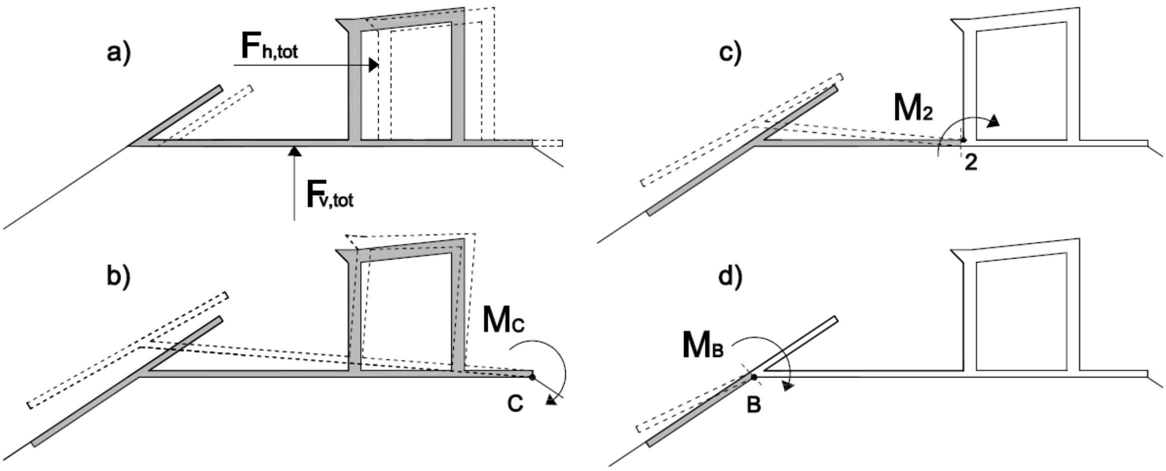

Fig. 5.22 Principal hydraulic failure modes of the OBREC device on a rubble-mound breakwater: a) Sliding failure between the structure and the rubble-mound foundation; b) Overturning failure around the base heel C; c) Breakage of the base plate on point 2; d) Breakage of the shaft on point B.

The stability against the sliding is evaluated by applying the criteria as defined in the Eq.5.5:

$$\mu_f W - (\mu_f F_{v,tot} + F_{h,tot}) \; > \; S_S \tag{5.5}$$

where S_S is the margin of safety for sliding failure, W is the buoyancy-reduced weight of the OBREC superstructure, μ_f is the friction coefficient assumed to be 0.7 in this analysis, $F_{v,tot}$ and $F_{h,tot}$ are respectively the total vertical and horizontal wave-induced force acting on the device. The stability against the overturning is evaluated by applying the following relation:

$$(M_G - M_C) \; > \; S_M \tag{5.6}$$

where S_M is the margin of safety for overturning failure, M_G the stabilizing moment around point-C ue to the mass of the OBREC element and MC is the wave-generated moment around point-C due to the total force acting on the device. Regarding the local structural failures, the wave-generated moment around point-2 and point-B are considered in the present work. The moments M_2 and M_B, positive when clockwise, are the moment due to the dynamic forces acting on the parts of the device considered in these local failures (in grey in Fig. 5.22) on the left of point-2 and point-B, respectively. Contrary to the physical and numerical model tests, for a better understanding of the failure modes, the machine room behind the vertical wall, similar to the real prototype installed in Italy [62], is considered, as shown in the sketches displayed in Fig. 5.22. It is worth underling that the present analysis takes into account only the force generated by the waves exerted on the structure, thus not considering the weight of the device. This is due to the geometrical differences that can be found between the OBREC device tested here, that fits the one tested in laboratory, and the real one, e.g. the small thickness of the different parts tested in the lab.

The goal is to analyse the influence of the shaft for the critical conditions in terms of failure modes for different wave conditions. Consequently, the hydraulic failures modes are analysed considering only the destabilizing forces and moments: $F_S = \mu_f \cdot F_{v,tot} + F_{h,tot}$ for sliding, M_C for the overturning around the base heel and M_2 and M_B for the two local failure modes.

Fig. 5.23 shows, on the left side, the time series of the destabilizing force F_S and moments M_C, M_2 and M_B for the test *Shaft test*_02 with $d_d = 0.10$ m when the highest wave interacts with the OBREC superstructure. Dotted red lines with circles indicate the instants of the four maximum destabilizing terms. The dynamic pressure distribution along the device at the four instants is plotted on the right side. The figure clearly shows that the critical conditions for global stability, i.e. sliding and overturning, occur at different instants. The maximum value of F_S occurs when the wave reaches the vertical wall ($t = 10.41$ s). Fig. 5.23a shows a double-peak behaviour of the destabilizing forces F_S. A first peak occurs when the waves run up the ramp crest, while the second and larger peak can be seen when the waves impinge on the wall. At this latter instant, the force acting on the wall is maximum, while those acting on the frontal ramp and underneath the structure have values lower than their peak values, as previously discussed and shown in Fig. 5.17. Regarding the overturning moment M_C around the base heel (Fig. 5.23b), the critical condition occurs when the waves is rising along the frontal ramp ($t = 10.00$ s). At this instant, the force underneath the device is maximum and the vertical wall is still unloaded, as can be observed in Fig. 5.23f. The two critical conditions for global stability are therefore not simultaneous, considering that the overturning moment M_C has very low values at the time of maximum F_S, due to the positive stabilizing contribution of the vertical forces acting on the ramp. The instant $t = 10.00$ s represents also the instant with the maximum values of the overturning moment M_2 around the point-2 (Fig. 5.23c). Finally, the maximum positive moment around point-B on the shaft occurs during the run-down, $t = 9.91$ s, when the frontal ramp is unloaded (Fig. 5.23-h), thus only the pore pressure component acting under the shaft contributes to the maximum positive moment on point-B.

The analysis shows that the critical conditions for the OBREC global failure modes occur at different time instants, i.e. the critical forces acting on the device are different for the different failure modes. This is a relevant difference compared to the traditional crown-wall breakwaters, where the peak values of the destabilizing forces for sliding, and the overturning moment around the heel structure occur always simultaneously [212].

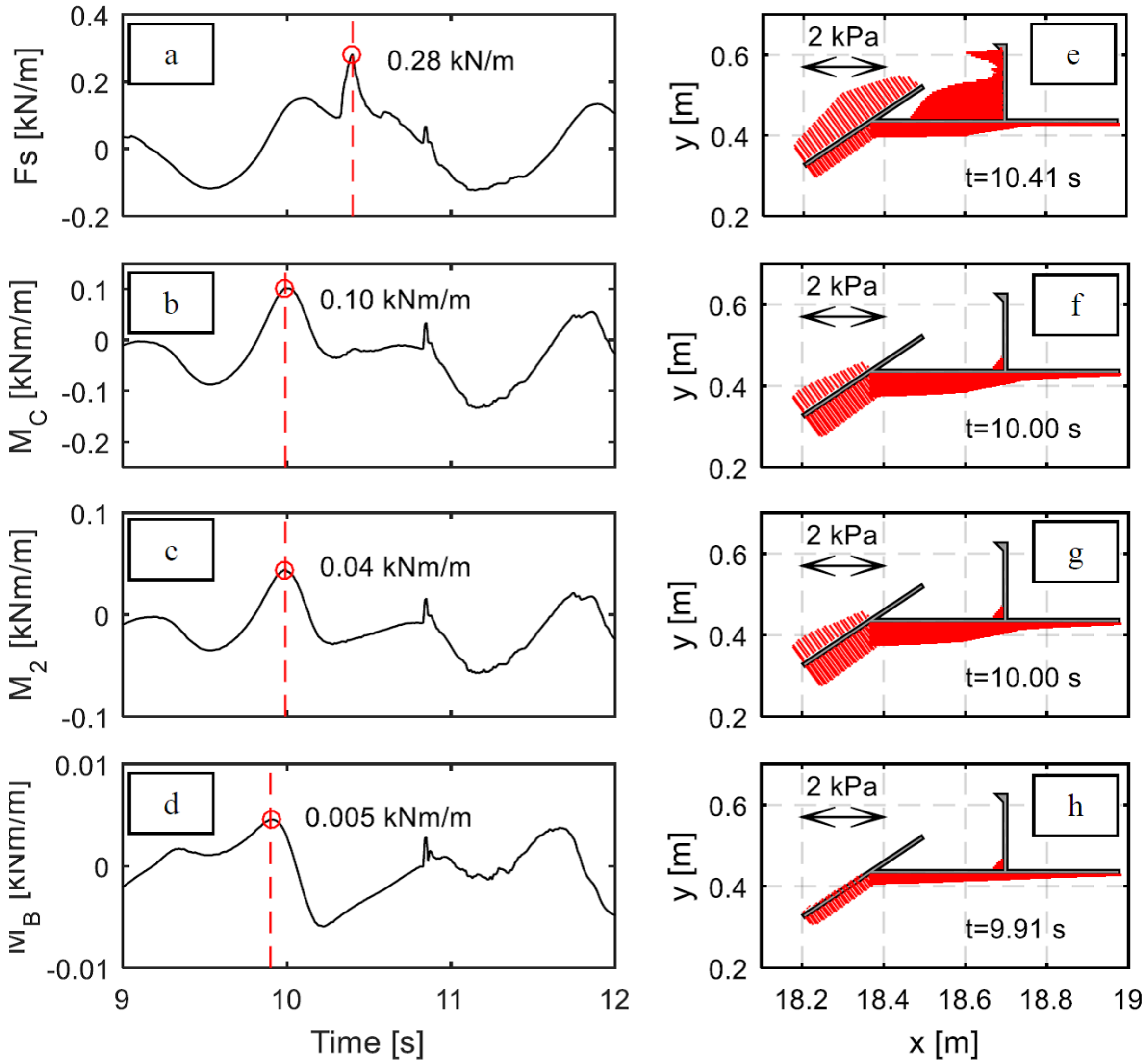

Fig. 5.23 On the left side, the destabilizing force F_S and moments M_C, M_2 and M_B for the test *Shaft test*_02 with $d_d = 0.10$ m. On the right side, the dynamic pressure distribution along the device at the instants of the maximum destabilizing forces and momentum.

5.5.2 Analysis of the submerged ramp

5.5.2.1 Influence of the shaft on F_{base}

The present section describes the influence of the shaft on the vertical force acting on the horizontal base F_{base}. Fig. 5.24 shows the maximum force acting on the OBREC base with the shaft, $F_{base,draft}$, and without the shaft, $F_{base,no-draft}$, as function of H_{m0}/h.

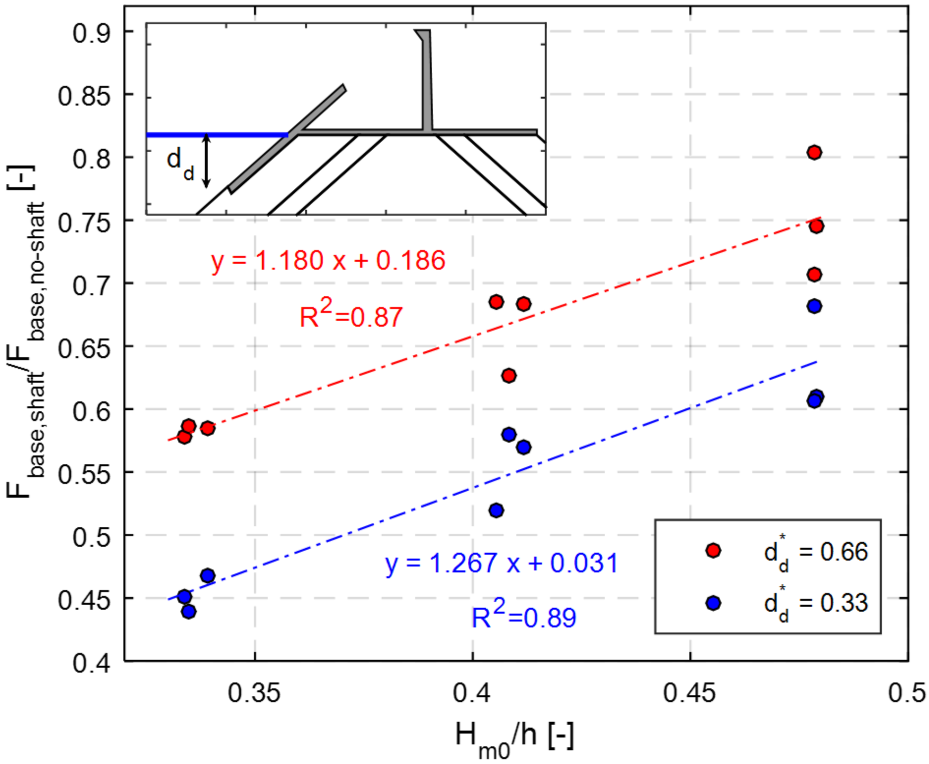

Fig. 5.24 Influence of the dimensionless parameter H_{m0}/h on the ratio between the maximum force acting on the horizontal base of the OBREC with the shaft, $F_{base,draft}$, and without the draft, $F_{base,no-draft}$.

A dimensionless parameter that considers the relative shaft length is defined as $d_d^* = (h - d_d)/h$, being $d_d^* = 1$ the case without the shaft. The red points indicate the cases with small shaft length (i.e. $d_d^* = 0.66$), while the blue points represent the results for the large shaft length ($d_d^* = 0.33$). Fig. 5.24 clearly evidences the importance of the submerged ramp on the reduction of the F_{base}, considering that the ratio $F_{base,shaft}/F_{base,no-shaft}$ is lower than the unit for all the numerical tests. Furthermore, the vertical force on the horizontal base reduces accordingly to the increase of the shaft length. It can also be seen that this reduction decreases with the increasing of the ratio H_{m0}/h. For large shaft length ($d_d^* = 0.33$) and small wave height (H_{m0}/h =0.33), the maximum force on the OBREC base can be less than the half of the force acting on the configuration without the submerged ramp. Conversely, the influence of the shaft is slightly reduced for relative high waves and small shaft, with a reduction of the upward force due to the presence of the shaft of only 20%. The points fit well into two linear laws, as can be observed in Fig. 5.24, where associated empirical coefficients are displayed, together with the corresponding correlation coefficients R^2.

Fig. 5.25 is divided into three panels for each of the three significant wave heights considered in this investigation. Each panel contains the dimensionless maximum vertical force on the horizontal base, $F_{base}/(\rho g H_{m0} L_{BC})$, as a function of d_d^* for different peak periods, T_p. For all the three panels, the higher forces can be noted for dd*=1.0, while the dimensionless force decreases for larger shaft length for all the tests. Regarding the influence of the peak period T_p, for the test with $H_{m0} = 0.14$ m (bottom panel in Fig. 5.25), the uplift force on the base increases with the increase of T_p. For smaller significant wave heights, the tendency is slightly different and the highest forces are obtained for the peak period $T_p = 1.8$ s. These differences might be addressed considering that the analysis has been carried out taking into account the force due to the H_{max} in the time series, thus the forces strongly depend on the period of a single wave more than the spectral peak period of the generated time series. The numerical simulation confirms that the shaft is not only increasing the overtopping rate into the frontal reservoir, as described by Iuppa [125], but also it significantly reduces the vertical forces exerted on the OBREC base.

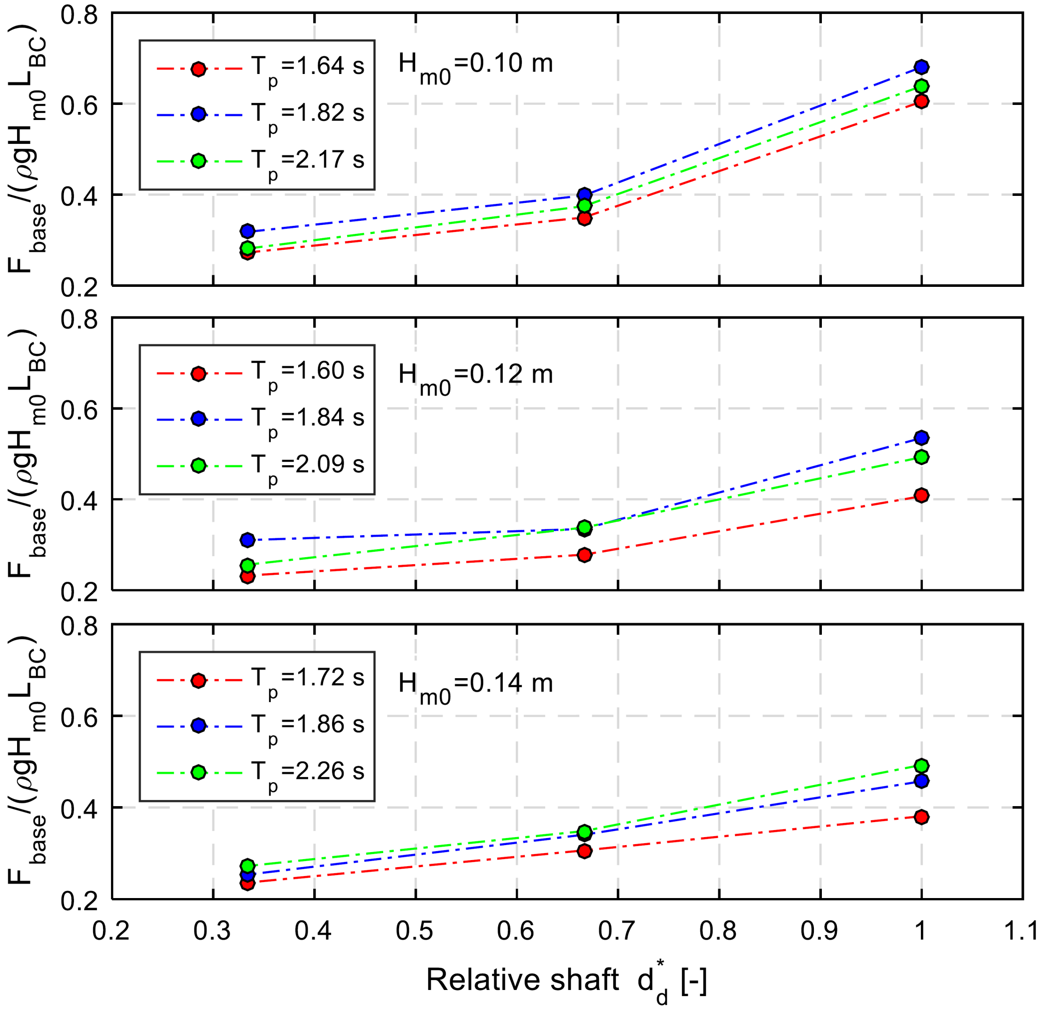

Fig. 5.25 Dimensionless maximum vertical forces on the base,$F_base/(\rho g H_{m0} L_{BC})$, function of the d_d^* for different peak periods, T_p, and significant wave height, H_{m0}.

5.5.2.2 Influence of the shaft on the stability analysis

The presence of the submerged ramp has consequences on the global stability of the entire superstructure. In order to analyse this, the maximum values of the destabilizing forces, F_S and moments M_C and M_2 for the three shaft geometries are here compared. Top panel in Fig. 5.26 shows the maximum destabilizing force Fs on the OBREC with the shaft, FS,shaft, divided by the one without the shaft, FS,no-shaft, as function of Hm0/h.

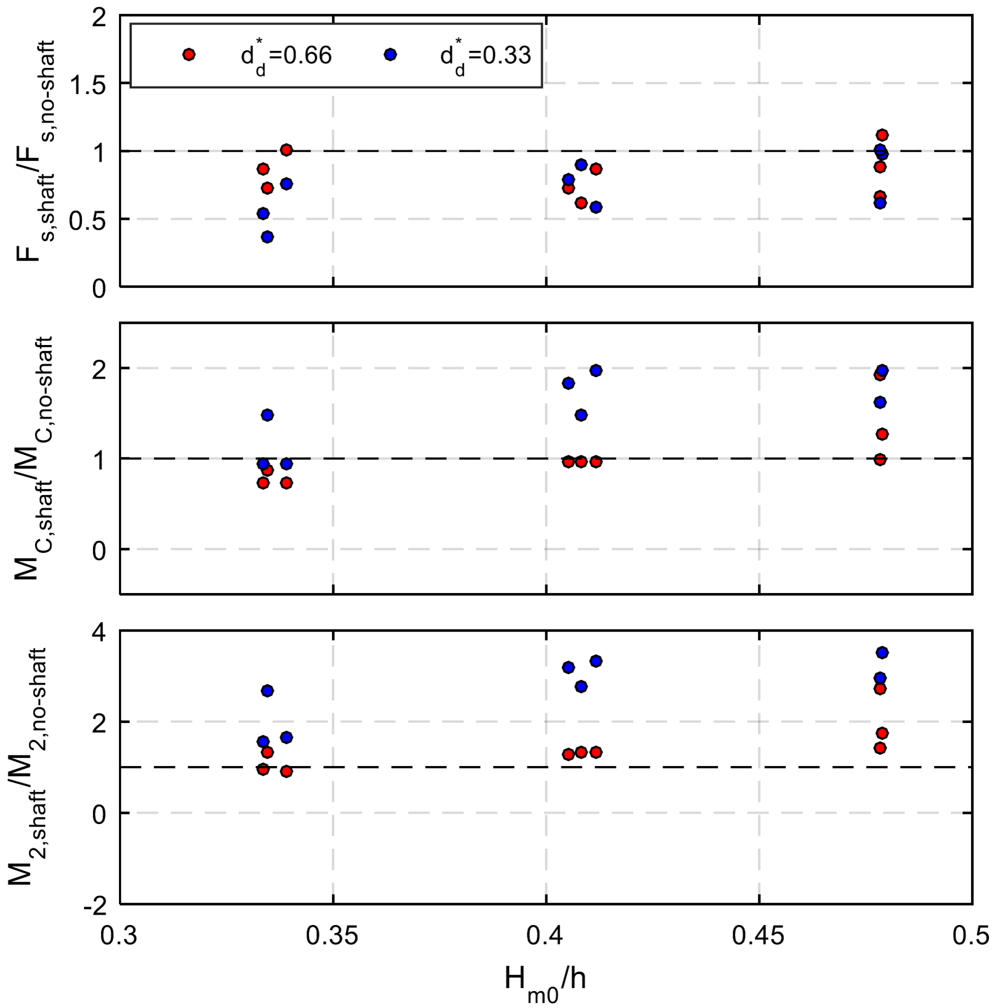

Fig. 5.26 Influence of the H_{m0}/h on the ratio between the maximum destabilizing force F_S (top panel), moments M_C (middle panel) and M_2 (bottom panel) on the OBREC with and without the shaft.

For almost all the numerical test, $F_{S,shaft}$ is smaller than $F_{S,no-shaft}$, confirming the positive contribution of the shaft also on the stability of the device against the sliding. In particular, the results show a higher reduction of F_S for lower wave height and larger shaft ($d_d^* = 0.33$), while the difference in terms of maximum FS between the two shaft configurations become less evident for higher significant wave height. The middle panel in Fig. 5.26 shows the influence of H_{m0}/h on the ratio between the maximum moments M_C on the OBREC hell with and without the shaft. Contrary to the results displayed in the top panel, the results indicate a negative influence of the shaft for this hydraulic failure mode. In particular, higher values of the overturning moment M_C can be seen for the configuration with the highest shaft ($d_d^* = 0.33$).

The ratio $M_{C,shaft}/M_{C,no-shaft}$ increases with the increase of the significant wave height, reaching values up to 2. This negative effect of the shaft in the maximum clockwise moment around point-C is due to the uplift force underneath the shaft when the waves start to rise the frontal ramp, whose lever arm respect to the point-C increase with the increase of the shaft. Similar results can be noted for the moment M_2, with values of the ration $M_{2,shaft}/M_{2,no-shaft}$ around 3 for high values of H_{m0}/h and $d_d^* = 0.33$.

Bearing in mind that the sliding represents the most typical critical failure for traditional crown-wall breakwater [212], further details on the influence of the shaft on the total destabilizing force for sliding failure are shown in Fig. 5.27.

This figure indicates the time series for $F_{h,total}$, $F_{v,total}$ and F_S for the three values of d_d^* for test $Shaft\ test$_01, when the highest wave approaches to the structure. On the lower panel, it can be see that, for the same incident wave height, the maximum value of F_S decreases with the increase of the shaft dimension, as discussed previously and shown on top panel of Fig. 5.26. Please note that the maximum values of F_S appear at the second peak of the $F_{h,total}$ time series, i.e. when the highest wave reaches the vertical OBREC wall. Although at this instant the configuration with the largest shaft has the highest values of $F_{h,total}$ (top panel), the vertical component of the total force, $F_{v,total}$, (middle panel) is strongly influenced by the presence and geometry of the shaft. In particular, at the instant of F_S maximum, the $F_{v,total}$ peak value decreases with the increase of the shaft until reaching negative values for $d_d^* = 0.33$. Therefore, $F_{v,total}$ is acting downward for large shaft, contributing to stabilize the OBREC superstructure against the sliding failure mode.

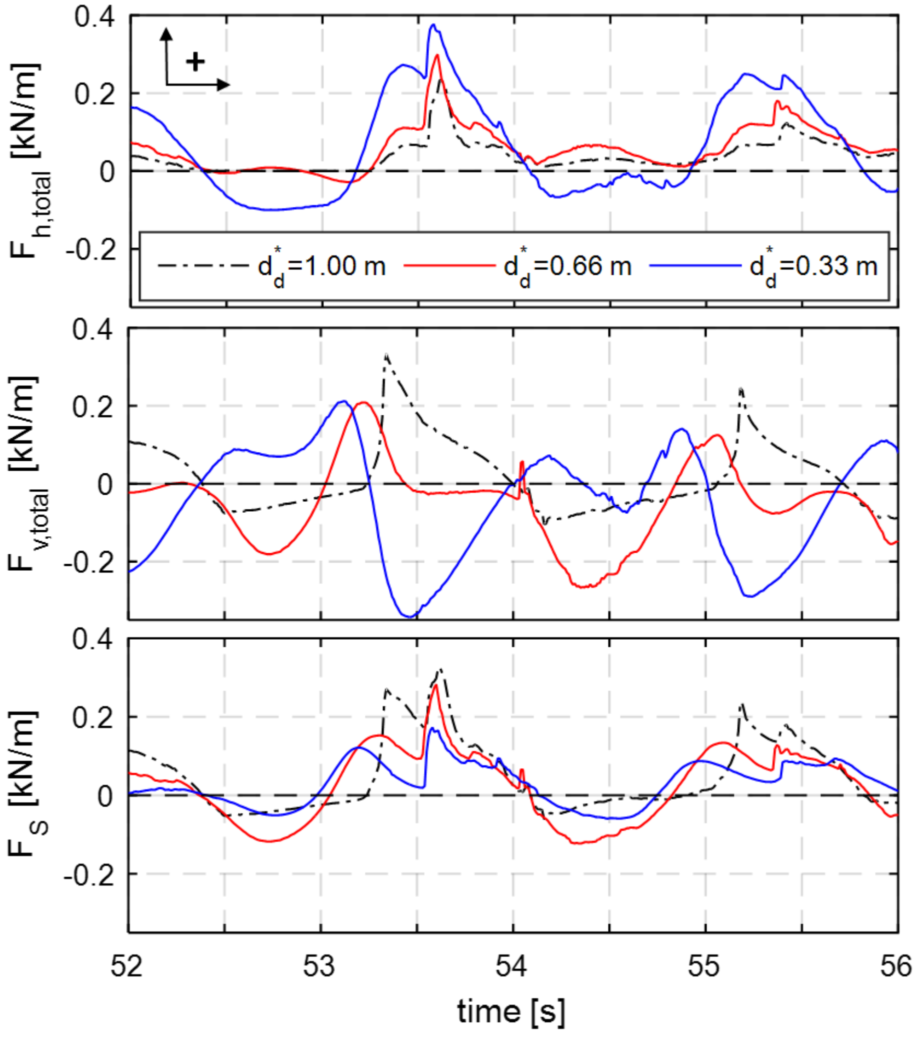

Fig. 5.27 Time series of $F_{h,total}$, $F_{v,total}$ and F_S for the three values of d_d^* for the $Shaft\ test$_01.

5.5.2.3 Local stability of the shaft

It is clear that the local stability of the non-conventional geometry of the shaft has a relevant importance on the OBREC design. In this regard, the numerical model allows evaluating the time series evolution of the moment around the point-B for each test. The results show that the total moment due to the dynamic forces on the shaft can be both positive (clockwise moment) and negative (counterclockwise moment) depending on the time instant. Fig. 5.28 shows an example of the dimensionless moment time series around point-B, $M_B/[\rho gh(d_d/\sin\alpha)^2]$, due to the dynamic force acting on the frontal ramp under the SWL (dotted blue line) and underneath the ramp (dotted red line) for the test $Shaft\ test$_5 with $dd = 0.10$ m.

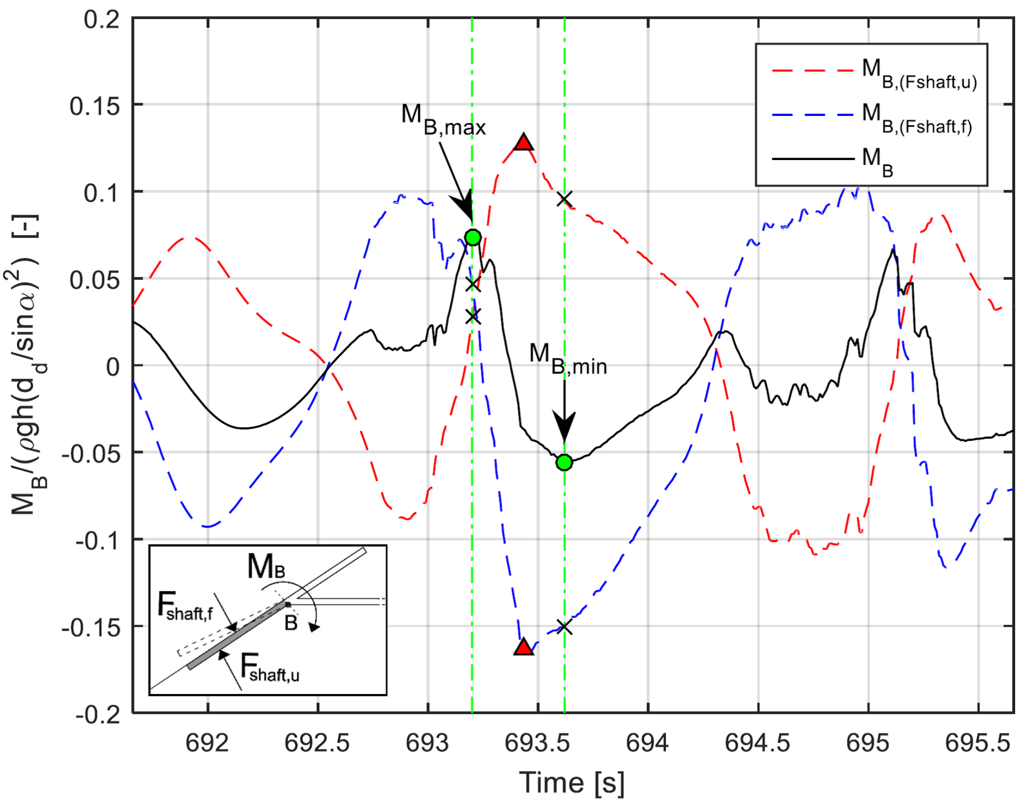

Fig. 5.28 Time series of dimensionless moment around the Point-B due to the dynamic force acting the frontal ramp under the SWL, (dotted blue line) and underneath the ramp (dotted red line) for the $Shaft\ test$_05 with $d_d = 0.10$ m. The continuous black line indicates the total dimensionless moment, computed as the sum of the two components.

The total dimensionless moment, calculated as the sum of the two components, is displayed with a continuous black line. Two green circles specify the maximum and minimum total dimensionless moment around the point-B. When the maximum force is acting on the ramp, the negative moment due to the force on the frontal part of the shaft, $M_{B,(Fshaft,f)}$, and the positive moment due to the force underneath the shaft,$M_{B,(Fshaft,f)}$, reach their peak values, indicated with red triangles in Fig. 5.28.

Since the two opposite moment peaks occur simultaneously, max and min. total moments occur at different instants. Fig. 5.28 shows the instant of the minimum, $M_{B,min}$, and the maximum dimensionless moment around the point-B, $M_{B,max}$. When $M_{B,max}$ is registered, both the moments due to the dynamic force on the frontal shaft and underneath have positive values. Clockwise moment at point-B is produced mainly due to the time lag between the run-up and run-down of the waves on the smooth ramp and the water oscillation in the porous media underneath the shaft. It is worth underling that the peak of the clockwise total moment is in magnitude higher than the maximum negative total moment. The same behavior occurs for all the tests analyzed here, with an average value of $|M_{B,max}/M_{B,min}|$ around 1.4. Moreover, contrary to the negative moment that always occurs when the highest wave impinges the OBREC ramp, maximum positive moment can occur also for waves smaller than H_{max}.

Finally, Fig. 5.29 shows the dimensionless maximum total moment around point-B due to the dynamic force acting on the shaft, $M_{B,max}/[\rho gh(d_d/\sin\alpha)^2]$, as a function of H_{m0}/h. Although a relative high scatter is observed, $M_{B,max}$ increases with the increase of both the significant wave height and the linear dimension of the shaft $d_d/\sin\alpha$. The results fit a linear law, whose fitting empirical coefficients are displayed in ig. 5.29 with $R^2 = 0.74$.

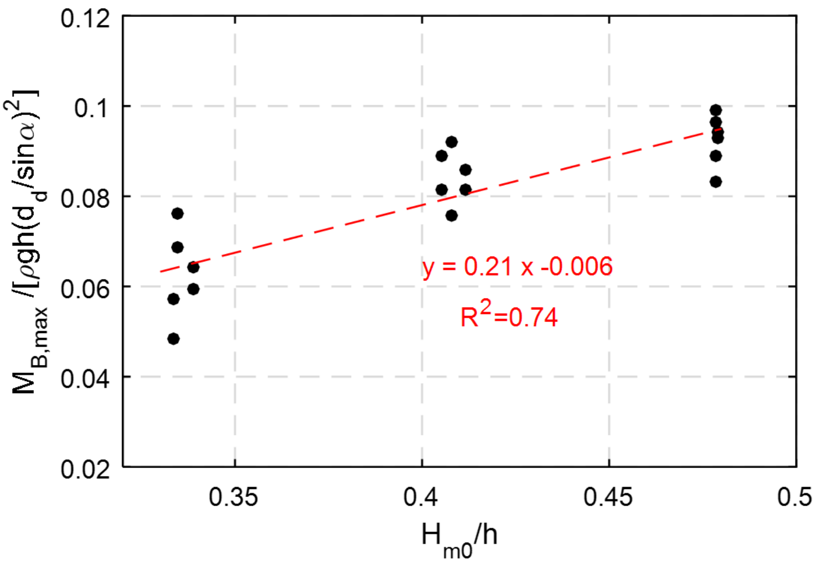

Fig. 5.29 Dimensionless maximum total moment around Point-B due to the dynamic force acting the shaft as a function of H_{m0}/h.

5.6 Conclusions

This chapter describes the results obtained with the use of an advanced numerical model (IH2VOF) to evaluate the interaction between irregular waves and the OBREC device, following the approach known in literature as *'Composite modelling'*.

IH2VOF has been extensively validated matching the results with the experimental data from the laboratory tests described in Chapter 4. The validation process was based on the comparison of the free surface elevation in front of the structure and the wave loading between the measured and numerical signals. The statistical and spectral parameters of the free surface elevation showed that the model very well simulates the energy evolution along the wave flume as well as the interaction of the waves with the device and the porous media foundation. Moreover, the wave pressure peaks calculated at the sloping ramp and base reservoir were highly satisfactory, while a slight overestimation of the loading at the vertical wall was observed. The overall validation process also included a visual comparison wave-by-wave in the time domain of the free surface elevation in front of the device, the pressure exerted on the 14 gauges located along the model and the computed resultant forces, with overall good results.

The analysis has shown how the use of IH2VOF can overcome some limitations of the physical model tests, which do not fully represent the wave-structure interaction process. In this regard, the numerical model provided a deeper understanding on the pressure behaviour along the different parts of the structure, in particular in locations where the measurement was not available. Indeed, the use of the numerical model allowed to analyse the overall horizontal and vertical force acting on the OBREC, including the components under the ramp where no direct measurements were provided in the laboratory.

Results demonstrated that the maximum vertical and horizontal forces for each single incident wave were not simultaneous, which indicate a significant positive aspect regarding the global stability of the device. The analysis showed that the numerical uplift forces at the OBREC base, which considers the different porous media characteristics and the continuous pressure distribution, were more accurate than those measured in the laboratory. The analysis revealed an overestimation of the resultant uplift forces on the OBREC base, computed from the pressure signals measured in the laboratory, of about 17%, mainly due to the limited information of pressure acting underneath the structure.

Finally, additional numerical simulations on OBREC geometries not tested in the laboratory were carried out in this study. The analysis aimed at investigating the influence of the submerged ramp length on the reduction of the uplift force at the horizontal base and its effects on the global and local stability of the superstructure. Results confirmed the importance to extend the ramp under the SWL. The presence of this peculiar geometry has a positive effect due to the significant reduction of the upward forces exerted at the OBREC base.

Finally, the stability against sliding and overturning, as well as the local failures, were evaluated comparing three different shaft dimensions. The analysis showed that the critical conditions for the OBREC global failure modes occurred at different time instants, i.e. the critical forces acting on the device were different for the different failure modes. Results have shown a positive effect of the shaft due to the increase of the global stability against the sliding failure mode, which represents the most typical critical failure for superstructures on rubble-mound breakwater [212].

Chapter 6

The OBREC prototype in Italy

6.1 Introduction

Laboratory modelling, where structures are tested at a small scale, is the most accepted standard for breakwater design. However, the use of laboratory models is not always sufficient to obtain an accurate structural response of complex maritime structures, due to the scale effects. Regarding the wave loading exerted on small-scale models, the problem of the scale effects is an intriguing subject and, for some aspects, still under debate. It is well-known that these effects are almost negligible for quasi-static loads, so the Froude scale is widely accepted in order to reproduce loading on structures at prototype scale. Conversely, during violent wave impacts of very short duration, the compressibility of the air pocket can strongly influence the magnitude of the generated pressure, thus they cannot simply be scaled by Froude. Indeed, it is commonly believed that application of the Froude scaling law can cause a significant overestimation of the impact pressures at prototype scale, as argued by many Authors [47, 65, 6].

Due to these aspects, field tests on prototype would help to understand the wave-structure interaction better, particularly for coastal structures with a non-conventional geometry. However, on the other hand, field tests on coastal structures at full-scale are very expensive, difficult to carry out in high energy environments, and those who were performed are few and of short duration. The boundary conditions cannot be manipulated and the test cannot be repeated, thus the data contains a very large amount of uncertainties [135]. These reasons explain why the field test on breakwaters are infrequent in coastal engineering.

Regarding the development of WEC devices, the necessity of prototypes tested in the field is of utmost importance in order to demonstrate their feasibility and structural functionality, especially against extreme wave conditions. These tests aim at obtaining a complete knowledge of the wave-structure interaction and structural response of a device, without the problem of scale effects. Please note that the construction of a prototype WEC device at full-scale is a relevant step for their development and necessary to demonstrate also its performance in terms of energy production. Indeed, the overall efficiency of the WEC device cannot be evaluated with small scale models, while the use of the existing numerical modelling offers only a very rough estimation of the energy production.

Due to these reasons and considering the non-conventional shape of the OBREC device integrated into a rubble-mound breakwater, research on prototype at full-scale tested in a real environment is essential for its development. A full-scale device has been installed at the port of Naples in Italy (see Fig. 6.1) at the end of 2015. This prototype represents the world's first OverTopping Device integrated into an existing coastal defence structure. The monitoring of the device in Naples is aimed at investigating the performance of the device, providing detailed validation of laboratory measurements in order to identify the scale effects and to ensure more reliable design methods. It is important to underline that the stability analysis of this prototype was based on the results of experimental tests conducted on small-scale models (see Chapter 4), as well as on the large experience of the OBREC's developers concerning the design of non-conventional breakwaters.

This chapter provides detailed information on the prototype and the ongoing field monitoring activity. It should be pointed out that the data of only a few extreme storms have been collected, and that the complete analysis of the monitoring is clearly out of the scope of the present research. The main goal of the field tests in Naples is to acquire data during the winter storm events, using the pilot plant as a large-scale device monitored in a real environment, in which the data are collected and analysed for further applications of the OBREC installation on more energetic and exposed coastal areas.

6.2 Prototype design

The full-scale prototype has been designed on the base of hydraulic and structural performance evaluated with the two complementary laboratory campaigns: the first one conducted in 2012 and described by Vicinanza et al. [276], and the second one carried out in 2014, whose results are described in Chapter 4.

Regarding the hydraulic performance of the prototype, the reflection coefficient and the mean overtopping discharge for wave conditions with different return periods have been

Fig. 6.1 Lateral view of the OBREC device in Italy.

estimated considering the laboratory results and the semi-empirical formulas proposed by Vicinanza et al. [276] and Iuppa et al. [126]. Please note that the freeboard of the prototype (i.e. the vertical distance between the higher point of the machine room and the still water level) was designed to be equal to the crest of the existing breakwater in Naples, which is 4.70 m. Due to the integration of the OBREC prototype into an existing breakwater, this choice was considered the best option to reduce the environmental and visual impact of the prototype, ensuring, at the same time, performance in terms of overtopping and reflection similar to the ones estimated on the adjacent rubble-mound breakwater. Please consider that the field monitoring tests are aimed at providing more details of these hydraulic performance, with the direct measurement and evaluation of the difference between the innovative and the traditional breakwaters.

Concerning the structural functionality of the prototype, the global and local stability analysis has been evaluated, during the preliminary design, considering the results of the maximum wave pressure exerted on the different parts of the small-scale model with flat ramp tested in laboratory. In detail, the semi-empirical formulas proposed in Chapter 4 for the estimation of the resultant forces exerted on the OBREC have been used for its design in prototype scale. Different case scenarios have been considered for the stability analysis, adopting the methodology described in Section 4.3.5, and schematized in Table 4.3. The structure has been designed considering the wave condition at the toe of the device ($H_{m0,50}$ = 6.70 m and $T_{p,50}$ = 12 s) having a return period of 50 years.

6.3 Selecting of the site

6.3.1 Energetic source

The full-scale OBREC has been installed in 2015, integrated into the San Vincenzo rubble-mound breakwater in Italy. It is installed in a region characterized by a mean yearly wave power of ≈ 3.51 kW/m as evaluated by [157]. The authors calculated the energy resources through numerical simulations performed on the entire Mediterranean basin for the period 2001-2010 using a third generation ocean wave model (WAM wave model [104]) forced with six-hourly wind field obtained from European Centre for Medium-Range Weather Forecast (ECMWF). The model results are extensively validated against most of the available wave buoy and satellite altimeter data. Fig. 6.2 shows the energetic flux on the entire domain evaluated in the analysis.

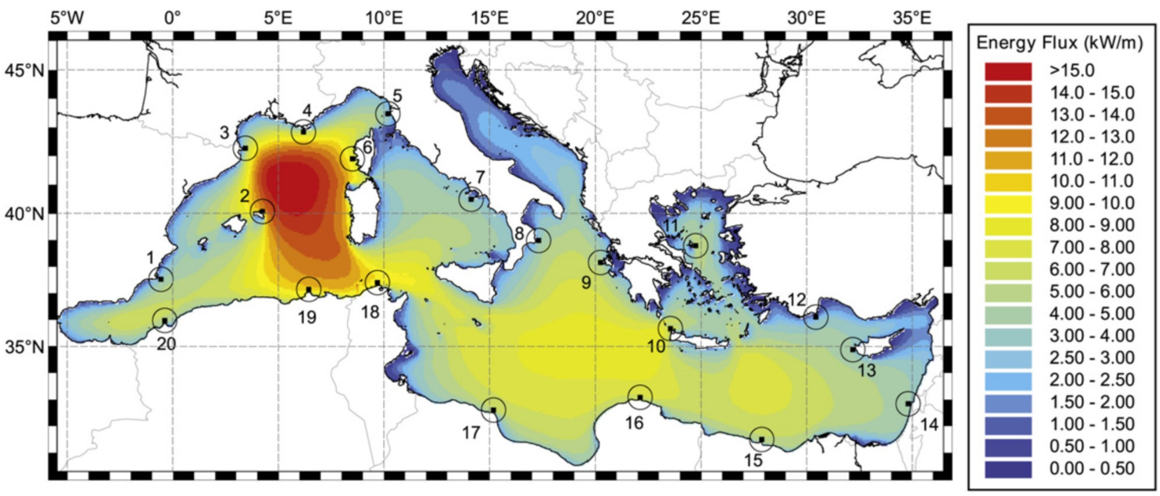

Fig. 6.2 Average power in the Mediterranean between 2001 and 2010 (source [157]).

It is important to point out that for future estimation of the OBREC efficiency and energy production, it becomes imperative to have a more accurate and complete wave energy assessment of the interested area in front of the structure. Therefore, further studies with numerical models calibrated with wave measured data are required to identify more accurately the wave energy resource in this area.

Taking into account the analysis carried out by Liberti et al. [157], the mean wave power is rather low if compared to the 11 kW/m on the north-west of Sardinia (Italy) [273, 275] or, even more, if compared to the 60-70 kW/m on the Atlantic European coasts [184, 103]. The southern region of the Tyrrhenian Sea and, even more, the Gulf of Naples are characterized by a significant seasonal variability, with storm season during the winter (December-March) and long periods of calm (i.e. when the significant wave height of the sea state is lower than 0.50 m) in the summer.

Despite what one may think, these aspects can be considered positive for this stage of development, allowing to safely operate during the maintenance activities and the installation of the instrumental equipment for the monitoring of the prototype. On the other hand, being the structure placed on intermediate depth, no depth breaking conditions occur, not even for extreme storms. As a consequence, the pilot is exposed to important environmental conditions if compared to other hybrid WECs located in shallow water. The real challenge of the OBREC monitoring is then to demonstrate the feasibility, structural reliability and to evaluate the overall performance, particularly during the relevant storm conditions.

6.3.2 Description of the existing breakwater

The port of Naples in Italy is protected by two main breakwaters: one detached almost parallel to the coast, the Duca d'Aosta breakwater, and a second breakwater in the western area of the port, the San Vincenzo breakwater [82, 28]. The area chosen to locate the OBREC prototype is in the middle of the San Vincenzo breakwater. An overall plan view of the location of the OBREC is shown in Fig. 6.3.

The San Vincenzo breakwater is a conventional rubble-mound breakwater with a length of about 1475 m. The armour layer for the first 1150 m is made of grooved concrete cubes with holes (antifers) of 2 m long and weighting 12 tons, while the armour layer in the last 325 m of the breakwater consists of tetrapods. The breakwater core consists of quarry run (5 to 50 Kg) while the filter layer is composed of rock (50 kg to 1 ton). An access road at the rear side of the structure allows the access along the breakwater and it has a width of 14.80 m. The design crest level of the armour layer crest is 4.50 m above the mean water level (MWL) while the access road is +2.50 m above MWL. The actual slope of the armor layer at the mean water level is around 1:2. The bathymetric chart of the port of Naples indicates that the layout of the San Vincenzo breakwater is almost perpendicular to the isobaths, with depths of 18 m near the coast until reaching 35 m at the end of the breakwater. The depth at

Fig. 6.3 Position of the OBREC prototype at the port of Naples in Italy.

the toe of the breakwater where the OBREC is installed is 25 m and the mean annual tidal range at the specific site is about 60 cm.

6.4 Geometry of the device

The OBREC has been installed along 6 meters of the San Vincenzo breakwater, substituting a part of the armour layer for a total area of $75\ m^2$. The prototype is placed almost in the middle of the San Vincenzo breakwater, in front of an existing building which is currently used as a laboratory hub for scientists and researchers for the field monitoring activities during storms. Fig. 6.4 shows the lateral and frontal view of the OBREC. This prototype consists of two adjacent geometrical configurations denominated RS-Lab (Real Scale Laboratory) and NW-Lab (Natural Waves Laboratory). RS-Lab and NW-Lab configurations are located respectively on the left and right side of the pilot, as shown in Fig. 6.4. The two configurations are similar, except for the crest freeboard of the frontal ramp, that measure values are for the RS-Lab and the NW-Lab respectively 1.70 m and 1.00 m (Fig. 6.5). The other relevant modification between the RS-Lab and NW-Lab configuration is the horizontal reservoir width, which measures respectively 2.5 m (RS-Lab) and 3.7 m (NW-Lab). The intention is to improve the overall knowledge of the wave-OBREC interaction. The RC-Lab configuration represents the best configuration for the low energetic site condition, while the NW-Lab is considered a large-scale model, which is more suitable for higher energetic coastal regions [63, 61, 71].

Fig. 6.4 Cross sections of the two adjacent configurations of the OBREC at the port of Naples.

The prototype consists of a frontal planar ramp with a submerged part at an angle of 78° and an emerged part with a slope of 22°. The average value of the two slopes is similar to the one of the existing breakwater in Naples. In order to facilitate the construction operations, the ramp consists of 3 pre-cast concrete structures with a thickness of 20 cm. They are located adjacent to each other and connected to the base reservoirs located behind them. Contrary to the frontal ramp, the two reservoirs consist of a concrete slab foundation cast in situ and anchored to the ground by micropiles. It is necessary to say that this ground anchoring system can be considered reasonable considering that the OBREC installed in Naples is a pilot used for field monitoring. Although highly pricing, this foundation system increases the overall stability of the structure, ensuring a higher safety factor of the OBREC stability even during storm conditions with high return periods.

Three vertical walls, with a thickness of 40 cm, separate and define the sideways of the two reservoirs. These walls have the same inclination as the frontal ramp. As shown in Fig. 6.5, the reservoir of the RS-Lab configuration is 2.5 m x 2.4 m, while its internal depth is 0.4 cm. The reservoir of the NW-Lab configuration is 3.7 m x 2.4 m, with an internal depth of 0.3 m. At the rear side of the two reservoirs, a machine room (6.0 m x 3.4 m) with an internal area of 11.4 m^2 has also been constructed in situ. The crest of the seaward part

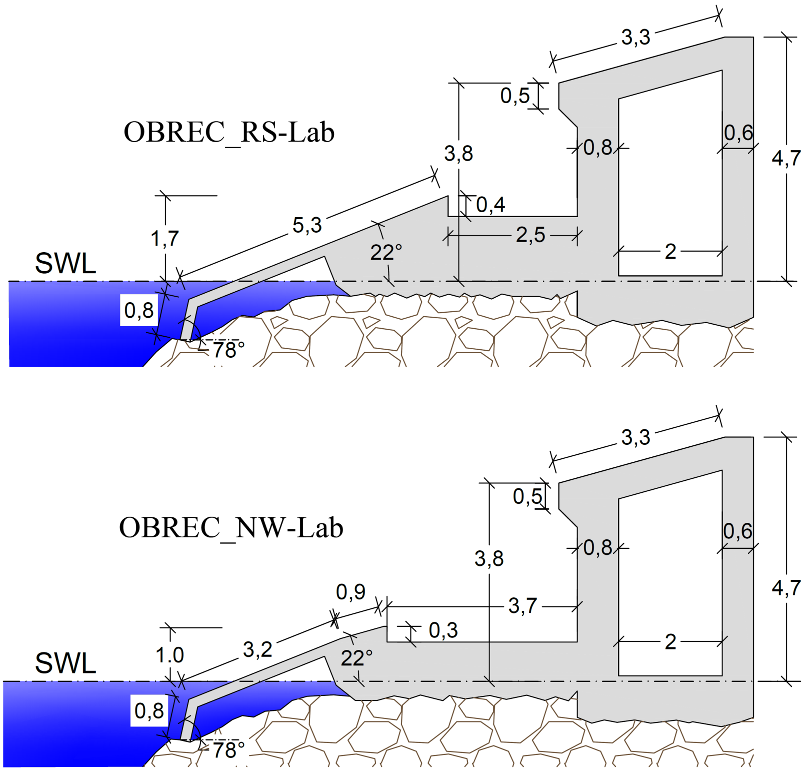

Fig. 6.5 Cross sections of the two adjacent configurations of the OBREC at the port of Naples.

of the machine room is 3.8 m with respect to the mean water level. This room provides accommodation of the instrumentation used for the prototype field monitoring. A triangular bull-nose is installed on top of the vertical wall of the machine room in order to reduce the overtopping at the rear side of the prototype. This concrete structure has a slope of 45° and its functionality has been largely demonstrated by Vicinanza et al. [276] and several other authors [141, 211] who conducted tests on traditional breakwaters and seawalls. Water stored in the frontal reservoirs flows in the machine rooms thought five circular pipes (two pipes of ϕ250 for both reservoirs and an additional one of ϕ170 only for the NW-Lab configuration) placed in the vertical seaward wall of the machine room.

6.5 Prototype construction

The OBREC installed in Naples is a unicum with regards to overtopping devices installed in breakwaters. A short description of the civil works is here presented and considered of interest for further future applications of this technology into existing rubble-mound breakwater.

The prototype construction started in July 2015 and civil engineering works ended at the end of September 2015. Civil works started with the construction of an access ramp made of sand and gravel with an excavator machine. The ramp allowed a mobile crane to reach the top of the breakwater from the road. The mobile crane was used to move 4 rows of two layers of antifers from the breakwater crest until reaching the sea water level (Fig. 6.6). A total of 30 antifers were located in part on the two sides of the pilot and others placed at the lower side of the armor layer below the sea water level.

A row of antifers was provisionally placed at the seaward of the excavation area in order to protect it from the wave motion. A micropiles drilling rig was then placed in the foundation area with the mobile crane. The OBREC foundation consists of 12 concrete micropiles with a length of 10 m and 300 mm of diameter with steel tubular reinforcement of 250 mm. Fig. 6.6b shows the phase of the micropiles excavation by means of the micropiles drilling rig. The micropiles constitute a ground anchor system, installed for two reasons: to increase the overall stability of the underlying breakwater and to ensure required safety factor to the pilot stability, especially towards uplift loading during extreme storms.

After the installation of the micropiles, the row of antifers placed seawards of the excavation area was removed (Fig. 6.6c) and the base of the two reservoirs was built. The latter consists of a reinforced slab with a thickness of 75 cm for the lowest reservoir and 125 cm for the highest one. In order to facilitate the slab construction, the reinforcement was previously assembled and then located in the area by the mobile crane (Fig. 6.6d). Once the bottom slab was completed and cast in situ, the prefabricated ramps were inserted in front of the slab, each adjacent to one other, fixed and cast with the slab (Fig. 6.6e).

After the ramp installation, the machine room and the 3 lateral walls of the reservoirs were built. A special concrete form-work was used for the vertical frontal wall (Fig. 6.6f). The temporary polystyrene mold, into which concrete was poured, portrays a rocky wall in order to create a natural rock camouflage. This camouflage was an operation adopted to reduce the visual and environmental impact of the prototype integrated into the San Vincenzo Breakwater. This improved the integration, not only from the geometrical point of view but also with regards to the shape and colour of the existing structure.

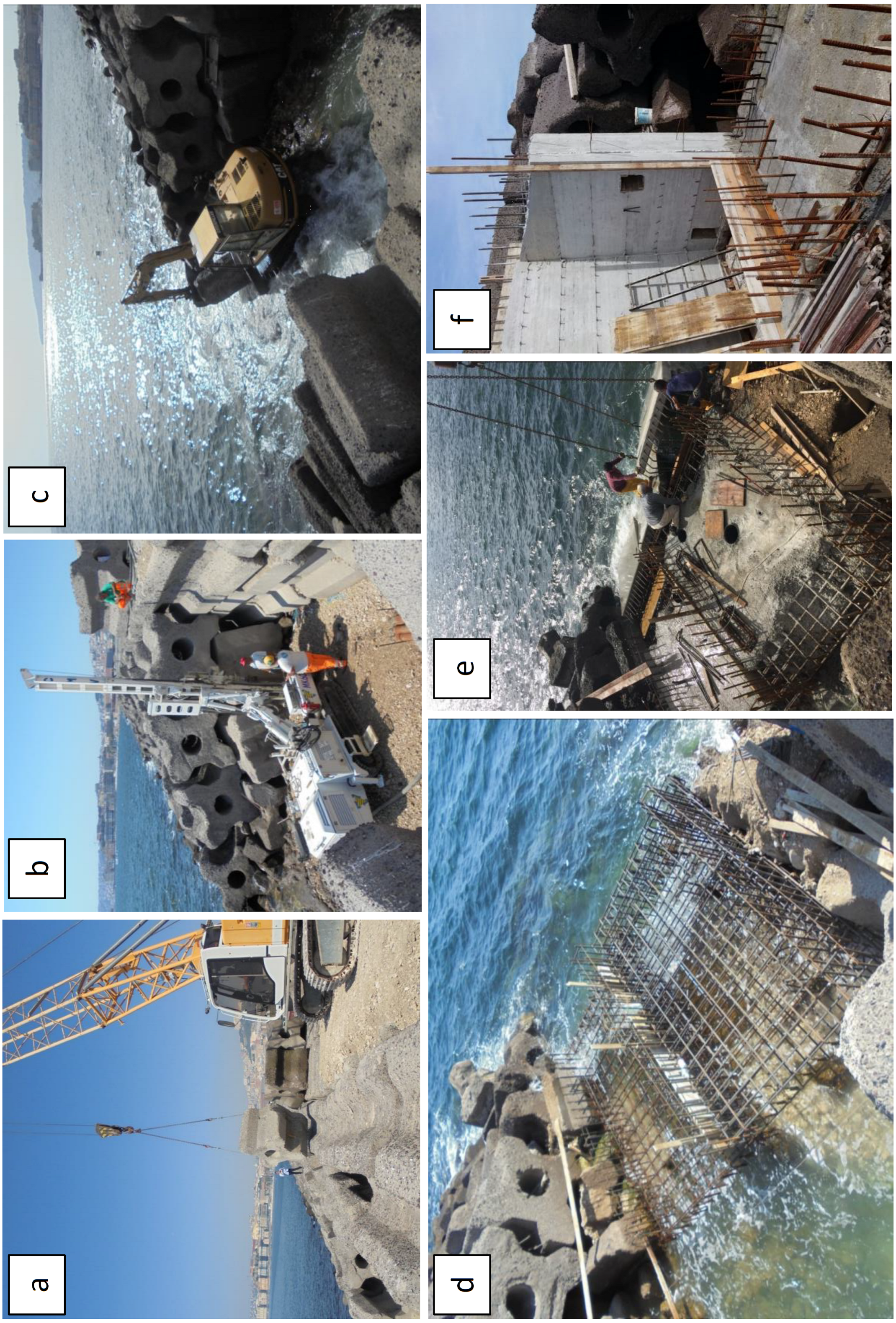

Fig. 6.6 Construction phases of the OBREC prototype in Naples.

6.6 Instrumentation

The OBREC prototype in Naples is supplied with an instrumental system designed to measure and evaluate the overall performance of the device, including the performance in terms of electricity production. In this section, an overview of the instrumentation installed in the OBREC is described.

6.6.1 Wave buoy

The in-situ wave measurements are essential for the design, construction and operational planning of ports and harbours, as well as for the field test monitoring of the WEC device. For these reasons, a modern wave buoy, denominated Directional Wave Spectra Drifting Buoy (hereafter DWSD-buoy) is installed in front of the prototype at a distance of 100 meters to measure the time series and to compute the wave spectra of the wave field in front on the device. This innovative buoy is based on the Global Positioning System (GPS) receiver developed by the Lagrangian Drifter Laboratory of the Scripps Institution of Oceanography in San Diego.

The GPS measurement principle is based on the Doppler shift of the satellite signal frequency and it provides the three velocity components of the buoy and thus of the sea surface, under the assumption that the buoy is a good water surface follower. The advantages of this technology applied to the buoy are both practical and economical [147]. The GPS receiver is very cost-effective and can be implemented in small, light-weight buoys, which can be deployed from small boats. The contained dimensions of the DWSD-buoy result in a better response of the instrument to high wave frequencies, thus extending the observation range. Furthermore, since there are no moving parts, fluxgate compasses and the velocity of the water surface is measured in a fixed reference frame from external GPS signals, and the DWSD does not need calibration. If the DWSD-buoy is deployed as a fixed installation, as is the case in Naples, particular care is needed in the design of the mooring line to avoid the buoy and the GPS antenna to be submerged, thus stopping the velocity data acquisition and introducing gaps in the velocity time series. The submerging force can be reduced by reducing the mooring line angle with conventional mooring design solutions, utilizing a secondary float or a natural rubber bungee. A possible alternative to a vertical mooring could be a horizontal mooring to a vessel or float. Such a configuration mitigates the problem of the buoy submersion while preventing the buoy from getting adrift [287]. A potential disadvantage of this innovative system is the possible errors and biases of the GPS measurements, classified as satellite-dependent errors, signal propagation-dependent errors and receiver-dependent errors [132].

Stemming from the drifter design adopted by the Global Drifter Program (GDP) [198, 175, 58], the DWSD-buoy adopted in Naples consists of a sphere with a diameter of 0.39 m, 12 Kg weight and replaceable alkaline or lithium batteries (Fig. 6.7).

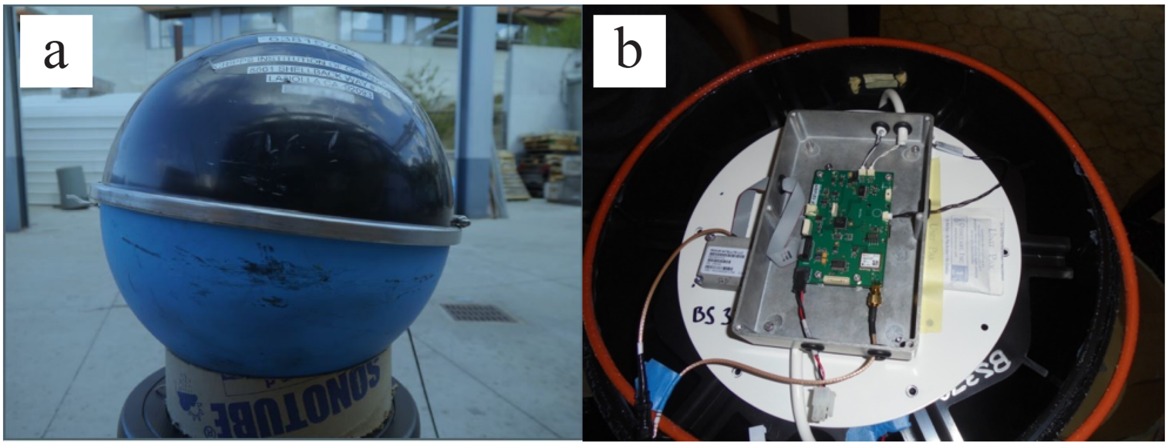

Fig. 6.7 The DWSD buoy (a) and its internal layout (b).

The buoy measures the vertical (w), zonal (east-west, u) and meridional (south-north, v) velocity components of the buoy. Times series of u(t), v(t) and w(t) are sampled for ≈ 17 min at 2 Hz and are split into 4 overlapping segments of 256 s that are subsequently averaged. The power spectral density, co-spectra and quadrature-spectra parameters are derived with the Fourier transforms of the correlation functions of each pair of the velocity time-series, giving the First-5 independent Fourier coefficients (a_0, a_1, a_2, b_1, b_2) [160] and thus the wave spectra for each hourly (and optionally, half-hourly) sea state. For each measured sea state, the three velocity components, the computed First-5 Fourier coefficients and the directional wave parameters can be stored on-board into an optional data logger. Platform information (timestamp latitude, longitude, battery voltage, internal pressure, temperature and humidity) at the start of data collection, directional wave parameters and the first 5 Fourier coefficients from 0.031 Hz to 0.496 Hz with 1/256 Hz bandwidth are transmitted to shore in real-time through the Iridium satellite system. Using two-way Iridium communication, the GPS-based wave buoy can be programmed while deployed to modify the duration of sampling in multiples of 256 seconds, deployment depth, as well as toggle First-5 reporting to shore for power consumption and telemetry cost savings.

All of the transmitted wave data, as well as platform status, are accessible in real time on a dedicated website. Details of the data processing for directional and non-directional wave spectra and related wave parameters, such as the significant wave height, peak and mean periods, as well as mean and peak direction, are provided by Centurioni et al. [57]. The data gathered by mean of the GPS-based buoy currently installed in the Gulf of Naples are also used to improve the reliability of wave forecasting in this area as well as to calibrate and validate the numerical models for a detailed wave energy site assessment in this coastal area.

6.6.1.1 Wave buoy validation

This innovative technology has been compared and validated with a well-established wave measurement instrument such as the Acoustic Doppler Current Profiler (hereafter ADCP). The DWSD-buoy was deployed for approximately 6 days, from May 12 to May 18, 2016, at 40°49.668' N and 14° 13.984' E and was co-located with an ADCP at a water depth of 17.5 m and within 30 m of distance. The bottom-mounted, upward-looking, four beams, 600 kHz, ADCP by RDI is part of a wave measurement facility of the Stazione Zoologica 'Anton Dohrn', in Naples.

The ADCP directional wave measurement principle [148, 250] is based on computing the water velocity from the Doppler shift of the backscattered acoustic pulses along the four inclined beams. The non-directional wave spectra are computed in Earth's coordinates from the water velocity data. The ADCP also measures the non-directional spectra through echo ranging (surface track) and bottom pressure with a pressure transducer, providing alternative measurements of the surface elevation and of the water depth. It should be noted that the methodology used by the ADCP software to compute the directional wave parameters is different from the one used by the DWSD. The ADCP software uses the Maximum Likelihood Method (MLM, e.g. [250]) that computes the spectra from each velocity time series at each sensor, from which the wave phase information is subsequently obtained.

In order to calculate the peak wave frequency f_p from the non-directional wave spectra, and the peak wave direction D_p from the directional wave spectra, a separation of Wind Sea and Swell components has been processed. Although various methods for the identification of Swell and Wind-Sea have been proposed in literature [214, 215], in this analysis a simple method is used to identify Wind-sea and Swell, setting a constant splitting frequency. Consequently, the separation has been made choosing a proper frequency separation (f_s) which separates the wave spectra into the wind-sea and swell part.

Since the main objective of the test campaign was to compare the two different wave measurement instruments, the same frequency separation (f_s = 0.11 Hz) has been used for the spectral partitioning. Considering the selected area, this method, although very simple, appears reliably satisfying considering that Wind-sea and Swell occur markedly separated in the frequency domain.

Fig. 6.8 shows an example of the computed non-directional spectra. This example shows the frequency separation of the two domains, swell and wind waves, having two evident distinct peaks. The comparison analysis presented here is based only on the wind-sea part of the spectra, thus T_p than D_p has been both computed considering the peak wave frequency fp in the range of 0.11 Hz < f_p < 0.49 Hz. Conversely, the significant wave height H_{m0} has been computed considering the entire spectrum.

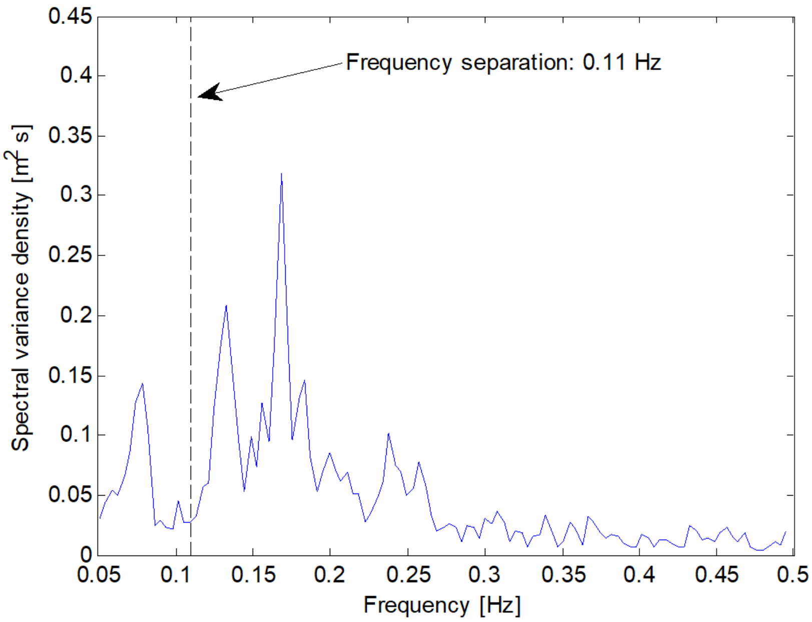

Fig. 6.8 Example of the non-directional spectral variance density $E(f)$ showing the separation frequency (f_s) used to partition the wave spectrum between wind and swell.

The non-directional wave parameters from the ADCP were computed from both the velocity and surface tracking spectra using a frequency bandwidth of 0.0078 Hz and using the same separation frequency ($f_s = 0.11$) Hz used for the DWSD analysis. As a self-consistency check for the ADCP, the wave parameters for which T_p computed from the two spectra differed by more than 1s, were discarded.

The spectral wave parameters measured by the DWSD-buoy are compared with those measured by the ADCP. For qualitative evaluation of the comparison results, statistical indicators such as Bias and Root Mean Square Error (RMSE) are computed. These parameters are defined as follows:

$$Bias = \frac{1}{N}\sum_{i=1}^{N}(y_i - x_i) \tag{6.1}$$

$$RMSE = \sqrt{\frac{1}{N-1}\sum_{i=1}^{N}(y_i - x_i)^2} \tag{6.2}$$

where y_i and x_i indicate the wave parameters at the i-th sea state respectively measured by the DWSD-buoy and the ADCP, while N=139 is the number of sea state here considered for the comparison analysis. Fig. 6.9a shows the comparative analysis of the significant wave height H_{m0} measured by the two wave instruments. It can be noted that the measured data looks very similar without any substantial deviation, especially when the significant wave height exceeds 0.5 m. The comparison shows clearly very good agreement, considering the very different instrumental techniques used, with a Bias of 0.038 m and a RMSE of 0.07 m. Such a good correlation between two diverse wave sensors confirms the high-quality of this innovative GPS-based buoy. It is worth pointing out that for practical coastal and maritime engineering application, sea states with values of Hm0 lower than 0.50 m are often considered as a calm condition. If only the sea states greater than this threshold are considered in the comparison, then the result shows a very high correlation with a Bias of 0.01 m and RMSE of 0.05 m. The correlation of the peak period T_p between the ADCP and the DWSD-buoy is shown in Fig. 6.9b. The peak periods considered in the analysis refer to the peak related to the Wind-Sea part of the non-directional spectra (0.11 Hz < f_s < 0.49 Hz). The results of peak periods show some small difference between the two instruments (Bias of -0.12 sec and the RMSE of 1.1 sec), mainly when the calculated wave spectra have multiple peaks of approximately equal magnitude also in the wind sea frequency range. Fig. 6.9c shows the comparison of the peak wave direction D_p measured by the DWSD-buoy and the ADCP, confirming a relatively good agreement of the instruments with a Bias of 2.0°, RMSE of 20°, which can be considered acceptable for engineering applications of this technology. Finally, Fig. 6.10 shows the time history of the three computed parameter H_{m0}, T_p and D_p measured from the DWSD-buoy and the ADCP, for a visual comparison, confirming the good results.

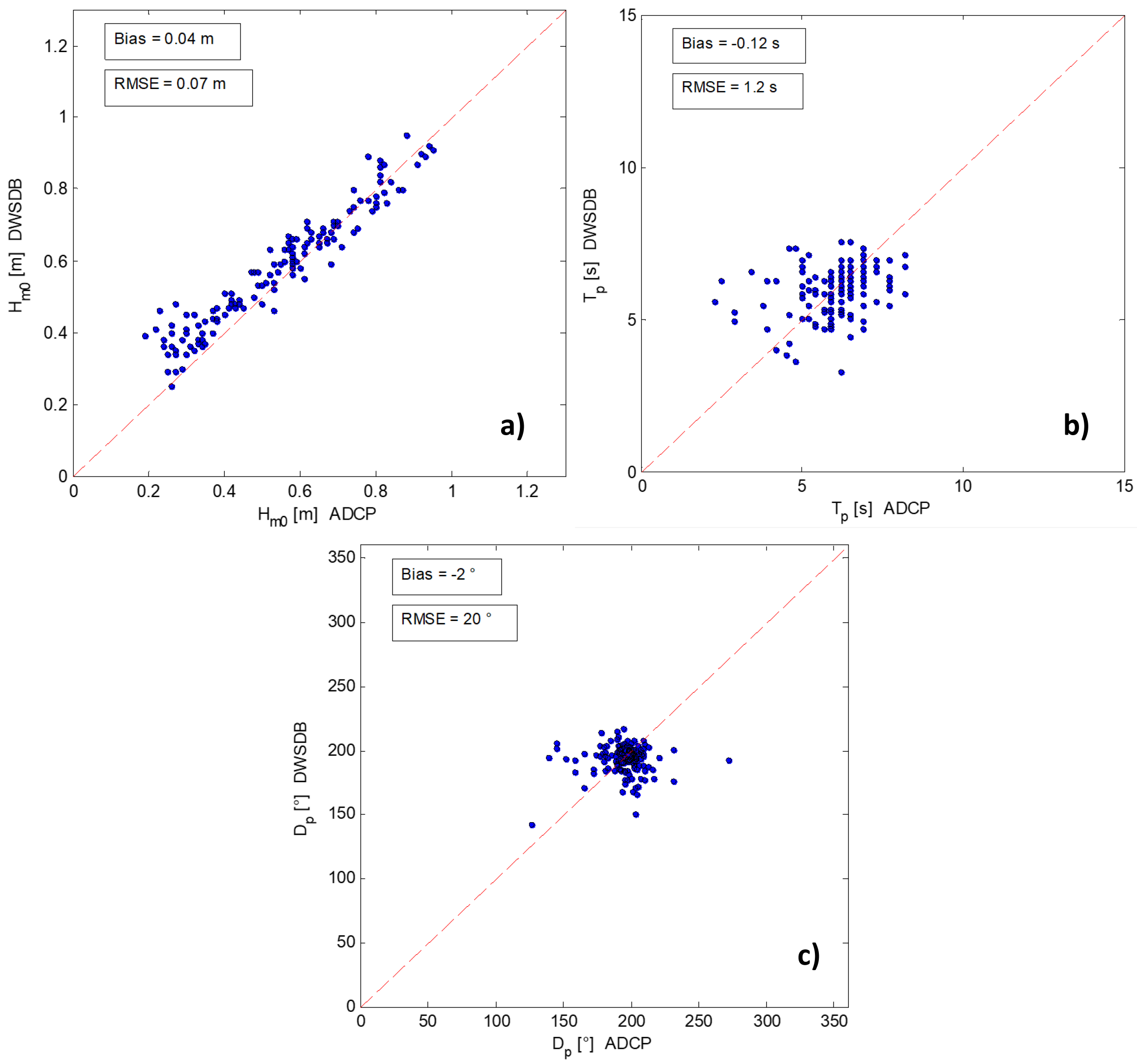

Fig. 6.9 Comparison of the significant wave heights, H_{m0} (panel a), peak period, T_p (panel b), and peak direction, D_p (panel c), between the DWSD-buoy and the ADCP.

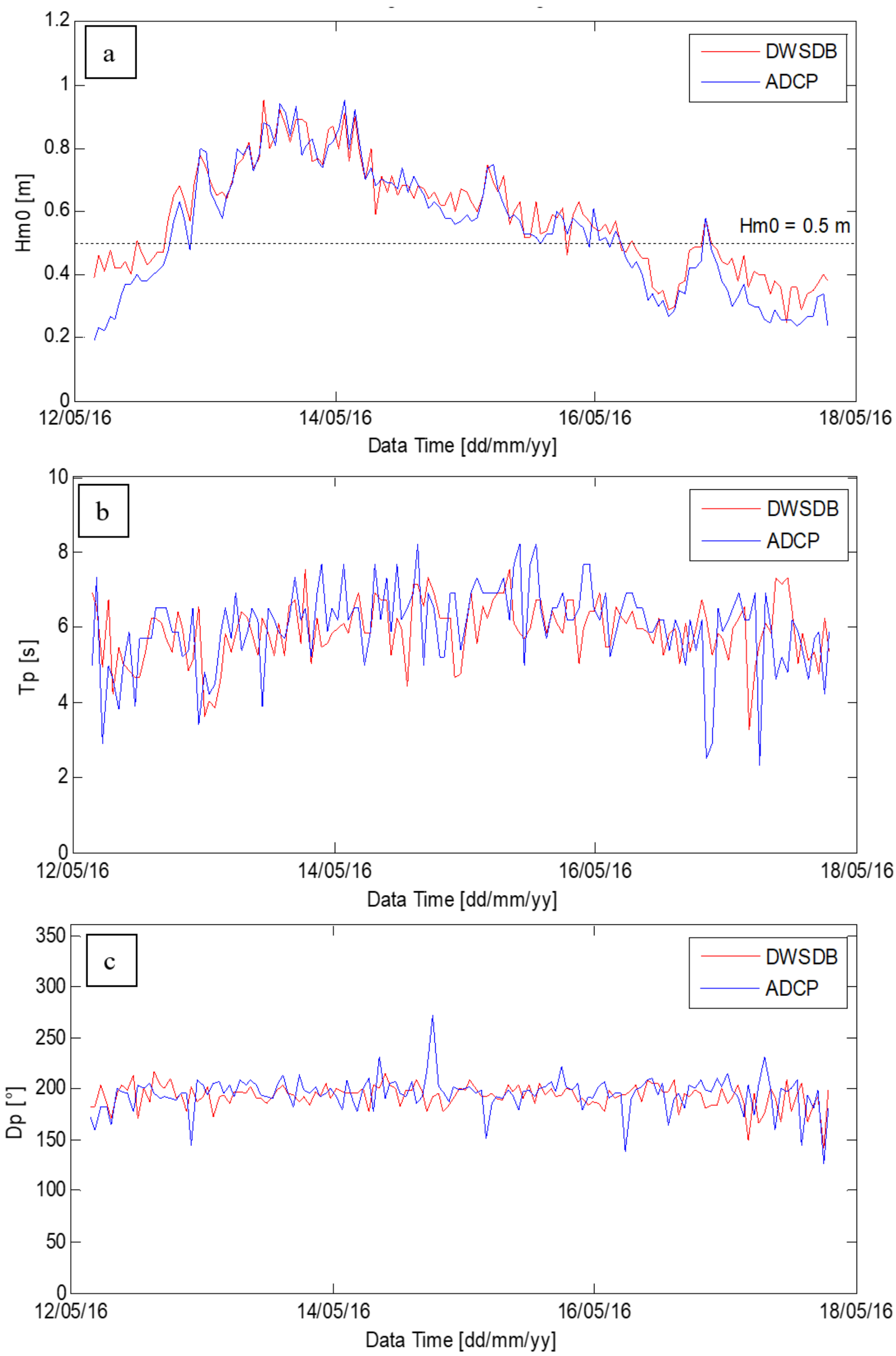

Fig. 6.10 Data series of the significant wave height H_{m0} (panel a), peak period T_p (panel b) and peak direction D_p (panel c) measured with the DWSD-buoy and the ADCP.

6.6.2 Pressure transducers

The wave pressure exerted on the OBREC is measured by 8 Flush Membrane Transmitter FPT (TRAFAG FPT100.0A) located on the different parts of the device: the ramp, base reservoir and the vertical seaward wall of the machine room (Fig. 6.11). The instruments feature flush membranes with the smooth and plain surface and a completely welded sensor system. The range of the pressure is 0-100 bar with an accuracy of ±0.4 % FS.

Fig. 6.11 Detail of the pressure transmitters installed on the vertical wall (left panel) an on the frontal ramp (right panel) of the full-scale device in Naples.

Currently, the wave pressure data are gathered only during storm conditions (Fig. 6.12) for sea states with significant wave height greater than 2 meters. The measurement is recorded at 1000 Hz and synchronized with the data acquisition system of the pressure sensors, sampling at 100 kHz, in order to capture the possible impact pressures that would act on the structure under extreme wave conditions. The aim is to acquire and analyse pressure data in order to compare it with existing formula in literature, and validate the pressure data measured in the experimental test in small-scale carried out in 2012 [276] and formulas provided in Chapter 4 after the second test campaign on the OBREC.

Two high-resolution cameras are used to capture the wave profile when waves overtop the ramp and impact on the vertical wall. The coupled analysis of the pressure transmitters and the cameras provide details on the hydrodynamic behaviour and the interaction wave-structure in order to have a better understanding of the distribution of the pressures acting on the prototype, as well as on the identification of the shape that the wave surface takes before the ramp and in front of the vertical wall of the OBREC.

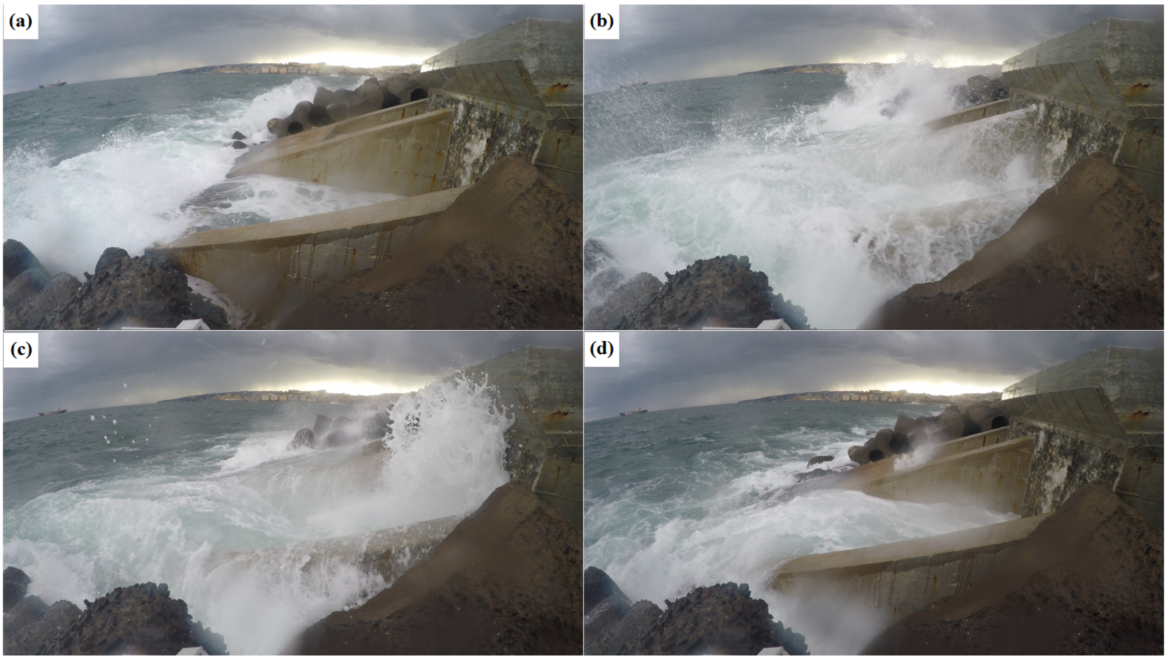

Fig. 6.12 OBREC prototype under wave storm (January 2016). a) wave runup on ramp; b) wave overtops into the two reservoirs; c) water jet hits on vertical wall and parapet; d) backwash.

6.6.3 Low-head turbines

Regarding the system used to evaluate the energy production performance of the prototype, three low-head turbines were installed at the end of 2015 in the machine room for stress tests during wave storm conditions. The turbines installed in 2015 are vertical axial flow propeller turbines with fixed runner blades. The water passes through a guide vane assembly and it turns the propeller connected to the generator. The water then exits through a draft tube that is immersed in the water. A scheme of the turbine system is presented in Fig. 6.13.

A micro-hydro permanent magnet generator is coupled to each turbine. It converts the potential energy of a watercourse to electricity by drawing the water through a constriction, which has sufficient velocity to turn a propeller and hence the generator, generating electricity. The total nominal power installed in the machine room was 2.5 kW with one turbine of 1.5 kW and two of 0.5 kW each (Fig. 6.14).

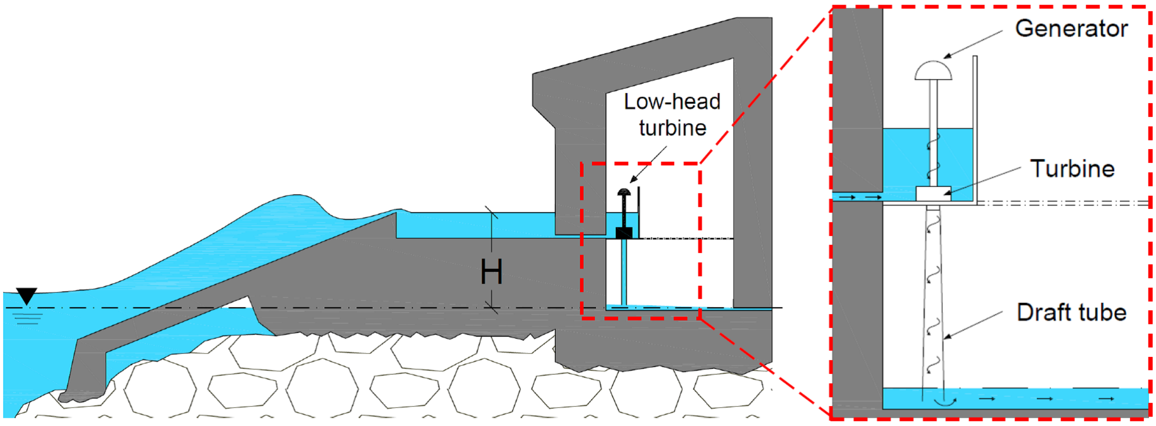

Fig. 6.13 Cross section of the OBREC (*RS – Lab*) with the turbine installed in the machine room (left panel) and details of the system (right panel)

The propellers were equipped with a Maximum-Power-Point-Tracking (MPPT) charge controller, used to maximize power extraction under all conditions. The major principle of the MPPT is to extract the maximum available power by making the turbines operate at the most efficient voltage (maximum Power Point). In off-grid situations, such as the one occurred during the stress tests, the MPPT regulator was set up to divert surplus power to a diversion load consisting of a hot water heater. This instrument is typically used to ensure that turbines can run at a constant speed and surplus power can be used rather than wasted. The generated power was delivered to a battery bank, which is required to store power in off-grid situations. Batteries were arranged in parallel to increase storage capacity. It is worth underlining that, due to the limitation of research funds, the three turbines installed in the machine room were undersized.

An innovative hybrid multi-field turbine, obtained by coupling different types of turbines is presently under development and planned to be installed at the end of 2018. In detail, a semi-Kaplan of 1 kW coupled with an Archimedean Screw Turbines with 7 kW of nominal power is going to be installed at the end of 2018. In the future the aim is to install a set of semi-Kaplan turbines for a total power of 20 kW, ranging between 0.9 to 1.6 m of water head and 0.35 to 0.85 m^3/s of water flow.

The very flexible inflow/outflow structure and the easily upgradable electromechanical system have been designed in order to set-up and evaluate the optimal control strategy for the turbines. The scope is to find the "best" leading technology for overtopping hydro-marine turbines, via cost-benefit analysis. For this reason, performance and reliability are closely monitored under different stress tests, i.e. start & stop cycle in the marine environment with

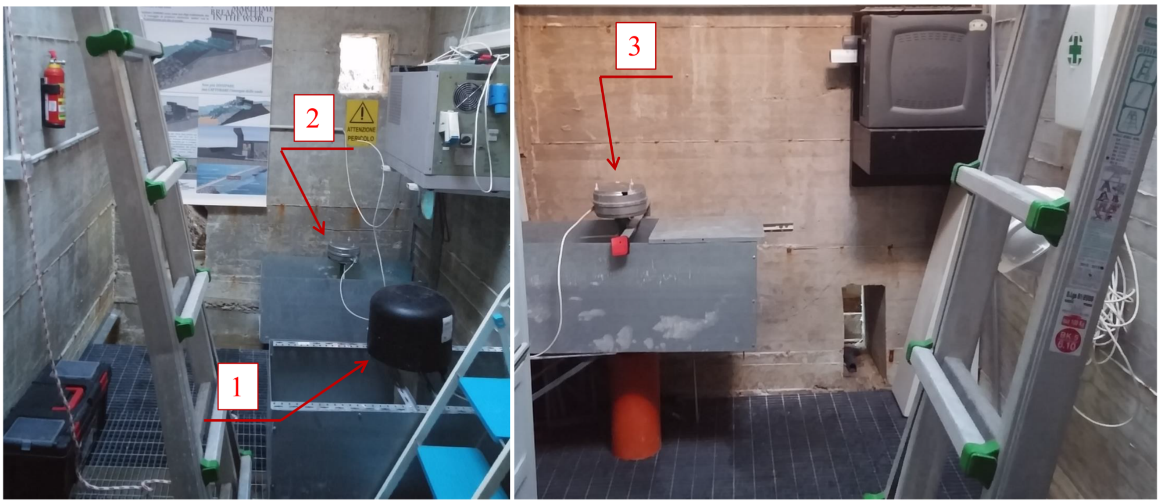

Fig. 6.14 Fixed-Kaplan low-head turbines installed at the end of 2015 in the machine room of the OBREC prototype in Naples

a highly variable combination of the flow rate/hydraulic head. Future research activities on the prototype will provide a definitive power matrix for a large spectrum of wave conditions.

6.7 Conclusions

For the development of innovative WEC-integrated breakwaters, such as the OBREC device, the study of the performance at full-scale tested in a real environment is often considered mandatory to demonstrate the technology maturity and thus contributing to the achievement of the final step of the development, i.e. their commercialization.

Recent works to provide ways of measuring the progress and the value of technology R&D processes were focused on adapting the Technology Readiness Levels (TRL), a method to estimate the technology maturity of new technologies, to specific wave energy terms focusing on 'functional readiness' and 'lifecycle readiness'. The first one indicates the readiness to convert the wave energy and export it to the grid, in addition to other functions such as station keeping and remote monitoring. A TRL scale gives indications of how these should be demonstrated at different levels. The lifecycle readiness states for the readiness in non-functional areas that are important to utilities, which include operational readiness, supply chain readiness, risk reduction and also cost estimation and reduction. Please note that the selection of one or another level for WEC technologies could be in some cases questionable or object of debating. Regarding the OBREC device, it can be considered at the Level-5, i.e. when a representative model or prototype system is tested on the relevant environment but its energy production performances are not entirely demonstrated in the field.

Despite the significant effort on the analysis at small scale carried out on the OBREC adopting both physical and numerical modelling, as well as the use of field test at full-scale, the device is still under development. Please note that at the time of writing, the monitoring of the prototype installed in Naples allowed only to evaluate the wave pressure along the different parts of the OBREC for few sea states occurred during the winter season in 2017/2018. The analysis of the field data is still ongoing and, for evident reasons, is beyond the scope of this research work.

In the author's opinion, more work needs to be done, in particular on the mechanical apparatus to be adopted for the energy conversion. Although the wave-structure interaction on this device has been thoroughly studied over the last years, very few studies, and only at theoretical levels, have been conducted on the device performance in terms of energy production. Regarding the instrument adopted for the energy conversion, the hydro turbines used for OTD-devices, such as Kaplan turbines, have the benefit of being a mature technology used for many decades for power generation. However, only limited stress tests were carried out in order to evaluate the performance of low-head turbines applied to this specific innovative device.

Chapter 7

Innovative caisson integrated with an OBREC device

7.1 Introduction

The OBREC integrated into rubble-mound breakwaters has been deeply investigated over the last years with physical (see Chapter 4) and numerical model tests (Chapter 5), and it is still under development with the ongoing monitoring activities at full-scale in real environments (Chapter 6). The relatively simple geometry of this OTD-device, with a single frontal ramp and a reservoir, makes the technology suitable to be fully integrated also into vertical structures.

In the last few decades, vertically-faced caissons have seen a resurgence mainly due to the increasing need for breakwaters in relatively deep water areas (i.g. water depth higher than 15-20 m) or when there is a scarcity of rock materials, which makes them attractive when compared with rubble-mound breakwaters from a cost, design and constructibility perspective. As described in Chapter 2, many innovations have been presented over the last decades to overcome the limits of traditional vertically-faced breakwaters. One of the greatest disadvantages of these harbour defence structures is the high reflection pattern in front of them and their exposure to large impulsive wave forces. If the reflection and the impact pressure are relevant issues, several structural measures can be taken, such as the use of top-sloping caissons, curved slit and perforated breakwaters, as well as caissons with stilling water basin in front of it. Despite the different performance of the over-mentioned non-conventional configurations, all the typologies share the same scope, which is to protect the harbour by dissipating a larger amount of wave energy when compared to that dissipated by traditional caissons.

Starting from the development of the OBREC integrated into rubble-mound breakwater and the SSG-integrated into a vertical breakwater [171], and taking into account the existing concept of the vertical caisson with a 'stilling water basin' as presented in Chapter 2, a novel caisson is here proposed, which consists of the integration of the OBREC device in a vertical structure. The structure is composed of a vertically-faced caisson with a sloping ramp, a reservoir and a set-back crown-wall located on the top. At the rear side of the crown-wall, a machinery room is built to accommodate the instrumental apparatus for the energy conversion (i.e. low-head turbines and generators). An artistic sketch of this novel caisson is shown in Fig. 7.1. As in the case of traditional vertically-faced structures, the principal function of this caisson is the defence and protection of the inner area of the harbours. However, instead of completely reflecting the energy from the waves, it is designed to absorb part of the energy and convert it into electricity. This concept design adds a revenue wave generation function to a breakwater, adding benefits due to WEC integration (sharing-cost). This technology can be applied for new breakwaters port expansions, or integrated into existing superstructure which have to be rebuilt due to the maintenance activities or upgrades due to climate change. As for the case of rubble-mound breakwater, the costs of the OBREC installation into new vertical breakwaters are lower compared to stand-alone WEC devices, considering that the caisson would be built regardless of the inclusion of the WEC, and geometrical changes affect only the superstructure.

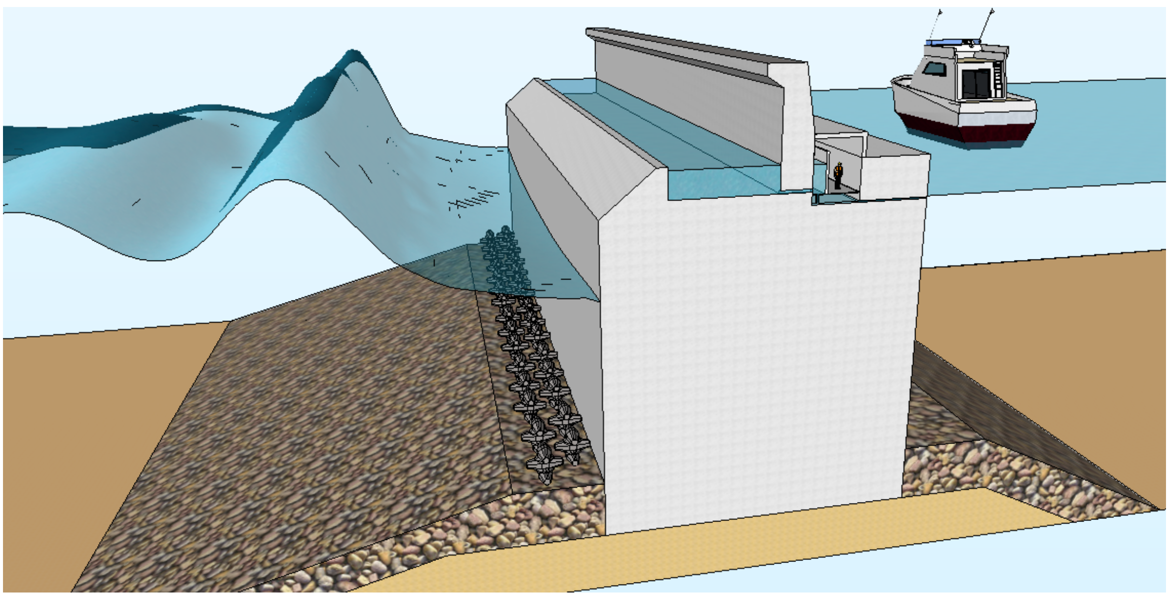

Fig. 7.1 Concept design of the innovative caisson integrated with an OBREC device.

The primary goal for coastal engineers involved in the development of a new concept idea of a WEC-integrated caisson, is to study its hydraulic and structural performance, evaluating the device with the classical methodology used for traditional coastal defence structures. Therefore, the main aim is to focus on the phenomena such as the reflection, overtopping discharge and wave loading for stability analysis, by comparing the results with those of the conventional vertical structures.

The results presented in this Chapter are obtained adopting the numerical analysis carried out on a OBREC-integrated caisson. The numerical model used is IH2VOF, which has been extensively adopted for the wave-structure analysis of vertical caissons by many authors [152, 163, 163], demonstrating that it is capable of predicting the hydraulic response of vertical caissons very accurately. Furthermore, IH2VOF has been thoroughly validated against physical model tests as shown in Chapter 5, indicating that the model can reproduce the wave interaction with the OBREC device with high levels of accuracy.

The Chapter is organized as follows. The numerical model set-up is presented in Section 7.2 with a description of the numerical domain, the grid size dimensions, the generated wave characteristics as well the different OBREC superstructure tested. Section 7.3 is devoted to the numerical results of the overtopping and reflection, with a comparison between traditional and innovative caissons. A dimensional analysis is also presented, with the evaluation of the influence of the principal geometrical parameters on the overall hydraulic performance. The analysis of the wave forces exerted on the different configurations is presented in 7.4. Finally, conclusions are drawn at the end of the Chapter.

7.2 Numerical model set-up

At this early stage of development, the aim of the numerical analysis is to provide a preliminary optimization of the innovative caisson by evaluating the parameters that might have an influence on the hydraulic performance. Furthermore, the results of the OBREC integrated in a caisson are compared to the ones obtained on a traditional vertical breakwater having the same overall dimensions. Both structures are located on an identical mound-foundation. The only difference between the two caissons is the superstructure, which consists of a conventional crown-wall for the traditional caisson and an OBREC device with a ramp, a reservoir and a set-back wall for the innovative structure. The numerical tests have been carried out at 1:30 length scale (Froude scaling) compared to the hypothetical prototype. Therefore, a crest freeboard (R_c) of 0.233 m and a caisson width ($B_{caisson}$) of 0.667 m have been considered. The geometry of the traditional and innovative caissons is displayed in Fig. 7.2.

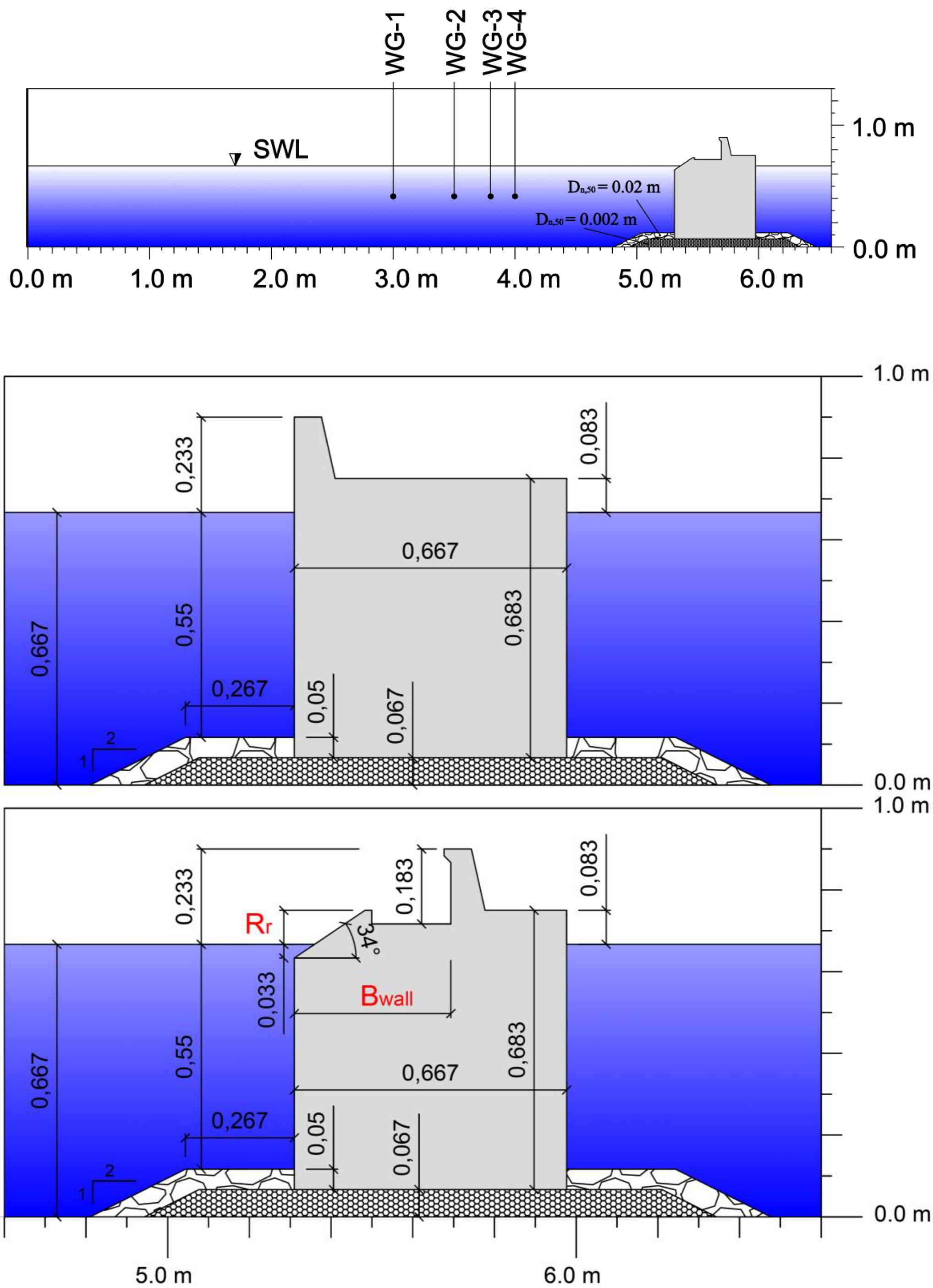

Fig. 7.2 Layout of the two-dimensional numerical domain, with the position of the innovative caisson and the numerical wave gauges (WG) on the upper panel; Cross-section of the traditional caisson (central panel) and the innovative caisson integrated with the OBREC device (bottom panel).

The reason the numerical models are performed at small scale is that IH2VOF has been already validated in similar scale (see Chapter 5) by comparing the numerical results with those measured at small scale laboratory tests carried out at Aalborg University (Chapter 4). Therefore, the use of a pre-validated model strongly limits the introduction of additional uncertainties in the analysis.

The geometrical parameters of the innovative caisson evaluated in the present analysis are the crest freeboard of the ramp, indicated as R_r, and the horizontal distance between the seaward caisson face and the set-back crown-wall, B_{wall}. These two parameters have been considered as the leading ones in the design of the device, hence their influence on the hydraulic and structural response of the novel caisson is investigated in this Chapter.

As shown in Fig. 7.2, the ramp has a slope of 34° with respect to the horizontal. The slope has been selected considering the same values of the flat ramp slope of OBREC device integrated in rubble-mound breakwater tested in laboratory and described in Chapter 4. Please consider that Kofoed [138] conducted physical model on an offshore overtopping device, investigating the role of the ramp angle on the wave overtopping discharge into the reservoir. The results indicated that a ramp with a slope lower than 30° had a slightly better performance in terms of hydraulic efficiency (maximum gain about 4%) compared to a ramp with an inclination of 30° and 35°. However, the Author argued that a ramp with a low angle slope could lead the steepest waves to collapse as plunging waves, increasing the energy losses and possible higher pressure on the frontal ramp due to the breaking process. Kofoed [138] expressed a formula for the overtopping behaviour of offshore OTD devices with a single level reservoir, indicating an empirical coefficient that takes into account the reduction of hydraulic efficiency for slope angles α deviating from $\cot\alpha = 1.7$ (α=30°), which was assumed by the author as the optimal slope inclination for the offshore OTD-devices. Following this suggestion, the frontal ramp of the flat configuration in the OBREC device was then designed steep enough (34°) to minimize the occurrence of the breaking waves and maximize the wave overtopping into the reservoir (see Chapter 4). Therefore, the equal slope is adopted in this analysis for the OBREC integrated into a vertical caisson.

Three values of R_r, and as many of B_{wall} are considered, for a total of nine different geometrical configurations (see Fig. 7.3). These configurations are tested using the identical numerical domain, set up with a total length of 6.6 m and a height of 1.30 m, as displayed in top panel of Fig. 7.2.

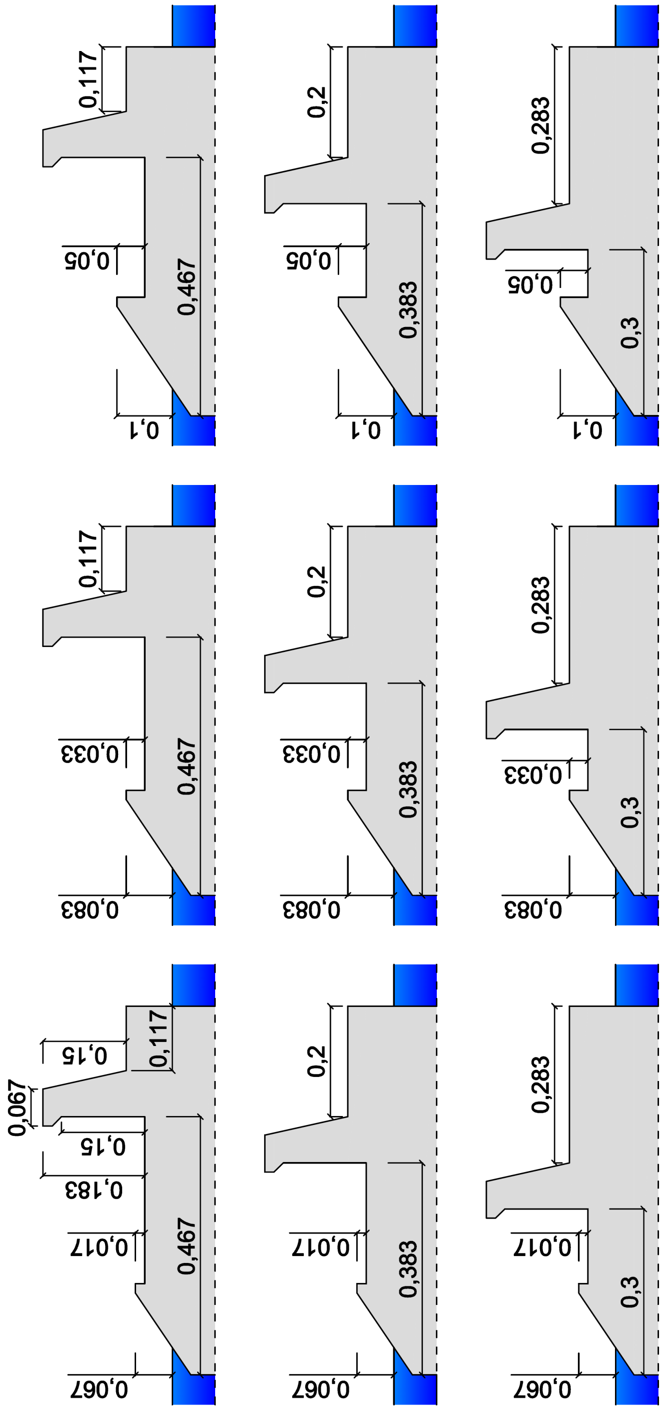

Fig. 7.3 Nine geometrical configurations of the OBREC-caisson tested with IH2VOF.

The material properties of the porous layers are set according to the numerical test set-up described in Chapter 5, which has been thoroughly validated against the laboratory tests described in Chapter 4. The porous media characteristics are shown in Table 7.1. In detail, the porous media below each caisson base is composed of an internal layer with a nominal diameter $D_{n,50}$ = 5 mm, and seaward and leeward external armour layers with $D_{n,50}$ = 20 mm. Furthermore, the value of α in VARANS equations (see Eq. 5.4) is constant and set to 200 for all the porous layer, while β is set to 0.8 for the internal layer and 1.0 for the external layers, according to Lara et al. [152], Losada et al. [163],and Guanche et al. [101]. The added mass coefficient, c, is set to a constant value for all porous media with a value equal to 0.34, according to the suggestion of van Gent [269].

The base reservoir is modelled in IH2VOF as a closed structure, similar to the OBREC integrated in a rubble-mound breakwater described in Chapter 5. Only extreme wave conditions are generated for this analysis, hence the OBREC model's reservoir is sutured during whole duration of the numerical tests. Considering that R_r/H_{m0} ranges between 0.200 and 0.643, the assumption of a closed reservoir as modelled with IH2VOF in this Chapter can be considered valid, based on the results of the overtopping into the reservoir obtained by Iuppa et al. [126].

Based on the suggestion of the IH2VOF's developers, the seaward vertical face of the caisson is located in the numerical domain at a distance of 5.31 m from the wavemaker (inlet boundary layer), corresponding to 1.2-1.5 times the deep water wave length $L_{-1,0}$ based on the energy period $T_{-1,0}$. The first wave gauge ($WG-1$) is placed at 3 m from the inlet and the other three free surface gauges at 0.50 m, 0.80 m and 1.00 m from the position of $WG-1$. The numerical incident and reflected spectra are separated and estimated using the Zelt and Skjelbreia [291] method.

Table 7.1 Porous media characteristics of the mound foundation

	n $[-]$	$D_{n,50}$ (m)	α $[-]$	β $[-]$	c $[-]$
Internal layer	0.40	0.005	200	0.80	0.34
External layer	0.45	0.020	200	1.00	0.34

Waves are generated as a fixed value boundary condition (Dirichlet-type boundary condition), which represents the simplest condition to be implemented in a numerical model, based on wave theories that give analytical expression for free surface and velocity distribution throughout the waver column. Waves are generated considering the free surface level at the inlet boundary, which forces the model to set the VOF function equal 1 (water) below and 0 (void) over it, and the vertical and horizontal velocity components.

First order irregular wave time series are generated in IH2VOF as a linear superposition of Stokes I waves for a given number of components (N=512). A standard JONSWAP-type spectrum [105], with a peak enhancement factor of 3.3, is considered for all the tests. The numerical wavemaker is equipped with a control system for a combined wave generation and active wave absorption of the reflected waves. The active wave maker absorption is included in the inlet boundary layer following a procedure similar to the one used in physical wave flume and proposed by Schäffer and Klopman [227]. Details of the implementation of the active absorption in IH2VOF are described in Lara et al. [154]. Please note that the procedure for wave generation is different from the one described in Chapter 5. The numerical tests carried out on the innovative caisson are not directly validated against physical model tests, thus waves are not generated replicating the wavemaker movement, as done on previous numerical analysis. Finally, an open boundary with a wave absorption condition is activated at the outlet boundary layer, following the methodology proposed by Schäffer and Klopman [227]. Nine tests are simulated in the numerical flume in order to analyse the structure. Table 7.2 summarises the incident wave parameters calculated in the numerical domain at the toe of the caisson models. Each signal is adopted for all the geometrical configurations, for a total of 90 numerical tests (9 wave conditions x 10 geometrical configurations). This procedure allows comparing wave-by-wave the different geometries tested in the numerical tank, evaluating in more details the difference in terms of wave reflection, overtopping discharge and wave loading exerted on the structures. A constant water depth, h, of 0.667 m is considered for all the tests.

The total duration of each test is set to 1400 s, which allows obtaining a long time series with around 800-1200 waves, depending on the test. The data series was chosen to be long enough to fully define reliable wave spectra. Moreover, the length of each test can be considered sufficient to obtain consistent statistical values of the peak pressures/forces, as well as to perform the necessary statistical reliability for the wave overtopping analysis. Finally, Table 7.3 shows the nondimensional parameter ranges tested in this numerical analysis.

The grid system varies along the vertical and horizontal direction, as shown in Fig. 7.4. The horizontal direction is discretized into three regions: the first one with a non-uniform grid size mesh having a width that starts with 0.021 m, close to the wave maker, and it decreases until 0.007 m in the vicinity of the OBREC device. A second region has a grid

Table 7.2 Incident wave characteristics for numerical tests on innovative caisson integrated with an OBREC device

	H_{m0} (m)	T_p (s)	$T_{m,-1,0}$ (s)	$T_{m,01}$ (s)	$T_{m,02}$ (s)
$Test\_01\_caisson$	0.157	1.452	1.296	1.218	1.169
$Test\_02\_caisson$	0.156	1.552	1.461	1.370	1.312
$Test\_03\_caisson$	0.156	1.845	1.686	1.582	1.517
$Test\_04\_caisson$	0.193	1.484	1.380	1.294	1.240
$Test\_05\_caisson$	0.189	1.750	1.572	1.475	1.415
$Test\_06\_caisson$	0.190	1.896	1.775	1.666	1.596
$Test\_07\_caisson$	0.230	1.665	1.504	1.415	1.359
$Test\_08\_caisson$	0.230	1.845	1.712	1.607	1.541
$Test\_09\_caisson$	0.229	2.133	1.929	1.810	1.736

Table 7.3 Nondimensional parameter ranges for the numerical analysis of innovative caissons

	R_c/H_{m0} $[-]$	R_r/H_{m0} $[-]$	$B_{wall}/L_{-1,0}$ $[-]$	H_{m0}/h $[-]$	$h/L_{-1,0}$ $[-]$	$H_{m0}/L_{-1,0}$ $[-]$	h/H_{m0} $[-]$
MIN	1.015	0.290	0.069	0.233	0.154	0.043	2.901
MAX	1.501	0.643	0.190	0.345	0.272	0.074	4.287

mesh with constant values of 0.007 m and it covers the entire horizontal length of the caisson. Finally, a third region is characterized by non-uniform grid size mesh that increases until the end of the domain, with a final value of 0.015 m. As shown in the right panel of Fig. 7.4, the vertical direction is also discretized into three regions with a central area around the still water level characterized by a finer mesh resolution with a size of 0.007 m. On the upper and lower region, a less refined mesh grid is required and the mesh dimension along the vertical direction gradually increase until a value of 0.01 m on the bottom and 0.015 m on the top of the domain. As already described in Chapter 5, the errors due to the varying grid size are minimized using smoothly changing grids in the two directions, using a function defined in such a way that the second derivative of the coordinate of each cell is lower than 0.05, increasing the accuracy of the numerical solution.

The numerical domain and grid system defined here are slightly different from the one set-up for the validation analysis and presented in Chapter 5. Firstly, the absence of physical model tests to directly validate the present tests allows to set-up a domain with an optimized dimension and mesh grid size, defined in function of the generated wave conditions and based on the long experience of the IH2VOF developers. Regarding the mesh size, in case of non-breaking waves expected along the channel, it is recommended to set 70-100 cells per wavelength along the horizontal direction and 7-10 cells per wave height in the vertical direction. The use of the highly refined computational grid mesh around the area of interest of the OBREC model is necessary due to the non-conventional geometry of the device with the presence of a sloping ramp and a parapet on the top of the vertical set-back wall. Moreover, a fine grid resolution is chosen to resolve the large velocity variation near the solid wall during the wave impact. Please observe that the water depth and wave conditions tested in this analysis are greater than the ones considered in the previous tests described in Chapter 5, which explain the use on a slightly wider mesh size around the structure and the still water level. The resultant numerical domain has 539 cells in the x-direction and 153 cells in the y-direction, leading to a total of $82,467$ computational cells.

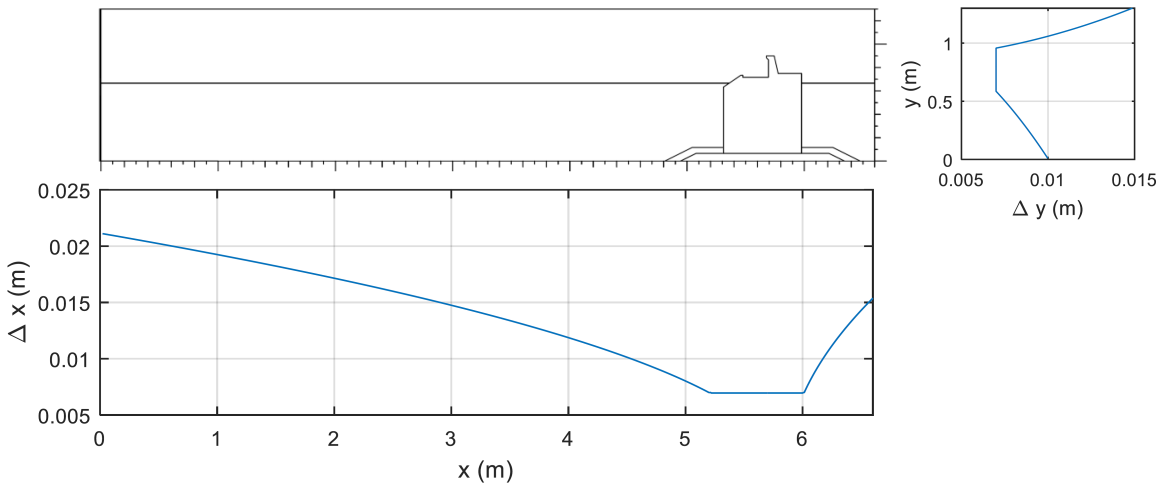

Fig. 7.4 Computational mesh resolution along the horizontal and vertical direction.

7.3 Hydraulic performance

7.3.1 Wave reflection

Vertically-faced structures are originally developed to protect harbours by reflecting the largest part of the incident wave energy. Allsop et al. [10] conducted physical model tests on a vertical breakwater, showing that the reflection coefficients, K_r, ranges between 0.85 and 0.90, with no relevant influence of the wave height and period. Generally speaking, larger and steeper waves interacting on the vertical structure can lead to a slight reduction of K_r due to the energy dissipation caused by the breaking wave conditions. An increase in the water level would reduce the breaking condition and increase the overtopping discharge, leading to a significant reduction of the reflection coefficients. An important parameter to take into account for the reflection in vertical breakwaters is the relative wave crest, R_c/H_{m0}. Allsop et al. [10] suggested assuming for design purpose a constant value of K_r equal to 0.9 when R_c/H_{m0} is higher than the unity. For the opposite case, K_r is calculated as $0.79+0.11 \cdot R_c/H_{m0}$. These two relations are widely accepted and used by harbour engineers for the design and evaluation of reflection coefficients on vertical breakwaters and seawalls, and they are reported in standards such as the USACE [260].

The scope of this section is to present the results of K_r for different tests conditions, comparing them with the empirical formula suggested by Allsop et al. [10]. Furthermore, the analysis of the influence of the different geometrical parameters on the reflection performance of the innovative caisson is carried out. Numerical results of the wave reflection coefficients in front of the structures are displayed in Fig. 7.5. Blue points indicate the reflection coefficients for the traditional caisson, while the red ones represent the values of K_r for the different configurations of the innovative OBREC integrated in a caisson. A dashed black line in Fig. 7.5 indicates the empirical relation proposed by Allsop et al. [10]. Numerical results of the reflection coefficients for the vertically-faced structure match very well with the relation proposed by Allsop et al. [10], with a mean value of the calculated reflection coefficients of 0.92. Please observe that R_c/H_{m0} is higher than the unity for all the numerical tests here analysed, thus the results obtained are very close to the value of 0.90 suggested by Allsop et al. [10]. Numerical results also confirm that the relative crest freeboard R_c/H_{m0} has almost no influence on the reflection coefficients for traditional breakwaters with high crest (R_c/H_{m0} > 1).

Fig. 7.5 shows also that the values of K_r for the innovative caisson are lower than those obtained for the traditional ones, ranging between 0.56 and 0.76. Therefore, K_r is reduced

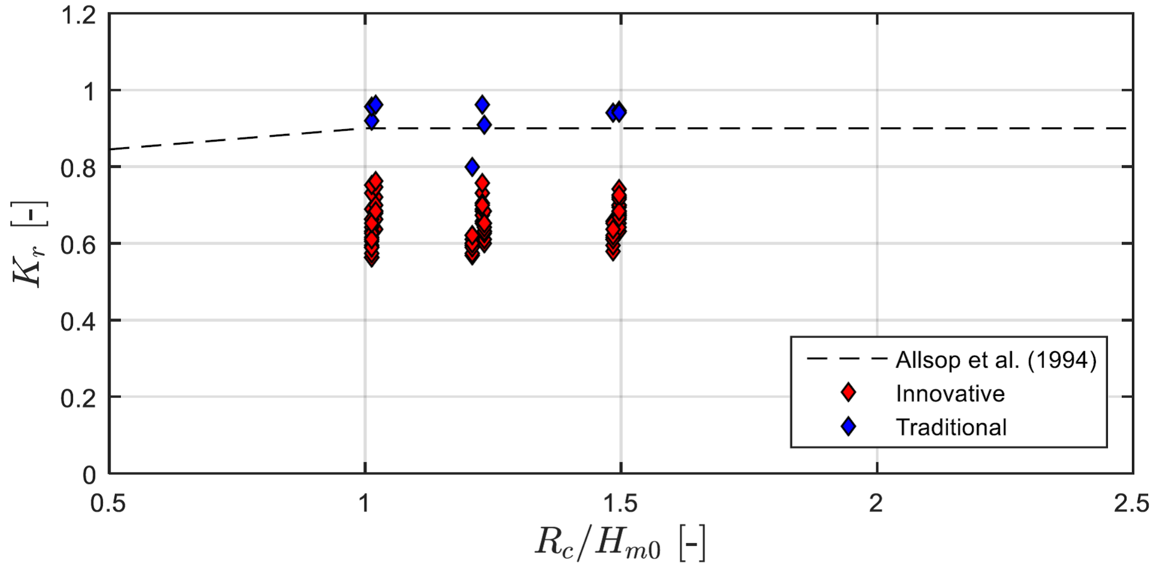

Fig. 7.5 Numerical data points of reflection coefficients for traditional and innovative caisson compared to the formula from Allsop et al. [10].

up to 40% compared to the ones computed on the vertical breakwater. Lower values were expected, due to the energy dissipation when waves interact with the non-conventional geometry of the superstructure. As for the high crested traditional caisson, the relative crest freeboard R_c/H_{m0} has very little influence on the reflection coefficient.

A further analysis is carried out by considering the influence of the ramp crest freeboard R_r and the position of the crown-wall B_{wall} on the reflection coefficients. Fig. 7.6 consists of nine panels, indicating the different incident wave conditions tested in this analysis, as shown in Table 7.2. In each row of Fig. 7.23, the significant wave height is the same, while the peak period increases from the left to the right panel. Contrary, the significant wave height increases from the top to the bottom panel of each column. Each panel displays the numerical values of K_r for different values of B_{wall} and R_r. Fig. 7.6 clearly indicates that the higher is the ramp crest R_r the higher is the reflection coefficient K_r, for all the wave conditions examined. Indeed, a larger amount of the small non-overtopped waves are directly reflected from the ramp with the increase its freeboard, leading to increasing the (bulk) reflection coefficient.

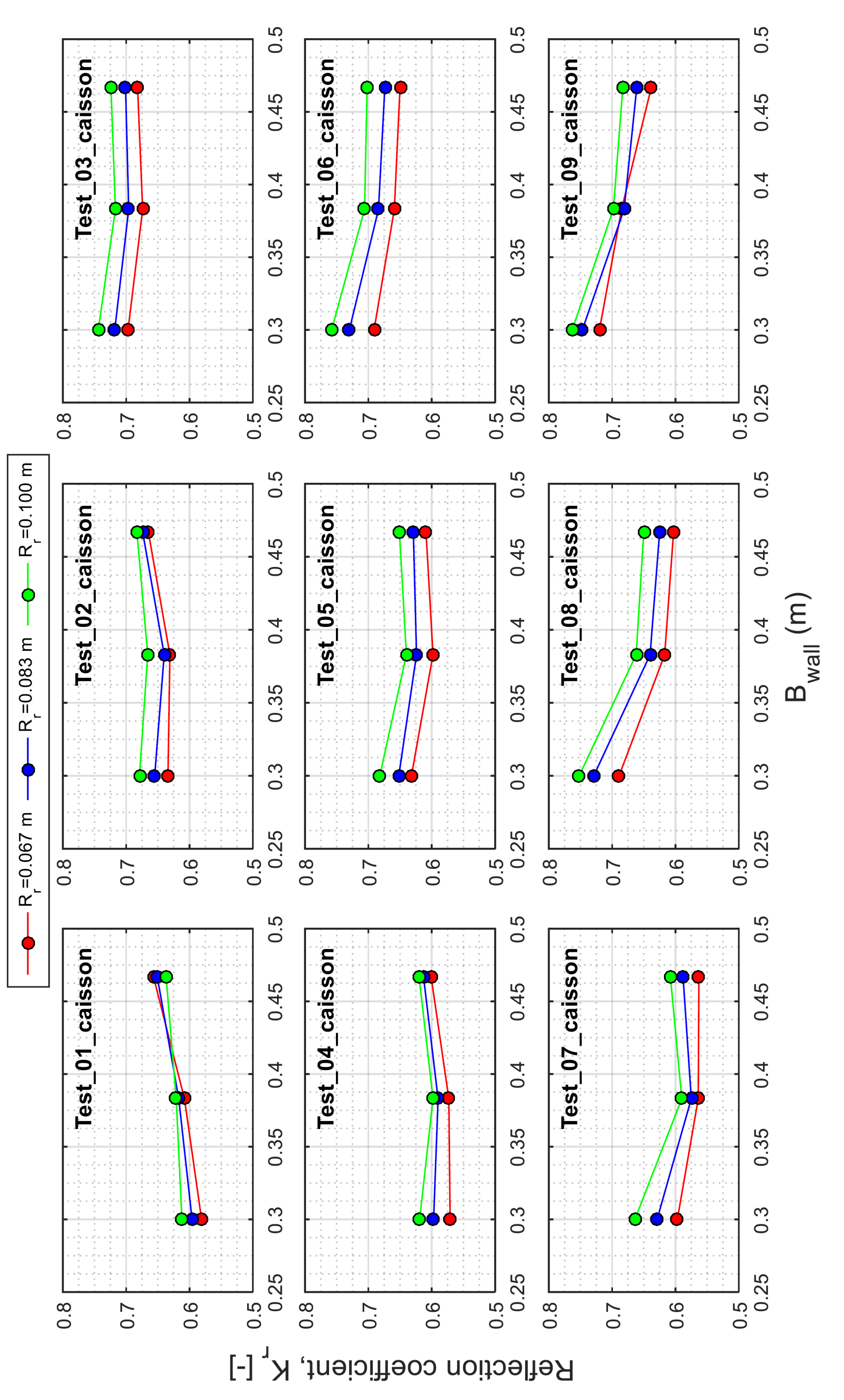

Fig. 7.6 Influence of crown-wall position B_{wall} and crest ramp R_r on the reflection coefficient K_r, for the nine wave conditions.

On the other hand, the influence of the B_{wall} is less evident, although a general trend can be noted with a slight reduction of K_r with the increase of B_{wall}, in particular for tests with higher significant wave heights (bottom panels on Fig. 7.6). More evident is the influence of the energetic period, and so the wavelength based on this period, $L_{-1,0}$, on the reflection coefficient. For each row on Fig. 7.6, the reflection coefficient increases from left to right panels, indicating that for the same significant wave height, K_r increases with the increase of the energetic period, i.e. the effect of the OBREC device on the reduction of the reflection is mitigated when the structure interacts with long waves.

Fig. 7.5 shows how the reflection coefficients decrease with the increase of the nondimensional parameter $(B_{wall}/L_{-1,0})/(R_r/H_{m0})$, which takes into account the over-mentioned parameters that influence the reflection. The points fit reasonably well to an exponential law $[y = a \cdot \exp(-b \cdot x) + c)]$, whose coefficients are evaluated fitting the data with a non-linear least square method. The reflection coefficient on the OBREC-caisson can be derived with the following relation:

$$K_{r,OBREC-caisson} = a \cdot \exp\left[-b \cdot \frac{(B_{wall}/L_{-1,0})}{(R_r/H_{m0})}\right] + c \qquad (7.1)$$

The values of the correlation coefficient R^2 is equal to 0.55 and the empirical coefficients in Eq. 7.1 are: a = 0.4263, b = 6.847 and c = 0.5782. Please note that the formula is valid for the parameter ranges indicated in Table 7.3.

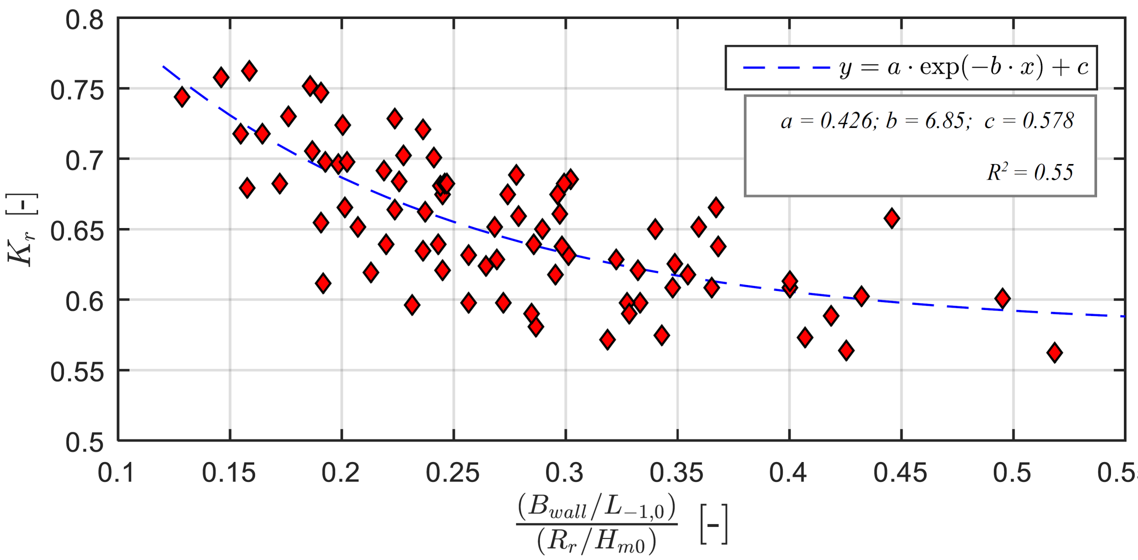

Fig. 7.7 Numerical results of reflection coefficients for the OBREC caisson breakwater function of the relative ramp crest, R_r/H_{m0}, and relative vertical wall position, $B_{wall}/L_{-1,0}$.

7.3.2 Wave overtopping

7.3.2.1 Influence of the geometric parameters

A further numerical analysis carried out on traditional and innovative OBREC-integrated caissons consists of the evaluation of the wave overtopping discharge at the rear side the crown-wall. The use of identical wave generation signals, for each of the different caisson configurations, allows comparing not only the mean wave overtopping discharge, q, per time unit and unit length of breakwater ($m^3/s/m$), but also to match the cumulated wave overtopping volume per unit of length (m^3/m) on time domain. Although the latter represents the damaging effect of wave overtopping much better, many studies have been carried out all over the world to investigate only the average wave overtopping discharge for the specific breakwater geometries, proposing empirical formulas by fitting data from experimental model tests.

The aim of this section is to evaluate the influence of the different geometrical parameters of the OBREC-integrated caisson on wave overtopping discharge. Please observe that wave overtopping data is calculated only for three wave conditions: $Test\_02\_caisson$, $Test\_05\_caisson$ and $Test\_08\_caisson$, for a total of 40 tests. The results of the cumulative wave overtopping volume are shown in three figures: Fig. 7.8 for $Test\_02\_caisson$, Fig. 7.9 for $Test\_05\_caisson$, and Fig. 7.10 for $Test\_08\_caisson$. Each of the three figures shows the cumulative wave overtopping volume for an equal incident wave condition. Left panels show the influence of the relative set-back crown-wall position, $B_{wall}/L_{-1,0}$, for each different relative ramp crest, R_r/H_{m0}. On the other hand, right panels show the influence of R_r/H_{m0} for each different relative position of the set-back wall, $B_{wall}/L_{-1,0}$. Black dashed lines are displayed in each panel, indicating the numerical results of the cumulative wave overtopping discharge at the rear side of the traditional vertically-faced structure. Please note that the different configurations have the same wall crest dimension (R_c = 0.183 m).

For the three figures, results clearly show a reduction in the wave overtopping volume with the increase of $B_{wall}/L_{-1,0}$. The position of the set-back wall is an important factor to consider for the OBREC design. Large values of B_{wall} lead to higher energy dissipation of the waves that overtop the ramp and break into the stilling basin, thus causing a significant reduction the wave overtopping at rear side of the innovative caisson. The results were expected, considering the performance of the OBREC device installed in the rubble-mound breakwater presented by Iuppa et al. [126], where the wave overtopping was found to decrease with the increase of the horizontal distance between the crown-wall and the crest of the ramp.

The results shown in the right panels of the three figures indicate a minor influence of R_r/H_{m0} on the overtopping volume, in particular for high significant wave height (Fig. 7.10). However, higher ramp crest almost always gives the higher wave overtopping values. As for the OBREC integrated into a rubble-mound breakwater, the frontal ramp in the OBREC-caisson works as a deflector, conducting the water jet on the exposed part of the set-back wall and, especially for short distance of the set-back wall, directly at the rear side of the structure.

In conclusion, the wave overtopping analysis suggests that the overtopping discharge for the OBREC-integrated caisson decreases with the increase of the $B_{wall}/L_{-1,0}$ ad with the decrease of R_r/H_{m0}, although the influence of the relative wall position is more significant than that of the relative ramp crest. This behaviour occurs for each of the three incident wave conditions considered in this overtopping analysis and shown in Fig. 7.8, Fig. 7.9 and Fig. 7.10.

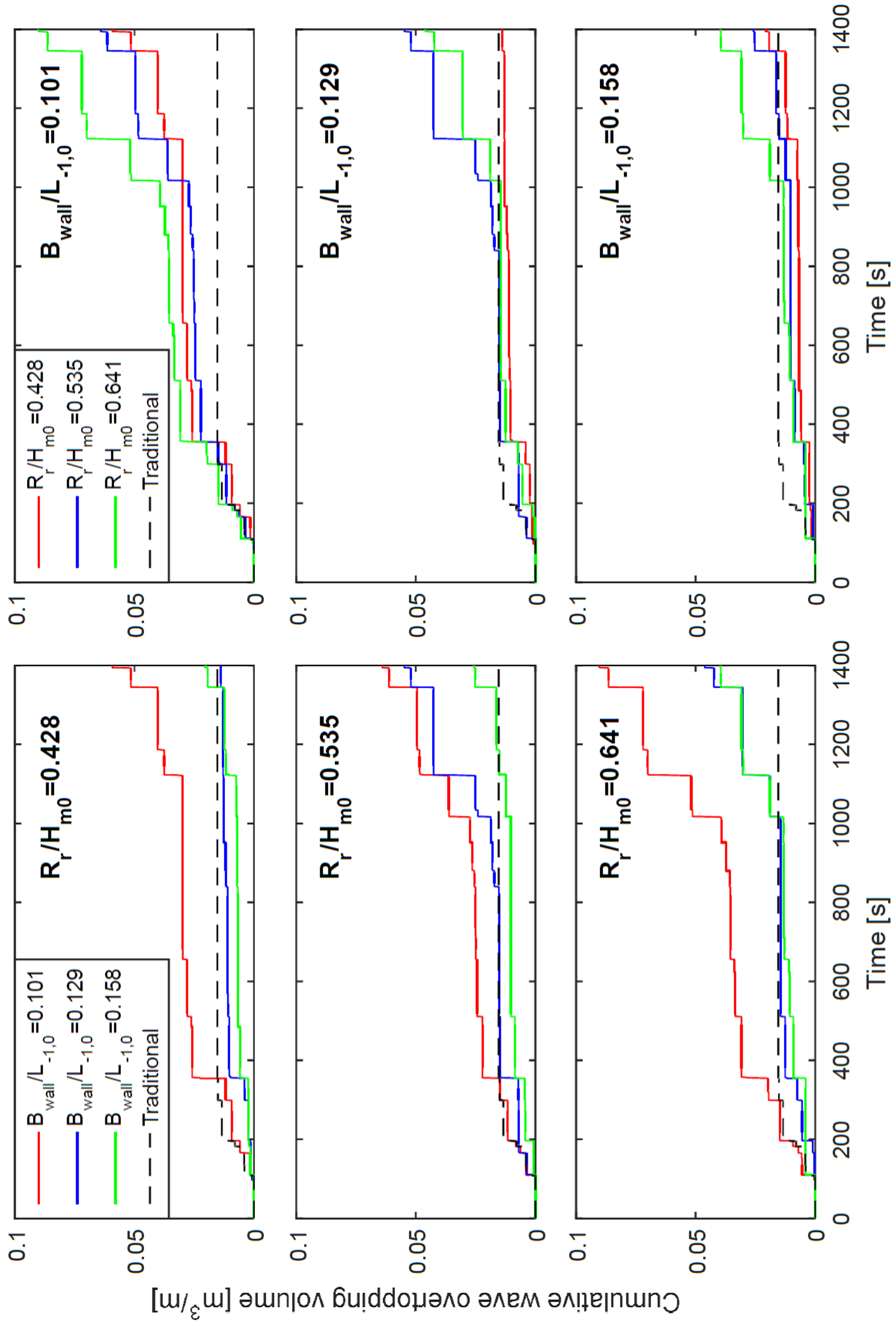

Fig. 7.8 Influence of the relative ramp crest, R_r/H_{m0}, and relative vertical wall position, $B_{wall}/L_{-1,0}$, on the cumulative wave overtopping volume for *Test_02_caisson*.

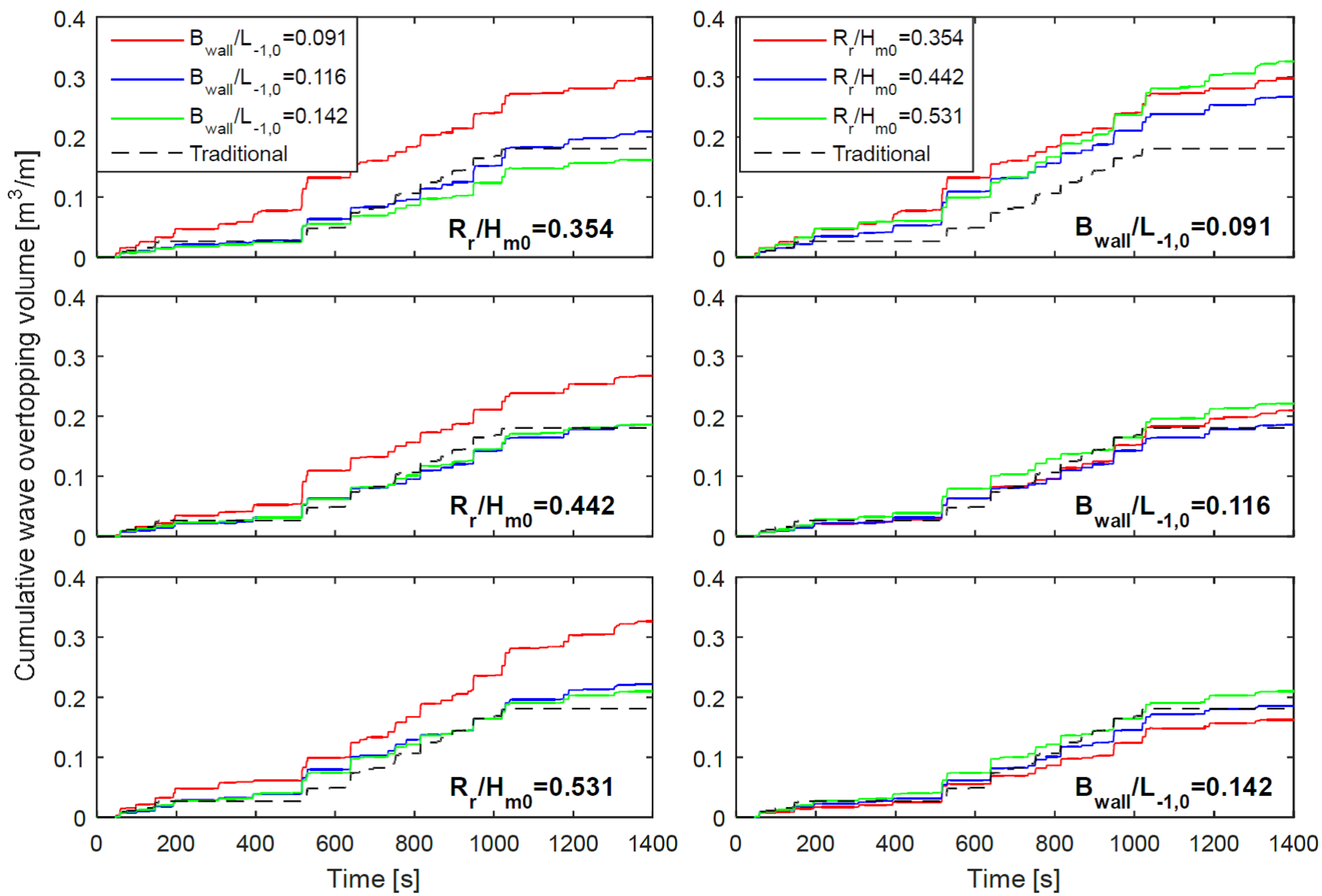

Fig. 7.9 Influence of the relative ramp crest, R_r/H_{m0}, and relative vertical wall position, $B_{wall}/L_{-1,0}$, on the cumulative wave overtopping volume for *Test_05_caisson*.

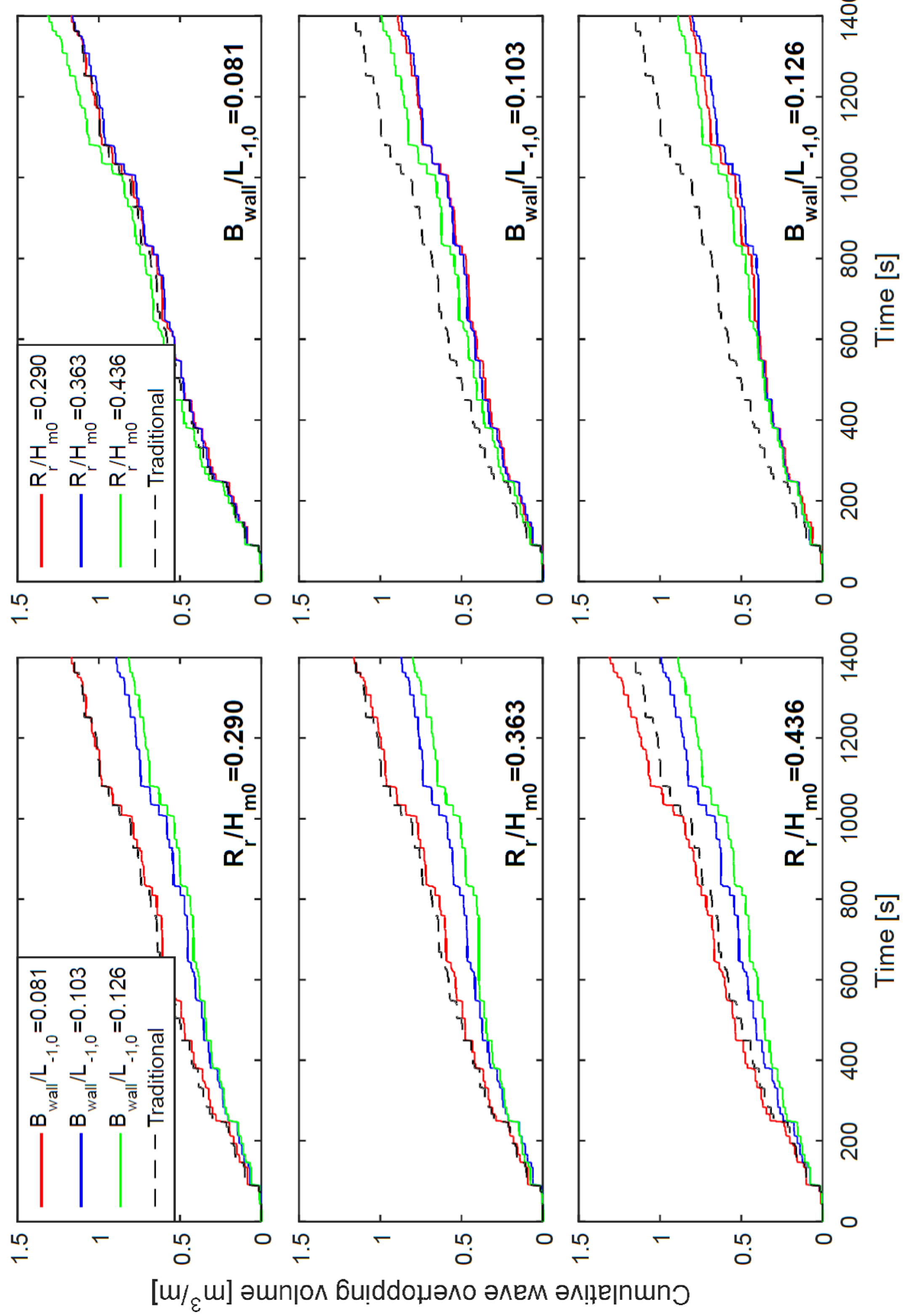

Fig. 7.10 Influence of the relative ramp crest, R_r/H_{m0}, and relative vertical wall position, $B_{wall}/L_{-1,0}$, on the cumulative wave overtopping volume for *Test_08_caisson*.

7.3.2.2 Comparison between innovative and traditional caisson

Regarding the comparison with the traditional vertical breakwater, different behaviours occur depending on the incident wave conditions. Fig. 7.8 represents the results for *Test_02_caisson*, characterized by the highest value of R_c/H_{m0}, which is equal to 1.5. In this condition, the computed wave overtopping at the rear side of the innovative structure is always higher compared to the one computed on traditional breakwater. The worst performance is yielded by the configuration with the highest R_r/H_{m0} and smallest $B_{wall}/L_{-1,0}$, where the mean wave overtopping for innovative breakwater is almost five times the one on conventional breakwater.

With the reduction of R_c/H_{mo} (see Fig. 7.9), the difference between the innovative and traditional caisson configurations is reduced. In this case, for the small dimension of $B_{wall}/L_{-1,0}$, the wave overtopping at the rear side of the innovative structure is higher than the one numerically measured for the traditional structure. Contrary, for higher values of the relative crown-wall position (middle and bottom-right panels of Fig. 7.9), the cumulative wave overtopping volume between the innovative and traditional structure are comparable.

Finally, for lowest values of R_c/H_{mo} (see Fig. 7.10), the wave overtopping volume behind the OBREC-integrated caisson is similar or lower than the traditional one, for almost all the different relative ramp crests, R_r/H_{m0} and crown-wall positions $B_{wall}/L_{-1,0}$. The better performance is yielded by the OBREC with the largest value of the relative distance between the set-back wall and the vertical part of the caisson (bottom right panel of Fig. 7.10), where the mean wave overtopping discharge is around the 60% of the one computed on traditional caisson.

7.3.2.3 Comparison with the EurOtop formula

A further step in the wave overtopping analysis is to compare the numerical results to the formula adopted in the EurOtop Manual [74] to estimate the mean wave overtopping discharge at the rear side of the vertical and steep walls. The EurOtop Manual represents the current state of the art for the analysis and prediction on wave wave overtopping on coastal defence structures. A guidance for the prediction of wave overtopping at vertical structures is presented in Chapter 7 of the EurOtop Manual, including recent works on this topic presented by Bruce et al. [41] and recently by van der Meer et al. [266]. A decision chart for the prediction of the mean discharge at vertical and composite vertical walls is also included in the EurOtop Manual, considering several case scenarios.

As previously described, the numerical model tests are carried out in a domain characterized by a flat bottom in front of the structures, a width slightly larger than the wavelength $L_{-1,0}$ and a relative intermediate water depth. In these conditions, shoaling and depth limiting effects on the spectral shape along the numerical domain can be negligible. The decision chart for wave overtopping on vertical structures divides the case '*without an influencing foreshore*' and structures with a sloping influencing foreshore, giving different formulas for each condition. The EurOtop Manual states that '... *A vertical wall with no influencing foreshore is mainly characterised by an (almost) horizontal foreshore and relatively deep water compared to the wave height*', without giving any limits to distinguish the case of shallow, intermediate and deep water conditions function. In literature various authors such as Holterman [113], Battjes and Groenendijk [25] and Hofland et al. [112] proposed some limits for the interpretation of the various classes of foreshore. For all of them, the shallowness of the foreshores is characterized by the water depth near the structure, h_t, normalized by the offshore wave height $H_{m0,o}$. Due to the flat bottom and the range of the relative water depth h/H_{m0} tested in this analysis and shown in Table 7.3, the results of the numerical analysis are compared to the Equation 7.1 ('no influencing foreshore') of EurOtop Manual [74]. The average wave overtopping discharge over vertical breakwaters and walls is given in EurOtop Manual by the following formula:

$$\frac{q}{\sqrt{g \cdot H_{m0}^3}} = 0.047 \cdot \exp\left[-\left(2.35\frac{R_c}{H_{m0}}\right)^{1.3}\right] \tag{7.2}$$

The empirical coefficients of the exponential formulas are derived from measured data and the reliability of the relationship is given by $\sigma(0.047) = 0.007$ and $\sigma(2.35) = 0.23$, where σ is the standard deviation of the parameter and the coefficients between brackets are mean values, μ, of the parameters. Fig. 7.11 displays the numerical results of nondimensional wave overtopping discharge for traditional and innovative caissons. The numerical data are compared to the Eq. 7.2 from the EurOtop Manual. The 5% under and upper exceedance limits (= 90%-confidence band) are reported in Fig. 7.11 with blue dotted lines, calculated by using $\mu(x) \pm 1.64 \cdot \sigma(x)$ for the two empirical coefficients.

Results show that the numerical data of mean wave overtopping for traditional and innovative breakwater match to the Eq. 7.2 with a high level of accuracy. As can be seen from Fig. 7.11, almost all the data are contained in the 90%-confidence band of the Eq. 7.2. Differences are more evident for high values of relative crest freeboard, where the scatter between the data are higher due to the low amount of wave overtopping discharge. Results indicate that the difference between the various configuration are very small and for preliminary design purpose the Eq. 7.2 can be used to estimate the wave overtopping discharge at the rear side of the OBREC-integrated caisson. Indeed, the wave overtopping is strongly dependent on the maximum height of the parapet, rather than on its position, as already observed by Benassai [26], who studied the wave overtopping behaviour on breakwaters with crown-wall located away from the leading edge of the caisson.

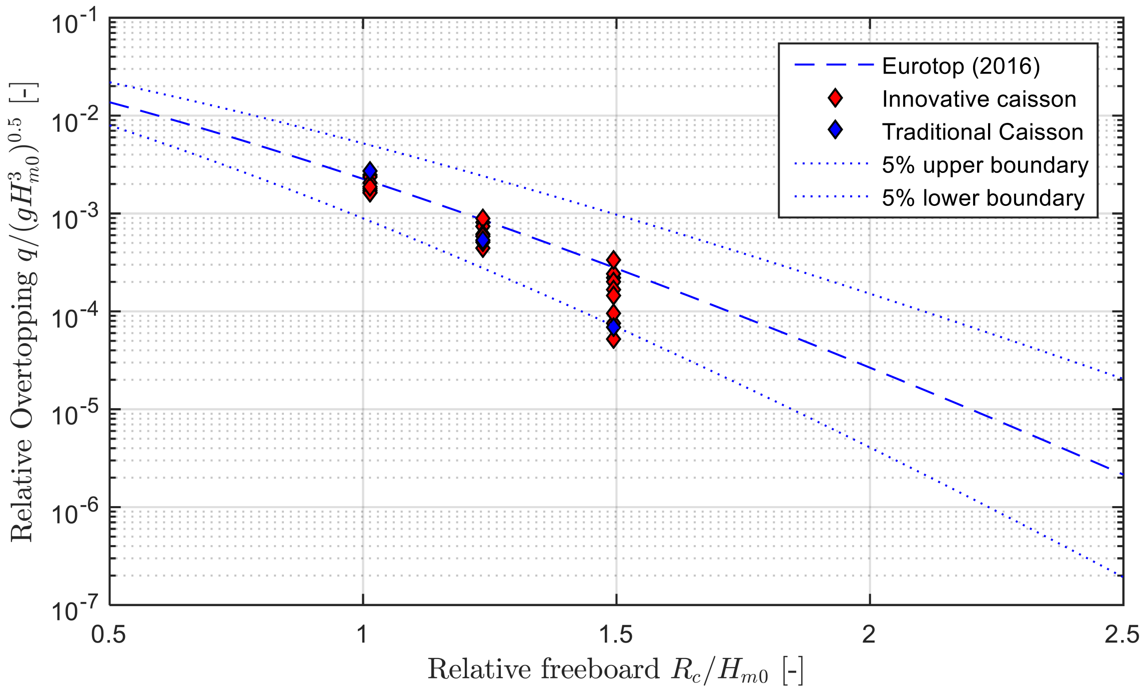

Fig. 7.11 Measured numerical data of the wave overtopping discharges over the traditional (blue points) and the innovative OBREC caisson (red points). Wave overtopping equation for vertical breakwater (Eq. 7.1 in the EurOtop Manual 2016 [74]) with 5% under and upper exceeedance limits (= 90%-confidance band) are reported with blue dotted lines

However, the analysis shows that the variation of B_{wall} leads to a difference between the numerical results of mean wave overtopping on innovative caisson and those estimated using Eq. 7.2. An influence factor, named γ_{OBREC}, is then introduced into Eq. 7.2 to take into account the different geometry of the innovative OBREC-integrated caisson. The equation turns into:

$$\frac{q}{\sqrt{g \cdot H_{m0}^3}} = 0.047 \cdot \exp\left[-\left(2.35\frac{R_c}{H_{m0} \cdot \gamma_{OBREC}}\right)^{1.3}\right] \tag{7.3}$$

Rewriting Eq. 7.3 leads to the expression of γ_{OBREC}, calculated for every numerical data point of the wave overtopping discharge for innovative caisson:

$$\gamma_{OBREC} = \left[\frac{-\left(2.35\frac{R_c}{H_{m0}}\right)^{1.3}}{\ln\left(\frac{q}{0.047\sqrt{g \cdot H_{m0}^3}}\right)} \right]^{(1/1.3)} \tag{7.4}$$

The values of γ_{OBREC} are plotted in Fig. 7.12 in terms of the dominating parameter, which is the relative position of the crown-wall $B_{wall}/L_{-1,0}$. The data fit relatively well (R^2 = 0.70) with the exponential law indicated in Eq.7.5:

$$\gamma_{OBREC} = 1.163 \cdot \exp\left(-1.737\frac{B_{wall}}{L_{-1,0}}\right) \tag{7.5}$$

The coefficient γ_{OBREC} is then introduced in Fig. 7.13, where the numerical data are better predicted by the Eq. 7.3 indicated with a black dashed line.

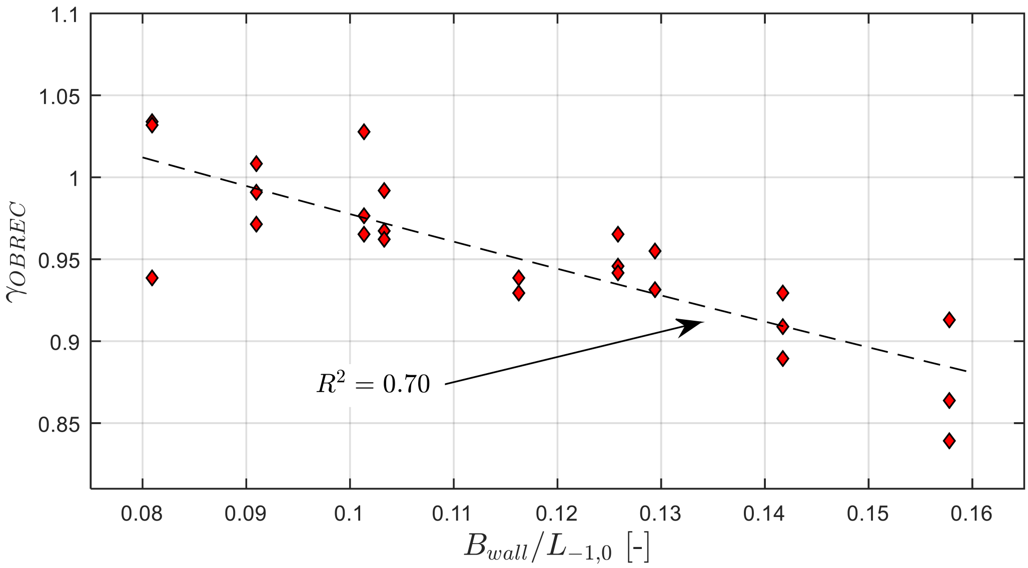

Fig. 7.12 Calculated γ_{OBREC} as a function of the relative vertical wall position, $B_{wall}/L_{-1,0}$

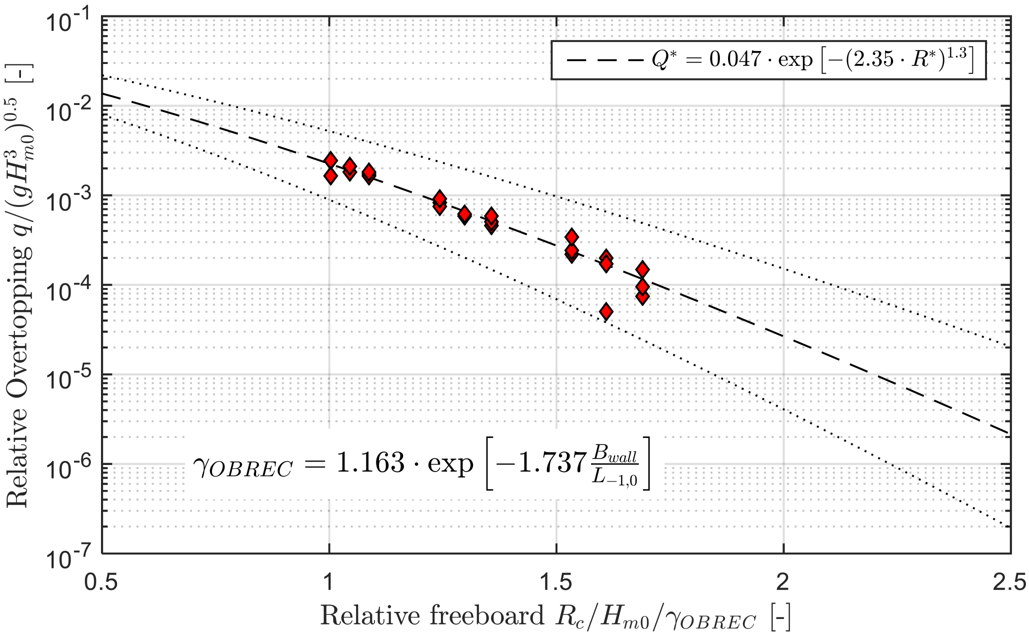

Fig. 7.13 Numerical data points of the wave overtopping compared to the formula from EurOtop Manual corrected with the coefficient γ_{OBREC} to take into acconto the OBREC geometry.

7.4 Wave loading

It this section, the analysis of the forces exerted on traditional and innovative caisson is presented. The methodology adopted to evaluate the loadings is similar to the one described in Chapter 5. The analysis is carried out considering the forces based on the average of the highest $1/250^{th}$ peaks of the forces in a given random sequence, denoted as $F_{1/250}$. Considering that the average number of waves for each test is around 1000 waves, the force is calculated as the average value of the 4 highest peaks in a time series. These peaks are evaluated considering a high-pass threshold that varies depending on the wave condition and the part of the structure on which the pressure is integrated. Furthermore, a minimum time window between impacts is set equal to T_{mean} in order to only take into account the local maximum force for each single incident wave. Please note that the resultant wave forces are calculated assuming a linear pressure distribution between the dynamic pressure numerically calculated in each cell.

A sketch of the wave pressure distribution and force exerted on the traditional and innovative caisson is displayed in Fig. 7.14. The figure also indicates how the total vertical ($F_{h,OBREC}$) and horizontal forces ($F_{v,OBREC}$) exerted on the innovative caisson are calculated, taking into account the loading on the vertical frontal face caisson, $F_{h,OBREC,caisson}$, the ramp, $F_{OBREC,ramp}$, the bottom reservoir, $F_{v,OBREC,res}$, the base caisson, $F_{v,OBREC,base}$, and the vertical wall, $F_{h,OBREC,wall}$. Contrary, the horizontal and vertical force exerted on the traditional vertically-faced structure is indicated as $F_{h,trad}$ and $F_{v,trad}$, respectively.

7.4.1 Wave loads compared to the Goda formulas

Although the numerical model has been validated extensively against physical model tests and semi-empirical formulas by Lara et al. [152], Losada et al. [163] and Guanche et al. [101], the first part of the present analysis is aimed at comparing the force exerted on the traditional caisson to the design formula usually adopted by engineers for design purpose.

As described in Chapter 2, the most adopted method for the evaluation of the force exerted on a vertical caisson is the ones described in Goda [95], in which a trapezoidal pressure distribution along the vertical wall and a triangular distribution on the base are assumed, regardless of whether the waves in front of the caisson are breaking or not. Regarding the design wave to be used, if seaward of a surf zone, Goda [95] recommends a value of $1.8 \cdot H_s$ to be used for practical design, corresponding to the 0.15% exceedance values for a Rayleigh wave height distribution, also corresponding to $H_{1/250}$, i.e. the arithmetic mean of the 0.4

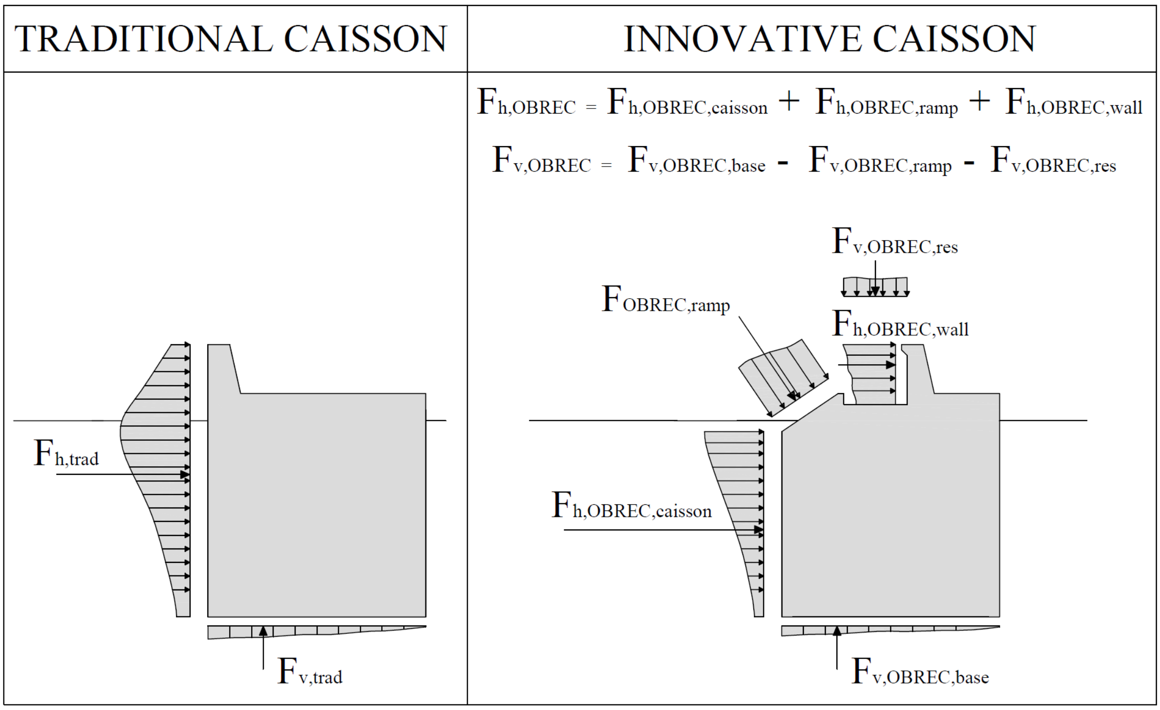

Fig. 7.14 Sketch of the wave pressure distribution and forces exerted on traditional vertical breakwater (left panel) and innovative caisson integrated with the OBREC device (right panel).

per cent highest waves. Considering the relatively deep water in front of the structure, a design wave $H_d = 1.8 \cdot H_{m0}$, is adopted in the analysis, where H_{m0} is the significant wave height calculated from the incident wave spectra. Regarding the period, Goda [95] suggests to use the significant wave period, $T_{1/3}$, i.e the mean of the periods associated to the average one-third of the highest wave height. However, the analysis on vertical breakwaters described in the PROVERBS project suggests using the peak period, T_p, instead of the significant period as indicated by Goda [95]. Following the suggestion of the PORVERBS, T_p is adopted in this analysis for the calculation of the Goda formulas. Finally, as indicated by Goda [95], the wavelength adopted for the calculation of the three coefficients, α_1, α_2 and α_3, is the local wavelength at water depth h_f, defined as the depth at the location at a distance $5H_s$ seaward the breakwater. Please observe that the ratio between the depth above the armour layer of the rubble foundation and the water depth in front of the breakwater, d/h, is equal to 0.82 for all the tests, hence the correction proposed by Takahashi [238] does not change the magnitude of the pressure calculated with the Goda formulas, i.e. no impulsive wave pressure condition occurs for the tests here considered.

Fig. 7.15 shows the comparison of the horizontal (left panel) and uplift forces (right panel) between the values calculated with the Goda formulas and the forces ($F_{1/250}$) calculated on the vertical breakwater with the numerical model. The two panels indicate the mean and standard deviation of the relative error, defined as the difference between the forces calculated with the Goda formulas minus the ones calculated with IH2VOF, divided by the former values. These errors are expressed in percentages and calculated for each of the nine numerical tests carried out on traditional vertically-faced structures. Results indicate a general good match between the data, with a slight overestimation of the horizontal force of 13.7% and an underestimation of the uplift force exerted on the structure of 12.5%.

The overall results can be considered highly satisfactory, bearing in mind the level of uncertainness associated with these semi-empirical formulas, as studied in Juhl and Van der Meer [133], Bruining [42] and Van der Meer et al. [262], and discussed in Chapter 4.1 of the PROVERBS (Vol. 2) [207] and recently reported in Agerschou [3]. For instance, Van der Meer et al. [262] showed the results of the ratio between the forces (horizontal and vertical) computed with Goda method and those measured in laboratory for different geometries and wave conditions with irregular waves, indicating a very large scatter of the results. With this in mind, the Authors concluded that "*the Goda method gives only a rough estimation of the force*" [262].

Please note than the widely adopted Goda formulas were originally proposed by the Author after laboratory tests using regular waves [96] and [93]. This can explain the slight discrepancy, well knows in literature, when results of tests carried out adopting irregular waves are compared with Goda formulas. On the other hand, the adoption of regular waves for wave loading on vertical structure results in a better agreement with the Goda formulas, as recently shown by [55].

7.4.2 Wave exerted forces on traditional and innovative caisson

The forces exerted on the traditional and innovative caisson are analysed in this section, investigating the influence of the two geometrical parameters B_{wall} and R_r. The total horizontal and vertical forces ($F_{1/1250}$), numerically computed on the innovative caisson as displayed in Fig. 7.14, are compared with the numerical horizontal and vertical forces calculated on the traditional vertically-faced structure.

Fig. 7.16 shows the influence of the relative ramp crest, R_r/H_{m0}, and the relative crown-wall position, $B_{wall}/L_{-1,0}$, on the ratio between the horizontal forces exerted on the innovative and traditional caisson, $F_{h,OBREC}/F_{h,trad}$. Dotted black lines are included in the panels,

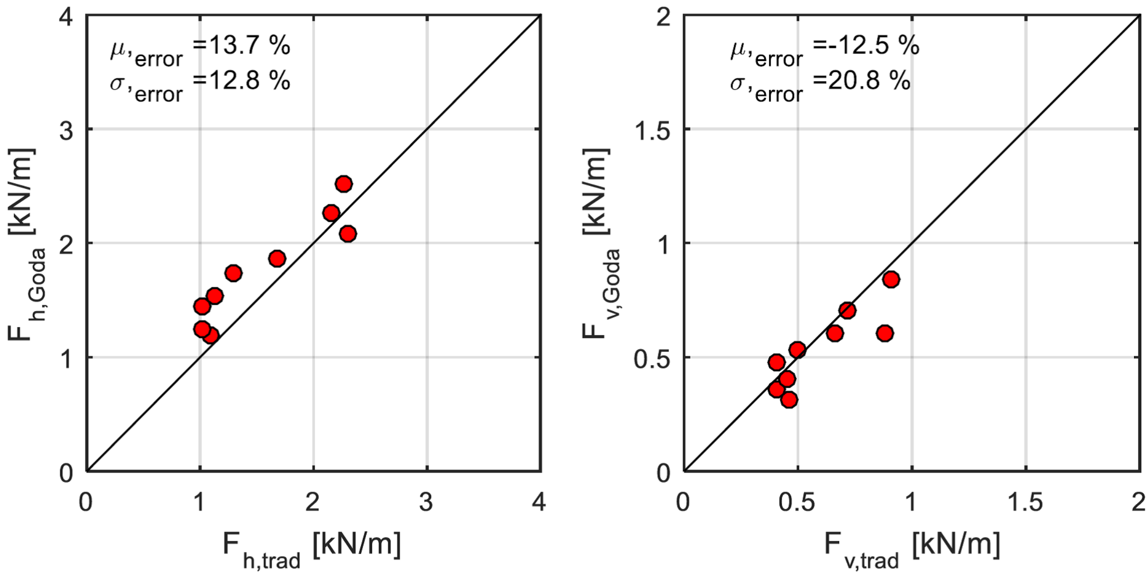

Fig. 7.15 Comparison between the numerical horizontal (left panel) and vertical forces (left panel) on traditional breakwater with those computed with Goda formulas [95].

indicating the condition where the total horizontal forces between the two different caisson configurations are equal. The left panel in Fig. 7.16 indicates that the ratio between innovative and traditional caisson is not influenced by R_r/H_{m0}. Contrary, the increase of the ration $B_{wall}/L_{-1,0}$ leads to a slightly reduction of the $F_{h,OBREC}$ compared to the one calculated on the vertical caisson (right panel).

As presented in previous sections, the increase of $B_{wall}/L_{-1,0}$ leads to reducing the overtopping at the rear side of the OBREC crown-wall. The reduction of the overtopping does not cause an increase of the total force on the structure, due to the energy dissipation of the waves that overtop the ramp and break in the reservoir. Furthermore, as will be shown in the next sections, the position of the set-back crown-wall in the OBREC-caisson influences the time lag between the maximum force peaks acting on the caisson and on the wall. Therefore, the increase of the B_{wall} further reduces the maximum total horizontal peak forces exerted on the innovative breakwater, compared to the traditional one. Results shown in Fig. 7.16 clearly indicate that the total horizontal forces exerted on the innovative caisson are, for most of the analysed cases, lower than the ones calculated on the vertical breakwaters, with a reduction up to 40%.

It is worth nothing that these results are similar to the ones obtained by Oumeraci et al. [206] on a caisson with a vertically lower part with semi-cylindrical shells that terminates with a plane slope on the top upper part. The authors calculates a reduction of the horizontal impact forces between 30 and 60% compared to the vertical flat front, depending on the prevailing waves and depth conditions. Similar results have been recently obtained by Misra et al. [180]. The authors conducted a numerical analysis on the Civitavecchia breakwater, characterized by a particular superstructure with curved and recessed parapet, compared to a traditional vertical structure. Results indicates that the use of the non-conventional geometry at the Civitavecchia breakwater reduces the total landward forces of around 20% compared to the ones computed on a vertical structure.

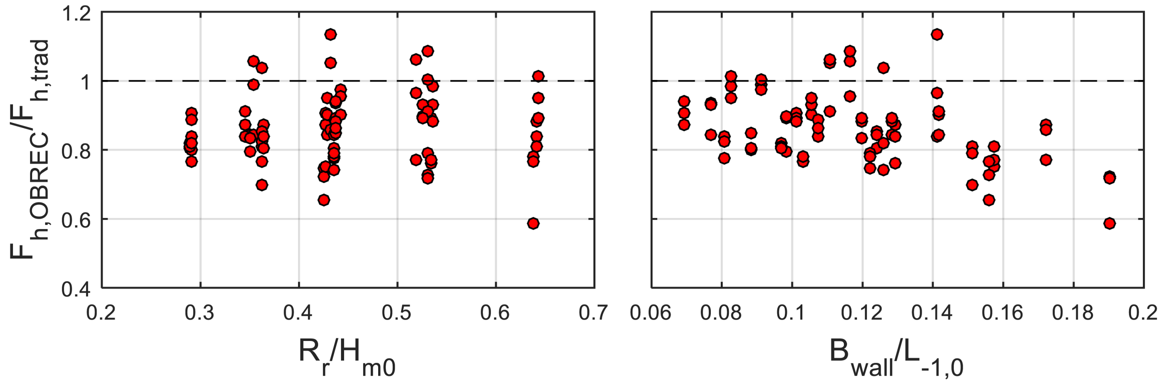

Fig. 7.16 Influence of the relative ramp crest R_r/H_{m0} (left panel) and the relative wall position $B_{wall}/L_{-1,0}$ (right panel) of the ratio between the total horizontal forces exerted on the innovative and traditional caisson, $F_{h,OBREC}/F_{h,trad}$.

Fig. 7.17 consists of 3 panels and indicates the values of the ratio $F_{h,OBREC}/F_{h,trad}$, for different values of B_{wall} and three incident wave conditions($Test\_01\_caisson$, $Test\_02\_caisson$ and $Test\_03\_caisson$), characterized by the same significant wave height (H_{m0} = 0.15 m) and three peak periods indicated on the top. Each panel shows the results for a fixed value of the ramp crest tested in this analysis. Results confirm the importance of the position of the crown-wall on the reduction of the total horizontal forces when compared to the ones computed on the vertical caisson. The increase of B_{wall} leads to a reduction of the ratio $F_{h,OBREC}/F_{h,trad}$ for almost all the tests shown in Fig. 7.17. Furthermore, for a fixed value of the relative crest ramp R_r/H_{m0}, i.e. for each of the three panels, results indicate that higher reduction of the force occurs with waves characterized by small peak periods. Conversely, as explained in the previous section, long waves are less influenced by the presence of the OBREC device embedded on the caisson, leading to only a slight reduction compared to the total forces computed on the vertically-faced structure. In detail, for the highest value of T_p and the lowest value of B_{wall}, the performance of the two configurations in terms of total horizontal wave forces are almost the same.

Fig. 7.18 displays influence of R_r/H_{m0} and $B_{wall}/L_{-1,0}$ on the ratio between the total vertical forces exerted on the innovative and traditional caisson $F_{v,OBREC}/F_{v,trad}$. Dotted

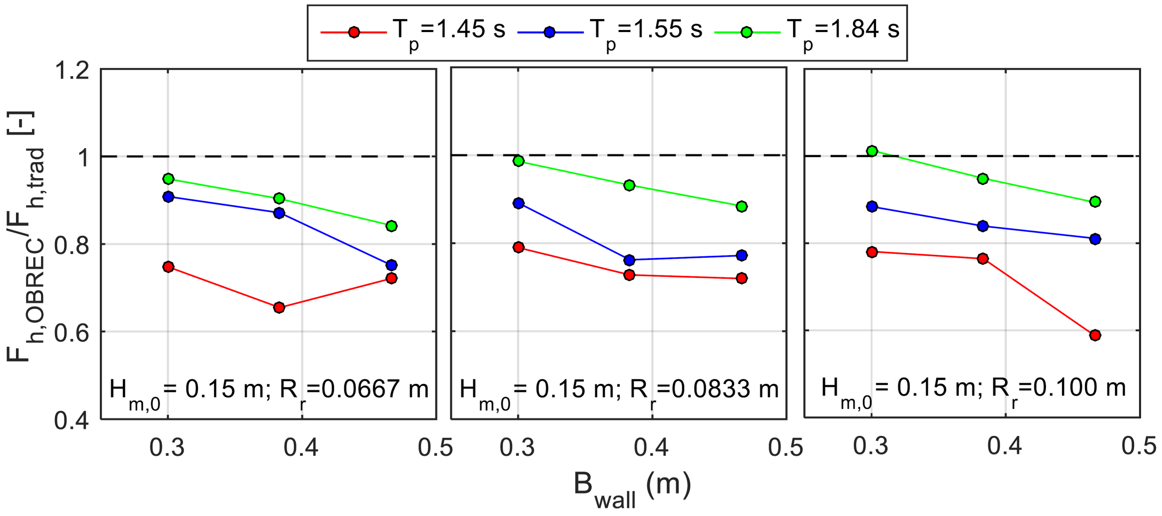

Fig. 7.17 Influence of the B_{wall} and R_r on the ratio $F_{h,OBREC}/F_{h,trad}$, considering tests with the same significant wave height, H_{m0} and three different peak periods, T_p.

black lines indicates the condition where the vertical forces between the two configurations are equal. The two panels in Fig. 7.18 show that $F_{v,OBREC}/F_{v,trad}$ is slightly reduced with the increase of R_r/H_{m0} (left panel) and $B_{wall}/L_{-1,0}$ (right panel). As expected, the introduction of the OBREC device on vertical caissons induces a reduction of vertical forces due to the relevant downward components exerting on the ramp and the bottom reservoir. Furthermore the wave energy dissipation inside the reservoir reduces further the total forces on the structure. Plesas obesrve that for higher values of R_r/H_{m0} and $B_{wall}/L_{-1,0}$ the downward forces on the OBREC is half of the vertical uplift exerting on the base caisson, thus increasing the overall stability of the innovative structure.

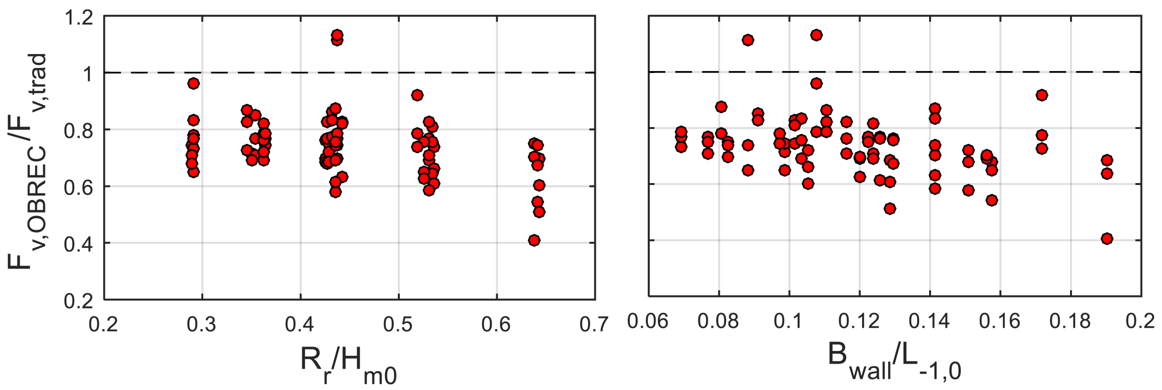

Fig. 7.18 Influence of the relative ramp crest R_r/H_{m0} (left panel) and the relative wall position $B_{wall}/L_{-1,0}$ (right panel) of the ratio between the total vertical forces exerted on the innovative and traditional caisson

Similarly, Fig. 7.19 indicates the values of the ratio $F_{v,OBREC}/F_{v,trad}$, for different values of B_{wall} and three wave conditions, with the same significant have weight and three different peak periods, which are displayed on the top. The results here displayed refer to *Test*_01_*caisson*, *Test*_02_*caisson* and *Test*_03_*caisson*. The panels show the results for three values of R_r considered in the present numerical analysis. As commented above, results show the importance of the B_{wall} on the reduction of the overall vertical forces. The increase of B_{wall} leads to a reduction of the ratio $F_{v,OBREC}/F_{v,trad}$ for all the tests displayed in Fig. 7.19. Moreover, higher values of the ramp crest freeboard R_r lead to a higher downward (stabilizing) forces, thus reducing the ratio between the total vertical forces on the OBREC-caisson compared to the ones exerted on the traditional vertically-faced breakwater, as can be noted moving from the left to the right panel in Fig. 7.19. Contrary to the results shown for the horizontal total forces displayed in Fig. 7.17, the change in peak period has a lower influence on the ratio $F_{v,OBREC}/F_{v,trad}$.

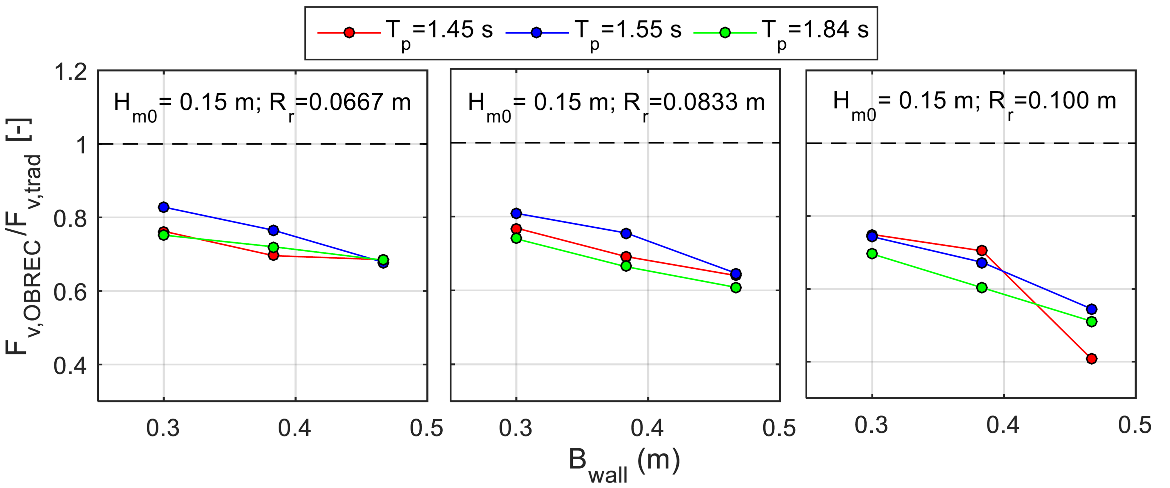

Fig. 7.19 Influence of the B_{wall} and R_r on the ratio $F_{v,OBREC}/F_{v,trad}$, considering tests with the same significant wave height, H_{m0} and three different peak periods, T_p.

7.4.3 Forces on the set-back wall

A set-back parapet on the top of vertical breakwaters has been adopted as a solution to reduce the impact pressure exerted on the caisson superstructure and its effect on the breakwater stability. Examples of breakwaters with capping walls set back with respect to the wall profile are the *Diga Duca degli Abruzzi* in Naples, the breakwater at the Civitavecchia Harbour in Rome, and the dike in Bagnara, described by Franco [81]. Although the importance of this non-conventional superstructure, scarce literature regarding the pressure and forces exerted on it exists around this subject.

Benassai [26] and Van der Meer and Benassai [261] investigated the wave pressure and forces on a small model reproducing different cross-sections of the breakwater proposed for the extension of the Civitavecchia Harbour in Italy. Local impact pressures on the set-back parapet were measured and different shapes of the signals were classified in schematic diagrams. Pressure signals on the structure were characterized by an oscillatory nature, which is influenced by the compression of the air-pocked trapped between the wave and the parapet. Benassai [26] demonstrated that the superstructure influenced the vertical slamming forces, which in turn has a relevant effect on the structure stability. Gonzales and Valdes [99] demonstrated that a set-back wall does not contribute to the total wave thrust on the structure, because the force exerted on it are out of phase with respect to the force on the main profile. The overall stability is increased due to the reduction of forces caused by the delay in wave action on the two surface and due to the prevention of impulsive breaking wave conditions caused by the wave discontinuity. Finally, the Italian Standards (*'Istruzioni tecniche per la progettazione delle dighe marittime'*) suggests that the superstructure 'must be verified according to the norms supposing that the maximum pressures exerted on it are given by the Hiroi formulas (p=1.5 ρ g H).

In this section, the numerical results of the horizontal forces exerted on the set-back wall of the innovative caisson are investigated. Please note that the height of the wall, i.e. the vertical distance between its crest and the bottom reservoir, a_{wall}, is constant and equal to 0.183 m (see Fig. 7.3). Moreover, the water depth, h, is also constant, hence the crown-wall has the same values of crest freeboard R_c. As a consequence, the various wall configurations are obtained with a horizontal translation of the wall, assuming constant its distance to the water level.

Fig. 7.20 shows how the nondimensional horizontal force on the wall, $F_{h,OBREC,wall}$ / $(\rho g H_{m0} a_{wall})$, varies with the ratio between the significant wave height and the water depth, H_{m0}/h. The three panels in Fig. 7.20 indicates the forces exerted on the wall for the three different dimensions of the frontal ramp crest, R_r. Moreover, in each panel the results are distinguished depending on the different crown-wall position, B_{wall}, compared to the vertical part of the caisson. On the top of Fig. 7.20, a sketch of the horizontal forces here considered is displayed. Results clearly indicate a pronounced linear dependency between the nondimensional forces on the wall and the ratio H_{m0}/h. The behaviour is similar to that observed by many authors [131, 212] that studied the resultant force exerted on crown-wall placed on the top of rubble-mound breakwaters. As can be observed the average pressure on the wall, computed as $F_{h,OBREC,wall}/(a_{wall})$, ranges between 0.7 to 3 $\rho g H_{m0}$, while the influence of the R_r and B_{wall} on the dimensionless forces is not clear.

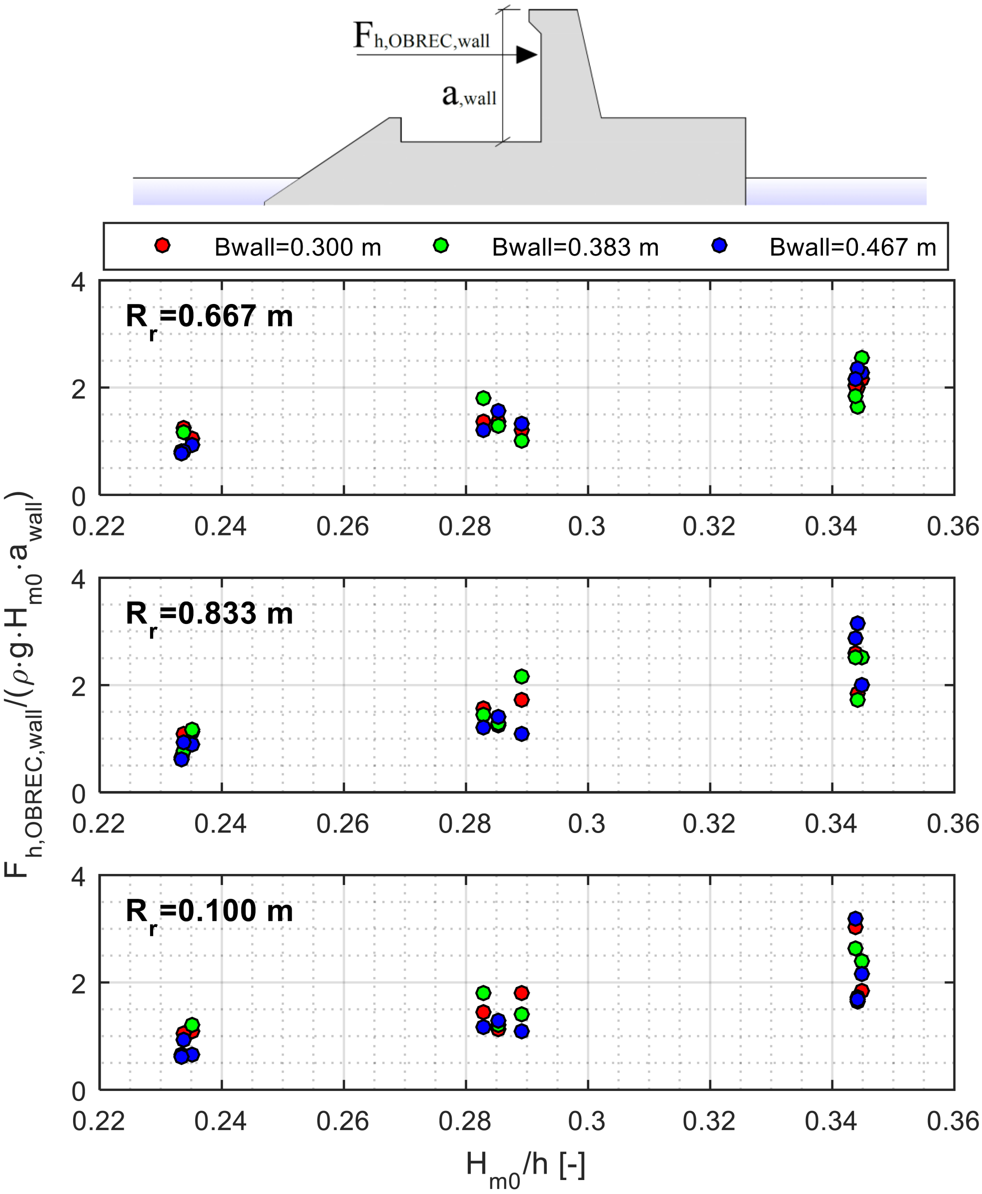

Fig. 7.20 Influence of H_{m0}/h on the non-dimensional force exerted at the set-back wall for different values of the ramp crest R_r and wall position B_{wall}.

The characteristic of the wave loading on the set-back wall is evaluated considering the time series of the forces exerting on in, where the occurrence of impact loads cannot be completely excluded. In this regards, Fig. 7.21 shows on the upper panel an example of the time series of the wave force on the set-back wall for the *Test_08_caisson* with the R_r=0.067 m and B_{wall} = 0.300 m. The signal shows evident rapid variations in time, with high force peaks typically described as impact wave loads. The so-called "church-roof" shape of the force signal can be recognized, as the ones occurred for wave breaking waves on vertical structure [207]. On the bottom panels of Fig. 7.21, nondimensional wave pressure distribution ($p/\rho g H_{m0}$) along the crown-wall are displayed for seven time instants. These instants are chosen as the representative instants including the one corresponding to the maximum force on the set-back wall (t = 435.865 s) for this specific test. Please observe that the reference system for the pressure distribution indicated on the seven bottom panels of Fig. 7.21 has its origin on the bottom part of the wall pointing on the tip of the wall, as indicated on the right part of the upper panel.

As can be observed in Fig. 7.21, the pressure on the set-back wall exhibits impact pressure, with p_{max} around 6 $\rho g H_{m0}$. It is worth noting that the pressure signals, especially on the upper part of the crown-wall, have relatively small peak pressure if compared to the general pressure peaks for violent impact loading on vertical walls, which can be up to 50 $\rho g H_{m0}$ at the still water level, as shown by many authors [228, 106, 8, 207, 48]. The energy dissipation due to the wave run-up over the ramp and on the reservoir attenuates the pressure peaks, as already recognized by Vicinanza et al. [276] and Contestabile et al. [64] on test campaign conducted on the OBREC installed on the rubble-mound breakwater.

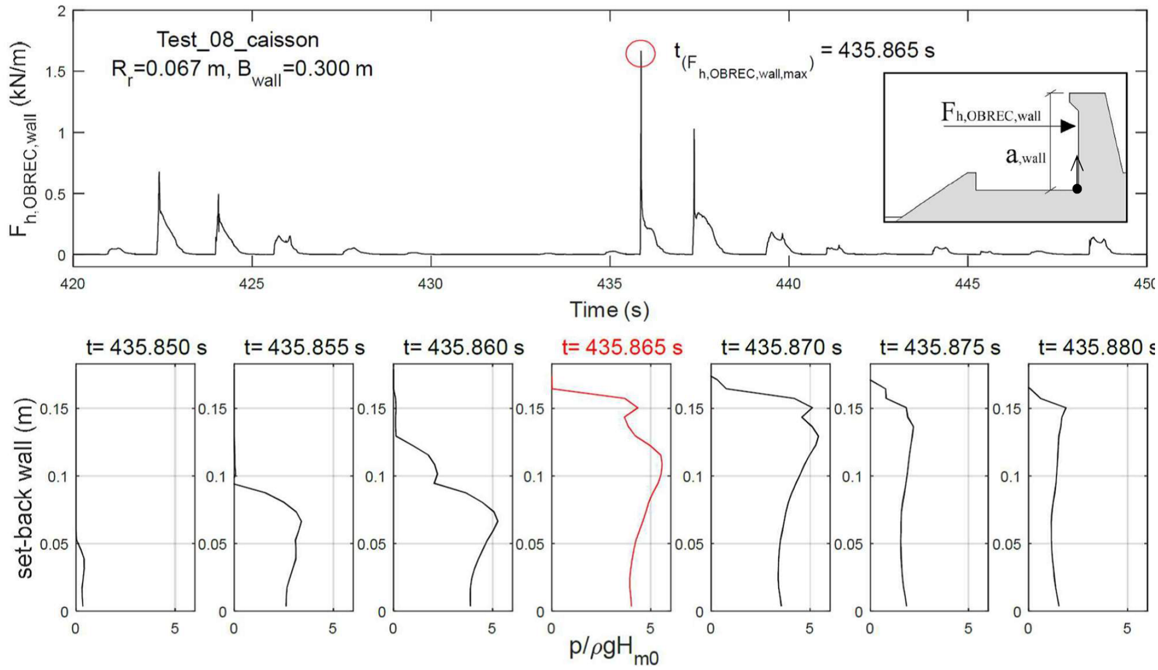

Fig. 7.21 Time series of the wave forces exerting on the set-back wall (upper panel) and nondimensional wave pressure distribution $p/\rho g H_{m0}$ along the wall for seven representative time instants (bottom panels) for *Test_08_caisson* with R_r = 0.067 m B_{wall} = 0.300 m

Finally, Fig. 7.22 indicates the variation of the horizontal force on the wall in function of the peak period T_p. The panels display the results the nine OBREC configurations considered in the numerical analysis, while each panel indicates the forces on the wall classified for the three significant wave heights computed at the toe of the structure. As already shown in Fig. 7.20, the horizontal forces on the wall strongly increase with the increase of H_{m0}. Unlike the results of the wave forces on the crown-wall on rubble-mound breakwater obtained from various authors [131, 212], for a set-back wall behind a crest ramp on a vertical caisson the forces are less dependent on the peak period.

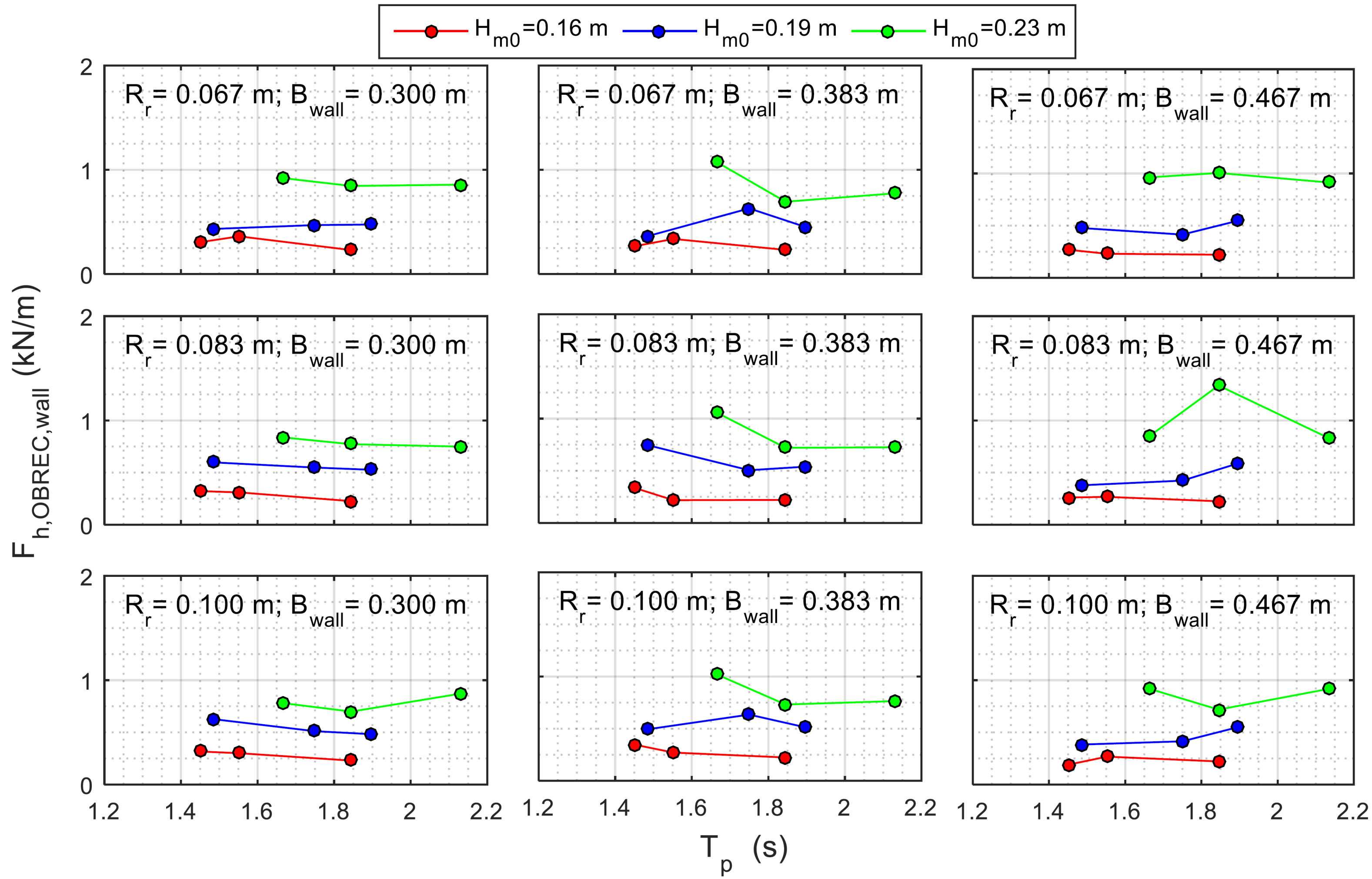

Fig. 7.22 Variation of the horizontal force on the wall in function of the peak period T_p for all the incident wave condition and geometrical configuration tested in the analysis.

7.4.4 Stability analysis

The design of a vertical breakwater required a stability analysis of the caisson and its foundation. In detail, the caisson must be designed to be safe against sliding and overturning. Moreover, the hydraulic stability and bearing capacity of the rubble-mound foundation and the seabed need to be investigated, considering that geotechnical failure may lead to the stability loss of the caisson situated on it. It is customary to evaluate the bearing capacity of the foundation using the traditional methodology in geotechnical engineering, with a foundation subjected to inclined and eccentric loads produced by the weight of the upright section and wave forces.

In this analysis, only the stability analysis of the caisson is considered. In coastal engineering, the overturning around the caisson heel has been traditionally considered as an overall failure mode of the structure. This method implicitly makes the assumption of a rigid foundation below the structure. In most cases, sliding is more severe than overturning, especially when the breakwater crest is relatively low. Indeed, the most common modes of failure caused by wave load due to plunging breakers are sliding, shear failure on the foundation, but rarely overturning [93, 239]. In reality, the overturning is a direct consequence of the hydraulic instability and failure of the yielding foundation. The traditional design procedure against the overturning of the caisson is considered by many authors (see for example Oumeraci [204] and Agerschou [3]) too simplistic and unrealistic as it does not take into account the loss of the bearing capacity and the capacity failure of the rubble-mound and sub-soil foundation. A technical framework for the stability analysis and foundation bearing capacity failure due to the dynamic structure-foundation interaction has been developed then by Oumeraci et al. [207].

For the over-mentioned reasons, only sliding on the rubble-mound foundation is here considered. This failure is much more severe than the overturning in most of the cases, especially when the breakwater crown-wall is relatively low, as the traditional caisson designed in Japan [239]. The safety factor of the traditional and innovative caisson again the sliding over the foundation, Cs, is computed as:

$$Cs = \frac{\mu(Mg - F_v)}{F_h} \tag{7.6}$$

where μ is the coefficient of (static) friction between the base caisson and the rubble foundation, F_h and F_v are the resulting overall horizontal and vertical wave forces numerically calculated on the innovative and traditional caisson as shown in Fig. 7.14; M is the mass of the monolithic structure per unit extension, including the sand fill and superstructure; and g is the acceleration due to the gravity. In the present analysis, the coefficient of friction is assumed to be 0.6, while the mass densities γ_c of the caisson could be assumed, based on classical design, to be 2.1 t/m^3 for the sand-filled caisson and 2.3 t/m^3 for the concrete superstructure. For the submerged part of the caisson, a mass density of 1.1 t/m^3 is considered. For the two configurations, the sand-filled caisson is assumed to be extended until 0.05 m (1.5 m in prototype scale) above the SWL.

The time series of the safety factors again the sliding, Cs, for the traditional and innovative caisson are analysed for each test. Please note that, contrary to the statistical analysis of the resultant horizontal and vertical forces, Cs is here considered as the minimum value during the test. The latter occurs at the instant of the maximum destabilizing forces, F_s, defined as:

$$F_s = F_h + \mu F_v. \tag{7.7}$$

Fig. 7.23 consists of nine panels, indicating the different incident wave conditions tested in this analysis, as shown in Table 7.2. In detail, in each row of the Fig. 7.23 the peak period increases from the left to the right panels, while the wave height increases from the top to the bottom panel of each column. Each panel displays the values of Cs for different values of B_{wall} and R_r. Horizontal red dotted-lines are included in the panels, indicating the numerical values of Cs calculated on the traditional vertically-faced structure.

Results show that the non-conventional geometry of the innovative caisson integrated with an OBREC device highly increases the overall stability of the structure compared to traditional breakwaters. The values of Cs computed on innovative caisson are greater than those calculated on the vertical structure for almost all the tests. The results confirm the behaviour already described when the comparison of the resultant forces on the caissons was examined. In particular, the relevant component of the downward force on the superstructure and the time lag between the vertical and horizontal forces, lead to a strong reduction of the maximum destabilizing forces F_s in the innovative breakwater, whose values range between the 60-90% of the ones computed on the traditional structure.

Contrary to the analysis on the forces, the influence of the peak period is slightly different and the minimum Cs is not always obtained for highest peaks period. It is worth considering that the resultant forces at instant of the minimum value of Cs in the time series strongly depend on the period of a single wave, more than the spectral peak period of the generated time series. Regarding the position of the crown-wall, it can be seen that similar behaviour described for the total forces can be replied here, particularly for tests characterized by large significant wave height (bottom panels in Fig. 7.23). It can be noted that safety coefficient Cs

against the sliding for lower values of B_{wall} assumes values similar to the one calculated on a vertical structure, while an increase of Cs is in general obtained with higher values of B_{wall}.

An example of the time series of the resultant horizontal (F_s), vertical (F_h) and destabilizing forces (F_s) is shown in Fig. 7.24 for *Test_08_caisson*. Three configurations of the innovative breakwater with different B_{wall} and a fixed ramp crest (R_r=0.067 m) are compared to the traditional structure. Please observe that this test is the one shown in Fig. 7.21, characterized by the occurrence of sporadic impact loadings on the set-back wall, in particular for the condition with B_{wall} = 0.300 m.

The top panel in Fig. 7.24 indicates a different behaviour between the total horizontal forces on the traditional breakwater and the innovative caisson. Due to the presence of the set-back wall, each signal of the innovative caissons is characterized by two distinctive peaks. The maximum horizontal forces for each wave occur when the latter impacts on the set-back wall (second peak), while the first peaks are in phase with those computed for the traditional breakwater, but shorter in magnitude due to the energy dissipation caused by the wave overtopping over the frontal ramp.

The central panel in Fig. 7.24 shows the signals of the total vertical forces exerted on the four different configurations. A different behaviour of wave structure interaction between innovative and vertical breakwater can be clearly distinguished. The vertical forces on the innovative breakwater increase until reaching a maximum value which is in phase and with similar magnitude of the one computed on the traditional breakwater. After this peak, the vertically downward component of the force exerted on the sloping ramp and the reservoir drastically reduces the total vertical forces on the innovative breakwater. It can be noted in this panel how the dimension of the reservoir influence the vertical forces on the caisson, i.e. the increase of the B_{wall} leads to a decreasing of the total vertical forces. Contrary to the traditional breakwater, the maximum vertical and horizontal forces exerted on the innovative breakwater occur at different time steps, whose time lag increase with the increase of B_{wall}.

Finally, the total destabilizing forces F_s (Eq. 7.7) are displayed in the bottom panel of Fig. 7.24. The example clearly indicates that an innovative caisson having a crest freeboard and caisson width equal to the one on traditional structure is characterized by a similar or greater stability, even for the conditions when an impact wave loading occurs on the set-back wall (red lines in Fig. 7.24 for B_{wall} =0.300 m).

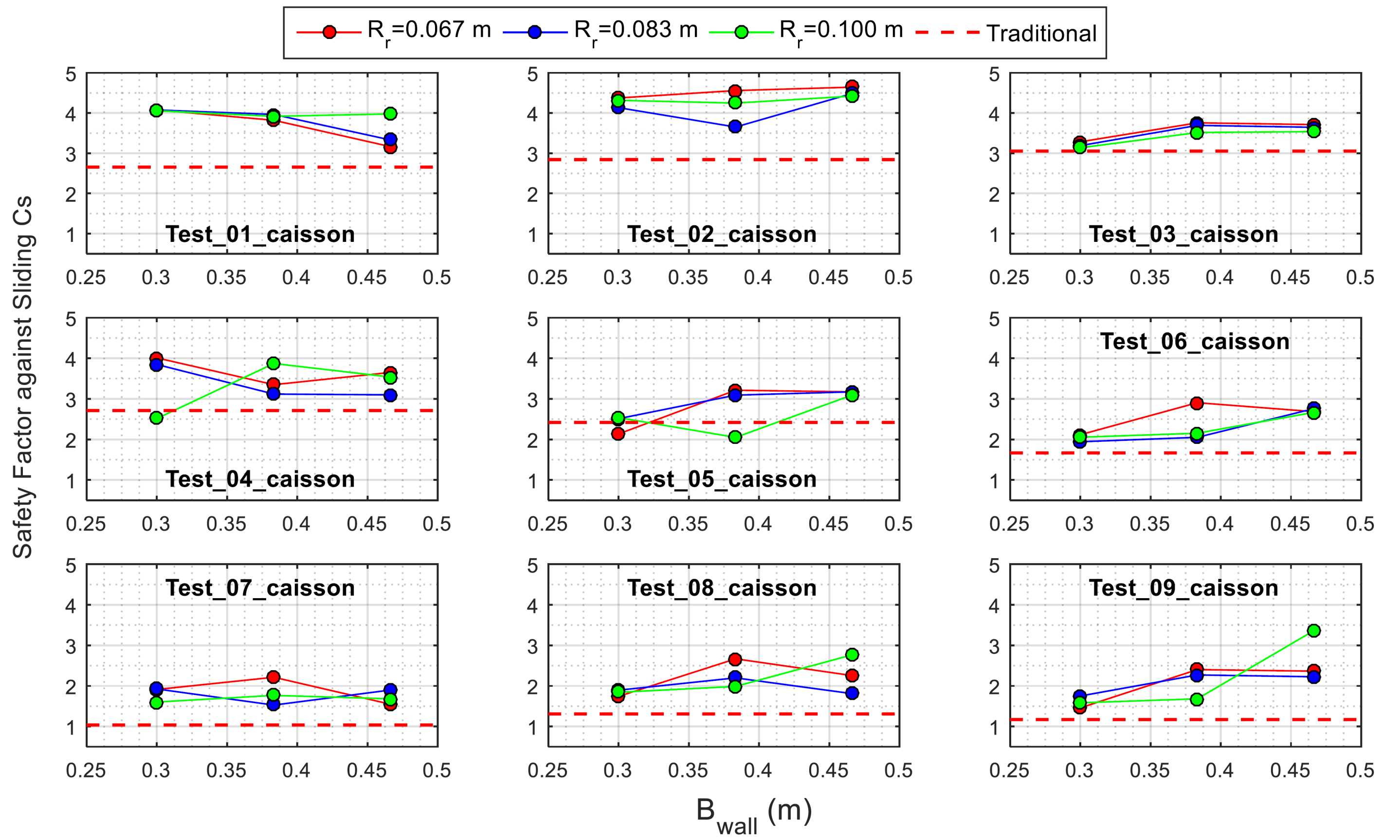

Fig. 7.23 Influence of crown-wall position B_{wall} and crest ramp R_r on the safety factor against the sliding, Cs, for the nine wave conditions. Red dotted-lines indicate the numerical values of Cs calculated on the traditional vertical structure.

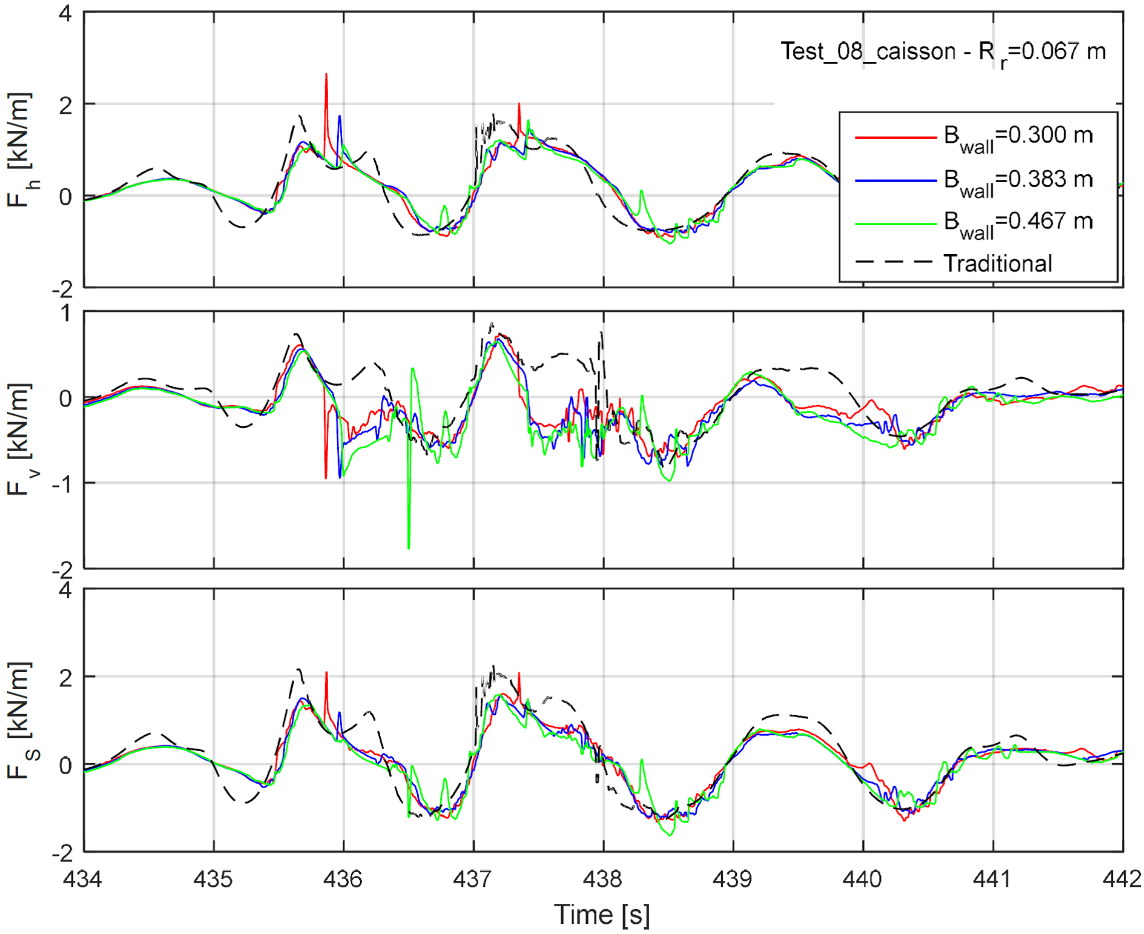

Fig. 7.24 Time series of the total horizontal (top panel) and vertical force (middle panel) on traditional and innovative caisson with a fixed value of crest ramp (R_r = 0.067 m). Bottom panel indicates the time series of the total destabilizing force $Fs = F_h + \mu F_v$. The test displayed is *Test_08_caisson*.

7.5 Conclusions

The hydraulic and structural performance of the OBREC device embedded in a vertical caisson is investigated in this chapter. The analysis is carried out adopting the IH2VOF model [163, 154], extensively validated in Chapter 5 against physical model experiments described in Chapter 4. The numerical modelling is applied to study the interaction between irregular waves and traditional and innovative breakwaters, comparing the results in terms of wave reflection, overtopping and resultant wave forces exerted on the structures. A total of 90 numerical model tests have been carried out in the present analysis.

Numerical simulations were performed on different OBREC configurations, allowing to investigate the influence of the ramp crest freeboard, R_r and the position of the set-back wall, B_{wall}, on the hydraulic performance, as well as their effects on the global caisson stability. Numerical results obtained on the innovative breakwater were then compared with those obtained on a vertical caisson with the same wall crest freeboard and caisson width. Results indicated that the integration of the OBREC device in a traditional vertically-faced structure has numerous advantages in terms of hydraulic and stability analysis.

Due to the wave dissipation on the ramp and reservoir, the reflection coefficients computed in front of the OBREC-caisson device were lower than those computed in front of the vertical breakwater. Therefore, an empirical relation, function of the relative crest freeboard R_r/H_{m0} and the relative wall position B_{wall}/L_{-10}, was provided in this chapter to estimate the reflection coefficients for different incident wave conditions and OBREC configurations.

Regarding the wave overtopping, results of the average overtopping discharge behind the set-back wall of innovative breakwater indicated that it significantly depends on the distance between the wall and the vertical face of the caisson, B_{wall}. In detail, the increase B_{wall} reduces the wave overtopping for all the incident wave conditions here analysed. The comparison between traditional and innovative caisson showed that the mean wave overtopping discharge for the different configurations match the equation suggested in the EurOtop Manual [74] for vertical structures, and almost all the numerical data are contained in the 90%-confidence band of this equation (Eq. 7.2). However, to predict the mean overtopping with more accuracy, a new coefficient was proposed in order to change the Eq. 7.2, taking into account the non-conventional geometry of the OBREC device.

The resultant vertical and horizontal wave forces exerted on traditional and innovative breakwaters were investigated for the stability analysis.

Regarding the horizontal forces, results indicated that the ratio between the horizontal forces exerted on innovative and traditional caisson is not influenced by R_r/H_{m0}. Contrary, the increase of the ratio $B_{wall}/L_{-1,0}$ leads to a slight reduction of the $F_{h,OBREC}$ compared to the one calculated on the vertical breakwater $F_{h,trad}$. Moreover, the resultant horizontal forces on the set-back wall occur later than those on the front wall, with a reduction of the total horizontal forces on the whole structure. Indeed, the increase of B_{wall} leads to a reduction of the ratio $F_{h,OBREC}/F_{h,trad}$ for almost all the tests here analysed. For a fixed value of the relative crest ramp R_r/H_{m0}, results indicated that higher reduction of the force occurs with waves characterized by small peak periods. Conversely, long waves are less influenced by the presence of the OBREC device installed on the caisson, leading to only a slight reduction compared to the total forces computed on the traditional vertically-faced structure. In detail, for the highest value of T_p and the lowest value of B_{wall}, the performance of the two configurations in terms of total horizontal wave forces were comparable.

Regarding the total vertical forces, results showed that the ratio $F_{v,OBREC}/F_{v,trad}$ is reduced with the increase of R_r/H_{m0} and $B_{wall}/L_{-1,0}$. As expected, the introduction of the OBREC device on vertical caissons induces a reduction of vertical forces due to the significant downward components exerted on the ramp and the bottom reservoir. Furthermore, the wave energy dissipation inside the reservoir reduces further the forces on the structure. For higher values of R_r/H_{m0} and $B_{wall}/L_{-1,0}$ the downward forces on the OBREC is half of the vertical uplift exerting on the base caisson.

Finally, the analysis of the loading exerted on the different configurations clearly underlined the advantage of adopting this novel solution with non-conventional shape due to the increase of the stability compared to the traditional structure. Results showed that the non-conventional geometry of the innovative caisson integrated with an OBREC device highly increases the overall stability of the structure. The values of Cs computed on innovative caissons were greater than those calculated on the vertical structure for almost all the tests, confirming the behaviour described for the resultant forces on the innovative and traditional caisson. In particular, the component of the downward force on the superstructure and the time lag between the vertical and horizontal forces, lead to a significant reduction of the maximum destabilizing forces F_s in the innovative breakwater, whose values range between the 60-90% of the ones computed on the traditional structure.

Chapter 8

Conclusions

8.1 General conclusions

The study of the hydraulic and structural response of the WECs (Wave Energy Converters) is of the utmost importance to ensure the highest levels of their survivability, reducing the risk of failures, which is generally very high due to the uncertainties related to the complex shape of the devices.

The present research has been conducted to close the gaps in the state of knowledge of an Overtopping Wave Energy Converter integrated into traditional breakwaters. The device, named OBREC, is studied in this thesis adopting physical and numerical modelling to investigate the hydraulic and structural functionality of the device. The principal conclusions that can be extracted from the research activities are summarized as follows.

The goal of the **Objective 1**, presented in Chapter 3, was to **evaluate the structural response of the OBREC integrated into rubble-mound breakwaters**. The experimental tests allowed to optimize the OBREC geometry, investigating the influence of the ramp shape (**Objective 1.1**) and reservoir width (**Objective 1.2**) on the wave-induced pressure and forces exerted on the model, while the use of numerical models allowed to evaluate the influence of the submerged ramp (**Objective 1.3**) on the local and global stability of the device.

Section 4.3.2 described the **influence of the ramp shape** on the pressure distribution and forces exerted on the OBREC. Results indicated that the forces on the flat ramp are greater than those measured on the curved one of around 30–40%. On the other hand, results showed that uplift forces at the base of the curved configuration are larger than those measured at the base of the flat configuration. No relevant differences between the two configurations were found on the resultant forces exerted on the vertical wall. Pressure at the 'bullnose' were measured in laboratory and results indicated that the forces on it for the flat configuration are greater than those on the curved configuration, for almost all the different incident wave conditions and geometries. The difference between the two configurations became more relevant considering the position of the resultant forces at the upper wall. Indeed, the forces at the wall on flat configuration were located at a higher position compared to the one on the curved configuration, hence influencing the overturning moment around the base. The phenomenon was due to the different slope angle of the ramp crest and it was clarified in the analysis by taking into account the path of the up-rushing water. The main conclusion that was drawn from this first comparison is that the total forces exerted on the OBREC with curved ramp are generally lower compared to the flat one, so the former configuration can offer a slightly better performance in terms of the overall stability.

Experimental tests allowed to study the **influence of the reservoir width** on the structural performance of the device integrated into rubble-mound breakwater. Results indicated that the reservoir width has a minor influence on the resultant forces exerted on the OBREC. The only remarkable influence is the pressure measured at the upper wall and the parapet. For the Extra-Large reservoir, waves do not impinge directly on the nose, resulting in lower pressure impulses, compared to the configuration with smaller reservoir. Contrary, maximum pressures on the nose occur for lower values of the reservoir width, because the water jet impacts directly on the parapet with an extreme impulsive load, while, for higher values of reservoir width, a large amount of wave energy is attenuated due to the dissipation in it.

Numerical simulations on the OBREC integrated into rubble-mound breakwater with geometries not tested in laboratory were carried in this research, using IH2VOF. The first analysis aimed at investigating the **influence of the submerged ramp** on the reduction of the uplift force on the base and its effects on the global and local stability of the superstructure. Numerical results confirmed the importance to design the ramp extension under the SWL of the OBREC device, due to the reduction of the upward forces exerted on the OBREC base. These forces were reduced accordingly to the increase of the shaft length. Indeed, for configurations with a large shaft length and a small wave height, the maximum force at the base was less than half of the force on the configuration without the shaft.

The stability against sliding and overturning, as well as the local failures, were evaluated comparing three different shaft dimensions. The analysis showed that the critical conditions for the global failure modes of the OBREC occurred at different time instants, i.e. the critical forces exerted on the device were different for the different failure modes. Results have shown a positive effect of the shaft due to the increase of the global stability against the sliding failure mode, which represents the most typical critical failure for superstructures on rubble-mound breakwater [212].

The **Objective 2** of this thesis aimed at **providing design formulas for the estimation of the forces exerted on the device for stability analysis**. Please note that, as reported by Iuppa et al. [126], the flat ramp has better performance in terms of overtopping in the frontal reservoir, increasing the hydraulic efficiency of the device and its capability to absorb energy from waves to convert into electricity. Based on the OBREC developers' experience, a planar ramp is much easier to build, reducing the time and cost of the construction activities. This is also documented in the previous literature on a similar device such as the SSG. Following these considerations, only the OBREC with a planar ramp was investigated further combining the data of experimental and numerical analysis. Section 4.3.4 presents the comparison between the measured forces and those computed with the semi-empirical design formulas used for traditional breakwaters. A new specific set of design formulas, summarized in Table 4.3, was presented to predict the total forces exerted on the frontal ramp, under the horizontal base, and on the upper and lower wall. An insight of the time series analysis of the total forces, described in Section 4.3.5, indicated that the maximum forces on different parts of OBREC were not simultaneous, and a method to estimate the total force to be applied on the structure is proposed in Eq. 4.35 and Eq. 4.36.

Following the approach known in literature as *'Composite modelling'*, the numerical modelling of the interaction between irregular waves and the device integrated into rubble-mound breakwater is investigated in Chapter 5. The model was used to extend the results of experimental test and to evaluate hydraulic and structural functionality, as well as the global and local stability of the device. IH2VOF has been validated, matching the results with the experimental data from the model test described in Chapter 4. The validation was based on the comparison of the free surface elevation in the wave flume and the wave pressure exerted on the OBREC device between the measured and numerical signals. The statistical and spectral parameters of the free surface elevation indicated that the model very well simulates the energy evolution along the wave flume as well as the interaction of the waves with the device and its foundation. The forces computed with IH2VOF at the sloping ramp and base reservoir were highly satisfactory, while a slight overestimation of the loading on the upper part of vertical wall was noted. The overall validation process included also a visual comparison wave-by-wave in the time domain of free surface elevation in front of the device, the pressure exerting on the gauges located along the model and the resultant forces, with overall good results.

The analysis has shown how the numerical modelling can be used as a complementary tool during the design process of this innovative breakwater device, completing and extending the database of the physical model tests. In this regard, the use of the numerical model allowed to analyse the overall horizontal and vertical force acting on the OBREC, including the pressure field under the ramp where no direct measurement was provided in the laboratory.

Results of this analysis showed that the maximum vertical and horizontal forces for each single incident wave were not simultaneous, which indicate a positive aspect regarding the global stability of the device. In detail, at the instant of the local maximum total horizontal force, the vertical force was zero or directed downward. Contrary, at the instant of the local maximum vertical force, the horizontal force acting on the device was around its minimum value. The analysis showed that the uplift forces exerted on the OBREC base calculated with IH2VOF, which considers the different porous media characteristics and the continuous pressure distribution, were more accurate than those computed using the signals measured by the three pressure transducers installed in the laboratory. The analysis revealed an overestimation of the resultant uplift forces on the OBREC base, computed from the pressure signals measured in the laboratory, of about 17%, mainly due to the limited information of pressure acting underneath the structure.

The principal of this study was to offer specific tools and new specific design formulas to the scientific community and engineers involved in this field to be adopted for the design of prototype devices at full-scale. The results of the analysis of the hydraulic and structural response of the OBREC have been adopted to estimate the total forces for the design and stability analysis of a full-scale prototype installed in Italy in 2015. The preliminary design of the device, its geometry, the instrumentation and the purpose of the present and future monitoring activities were described in Chapter 6. Please note that the device is currently under monitoring and the analysis of the field data was out of the scope of the present doctoral thesis.

The goal of the **Objective 3** was to **extend the applicability of the OBREC into vertical caissons**. In Chapter 7 an innovative application of the OBREC was presented, consisting of its integration in vertical caissons. The traditional and innovative caissons were numerically analysed with the use of IH2VOF and the results consisted of the comparison of the two configurations in terms of wave hydraulic (**Objective 3.1**) and structural performance (**Objective 3.2**) of the caissons. Numerical results obtained for the traditional caisson were validated against the well-established semi-empirical formulas proposed in literature, showing very good agreements. Afterwards, the influence of the ramp crest and the position of the set-back wall on the hydraulic and structural functionality of the innovative caisson were investigated with IH2VOF, comparing the results with those computed on the traditional structure.

The comparison between traditional and innovative caisson indicated that the complex shape of the OBREC significantly reduces the reflection in front of the device. However, due to the presence of the frontal ramp, the mean overtopping discharge at the rear side of the vertical set-back wall of the innovative caisson was slightly higher than the one computed on the conventional vertical-faced structure, in particular for high values of relative crest freeboard R_c/H_{m0}, i.e. low amount of wave overtopping discharge.

Finally, the results of the forces exerted on the device allowed to evaluate the global and local stability between the two typologies. In detail, the analysis of the forces on traditional and innovative caisson clearly indicated the advantage of adopting this novel solution due to the increase of the stability compared to traditional vertically-faced breakwater. The downward component of the forces at the frontal ramp and reservoir significantly reduces the total vertical forces, thus increasing the stability of the structure against the sliding failure. Moreover, the resultant forces on the set-back wall occur later than those on the vertical face caisson, with a further reduction of the total horizontal forces on the whole structure.

The results obtained in this research work adopting the composite modelling (laboratory + numerical model) offered a substantial contribution to the development of the OBREC device, which has been recently built in a prototype scale based on the results of small scale models.

In view of these results, it can be concluded that the objectives of this research have been successfully achieved.

8.2 Future research line

Despite several years of development process, the OBREC device continues to be investigated with the aim to obtain a technology proved to work through successfully in the next years and ready for the final commercialization phase.

The principal investigation line is to test the technology at full-scale in a real environmental field. The aim of this study would be principally to test the structural reliability as well as the feasibility of the instrumental apparatus installed for energy production. Only the monitoring of prototypes tested in the sea would provide information on the hydraulic efficiency of the device, allowing to accurately define the power matrix of the device optimized for a specific site.

In this work line, an effort should be made by mechanical engineers on the development of low-head hydraulic turbines applicable for this specific device. Although they are usually adopted in normal river hydro-power stations, the turbines in the OBREC have to operate at very low-head values ranging from 1 to 3 meters, which are not only on the lower limit of existing hydro power experience, but also an extremely wide variation. Secondly, due to the stochastic time distribution of the wave overtopping and the limited storage capacity, the turbines need to be regulated from zero to full load very frequently. Consequently, innovative low-head turbines need to be designed for this specific application.

Concerning the numerical modelling, a future line of investigation involves the possibility to model the device at large scale, calibrating the numerical model with the data obtained from the field monitoring in Naples (Italy). The analysis at full-scale of the hydraulic performance will provide fundamental information on pressures under real conditions without scale effects. Moreover, the empirical friction coefficients in the VARANS equations will be calibrated with the field data, fulfilling one of the most relevant gaps in the literature in the numerical modelling of wave interaction with porous media, as pointed out by Jensen et al. [130] and Losada et al. [162]. The expected results will also allow extending the range of application of the design formulas presented in Chapter 4, as well as providing useful indications for the stability analysis and the geometric optimization of the device.

Numerical modelling can be applied on the OBREC device also to evaluate the performance not only for extreeme condition but also during mild conditions. The aim is to simulate the wave overtopping entering into the reservoir when the latter is not completely saturated and the process of filling and emptying, as it occurs in real devices. These numerical simulations would offer a better comprehension of the hydraulic behaviour of the device, extending the range of application of the semi-empirical formulas for the overtopping into the reservoir presented by Iuppa et al. [126] after the physical model tests also for three-dimensional wave conditions (oblique incident waves).

Finally, a wide progress can be done on the development of the OBREC integrated into vertical caissons. The present thesis already showed results of the numerical modelling for the analysis of hydraulic behaviour of innovative caisson compared to a traditional vertical faced structure. However, it is highly desirable to test the caisson with this novel geometry via laboratory tests as well as further three-dimensional numerical simulations to study the effect of oblique waves on the hydraulic performance and on its global and local stability.

References

[1] 6349-7:1984, B. (1984). British standard code of practice for maritime structures, maritime structures. general criteria.

[2] 6349-7:1991, B. (1991). British standard code of practice for maritime structures, guide to the design and construction of breakwaters.

[3] Agerschou, H. (2004). *Planning and design of ports and marine terminals*. Thomas Telford.

[4] Aguado, A. and Sánchez-Naverac, V. (1978). Nuevo tipo de sección para diques en talud con espaldón. *Revista de obras publicas*, pages 353–359.

[5] Ahrens, J. P. (1981). Irregular wave runup on smooth slopes. Technical report, Coastal Engineering Research Center Fort Belvoir VA.

[6] Allsop, N. (1999). New design methods for wave loadings on vertical breakwaters under pulsating and impact conditions. *Coastal Structures' 99, Spain, Balkemare*.

[7] Allsop, N. (2000). Wave forces on vertical and composite walls chapter 4 in handbook of coastal engineering, pages 4.1-4.47, editor j. herbich. Technical report, ISBN 0-07-134402-0, publn. McGraw-Hill, New York.

[8] Allsop, N., McKenna, J., Vicinanza, D., and Whittaker, T. (1997). New design methods for wave impact loadings on vertical breakwaters and seawalls. In *Coastal Engineering 1996*, pages 2508–2521.

[9] Allsop, W., Bruce, T., Alderson, J., Ferrante, V., Russo, V., Vicinanza, D., and Kudella, M. (2014). Large scale tests on a generalised oscillating water column wave energy converter. In *Proc. HYDRALAB IV Joint User Meeting, Lisbon*.

[10] Allsop, W., McBride, M., and Colombo, D. (1994). The reflection performance of vertical walls and low reflection alternatives: Results of wave flume tests. In *Proceedings of the 3rd MCS Project Workshop, MAS2-CT92-0047, Monolithic (Vertical) Coastal Structures, De Voorst, The Netherlands*.

[11] Allsop, W., Vicinanza, D., and McKenna, J. (1996). Wave forces on vertical and composite breakwaters.

[12] Andersen, M. T. and Frigaard, P. B. (2015). Incentive-based financial support scheme for immature renewable energy systems. In *European Wave and Tidal Energy ConferenceEuropean Wave and Tidal Energy Conference*. Technical Committee of the European Wave and Tidal Energy Conference.

[13] Andersen, T. L., Clavero, M., Frigaard, P., Losada, M., and Puyol, J. (2016). A new active absorption system and its performance to linear and non-linear waves. *Coastal Engineering*, 114:47–60.

[14] Arena, F. (2014). Un impianto rewec3 per la produzione di energia elettrica da moto ondoso: dall'invenzione del prof. paolo boccotti alla costruzione del primo prototipo. In *In: Workshop Energia dal Mare le Nuove Tecnologie per i Mari Italiani, Rome, 2014*.

[15] Arena, F., Fiamma, V., Laface, V., Malara, G., Romolo, A., Viviano, A., Sannino, G., and Carillo, A. (2013a). Installing u-owc devices along italian coasts. In *ASME 2013 32nd International Conference on Ocean, Offshore and Arctic Engineering*, pages V008T09A061–V008T09A061. American Society of Mechanical Engineers.

[16] Arena, F., Romolo, A., Malara, G., and Ascanelli, A. (2013b). On design and building of a u-owc wave energy converter in the mediterranean sea: a case study. In *ASME 2013 32nd International Conference on Ocean, Offshore and Arctic Engineering*. American Society of Mechanical Engineers.

[17] Arena, F., Romolo, A., Malara, G., Fiamma, V., and Laface, V. (2016). The first worldwide application at full-scale of the rewec3 device in the port of civitavecchia: Initial energetic performances. In *Progress in Renewable Energies Offshore: Proceedings of the 2nd International Conference on Renewable Energies Offshore (RENEW2016), Lisbon, Portugal, 24-26 October 2016*, page 303. CRC Press.

[18] Arena, F., Romolo, A., Malara, G., Fiamma, V., and Laface, V. (2017). The first full operative u-owc plants in the port of civitavecchia. In *ASME 2017 36th International Conference on Ocean, Offshore and Arctic Engineering*, pages V010T09A022–V010T09A022. American Society of Mechanical Engineers.

[19] Ashlin, S. J., Sundar, V., and Sannasiraj, S. (2017). Pressures and forces on an oscillating water column–type wave energy caisson breakwater. *Journal of Waterway, Port, Coastal, and Ocean Engineering*, 143(5):04017020.

[20] Astobiza, O. (2016). Mutriku milestone: 1 gwh from waves to grid.

[21] Bagnold, R. (1939). Interim report on wave-pressure research. *Excerpt from the J. of the Institution of Civil Engineers*.

[22] Baird, B., Logan, S., van der Molen, W., Elliot, T., and Zimmer, D. (2016). Thoughts on the future of physical models in coastal engineering. In *International Conference on the Application of Physical Modelling in Coastal and Port Engineering and Science, Ottawa, Canada, May 10-13, 2016*.

[23] Barstow, S., Mørk, G., Mollison, D., and Cruz, J. (2008). The wave energy resource. In *Ocean wave energy*, pages 93–132. Springer.

[24] Battjes, J. A. (1971). Run-up distributions of waves breaking on slopes. *Journal of Waterways and Harbors Division*, 97(Paper 7923).

[25] Battjes, J. A. and Groenendijk, H. W. (2000). Wave height distributions on shallow foreshores. *Coastal engineering*, 40(3):161–182.

[26] Benassai, E. (1984). Some considerations on design of vertical wall breakwater. In *International Symposium on" Maritime structures in the Mediterranean sea", Athens*.

[27] Benassai, E. (2008). Le dighe marittime: progettazione, realizzazione, dissesti, manutenzione. *Liguori editore*, page 373.

[28] Benassai, E. (2014). L'evoluzione delle opere di difesa per il porto di napoli. *il giornale dell'ingegnere n*, 2.

[29] Birks, J. (2010). *Composite sea walls for energy generation*. 3rd year Thesis, Department of Civil Engineering and the Environment, University of Southampton, UK.

[30] Boake, C. B., Whittaker, T. J., Folley, M., Ellen, H., et al. (2002). Overview and initial operational experience of the limpet wave energy plant. In *The Twelfth International Offshore and Polar Engineering Conference*. International Society of Offshore and Polar Engineers.

[31] Boccotti, P. (2003). On a new wave energy absorber. *Ocean Engineering*, 30(9):1191–1200.

[32] Boccotti, P. (2007a). Caisson breakwaters embodying an owc with a small opening—part i: Theory. *Ocean Engineering*, 34(5-6):806–819.

[33] Boccotti, P. (2007b). Comparison between a u-owc and a conventional owc. *Ocean Engineering*, 34(5-6):799–805.

[34] Boccotti, P., Filianoti, P., Fiamma, V., and Arena, F. (2007). Caisson breakwaters embodying an owc with a small opening—part ii: A small-scale field experiment. *Ocean Engineering*, 34(5-6):820–841.

[35] Bosman, G., Van Der Meer, J., Hoffmans, G., Schüttrumpf, H., and Verhagen, H. J. (2009). Individual overtopping events at dikes. In *Coastal Engineering 2008: (In 5 Volumes)*, pages 2944–2956. World Scientific.

[36] Bradbury, A., Allsop, W., and Stephens, R. (1988). Hydraulics performance of breakwater crown walls.

[37] Braña, P. C. and Guillén, J. F. (2005). Wave forces on crown walls: evaluation of existing empirical formulations. In *Coastal Engineering 2004: (In 4 Volumes)*, pages 4087–4099. World Scientific.

[38] Brito-Melo, A. (2018). Press release wave pico plant 2018-04-23.

[39] Brito-Melo, A., Neuman, F., and Sarmento, A. (2008). Full-scale data assessment in owc pico plant. *International Journal of Offshore and Polar Engineering*, 18(01).

[40] Bruce, T. and O'Callaghan, J. (2013). Oscillating water column wave energy converters at the coast: a review and forward look. In *Coastal Structures 2011: (In 2 Volumes)*, pages 345–356. World Scientific.

[41] Bruce, T., Van der Meer, J., Allsop, N., Franco, L., Kortenhaus, A., Pullen, T., and Schüttrumpf, H. (2013). Eurotop revisited. part 2: vertical structures. *Proc. ICE, Coasts, Marine Structures and Breakwaters*.

[42] Bruining, J. (1994). Wave forces on vertical breakwaters: Reliability of design formula. Master's thesis, Delft University of Technology.

[43] Buccino, M., Banfi, D., Vicinanza, D., Calabrese, M., Giudice, G. D., and Carravetta, A. (2012). Non breaking wave forces at the front face of Seawave Slotcone Generators. *Energies*, 5(11):4779–4803.

[44] Buccino, M., Dentale, F., Salerno, D., Contestabile, P., and Calabrese, M. (2016). The use of cfd in the analysis of wave loadings acting on seawave slot-cone generators. *Sustainability*, 8(12):1255.

[45] Buccino, M., Vicinanza, D., Ciardulli, F., Calabrese, M., and Kofoed, J. P. (2011). Wave pressures and loads on a small scale model of the Svåheia SSG pilot project. In *Proceedings of the 9th European wave tidal energy conference. Southampton, UK*, pages 1–7.

[46] Buccino, M., Vicinanza, D., Salerno, D., Banfi, D., and Calabrese, M. (2015). Nature and magnitude of wave loadings at seawave slot-cone generators. *Ocean Engineering*, 95:34–58.

[47] Bullock, G., Hewson, P., Crawford, A., and Bird, P. (2000). Field and laboratory measurements of wave loads on vertical breakwaters. In *Proc. Coastal Structures*, volume 99, pages 613–621.

[48] Bullock, G., Obhrai, C., Peregrine, D., and Bredmose, H. (2007). Violent breaking wave impacts. part 1: Results from large-scale regular wave tests on vertical and sloping walls. *Coastal Engineering*, 54(8):602–617.

[49] Burcharth, H. F. (1993). Reliability evaluation and probabilistic design of coastal structures. In *International Seminar on Hydro-technical Engineering for Future Development of Ports and Harbors*.

[50] Burcharth, H. F. and Andersen, T. L. (2007). Overtopping of rubble mound breakwaters with front reservoir. In *Coastal Engineering 2006: (In 5 Volumes)*, pages 4605–4615. World Scientific.

[51] Burcharth, H. F., Andersen, T. L., and Lara, J. L. (2014). Upgrade of coastal defence structures against increased loadings caused by climate change: A first methodological approach. *Coastal Engineering*, 87:112–121.

[52] Canarios, P. (2018). Puerto de las nieves, agaete. *Available online: http://360.puertoscanarios.es/lasnieves/lasnieves.html*.

[53] Cappietti, L. and Aminti, P. L. (2012). Laboratory investigation on the effectiveness of an overspill basin in reducing wave overtopping on marina breakwaters. *Coastal Engineering Proceedings*, 1(33):20.

[54] Carayon, N., Marriner, N., and Morhange, C. (2011). Geoarchaeology of byblos, tyre, sidon and beirut. *Rivista di studi fenici*, 39(1):45–55.

[55] Castellino, M., Sammarco, P., Romano, A., Martinelli, L., Ruol, P., Franco, L., and De Girolamo, P. (2018). Large impulsive forces on recurved parapets under non-breaking waves. a numerical study. *Coastal Engineering*, 136:1–15.

[56] Cejuela, E., Negro, V., Esteban, M. D., López-Gutiérrez, J. S., and Ortega, J. M. (2018). From julius caesar to sustainable composite materials: A passage through port caisson technology. *Sustainability*, 10(4):1225.

[57] Centurioni, L., Braasch, L., Di Lauro, E., Contestabile, P., De Leo, F., Casotti, R., Franco, L., and Vicinanza, D. (2017a). A new strategic wave measurement station off naples port main breakwater. *Coastal Engineering Proceedings*, 1(35):36.

[58] Centurioni, L., Horányi, A., Cardinali, C., Charpentier, E., and Lumpkin, R. (2017b). A global ocean observing system for measuring sea level atmospheric pressure: Effects and impacts on numerical weather prediction. *Bulletin of the American Meteorological Society*, 98(2):231–238.

[59] Chorin, A. J. (1968). Numerical solution of the navier-stokes equations. *Mathematics of computation*, 22(104):745–762.

[60] Clarke, D. K., Hassan, H., and Salas, M. (1986). Euler calculations for multielement airfoils using cartesian grids. *AIAA journal*, 24(3):353–358.

[61] Contestabile, P., Di Lauro, E., Buccino, M., and Vicinanza, D. (2017a). Economic assessment of Overtopping BReakwater for Energy Conversion (OBREC): a case study in western Australia. *Sustainability*, 9(1):51.

[62] Contestabile, P., Ferrante, V., Di Lauro, E., and Vicinanza, D. (2017b). Full-scale prototype of an overtopping breakwater for wave energy conversion. *Coastal Engineering Proceedings*, 1(35):12.

[63] Contestabile, P., Ferrante, V., and Vicinanza, D. (2015). Wave energy resource along the coast of Santa Catarina (Brazil). *Energies*, 8(12):14219–14243.

[64] Contestabile, P., Iuppa, C., Di Lauro, E., Cavallaro, L., Andersen, T. L., and Vicinanza, D. (2017c). Wave loadings acting on innovative rubble mound breakwater for overtopping wave energy conversion. *Coastal Engineering*, 122:60–74.

[65] Cuomo, G., Allsop, W., and Takahashi, S. (2010). Scaling wave impact pressures on vertical walls. *Coastal Engineering*, 57(6):604–609.

[66] Cuomo, G., Tirindelli, M., and Allsop, W. (2007). Wave-in-deck loads on exposed jetties. *Coastal Engineering*, 54(9):657–679.

[67] Dalbéra, J.-P. (2006). Digue du port de fontvieille, monaco. *Available online: https://www.flickr.com/photos/dalbera/436562710*.

[68] del Estado, P. (2009). Rom 1.0-09. *Recomendaciones del diseño y ejecución de las Obras de Abrigo*.

[69] del Jesus, M., Lara, J. L., and Losada, I. J. (2012). Three-dimensional interaction of waves and porous coastal structures: Part i: Numerical model formulation. *Coastal Engineering*, 64:57–72.

[70] Di Lauro, E. (2015). Wave loading acting on the dimemo wave energy converter. Master's thesis, Department of Engineering, Second University of Naples, Italy.

[71] Di Lauro, E., Contestabile, P., and Vicinanza, D. (2017). Wave energy in Chile: A case study of the overtopping breakwater for energy conversion (OBREC).

[72] Energy, A. (2005). Oscillating water column wave energy converter evaluation report. *The Carbon Trust, Marine Energy Challenge*.

[73] EurOtop (2007). Wave overtopping of sea defences and related structures–assessment manual. *UK: NWH Allsop, T. Pullen, T. Bruce. NL: JW van der Meer. DE: H. Schüttrumpf, A. Kortenhaus. www. overtopping-manual. com.*

[74] EurOtop (2016). *Manual on wave overtopping of sea defences and related structures. An overtopping manual largely based on European research, but for worldwide application*. Van der Meer, J.W., Allsop, N.W.H., Bruce, T., De Rouck, J., Kortenhaus, A., Pullen, T., Schuttrumpf, H., Troch, P. and Zanuttigh, B., www.overtopping-manual.com.

[75] Evans, D. (1982). Wave-power absorption by systems of oscillating surface pressure distributions. *Journal of Fluid Mechanics*, 114:481–499.

[76] Falcão, A. (2010). Wave energy utilization: A review of the technologies. *Renewable and sustainable energy reviews*, 14(3):899–918.

[77] Falcão, A. (2017). *Modelling of Wave Energy Conversion*. Tech. Rep. (2017).

[78] Falcão, A. F. and Henriques, J. C. (2016). Oscillating-water-column wave energy converters and air turbines: A review. *Renewable Energy*, 85:1391–1424.

[79] Ferziger, J. H. and Peric, M. (2012). *Computational methods for fluid dynamics*. Springer Science & Business Media.

[80] Formentin, S. M., Palma, G., Contestabile, P., Vicinanza, D., and Zanuttigh, B. (2017). 2dv rans-vof numerical modeling of a multi-functional harbour structure. *Coastal Engineering Proceedings*, 1(35):3.

[81] Franco, L. (1992). Recent italian experience in the design and construction of vertical breakwaters. *Design and Reliability of Coastal Structures, short course during the 23rd ICCE in Venice*.

[82] Franco, L. (1994). Vertical breakwaters: the italian experience. *Coastal Engineering*, 22(1-2):31–55.

[83] Franco, L. (1996). Ancient mediterranean harbours: a heritage to preserve. *Ocean & Coastal Management*, 30(2-3):115–151.

[84] Franco, L., De Gerloni, M., and Van der Meer, J. (1995). Wave overtopping on vertical and composite breakwaters. In *Coastal Engineering 1994*, pages 1030–1045.

[85] Frigaard, P. and Andersen, T. L. (2010). Technical background material for the wave generation software awasys 5.

[86] Frigaard, P. and Andersen, T. L. (2014). Analysis of waves: Technical documentation for wavelab 3.

[87] Frigaard, P. and Brorsen, M. (1995). A time-domain method for separating incident and reflected irregular waves. *Coastal Engineering*, 24(3-4):205–215.

[88] Frostick, L. E., McLelland, S. J., and Mercer, T. G. (2011). *Users guide to physical modelling and experimentation: Experience of the HYDRALAB network*. CRC Press.

[89] Fugazza, M. and Natale, L. (1992). Hydraulic design of perforated breakwaters. *Journal of Waterway, Port, Coastal, and Ocean Engineering*, 118(1):1–14.

[90] Funakoshi, H., Katoh, H., Saito, T., Takahashi, S., and Oikawa, K. (1993). Development of a wave power extracting caisson breakwater. *Doboku Gakkai Ronbunshu*, 1993(474):37–39.

[91] Garrido, A. J., Otaola, E., Garrido, I., Lekube, J., Maseda, F. J., Liria, P., and Mader, J. (2015). Mathematical modeling of oscillating water columns wave-structure interaction in ocean energy plants. *Mathematical Problems in Engineering*, 2015.

[92] Geeraerts, J., De Rouck, J., Beels, C., Gysens, S., and De Wolf, P. (2007). Reduction of wave overtopping at seadikes: Stilling wave basin (swb). In *Coastal Engineering 2006: (In 5 Volumes)*, pages 4680–4691. World Scientific.

[93] Goda, Y. (1973). A new method of wave pressure calculation for the design of composite breakwaters. *Report of the Port and Harbour Research Institute*, 12(3):31–69.

[94] Goda, Y. (1985). Random seas and maritime structures.

[95] Goda, Y. (2010). *Random seas and design of maritime structures*. World scientific.

[96] Goda, Y. and Fukumori, T. (1972). Laboratory investigation of wave pressures exerted upon vertical and composite walls. *Coastal Engineering in Japan*, 15:81–90.

[97] Goda, Y. and Kakizaki, S. (1966). Study on finite amplitude standing waves and their pressure upon a vertical wall. *Rept. Port and Harbour Research Institute*, 5(10):57.

[98] Goda, Y., Nakada, H., Ohneda, H., Suzuki, M., Takahashi, S., and Shikamori, M. (1991). Results of field experiment of a wave power extracting caisson breakwater. In *Proceedings of Civil Engineering in the Ocean*, volume 7, pages 143–148. Japan Society of Civil Engineers.

[99] Gonzales, B. M. and Valdes, A. J. (1992). Influence of superstructure geometry on the behaviour of vertical breakwaters: two case studies.

[100] Guanche, R., Iturrioz, A., and Losada, I. (2015). Hybrid modeling of pore pressure damping in rubble mound breakwaters. *Coastal Engineering*, 99:82–95.

[101] Guanche, R., Losada, I. J., and Lara, J. L. (2009). Numerical analysis of wave loads for coastal structure stability. *Coastal Engineering*, 56(5-6):543–558.

[102] Günbak, A. and Gökce, T. (1984). Wave screen stability of rubble-mound breakwaters. In *International symposium of maritime structures in the Mediterranean Sea. Athens, Greece*, pages 99–112.

[103] Gunn, K. and Stock-Williams, C. (2012). Quantifying the global wave power resource. *Renewable Energy*, 44:296–304.

[104] Günther, H. and Behrens, A. (2011). The wam model. validation document version 4.5. 4. *Institute of Coastal Research Helmholtz-Zentrum Geesthacht, Germany*.

[105] Hasselmann, K., Barnett, T., Bouws, E., Carlson, H., Cartwright, D., Enke, K., Ewing, J., Gienapp, H., Hasselmann, D., Kruseman, P., et al. (1973). Measurements of wind-wave growth and swell decay during the joint north sea wave project (jonswap). *Ergänzungsheft 8-12*.

[106] Hattori, M., Arami, A., and Yui, T. (1994). Wave impact pressure on vertical walls under breaking waves of various types. *Coastal Engineering*, 22(1-2):79–114.

[107] Heath, T., Whittaker, T., and Boake, C. (2000). The design, construction and operation of the limpet wave energy converter (islay, scotland). In *Proceedings of 4th European wave energy conference*, pages 49–55.

[108] Herrera, M. P., Gomez-Martín, M. E., and Medina, J. R. (2017). Hydraulic stability of rock armors in breaking wave conditions. *Coastal Engineering*, 127:55–67.

[109] Higuera, P. (2015). *Application of computational fluid dynamics to wave action on structures*. PhD thesis, Universidade de Cantabria.

[110] Hiroi, I. (1919). On a method of estimating the force of waves. *Memoirs of Engineering Facility, Imperial University of Tokyo*, 10(1):19.

[111] Hirt, C. W. and Nichols, B. D. (1981). Volume of fluid (vof) method for the dynamics of free boundaries. *Journal of computational physics*, 39(1):201–225.

[112] Hofland, B., Chen, X., Altomare, C., and Oosterlo, P. (2017). Prediction formula for the spectral wave period tm-1, 0 on mildly sloping shallow foreshores. *Coastal Engineering*, 123:21–28.

[113] Holterman, S. (1998). Wave runup on dikes with a shallow foreshore. (in dutch) golfoploop op dijken met ondiep voorland. Master's thesis, MSc thesis, TU Delft, Delft.

[114] Horvath, E. (2009). *Wave loading at coastal wave energy converters*. PhD thesis, University of Edinburgh.

[115] Hsu, T.-J., Sakakiyama, T., and Liu, P. L.-F. (2002a). A numerical model for wave motions and turbulence flows in front of a composite breakwater. *Coastal Engineering*, 46(1):25–50.

[116] Hsu, T.-J., Sakakiyama, T., and Liu, P. L.-F. (2002b). A numerical model for wave motions and turbulence flows in front of a composite breakwater. *Coastal Engineering*, 46(1):25–50.

[117] Huang, Y., Shi, H., Liu, D., and Liu, Z. (2010). Study on the breakwater caisson as oscillating water column facility. *Journal of Ocean University of China*, 9(3):244–250.

[118] Huang, Z., Li, Y., and Liu, Y. (2011). Hydraulic performance and wave loadings of perforated/slotted coastal structures: A review. *Ocean Engineering*, 38(10):1031–1053.

[119] Hudson, R. Y. (1959). Laboratory investigation of rubble-mound breakwaters. *Reprint of the original paper as published in the Journal of the Waterways and Harbors Division of ASCE, proceedings paper 2171*.

[120] Hughes, S. and Nadal, N. (2009). Laboratory study of combined wave overtopping and storm surge overflow of a levee. *Coastal Engineering*, 56(3):244–259.

[121] Hughes, S. A. (2004). Wave momentum flux parameter: a descriptor for nearshore waves. *Coastal Engineering*, 51(11-12):1067–1084.

[122] Hull, P. and Müller, G. (2002). An investigation of breaker heights, shapes and pressures. *Ocean Engineering*, 29(1):59–79.

[123] Ibarra-Berastegi, G., Sáenz, J., Ulazia, A., Serras, P., Esnaola, G., and Garcia-Soto, C. (2018). Electricity production, capacity factor, and plant efficiency index at the mutriku wave farm (2014–2016). *Ocean Engineering*, 147:20–29.

[124] Iribarren, R. and Nogales, C. (1954). *Obras marítimas: oleaje y diques*. Dossat.

[125] Iuppa, C. (2015). *Ottimizzazione di dighe marittime a gettata per l'estrazione di energia dal moto ondoso*. PhD thesis, PhD thesis, Dipartimento Ingegneria Civile e Architettura, Universitá degli studi di Catania.

[126] Iuppa, C., Contestabile, P., Cavallaro, L., Foti, E., and Vicinanza, D. (2016). Hydraulic performance of an innovative breakwater for overtopping wave energy conversion. *Sustainability*, 8(12):1226.

[127] Jacobsen, N. G., van Gent, M. R., and Wolters, G. (2015). Numerical analysis of the interaction of irregular waves with two dimensional permeable coastal structures. *Coastal Engineering*, 102:13–29.

[128] Jarlan, G. (1961). A perforated vertical wall breakwater. *The Dock and Harbour Authority*, (486):394–398.

[129] Jayakumar, V. (1994). *Wave force on oscillating water column type wave energy caisson: an experiment study*. PhD thesis, Department of Ocean Engineering, Indian Institute of Technology, Madras, India.

[130] Jensen, B., Jacobsen, N. G., and Christensen, E. D. (2014). Investigations on the porous media equations and resistance coefficients for coastal structures. *Coastal Engineering*, 84:56–72.

[131] Jensen, O. J. (1984). *A monograph on rubble mound breakwaters*. Danish Hydraulic Institute.

[132] Joodaki, G., Nahavandchi, H., and Cheng, K. (2013). Ocean wave measurement using gps buoys. *Journal of Geodetic Science*, 3(3):163–172.

[133] Juhl, J. and Van der Meer, J. (1992). Quasi-static wave forces on vertical structures, reanalysis of data at danish hydraulic institure and delft hydraulics report. *Prepared for MAST G6-S Coastal Structures*.

[134] Kamphuis, J. (1995). Composite modelling-an old tool in a new context. In *Proceedings of the Congress of International Association for Hydraulic Research*, volume 1, pages 230–235. LOCAL ORGANIZING COMMITTEE OF THE XXV CONGRESS.

[135] Kamphuis, J. W. (2010). *Introduction to coastal engineering and management*, volume 30. World Scientific.

[136] Klopman, G. and Meer, J. W. v. d. (1999). Random wave measurements in front of reflective structures. *Journal of waterway, port, coastal, and ocean engineering*, 125(1):39–45.

[137] Kofoed, J. P. (2002). *Wave overtopping of marine structures*. PhD thesis, Citeseer.

[138] Kofoed, J. P. (2005). Model testing of the wave energy converter seawave slot-cone generator.

[139] Kofoed, J. P. (2007). Vertical distribution of wave overtopping for design of multi level overtopping based wave energy converters. In *Coastal Engineering 2006: (In 5 Volumes)*, pages 4714–4726. World Scientific.

[140] Kofoed, J. P., Vicinanza, D., Osaland, E., et al. (2006). Estimation of design wave loads on the ssg wec pilot plant based on 3-d model tests. In *The Sixteenth International Offshore and Polar Engineering Conference*. International Society of Offshore and Polar Engineers.

[141] Kortenhaus, A., Haupt, R., and Oumeraci, H. (2002). Design aspects of vertical walls with steep foreland slopes. In *Breakwaters, Coastal Structures and Coastlines: Proceedings of the International Conference Organized by the Institution of Civil Engineers and Held in London, UK on 26-28 September 2001*, volume 221. Thomas Telford.

[142] Kortenhaus, A. and Oumeraci, H. (1999). Classification of wave loading on monolithic coastal structures. In *Coastal Engineering 1998*, pages 867–880.

[143] Kortenhaus, A. and Oumeraci, H. (2001). Damping of horizontal and uplift forces on horizontally composite breakwaters. In *Coastal Engineering 2000*, pages 1724–1737.

[144] Kortenhaus, A., Oumeraci, H., Kohlhase, S., and Klammer, P. (1995). Wave-induced uplift loading of caisson breakwaters. In *Coastal Engineering 1994*, pages 1298–1311.

[145] Kortenhaus, A., Pearson, J., Bruce, T., Allsop, N., and Van der Meer, J. (2004). Influence of parapets and recurves on wave overtopping and wave loading of complex vertical walls. In *Coastal Structures 2003*, pages 369–381.

[146] Kramer, M. and Burcharth, H. F. (2002). Environmental design of low crested coastal defence structures: Delos d31 wave basin experiment final form-3d stability tests at aau.

[147] Krogstad, H. E., Barstow, S. F., Aasen, S. E., and Rodriguez, I. (1999). Some recent developments in wave buoy measurement technology. *Coastal engineering*, 37(3-4):309–329.

[148] Krogstad, H. E., Gordon, R. L., and Miller, M. C. (1988). High-resolution directional wave spectra from horizontally mounted acoustic doppler current meters. *Journal of Atmospheric and Oceanic Technology*, 5(2):340–352.

[149] Kuo, Y.-S., Lin, C.-S., Chung, C.-Y., and Wang, Y.-K. (2015). Wave loading distribution of oscillating water column caisson breakwaters under non-breaking wave forces. *Journal of Marine Science and Technology*, 23(1):78–87.

[150] Lamberti, A., Martinelli, L., Gabriella Gaeta, M., Tirindelli, M., and Alderson, J. (2011). Experimental spatial correlation of wave loads on front decks. *Journal of Hydraulic Research*, 49(sup1):81–90.

[151] Lara, J., Garcia, N., and Losada, I. (2006). Rans modelling applied to random wave interaction with submerged permeable structures. *Coastal Engineering*, 53(5-6):395–417.

[152] Lara, J., Losada, I., and Guanche, R. (2008). Wave interaction with low-mound breakwaters using a rans model. *Ocean engineering*, 35(13):1388–1400.

[153] Lara, J. L., Losada, I. J., Maza, M., and Guanche, R. (2011a). Breaking solitary wave evolution over a porous underwater step. *Coastal Engineering*, 58(9):837–850.

[154] Lara, J. L., Ruju, A., and Losada, I. J. (2011b). Reynolds averaged navier–stokes modelling of long waves induced by a transient wave group on a beach. In *Proceedings of the Royal Society of London A: Mathematical, Physical and Engineering Sciences*, volume 467, pages 1215–1242. The Royal Society.

[155] Leijon, M., Danielsson, O., Eriksson, M., Thorburn, K., Bernhoff, H., Isberg, J., Sundberg, J., Ivanova, I., Sjöstedt, E., Ågren, O., et al. (2006). An electrical approach to wave energy conversion. *Renewable energy*, 31(9):1309–1319.

[156] Lesser, J. A. and Su, X. (2008). Design of an economically efficient feed-in tariff structure for renewable energy development. *Energy policy*, 36(3):981–990.

[157] Liberti, L., Carillo, A., and Sannino, G. (2013). Wave energy resource assessment in the mediterranean, the italian perspective. *Renewable Energy*, 50:938–949.

[158] Liu, P. L.-F., Lin, P., Chang, K.-A., and Sakakiyama, T. (1999). Numerical modeling of wave interaction with porous structures. *Journal of waterway, port, coastal, and ocean engineering*, 125(6):322–330.

[159] Liu, Y., Shi, H., Liu, Z., and Ma, Z. (2011). Experiment study on a new designed owc caisson breakwater. In *Power and Energy Engineering Conference (APPEEC), 2011 Asia-Pacific*, pages 1–5. IEEE.

[160] Longuet-Higgins, M. S. (1961). Observations of the directional spectrum of sea waves using the motions of a floating buoy. *Ocean wave spectra*.

[161] Losada, I. J., Dalrymple, R. A., and Losada, M. A. (1993). Water waves on crown breakwaters. *Journal of waterway, port, coastal, and ocean engineering*, 119(4):367–380.

[162] Losada, I. J., Lara, J. L., and del Jesus, M. (2016). *Modeling the interaction of water waves with porous coastal structures*. PhD thesis, American Society of Civil Engineers.

[163] Losada, I. J., Lara, J. L., Guanche, R., and Gonzalez-Ondina, J. M. (2008). Numerical analysis of wave overtopping of rubble mound breakwaters. *Coastal engineering*, 55(1):47–62.

[164] Lucio, D., Tomás, A., Camus, P., Lara, J. L., de Eulate, M. F. Á., Vidal, C., and Losada, Í. J. (2017). Probabilistic hydraulic design verification of the breakwater of laredo's port (cantaria, spain). In *International short course and conference on applied coastal research 2017, Santander, 3rd October – 6th October 2017*.

[165] Magagna, D. and Uihlein, A. (2015). 2014 jrc ocean energy status report. *European Commission Joint Research Centre*.

[166] Malara, G., Gomes, R., Arena, F., Henriques, J., Gato, L., and Falcão, A. (2017a). The influence of three-dimensional effects on the performance of u-type oscillating water column wave energy harvesters. *Renewable Energy*, 111:506–522.

[167] Malara, G., Romolo, A., Fiamma, V., and Arena, F. (2017b). On the modelling of water column oscillations in u-owc energy harvesters. *Renewable Energy*, 101:964–972.

[168] Maliki, A. Y., Musa, M. A., Ahmad, M., Zamri, I., and Omar, Y. (2017). Comparison of numerical and experimental results for overtopping discharge of the obrec wave energy converter. *Journal of Engineering Science and Technology*, 12(5):1337–1353.

[169] Mansard, E. P. and Funke, E. (1980). The measurement of incident and reflected spectra using a least squares method. In *Coastal Engineering 1980*, pages 154–172.

[170] Margheritini, L., Frigaard, P., Vicinanza, D., et al. (2008). Sea slot cone generator overtopping performance in 3d conditions. In *The Eighteenth International Offshore and Polar Engineering Conference*. International Society of Offshore and Polar Engineers.

[171] Margheritini, L., Stratigaki, V., Troch, P., et al. (2012). Geometry optimization of an overtopping wave energy device implemented into the new breakwater of the hanstholm port expansion. In *The Twenty-second International Offshore and Polar Engineering Conference*. International Society of Offshore and Polar Engineers.

[172] Margheritini, L., Vicinanza, D., and Frigaard, P. (2009). Ssg wave energy converter: Design, reliability and hydraulic performance of an innovative overtopping device. *Renewable Energy*, 34(5):1371–1380.

[173] Martin, F. L., Losada, M. A., and Medina, R. (1999). Wave loads on rubble mound breakwater crown walls. *Coastal Engineering*, 37(2):149–174.

[174] Matos, A., Madeira, F., Fortes, C., Didier, E., Poseiro, P., and Jacob, J. (2016). Wave energy at azores islands.

[175] Maximenko, N., Lumpkin, R., and Centurioni, L. (2013). Ocean surface circulation. In *International Geophysics*, volume 103, pages 283–304. Elsevier.

[176] McKenna, J. E. (1997). *Wave forces on caissons and breakwater crown walls.* PhD thesis, Queen's University of Belfast.

[177] McStay, P. (1995). *An Experimental Study of Cylindrical Oscillating Water Column Wave Power Devices*. PhD thesis, MSc. Thesis, The Queen's University of Belfast.

[178] Medina-Lopez, E., Allsop, N., Dimakopoulos, A., and Bruce, T. (2015). Conjectures on the failure of the owc breakwater at mutriku. In *Proceedings of Coastal Structures and Solutions to Coastal Disasters Joint Conference, Boston, Massachusetts*.

[179] Minikin, R. C. R. (1963). *Winds, waves, and maritime structures: Studies in harbour making and in the protection of coasts*. Griffin.

[180] Misra, S., Narayanaswamy, M., Bayram, A., and Shi, F. (2011). Optimization of caisson breakwater superstructure geometry using a 2dv rans-vof numerical model. *Coastal Engineering Proceedings*, 1(32):49.

[181] Mittal, R. and Iaccarino, G. (2005). Immersed boundary methods. *Annu. Rev. Fluid Mech.*, 37:239–261.

[182] Molines, J., Herrera, M. P., and Medina, J. R. (2018). Estimations of wave forces on crown walls based on wave overtopping rates. *Coastal Engineering*, 132:50–62.

[183] Morihira, M. and Kunita, O. (1979). Model experiments on hydraulic characteristics of sloped wall breakwater. *Coast. Eng. Japan*, 26:288–295.

[184] Mork, G., Barstow, S., Kabuth, A., and Pontes, M. T. (2010). Assessing the global wave energy potential. In *ASME 2010 29th International conference on ocean, offshore and arctic engineering*, pages 447–454. American Society of Mechanical Engineers.

[185] Müller, G. and Whittaker, T. (1993). An investigation of breaking wave pressures on inclined walls. *Ocean engineering*, 20(4):349–358.

[186] Muller, G. and Whittaker, T. (1995). Field measurements of breaking wave loads on a shoreline wave power station. *Water and Maritime Engineering*, 112(3):167–172.

[187] Musa, M. A., Maliki, A. Y., Ahmad, M. F., Sani, W. N., Yaakob, O., and Samo, K. (2017). Numerical simulation of wave flow over the overtopping breakwater for energy conversion (obrec) device. *Procedia engineering*, 194:166–173.

[188] Mustapa, M., Yaakob, O., Ahmed, Y. M., Rheem, C.-K., Koh, K., and Adnan, F. A. (2017). Wave energy device and breakwater integration: A review. *Renewable and Sustainable Energy Reviews*, 77:43–58.

[189] Nakada, H., Ohneda, H., Takahashi, S., Shikamori, M., and Nakazono, T. (1992). Field experiments of a wave power converter with caisson breakwater. In *Renewable Energy, Technology and the Environment (Third Edition)*, pages 2530–2535. Elsevier.

[190] Naty, S., Viviano, A., and Foti, E. (2016). Wave energy exploitation system integrated in the coastal structure of a mediterranean port. *Sustainability*, 8(12):1342.

[191] Negro, V., Varela, O., García, J., and López, J. (2008). Diseño de diques verticales. *Colegio de Ingenieros de Caminos, Colección Seinor*, (26).

[192] Negro Valdecantos, V. (2008). Las formas en la ingeniería del mar. *Ingeniería y Territorio*, 2(84):4–9.

[193] Negro Valdecantos, V., López Gutiérrez, J. S., and Polvorinos Flors, J. I. (2013). Comparative study of breakwater crown wall–calculation methods. In *Proceedings of the Institution of Civil Engineers-Maritime Engineering*, volume 166, pages 25–41. Thomas Telford (ICE Publishing).

[194] Negro Valdecantos, V., Martín Antón, M., Campo Yagüe, J. M. d., López Gutiérrez, J. S., and Esteban Pérez, M. D. (2018). Crown walls in mass and reinforced concrete: The way to aesthetics in maritime works. ICE.

[195] Neumann, F. and Le Crom, I. (2011). Pico owc-the frog prince of wave energy? recent autonomous operational experience and plans for an open real-sea test centre in semi-controlled environment. In *Proceedings of the 9th European wave and tidal energy conference (EWTEC 2011), Southampton, UK*.

[196] Neumann, F., Sarmento, A., et al. (2001). Owc-caisson economy and its dependency on breaking wave design loads. In *The Eleventh International Offshore and Polar Engineering Conference*. International Society of Offshore and Polar Engineers.

[197] Neves, M. G., Reis, M. T., Losada, I. J., and Hu, K. (2008). Wave overtopping of póvoa de varzim breakwater: physical and numerical simulations. *Journal of waterway, port, coastal, and ocean engineering*, 134(4):226–236.

[198] Niiler, P. (2001). .1 the world ocean surface circulation. In *International Geophysics*, volume 77, pages 193–204. Elsevier.

[199] Nørgaard, J. Q. H., Andersen, L. V., Andersen, T. L., and Burcharth, H. F. (2012). Displacement of monolithic rubble-mound breakwater crown-walls. *Coastal Engineering Proceedings*, 1(33):7.

[200] Nørgaard, J. Q. H., Andersen, T. L., and Burcharth, H. F. (2013). Wave loads on rubble mound breakwater crown walls in deep and shallow water wave conditions. *Coastal Engineering*, 80:137–147.

[201] OCDI (2009). *Technical standards and commentaries for port and harbour facilities in Japan*. Overseas Coastal Area Development Institute of Japan.

[202] Oliveira, P., Taveira-Pinto, F., Morais, T., and Rosa-Santos, P. (2016a). Experimental evaluation of the effect of wave focusing walls on the performance of the sea-wave slot-cone generator. *Energy Conversion and Management*, 110:165–175.

[203] Oliveira, P., Taveira-Pinto, F., Morais, T., and Rosa-Santos, P. (2016b). Performance enhancement of an overtopping based wave energy converter. In *Proceedings of the 6th International Conference on the Application of Physical Modelling in Coastal and Port Engineering and Science, Ottawa, Canada*.

[204] Oumeraci, H. (1994). Review and analysis of vertical breakwater failures - lessons learned. *Coastal Engineering*, 22(1-2):3–29.

[205] Oumeraci, H. (1999). Strengths and limitations of physical modelling in coastal engineering–synergy effect with numerical modelling and field measurement. In *Proceedings of HYDRALAB-workshop in Hannover, Germany*, pages 7–38.

[206] Oumeraci, H., Klammer, P., and Partenscky, H. (1993). Classification of breaking wave loads on vertical structures. *Journal of waterway, port, coastal, and ocean engineering*, 119(4):381–397.

[207] Oumeraci, H., Kortenhaus, A., Allsop, W., de Groot, M., Crouch, R., Vrijling, H., and Voortman, H. (2001). *Probabilistic design tools for vertical breakwaters*. CRC Press.

[208] Oumeraci, H. and Partenscky, H. (1991). Wave-induced pore pressure in rubble mound breakwaters. In *Coastal Engineering 1990*, pages 1334–1347.

[209] Palma, G., Contestabile, P., Mizar Formentin, S., Vicinanza, D., and Zanuttigh, B. (2016). Design optimization of a multifunctional wave energy device. In *Progress in Renewable Energies Offshore: Proceedings of the 2nd International Conference on Renewable Energies Offshore (RENEW2016), Lisbon, Portugal, 24-26 October 2016*, page 235. CRC Press.

[210] Patterson, C., Dunsire, R., and Hillier, S. (2010). Development of wave energy breakwater at siadar, isle of lewis. In *Coasts, marine structures and breakwaters: Adapting to change: Proceedings of the 9th international conference organised by the Institution of Civil Engineers and held in Edinburgh on 16 to 18 September 2009*, pages 1–738. Thomas Telford Ltd.

[211] Pearson, J., Bruce, T., Allsop, W., Kortenhaus, A., and Van Der Meer, J. (2005). Effectiveness of recurve walls in reducing wave overtopping on seawalls and breakwaters. In *Coastal Engineering 2004: (In 4 Volumes)*, pages 4404–4416. World Scientific.

[212] Pedersen, J. (1996). *Wave Forces and Overtopping on Crown Walls of Rubble Mound Breakwaters: an Experimental Study*. PhD thesis, Aalborg University.

[213] Pedersen, J. and Burcharth, H. F. (1993). Wave forces on crown walls. In *Coastal Engineering 1992*, pages 1489–1502.

[214] Portilla, J., Ocampo-Torres, F. J., and Monbaliu, J. (2009). Spectral partitioning and identification of wind sea and swell. *Journal of atmospheric and oceanic technology*, 26(1):107–122.

[215] Portilla-Yandún, J., Cavaleri, L., and Van Vledder, G. P. (2015). Wave spectra partitioning and long term statistical distribution. *Ocean Modelling*, 96:148–160.

[216] Preen, S. and Robertshaw, G. (2010). Development of a generic caisson design for an oscillating water column power generator. In *Coasts, marine structures and breakwaters: Adapting to change: Proceedings of the 9th international conference organised by the Institution of Civil Engineers and held in Edinburgh on 16 to 18 September 2009*, pages 2–266. Thomas Telford Ltd.

[217] Raju, V., Jayakumar, J., Neelamani, S., et al. (1992). Concrete caisson for also kw wave energy pilot plant: Design, construction and installation aspects. In *The Second International Offshore and Polar Engineering Conference*. International Society of Offshore and Polar Engineers.

[218] Raosa, A. N., Zanuttigh, B., Lara, J. L., and Hughes, S. (2012). 2dv rans-vof modelling of depths and velocities of overtopping waves at overwashed dikes. *Coastal Engineering Proceedings*, 1(33):62.

[219] Ravindran, M. (1995). Indian wave energy programme-progress and future plans. In *Proc. of the 2ˆ< nd> European wave power conf.*, pages 14–19.

[220] Research, C. I., Association, I., en Regelgeving (Netherlands), C. C. U. R., and d'études maritimes et fluviales (France), C. (2007). *The Rock Manual: The use of rock in hydraulic engineering*, volume 683. Ciria.

[221] Rodi, W. (2017). *Turbulence models and their application in hydraulics*. Routledge.

[222] Romano, A., Bellotti, G., Briganti, R., and Franco, L. (2015). Uncertainties in the physical modelling of the wave overtopping over a rubble mound breakwater: the role of the seeding number and of the test duration. *Coastal Engineering*, 103:15–21.

[223] Sainflou, G. (1928). Essai sur les digues maritimes verticales. *Annales de ponts et chaussées, vol 98, tome II, 1928 (4) pp 5-48*.

[224] Salerno, D. (2011). *Experimental investigation on an overtopping wave energy converter*. PhD thesis, University of Naples "Federico II", Naples, Italy, (in Italian).

[225] Saville, T. (1962). An approximation of the wave run-up frequency distribution. *Coastal Engineering Proceedings*, 1(8):4.

[226] Schäffer, H. and Jakobsen, K. (2003). Non-linear wave generation and active absorption in wave flumes. In *Long Waves Symposium, Thessaloniki, Greece*.

[227] Schäffer, H. A. and Klopman, G. (2000). Review of multidirectional active wave absorption methods. *Journal of waterway, port, coastal, and ocean engineering*, 126(2):88–97.

[228] Schmidt, R., Oumeraci, H., and Partenscky, H.-W. (1993). Impact loads induced by plunging breakers on vertical structures. In *Coastal Engineering 1992*, pages 1545–1558.

[229] Schüttrumpf, H. and van Gent, M. R. (2003). Wave overtopping at seadikes. *ASCE, proc. Coastal Structures 2003*, pages 431–443.

[230] Seed, M. and Langston, D. (2010). Wave energy – towards commercialization. In *International Conference on Ocean Energy (ICOE 2010), 06-08 October 2010, Bilbao, Spain.*

[231] Shih, R. and Anastasiou, K. (1992). Laboratory study of the wave-induced vertical loading on platform decks[video recording and impact pressure measurements on a perspex model in wave flume]. *Proceedings of the Institution of Civil Engineers: Water Maritime and Energy*, 96:19–33.

[232] Strati, F. M., Malara, G., and Arena, F. (2016). Performance optimization of a u-oscillating-water-column wave energy harvester. *Renewable Energy*, 99:1019–1028.

[233] Suchithra, N. and Koola, P. M. (1995). A study of wave impact of horizontal slabs. *Ocean Engineering*, 22(7):687–697.

[234] Suh, K.-D., Kim, S.-W., Mori, N., and Mase, H. (2011). Effect of climate change on performance-based design of caisson breakwaters. *Journal of Waterway, Port, Coastal, and Ocean Engineering*, 138(3):215–225.

[235] Suzuki, M., Arakawa, C., Takahashi, S., et al. (2004). Performance of wave power generating system installed in breakwater at sakata port in japan. In *The Fourteenth International Offshore and Polar Engineering Conference*. International Society of Offshore and Polar Engineers.

[236] Takahashi, S. (1988). A study on design of a wave power extracting caisson breakwater. *Wave Power Laboratory, Port and Harbour Research Institute, Japan*.

[237] Takahashi, S. (1991). Experimental study on wave forces acting on perforated caisson breakwaters. *Rep. Port Harbor Res. Inst.*, 30(4):3–34.

[238] Takahashi, S. (1994). A proporsal of impulsive pressure coefficient for design of composite breakwater. In *Proceedings of the International Conference on Hydro-Technical Engineering for Port and Harbor Construction, 1994*, volume 1, pages 489–504.

[239] Takahashi, S. (2002). Design of vertical breakwaters. Technical report, Citeseer.

[240] Takahashi, S., Hosoyamada, S., and Yamamoto, S. (1994a). Hydrodynamic characteristics of sloping-top caissons. In *Proceedings of International Conference on Hydrotechnical Engineering for Port and Harbour Construction PHRI*.

[241] Takahashi, S., Nakada, H., Ohneda, H., and Shikamori, M. (1992). Wave power conversion by a prototype wave power extracting caisson in sakata port. *Coastal Engineering Proceedings*, 1(23).

[242] Takahashi, S., Shimosako, K., et al. (1994b). Wave pressure on a perforated wall caisson. In *Proceedings of the International Conference on Hydro-Technical Engineering for Port and Harbour Construction, Yokosuka*.

[243] Takahashi, S., Tanimoto, K., and Shimosako, K. (1990). Wave and block forces on a caisson covered with wave dissipating blocks. *Report of Port and Harbor Research Institute, Yokosuka, Japan*, 30(4):3–34.

[244] Takahashi, S., Tanimoto, K., and Shimosako, K. (1993). Experimental study of impulsive pressures on composite breakwaters - fundamental feature of impulsive pressure and the impulsive pressure coefficient-. In *Rept. of Port and Harbour Research Institute*, volume 31(5), pages 33–72.

[245] Tallet, P. and Marouard, G. (2014). The harbor of khufu on the red sea coast at wadi al-jarf, egypt. *Near Eastern Archaeology (NEA)*, 77(1):4–14.

[246] Tanimoto, K. (1982). Theoretical and experimental study of reflection coefficient for wave dissipating caisson with a permeable front wall. *Report of the Port and Harbour Research Institute*, 21(3):44–77.

[247] Tanimoto, K. (1987a). Structures and hydraulic characteristics of breakwater (in japanese). *Report of Port and Harbour Research Institute*, 26:11–55.

[248] Tanimoto, K. (1987b). Structures and hydraulic characteristics of breakwater (in japanese). *Report of Port and Harbour Research Institute*, 26:11–55.

[249] Tanimoto, K. and Kimura, K. (1985). A hydraulic experiment study on trapezoidal caisson breakwaters. *Technical Note*, (528).

[250] Terray, E. A., Brumley, B. H., and Strong, B. (1999). Measuring waves and currents with an upward-looking adcp. In *Current Measurement, 1999. Proceedings of the IEEE Sixth Working Conference on*, pages 66–71. IEEE.

[251] Thiruvenkatasamy, K., Neelamani, S., and Sato, M. (2005). Nonbreaking wave forces on multiresonant oscillating water column wave power caisson breakwater. *Journal of waterway, port, coastal, and ocean engineering*, 131(2):77–84.

[252] Thorpe, T. (1995). *An assessment of the art OSPREY wave energy device*. ETSU.

[253] Torre-Enciso, Y., Marqués, J., and López de Aguileta, L. (2010). Mutriku. lessons learnt. In *Proceedings of the 3rd international conference on ocean energy*.

[254] Torre-Enciso, Y., Ortubia, I., de Aguileta, L. L., and Marqués, J. (2009). Mutriku wave power plant: from the thinking out to the reality. In *Proceedings of the 8th European Wave and Tidal Energy Conference, Uppsala, Sweden*, volume 710.

[255] Torres-Freyermuth, A., Losada, I. J., and Lara, J. L. (2007). Modeling of surf zone processes on a natural beach using reynolds-averaged navier-stokes equations. *Journal of Geophysical Research: Oceans*, 112(C9).

[256] Toumazis, A., Shih, W., and Anastasiou, K. (1989). Wave impact loading on horizontal and vertical plates. In *Proc. IAHR 89 Conf., Ottawa, Canada*, pages 21–25.

[257] Troch, P., De Rouck, J., and Burcharth, H. F. (2003). Experimental study and numerical modeling of wave induced pore pressure attenuation inside a rubble mound breakwater. In *Coastal Engineering 2002: Solving Coastal Conundrums*, pages 1607–1619. World Scientific.

[258] Tseng, R.-S., Wu, R.-H., and Huang, C.-C. (2000). Model study of a shoreline wave-power system. *Ocean Engineering*, 27(8):801–821.

[259] USACE (1984). Shore protection manual. *Army Engineer Waterways Experiment Station, Vicksburg, MS. 2v*, pages 37–53.

[260] USACE (2002). Coastal engineering manual. *Engineer Manual*, 1110:2–1100.

[261] Van der Meer, J. and Benassai, E. (1985). Wave forces and impacts on a circular and square caisson. In *Coastal Engineering 1984*, pages 2920–2932.

[262] Van der Meer, J., d'Angremond, K., and Juhl, J. (1995). Probabilistic calculations of wave forces on vertical structures. In *Coastal Engineering 1994*, pages 1754–1767.

[263] Van Der Meer, J., Provoost, Y., and Steendam, G. J. (2012). The wave run-up simulator, theory and first pilot test. *Coastal Engineering Proceedings*, 1(33):65.

[264] van der Meer, J. and Sigurdarson, S. (2016). *Design and construction of berm breakwaters*. World Scientific Publishing Company.

[265] Van der Meer, J. W. (1995). Conceptual design of rubble mound breakwaters. In *Advances In Coastal And Ocean Engineering: (Volume 1)*, pages 221–315. World Scientific.

[266] van der Meer, J. W., Allsop, W., Bruce, T., De Rouck, J., Pullen, T., Schuttrumph, H., Troch, P., and Zanuttigh, B. (2017). Update of the eurotop manual: New insights on wave overtopping. *Coastal Engineering Proceedings*, 1(35):40.

[267] Van der Meer, J. W. and Stam, C.-J. M. (1992). Wave runup on smooth and rock slopes of coastal structures. *Journal of Waterway, Port, Coastal, and Ocean Engineering*, 118(5):534–550.

[268] Van Doorslaer, K., De Rouck, J., Audenaert, S., and Duquet, V. (2015). Crest modifications to reduce wave overtopping of non-breaking waves over a smooth dike slope. *Coastal Engineering*, 101:69–88.

[269] van Gent, M. (1995). *Wave Interaction with Permeable Coastal Structures*. PhD thesis, Civil Engineering and Geosciences, Delft University.

[270] Van Gent, M. R., Smale, A. J., and Kuiper, C. (2004). Stability of rock slopes with shallow foreshores. In *Coastal Structures 2003*, pages 100–112.

[271] Vanneste, D. and Troch, P. (2012). An improved calculation model for the wave-induced pore pressure distribution in a rubble-mound breakwater core. *Coastal Engineering*, 66:8–23.

[272] Venu, M. (2012). Innovation lost to the waves.

[273] Vicinanza, D., Cappietti, L., Ferrante, V., and Contestabile, P. (2011a). Estimation of the wave energy in the italian offshore. *Journal of Coastal Research*, (64):613.

[274] Vicinanza, D., Ciardulli, F., Buccino, M., Calabrese, M., and Koefed, J. (2011b). Wave loadings acting on an innovative breakwater for energy production. *Journal of Coastal Research*, (64):608.

[275] Vicinanza, D., Contestabile, P., and Ferrante, V. (2013a). Wave energy potential in the north-west of sardinia (italy). *Renewable Energy*, 50:506–521.

[276] Vicinanza, D., Contestabile, P., Nørgaard, J. Q. H., and Andersen, T. L. (2014). Innovative rubble mound breakwaters for overtopping wave energy conversion. *Coastal Engineering*, 88:154–170.

[277] Vicinanza, D., Dentale, F., Salerno, D., Buccino, M., et al. (2015). Structural response of seawave slot-cone generator (SSG) from random wave CFD simulations. In *Proceedings of the International Offshore and Polar Engineering Conference*, pages 985–991.

[278] Vicinanza, D. and Frigaard, P. (2008). Wave pressure acting on a seawave slot-cone generator. *Coastal Engineering*, 55(6):553–568.

[279] Vicinanza, D., Margheritini, L., Kofoed, J. P., and Buccino, M. (2012a). The ssg wave energy converter: Performance, status and recent developments. *Energies*, 5(2):193–226.

[280] Vicinanza, D., Nørgaard, J. H., Contestabile, P., and Andersen, T. L. (2013b). Wave loadings acting on overtopping breakwater for energy conversion. *Journal of Coastal Research*, 65(sp2):1669–1674.

[281] Vicinanza, D., Stagonas, D., Müller, G., Nørgaard, J. H., and Andersen, T. L. (2012b). Innovative breakwaters design for wave energy conversion. *Coastal Engineering Proceedings*, 1(33):1.

[282] Victor, L., Troch, P., and Kofoed, J. P. (2011). On the effects of geometry control on the performance of overtopping wave energy converters. *Energies*, 4(10):1574–1600.

[283] Vílchez, M., Clavero, M., Lara, J. L., and Losada, M. A. (2016a). A characteristic friction diagram for the numerical quantification of the hydraulic performance of different breakwater types. *Coastal Engineering*, 114:86–98.

[284] Vílchez, M., Clavero, M., and Losada, M. A. (2016b). Hydraulic performance of different non-overtopped breakwater types under 2d wave attack. *Coastal Engineering*, 107:34–52.

[285] Viviano, A., Naty, S., and Foti, E. (2018). Scale effects in physical modelling of a generalized owc. *Ocean Engineering*, 162:248–258.

[286] Viviano, A., Naty, S., Foti, E., Bruce, T., Allsop, W., and Vicinanza, D. (2016). Large-scale experiments on the behaviour of a generalised oscillating water column under random waves. *Renewable Energy*, 99:875–887.

[287] Vries, J. d. and Bv, D. (2007). Designing a gps-based mini wave buoy. *International Ocean Systems*, 11(3):20.

[288] Whittaker, T., Beattie, W., Folley, M., Boake, C., Wright, A., Osterried, M., and Heath, T. (2004). The limpet wave power project–the first years of operation. *Renewable Energy*.

[289] Zanuttigh, B., Margheritini, L., Gambles, L., and Martinelli, L. (2009). Analysis of wave reflection from wave energy converters installed as breakwaters in harbour. In *Proceedings of the European Wave and Tidal Energy Conference (EWTEC), Uppsala, Sweden*, pages 7–10.

[290] Zanuttigh, B. and van der Meer, J. W. (2008). Wave reflection from coastal structures in design conditions. *Coastal engineering*, 55(10):771–779.

[291] Zelt, J. and Skjelbreia, J. E. (1993). Estimating incident and reflected wave fields using an arbitrary number of wave gauges. In *Coastal Engineering 1992*, pages 777–789.